UCRL 6516

UNIVERSITY OF CALIFORNIA

Ernest O. Lawrence

Radiation Laboratory

PLUTO QUARTERLY REPORT No. 8

LIVERMORE SITE

DISCLAIMER

SECRET

UNCLASSIFIED

UCRL-6516
Nuclear Ramjet
Engines, C-90
M-3679 (25th Ed.)
This document contains 272 pages,
including pp. i-vi and pp. 102a & b.
This is copy 142 of 186 Series A .

UNIVERSITY OF CALIFORNIA
Lawrence Radiation Laboratory
Livermore, California

Contract No. W-7405-eng-48

PLUTO QUARTERLY REPORT NO. 8*

(April-June 1961)

(Title: Unclassified)

by

The Nuclear Propulsion Division Staff

July 3, 1961

*Previous Quarterly Reports

No. 1, UCRL-5699
No. 2, UCRL-5829
No. 3, UCRL-5925
No. 4, UCRL-6036
No. 5, UCRL-6143
No. 6, UCRL-6258
No. 7, UCRL-6376

UNCLASSIFIED

RESTRICTED DATA

This document contains restricted data as defined in the Atomic Energy Act of 1954. Its transmittal or the disclosure of its contents in any manner to an unauthorized person is prohibited.

SECRET

DISTRIBUTION OF THIS DOCUMENT IS UNLIMITED

DISTRIBUTION

Series A

	Copy No.
LRL Livermore,	
Information Division	1 - 15
John S. Foster	16
Forrest Fairbrother	17
C. M. Van Atta	18
Roger E. Batzel	19 - 20
Theodore C. Merkle	21 - 25
Harry L. Reynolds	26
Richard P. Connell	27
James W. Bell	28
Robert W. Westbrook	29
Albert J. Kirschbaum	30
Henry C. McDonald	31
W. Blake Myers	32 - 36
Albert J. Rothman	37
Monte P. Hickenlooper	38
James S. Kane	39
W. E. Humphrey	40
William C. Grayson, Jr.	41
DASA Livermore Liaison Office,	
Norman G. Hunt	42
LRL Berkeley,	
R. K. Wakerling	43
Hayden S. Gordon	44
LRL Mercury, Nevada,	
James L. Olsen	45
Division of Military Application, Washington,	
Brig. Gen. A. W. Betts	46
U. S. Atomic Energy Commission, Washington,	
Irving Hoffman	47 - 48
Advanced Research Projects Agency	49
Air Force Special Weapons Center	50

DISTRIBUTION (Continued)

Series A

	Copy No.
Air Technical Intelligence Center	51
Air University Library	52
Albuquerque Operations Office	53
Allegany Ballistics Laboratory	54
Argonne National Laboratory	55
Army Ballistic Missile Agency	56 - 57
Atomic Energy Commission, Washington	58 - 61
Atomics International	62
Battelle Memorial Institute	63
Brookhaven National Laboratory	64
Bureau of Naval Weapons	65 - 68
Bureau of Naval Weapons (SPO)	69
Bureau of Ships	70
Canoga Park Area Office	71
Chance-Vought Aircraft, Inc., Dallas (BUWEPS)	72
Chicago Operations Office	73
Chicago Patent Group	74
Convair Division, San Diego	75
Convair Division, San Diego (BUWEPS)	76
Defense Atomic Support Agency, Sandia	77
Defense Atomic Support Agency, Washington	78
Director of Defense Research and Engineering (OSD)	79
duPont Company, Aiken	80
General Electric Company (ANPD)	81 - 86
General Electric Company, Richland	87 - 88
Jet Propulsion Laboratory	89
Lockheed Aircraft Corporation, Burbank	90
Los Alamos Scientific Laboratory	91 - 92
Marquardt Corporation	93 - 96
NASA Ames Research Center	97
NASA Flight Research Center	98
NASA George C. Marshall Space Flight Center	99

DISTRIBUTION (Continued)

Series A

	Copy No.
NASA Langley Research Center	100
NASA Lewis Research Center	101 - 105
National Aeronautics and Space Administration, Washington	106 - 107
Naval Air Development Center	108
Naval Ordnance Test Station	109
North American Aviation, Inc., Downey	110
Nuclear Development Corporation of America	111 - 112
Oak Ridge Operations Office	113
Office of the Chief of Naval Operations	114
Patent Branch, Washington	115
Phillips Petroleum Company (NRTS)	116
Pratt and Whitney Aircraft Division	117
RAND Corporation	118 - 119
San Francisco Operations Office	120
Sandia Corporation	121
School of Aviation Medicine	122
Strategic Air Command	123
Union Carbide Nuclear Company (ORNL)	124 - 133
USAF Headquarters	134
USAF Headquarters (OVCS)	135
Wright Air Development Division	136 - 141
Office of Technical Information Extension	142 - 186

UCRL-6516

PLUTO QUARTERLY REPORT NO. 8

Table of Contents

TABLE OF CONVERSIONS

°C	°F	°C	°F	°C	°F
0	32	650	1202	1250	2282
50	122	700	1292	1300	2372
100	212	750	1382	1350	2402
150	302	800	1472	1400	2552
200	392	850	1562	1450	2642
250	482	900	1652	1500	2732
300	572	950	1742	1550	2822
350	662	1000	1832	1600	2912
400	752	1050	1922	1650	3002
450	842	1100	2012	1700	3092
500	932	1150	2102	1750	3182
550	1022	1200	2192	1800	3272
600	1112				

Btu/second-in^3	= 1.82 megawatts/foot^3
Btu/second	= 1.0548 kilowatts
Btu/hour-ft^2-°F	= 5.676×10^{-4} watt/cm^2-°C
Btu/lb-°F	= 1.0 calorie/g-°C
calorie	= 4.186 joules or watt-seconds
pound	= 454 grams
inch	= 2.54 centimeters
cubic foot	= 1728 cubic inches
cubic inch	= 16.387 cubic centimeters
megawatt-day	= 1.05 gram U^{235} fissioned (200 Mev per fission)
pound/ft^2	= 0.4882 gram/centimeter^2
pound/in^2	= 70.30 grams/centimeter^2
barn	= 10^{-24} centimeter^2
gravity (g)	= 980.7 cm/sec^2 = 32.17 ft/sec^2

MUL-14122

UCRL-6516

PLUTO QUARTERLY REPORT NO. 8

(April - June 1961)

Lawrence Radiation Laboratory, University of California
Livermore, California

CHAPTER I. TORY II-A

SECTION I. PRELIMINARY STATEMENT TORY II-A-1

40-Mw POWER RUN

On May 14, 1961, the Tory II-A reactor was run for the first time at substantially high power levels and at temperatures equalling and exceeding the design point. The power level was held at 50 Mw for about two minutes, and was in excess of 10 Mw for sixteen minutes. The average fuel element temperature at the hottest axial station of the core was held at values around 2500°F for about one minute, and remained at a value of 1900°F or greater for fourteen minutes. No damage to the reactor was detected during the run or afterwards.

Data reduction has not progressed far enough to permit presentation of detailed results, but a number of general comments can be made at this time. A complete account will be presented in a separate report.

This run was intended to provide a first test of the reactor at power levels high enough to produce heat balance conditions in the core similar to those expected at design point (in particular, with heat transfer to the air stream predominating over radiation and conductive transfer among core components). A power of 40 Mw was chosen as sufficiently high to meet this condition while still not producing thermal stresses comparable to those expected at the design-point power of 150 Mw.

It was intended that the design-point fuel-element wall temperature of 2250°F should be reached. It was decided before the run that, since some points in the core were likely to show temperatures well above the average over the hottest core region, individual thermocouple readings should be allowed to go as high as 2500°F in order to be sure of bringing the average up to 2250°.

An airflow rate of 120 lb per sec was determined to be appropriate to match these power and temperature levels.

Because of the presence in the bunker airduct of some temporary sections of mild steel, unable to support the design inlet air temperature of 1060°F, air was supplied to the reactor at a temperature of 400°F.

The mode of operation, in brief, would be as follows:

a. Bring reactor airflow rate up to 30 lb/sec, at ambient temperature.
b. Raise reactor inlet air temperature to 400°F.
c. Raise reactor power until peak core temperatures are at 1900°F.
d. Raise power and airflow rate simultaneously, keeping core temperature constant at 1900°F, until flow rate is at 120 lb/sec.
e. Raise power until peak core temperatures average about 2250°F, or until individual thermocouples read 2500°F.
f. Shut down more or less in reverse order.

Following two days postponement for favorable weather, the run was started shortly before noon on May 14, 1961, with all components of the facility and reactor in satisfactory operating condition.

About two hours were occupied with preliminary steps involved in bringing the reactor up to the 100-kw power range, and then about one-half hour in going through the operating sequence listed above.

This procedure was carried out approximately as planned. Figure I-1 shows a history of reactor power, peak core temperature, and airflow rate during the run. The temperature trace is representative only, being taken from an estimated average of data available at the time of writing.

The only striking departure from planned operation is in the core-temperature history. The trace shown represents an average of fuel-element wall temperatures at the hottest axial station of the core. Although the real amplitude of this curve is still uncertain to perhaps 50°F, at the peak it seems clear that the intended value of 2250°F was exceeded by several hundred degrees. Two principle reasons lie behind this: First, it was found to be impossible for the operators to digest all the available data during the run, and the temperature indication to which the nuclear operator was giving most of his attention during the period of highest power happened to be one which gave a reading well below the core average. Second, the core radial-power distribution, and hence temperature distribution, was very flat ($\approx \pm 3$ percent) — consequently the differences from peak to average temperatures which we had

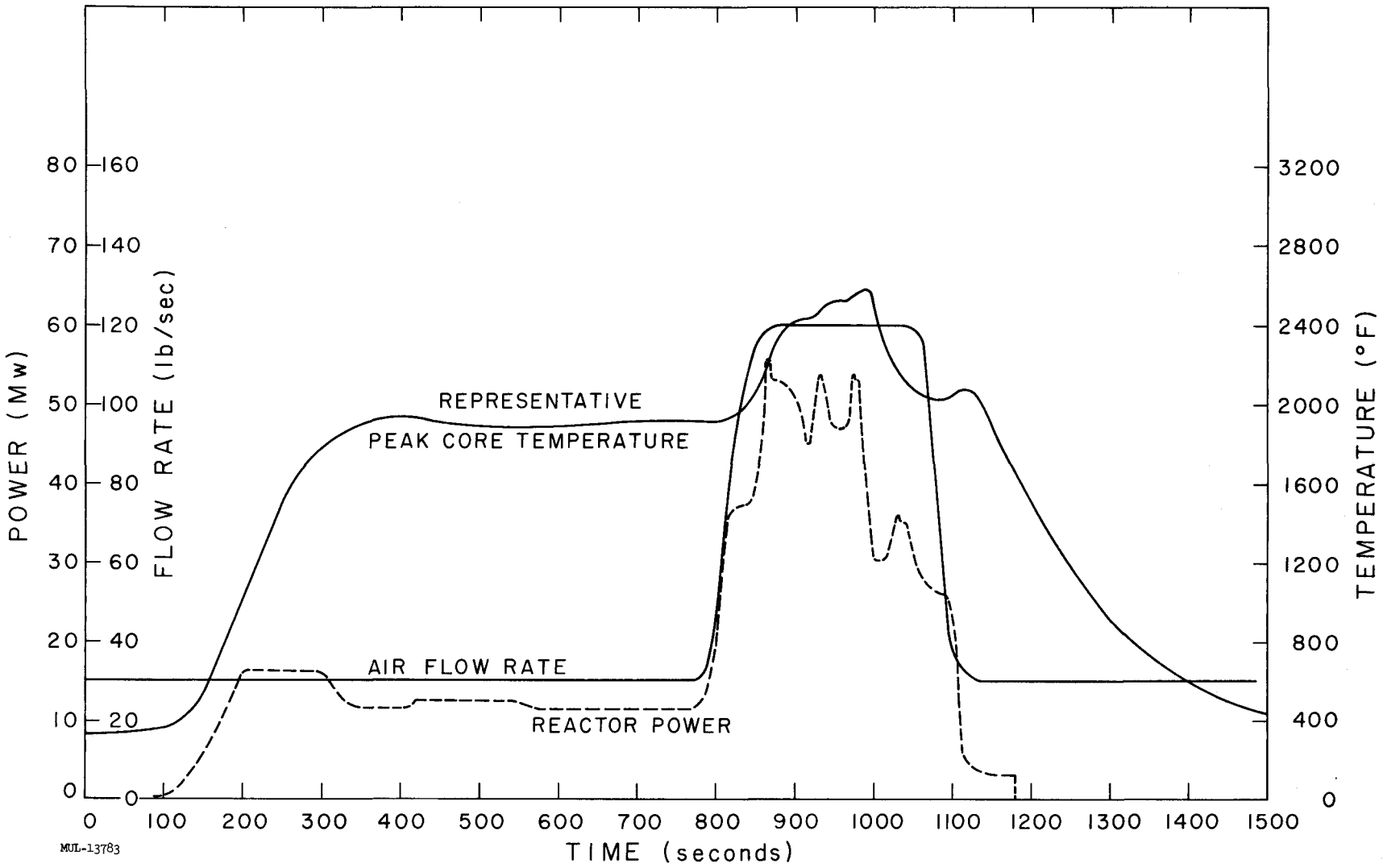

Fig. I-1. Tory II-A intermediate power run, May 14, 1961.

expected that we might encounter did not materialize, and the average came up fairly close to individual peak values.

Preliminary data on detailed behavior of the reactor with respect to heat deposition rates, temperatures, air pressures, radiation levels, and other observed parameters generally confirmed theoretical expectations, and do not indicate that difficulty should be expected in achieving operation at full power.

AERO-THERMODYNAMIC ASPECTS OF TORY II-A-1 OPERATION, MAY 14, 1961 (PRELIMINARY)

Pertinent parameters for the low-flow phase of the test appear to be the following:

a. Flow rate = 30 ± 2 pps.
b. Inlet air total temperature = 400 ± 20°F.
c. Total reactor power = 10 ± 1 Mw.
d. Maximum measured fuel-element temperature = 1991°F.
e. Radial power distribution near reactor midplane appeared to be uniform to ± 3% (azimuthal effects accounted for).
f. Probable average fuel-element temperature at hottest axial station = 1994°F.
g. Probable average unperturbed fuel-element exit-air total temperature = 1876°F.
h. Probable nozzle air total temperature = 1593°F.
i. Measured nozzle air total temperature = 1690°F (evidence of nonmixed conditions).
j. Unperturbed fuel-element temperature deviation at hottest location = 140°F.

Pertinent parameters for the high-power phase of the test appear to be the following:

a. Flow rate = 122 pps ± 5 pps.
b. Inlet air total temperature = 400 ± 20°F.
c. Total reactor power = 50 ± 3 Mw.
d. Maximum measured fuel-element temperature = 2712°F.
e. Radial power distribution near reactor midplane appeared to be uniform to ± 3% (azimuthal effects accounted for).
f. Probable average fuel-element temperature at hottest axial station = 2600°F.

g. Probable average unperturbed fuel-element exit-air total temperature = 2320°F.
h. Probable nozzle air total temperature = 1927°F.
i. Measured nozzle air total temperature = 2064°F (evidence of nonmixed conditions).
j. Measured reactor pressure differential = 31 psi.
k. Probable nozzle total pressure = 35.5 psia.
l. Probable reactor inlet total pressure = 65 psia.
m. Unperturbed fuel-element temperature deviation at hottest location = 280°F.

Reactor structural temperatures were found to be the following at 50 Mw.:

	X/L = 0.71	X/L = 0.92
a. Shroud	549°F	542°F
b. Tie rod	655°F	695°F
c. Slats	2468°F	2599°F
d. Outer links	1658°F	1786°F
e. Wiper seals	1464°F	1427°F
f. Base plate springs	527°F	
g. Tie rod exit hubs	2056°F	
h. Front support structure	503°F	

The temperatures of the water-cooled components were found to be reasonable.

During the test, reactor fuel elements were at temperatures greater than 1900°F for 840 seconds (14 minutes). During the high-power phase of the experiment, fuel elements were at temperatures in excess of 2500°F for 68 seconds. Temperatures in excess of design limit (2550°F) occurred for 14 seconds. Equilibrium conditions were probably not present at the end of this 14-second period.

Reactor volume averaged fueled-element temperature at 50 Mw appears to be 2155°F.

TORY II-A-1, MAY 14, 1961 RUN; FISSION FRAGMENT LOSS

It was expected that fission fragments would be lost from Tory II-A-1 during the demonstration run of 5-14-61. The anticipated loss fraction was 0.001 of the number of fragments made during operation. The observed fraction was 1/16 of this, or 6×10^{-5}. The latter fraction is accurate to an order of magnitude. Pertinent comments are listed below:

1. Altitude at test point: 4400 ft M.S.L. (mean sea level).
2. Wind direction during run: W.-S.W.
3. Wind velocity during run: 15-20 mph.
4. A stable layer of air existed above 6000 ft M.S.L. (i.e., 1600 ft above ground level). There was no inversion. However, the stable layer acted to confine the effluent to altitudes below 6000 ft M.S.L.
5. As the radioactive cloud moved away toward the northeast, L.R.L. detector No. 3 peaked at 30 mr/hr four minutes after shutdown. (See Figs. I-2, I-3, and I-4). At the same time, detector No. 4 (3500 ft south of No. 3) showed 0.23 mr/hr. Triangulation procedures give an altitude of the radioactive cloud center as 1250 ft above the ground, which is in very good agreement with the earlier conclusion.
6. At the time the cloud passed detector No. 3, it is thought to have been 1.0-mile long, 1500-ft wide, 1000-ft high, and was traveling at 15 mph.
7. During the run, 2.05×10^4 Mw-sec of nuclear power was generated (i.e., 6.8×10^{20} fissions).
8. The reactor lost fragments due to 4.4×10^{16} fissions.
9. The fractional fission fragment loss is 6×10^{-5}.
10. Data from the detectors and the L-20 airplane are not in conflict with the above statements.

SECTION II. NEUTRONICS

The Tory II-A-1 test of May 14, 1961 has been studied in detail to see how well the neutron diffusion calculations agreed with actual experimental results. Specifically, the reactivity costs due to increased temperature were examined. The results of the comparison were extremely gratifying, for the Angie prediction of the required change of control vane angle was within 10 percent of the observed vane-angle change. The radial power density was observed to be flat within ± 3 percent at 50 Mw, which also exceeded expectations.

During the test, the core was sustained at 10 Mw for several minutes and was then taken to 50 Mw for a short time. Table I-1 lists a group of selected parameters at the two power levels and also those values appropriate to the then anticipated test. On the basis of the latter values, predictions were made.

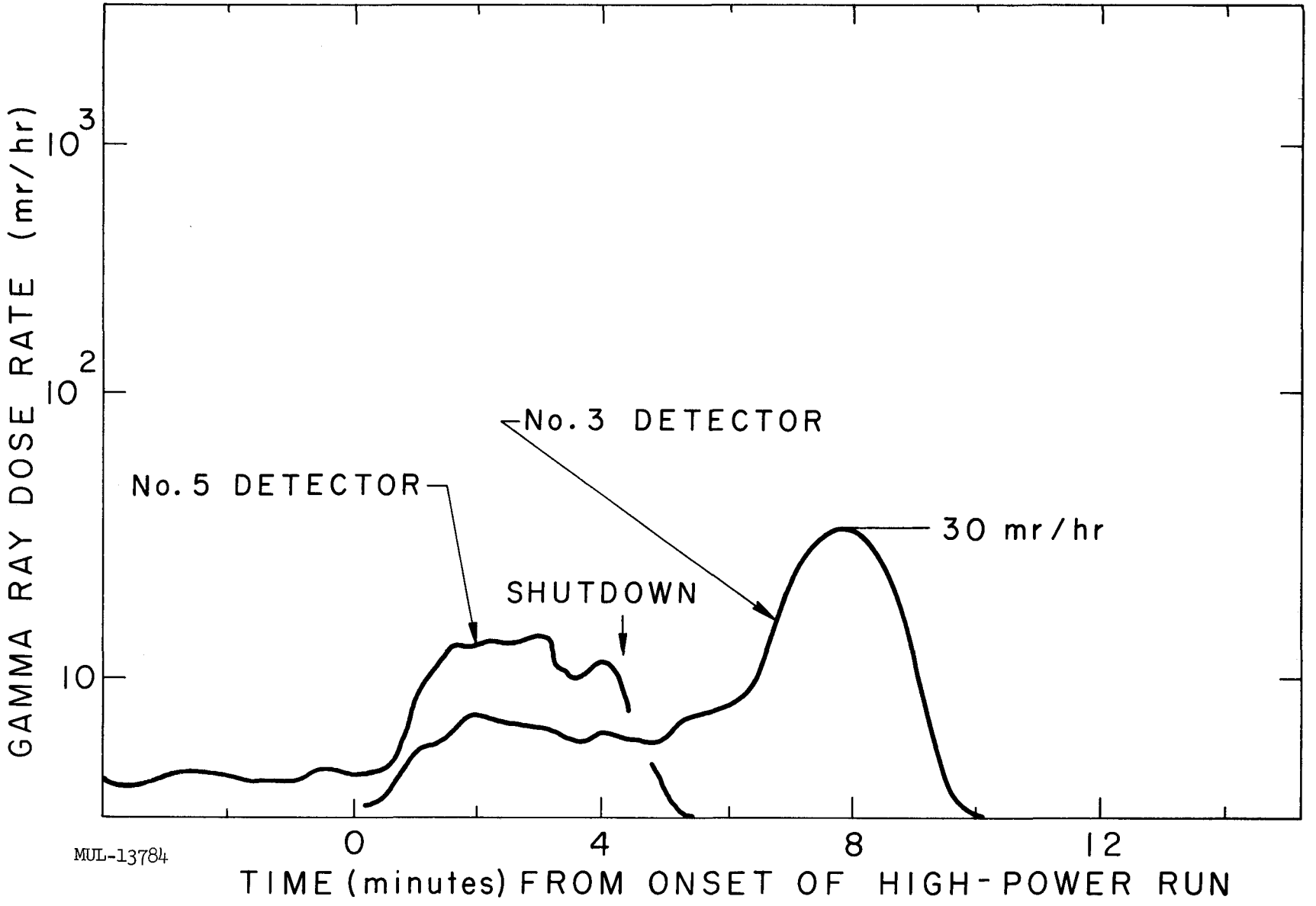

Fig. I-2. Record of radioactive cloud passage over Detector No. 3 (1.3 miles N.E. from reactor). Data from Detector No. 5 (1.3 miles E.-S.E. from reactor) show interval of reactor operation.

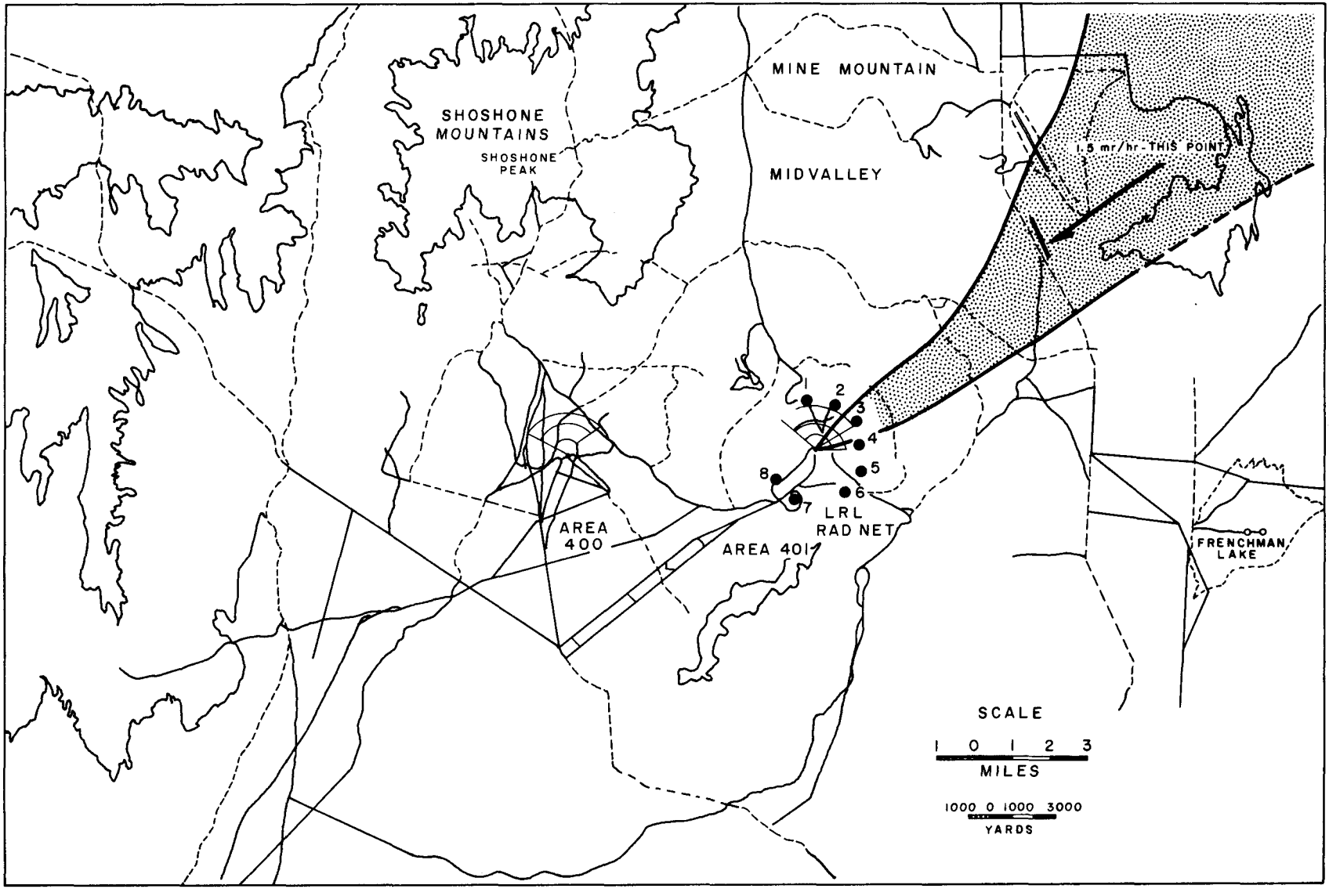

MUL-13839

Fig. I-3. Plan – Tory II-A survey – cloud sampling, May 14, 1961. Maximum reading 1.5 mr/hr (as reported by aerial monitor).

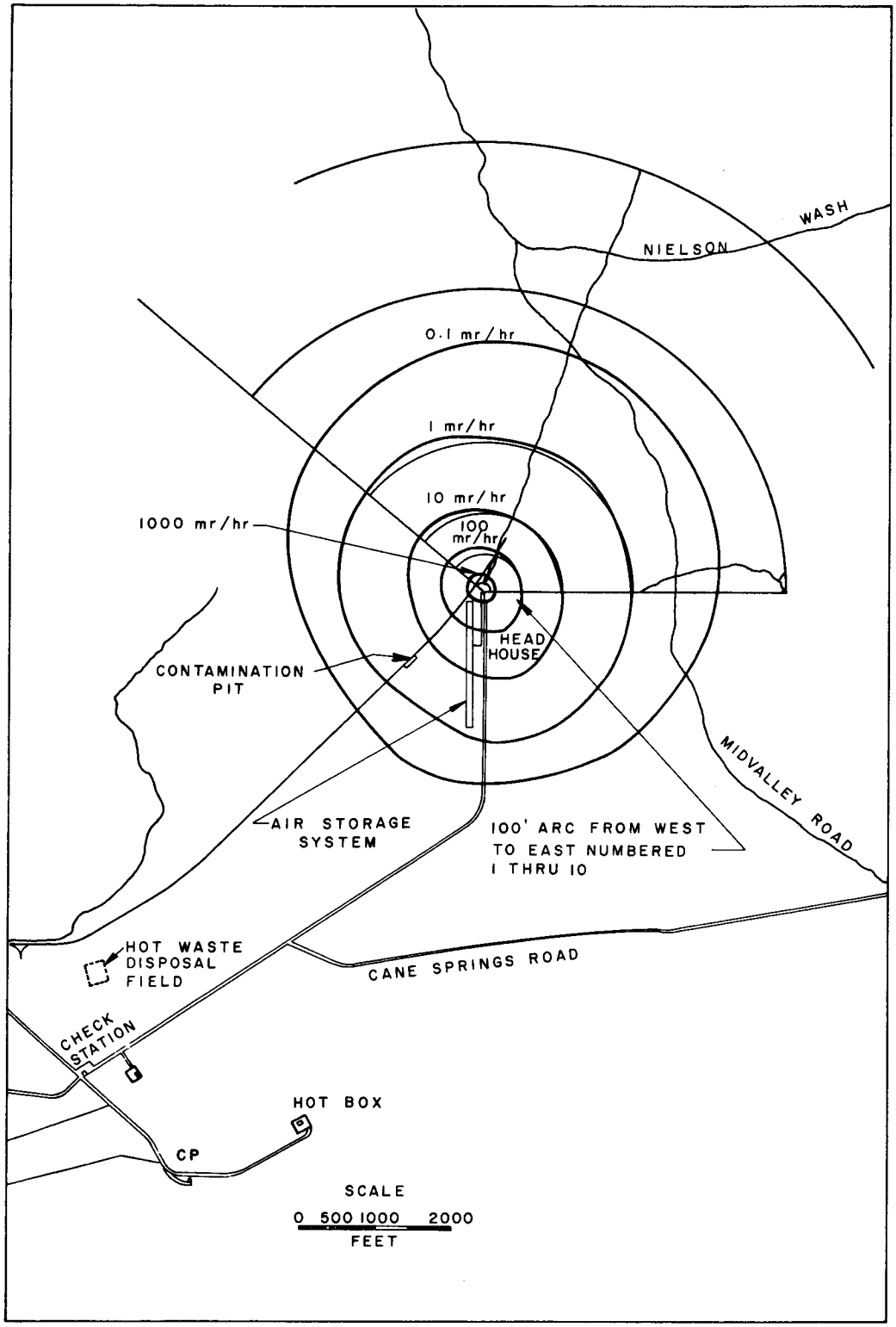

MUL-13840

Fig. I-4. Plan – Tory II-A survey – initial H + 2 hr - 43 min, May 14, 1961, area 401, midtime – 1643, (reactor in place).

Table I-1. Predicted and Measured Parameters for the May 14, 1961 Tory II-A-1 Operation at NTS.

	Measured		Predicted
1. Peak power	10 ± 1 Mw	50 ± 3 Mw	40 Mw
2. Radial power deviation from flat	3%	3%	5%
3. Critical vane angle	88°	100°	95° ± 5°
4. Front support structure temp	499°F	503°F	400°F (assumed)
5. Base plate temp	1876°F	2380°F	1920°F
6. Average fuel-element temperature at hottest axial station	1944°F	2600°F	2250°F

At room temperature, the critical vane angle was found to be 66.7°. Therefore, a 33.3° change in position was realized in going to 50 Mw and 2600°F peak temperature. This represents approximately 3% in reactivity according to calculations, which, although significant, is not a large amount of reactivity. Comparisons between experiment and calculation should be made, recognizing the fact that considerable uncertainty will exist in any conclusion because of the many complications in the Tory II-A-1 design.

An analysis has, nevertheless, been made, and is listed in Table I-2. The Angie calculations furnish a dependence of K_{eff} on vane angle, and this was employed in determining the Δk (exper.) listed below. Calculated geometric effects were separated into axial and radial expansion effects. If these are assumed to be accurately represented in Angie, comparison between the calculated and observed nuclear (i.e., spectrum) effects may be made.

Table I-2. Comparison Between Observed and Predicted Reactivity Effects.

Condition	Fuel temp °F†	Vane angle	$-\Delta k$ (exp)	$-\Delta k$ (axial)	$-\Delta k$ (radial)	$-\Delta k$ (nuclear)	$\frac{\Delta k\,(\text{nucl.})\text{calc}}{\Delta k\,(\text{nucl.})\text{exp}}$*
Room temp		66.7°	--	--	--	--	
Predicted	2250	95.0°	0.0233	0.0049	0.0059	0.0125	(1.00)
10 Mw	1944	88°	0.0205	0.0047	0.0054	0.0121	1.16
50 Mw	2600	100°	0.0290	0.0057	0.0076	0.0158	1.01

* $\Delta k\,(\text{nucl.})_{exp}$ $\Delta k\,(\text{ax.})_{calc}$ $-\Delta k\,(\text{rad.})_{calc}$ = $\Delta k\,(\text{nucl.})\text{calc.}$

† Average fuel tube temperatures at hottest axial station.

An error of ± 1° in vane angle can contribute ± 6% in Δk (nuclear) for the 50 Mw case. Possible "barreling out," or radial swelling of the core can alone account for a 3° increase in vane angle. Approximation of the core in the Angie calculation as isothermal implies a ± 1° uncertainty. Other issues could easily bring the uncertainty in $[\Delta k_c/\Delta k_e]$ nuclear to ± 30%. The equivalent (Δk) uncertainty is only ± 0.003. The above reactivity ratio is not in close accord with a recent finding from calculations applied to a bare BeO Hot Box experiment. There, $[\Delta k_c/\Delta k_e]$ nuclear $\simeq 1.5 \pm 0.3$. "Barreling" of the core would act to decrease $\Delta k(\text{nucl.})_{exp}$ and thereby increase the ratio. Once again we see that basic uncertainties prevent a careful analysis.

Temperatures in the forward cut of the core relative to the center appeared to be much higher than anticipated. Aerothermodynamic calculations indicate that the power density is 15-20% higher relative to the peak than Angie predicted. See Fig. I-5. Additional evidence from the December 9, 1960, fission traverse experiment at room temperature, tends to confirm the disagreement. There, a 15% higher power density relative to the peak is noted in the experiment than in Angie, in the core region close to the forward reflector. The disagreement is not understood.

Calculations show that if the reactor is operated at 2250°F peak temperature and 150 Mw during the forthcoming run, the reactor should be critical at a vane angle of 94°, which is smaller than the value (100°) realized on May 14, 1961. The main reason is that the past test was conducted 350°F in excess of the planned value.

SECTION III. CONTROLS

SUMMARY

All Tory II-A control systems performed satisfactorily during the low-power runs conducted during this quarter and during the 40-Mw run conducted on May 14, 1961. During the run, reactor power was controlled over the range 400 kilowatts to 50 megawatts using automatic log power control. Airflow rate through the reactor was controlled by the airflow operator using the 6-in. pressure control valve (AV-4) in the manual servo mode. There have been no deviations of actual control system performance from intended performance during any of the operations carried out thus far. The automatic power control system has now demonstrated its ability to accurately and safely

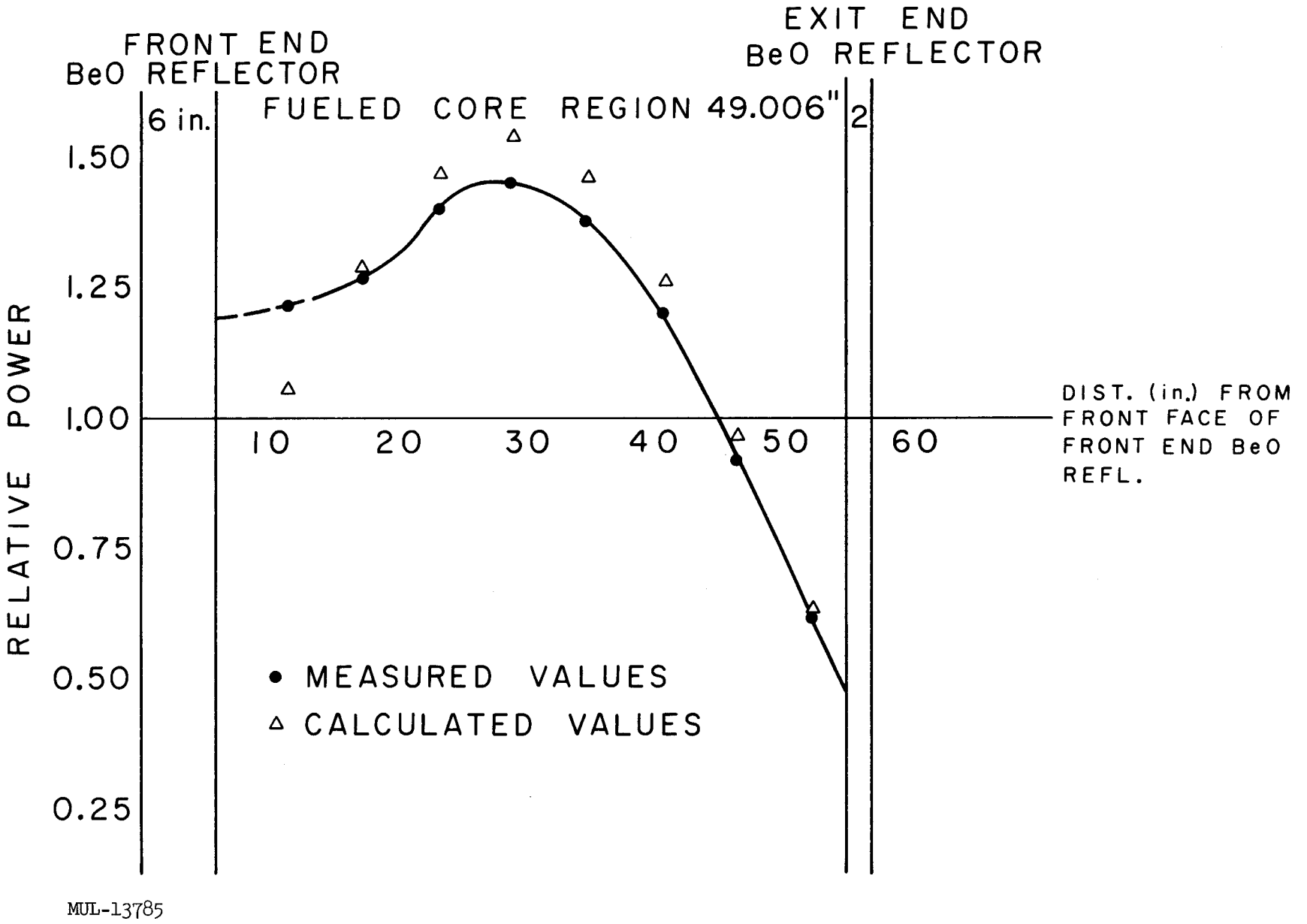

Fig. I-5. Tory II-A-1, best estimate of axial power distribution as deduced from May 14, 1961 demonstration run. Power level, 50 Mw; average core temperature, 2155°F (measured); average core temperature in calculations, 1971°F.

control reactor power level over many decades. All control systems are considered proven for further high-power testing.

TORY II-A OPERATIONS

There were four Tory II-A nuclear runs having significance as regards the control systems.

April 27 Nuclear Run. During this run the reactor transfer function was experimentally verified. The transfer function was determined using frequency response techniques. The vernier rod was used to insert a sinusoidal δk input to the reactor of approximately $\pm 2\,¢$ (± 2.5-inches rod displacement). Log power amplifier P4 was used to detect reactor power-level variation. The reactor transfer function was determined at two power levels: 30 watts and 7 kw. The results are plotted in Figs. I-6 and I-7 along with predicted values, using $\ell^* = 50\mu s$ and $\ell^* = 70\mu s$. As can be seen, there is close correspondence between the predicted and measured transfer function. Based on the measured transfer function, it is concluded that Tory II-A has an $\ell^* \cong 70\mu s$.

May 3 Nuclear Run. The May 3 nuclear run was the first attempt to use automatic log power control. The reactor was taken to approximately 200 kw under manual control at which time a transfer to log power automatic using log power amplifier P1 was attempted. It was intended to demonstrate stability of the automatic log power system at low power levels during this run. A scram occurred at the moment of transfer and operations were concluded pending diagnosis of the scram.

Examination of the run data showed that the vernier rod had not been centered prior to going to the automatic mode as is required, but rather was full out. In the automatic mode, the vernier rod is given an initial demand asking for rod at center position. This difference caused the vernier rod to jump in approximately 30 inches as the mode transfer was made. A power drop resulted which the automatic control system attempted to correct by demanding the rod go back to the full-out position. This positive change in power caused an instantaneous indicated period of approximately 4 seconds and initiated a scram from log power channel P4, which had a period scram level set point at 5 seconds.

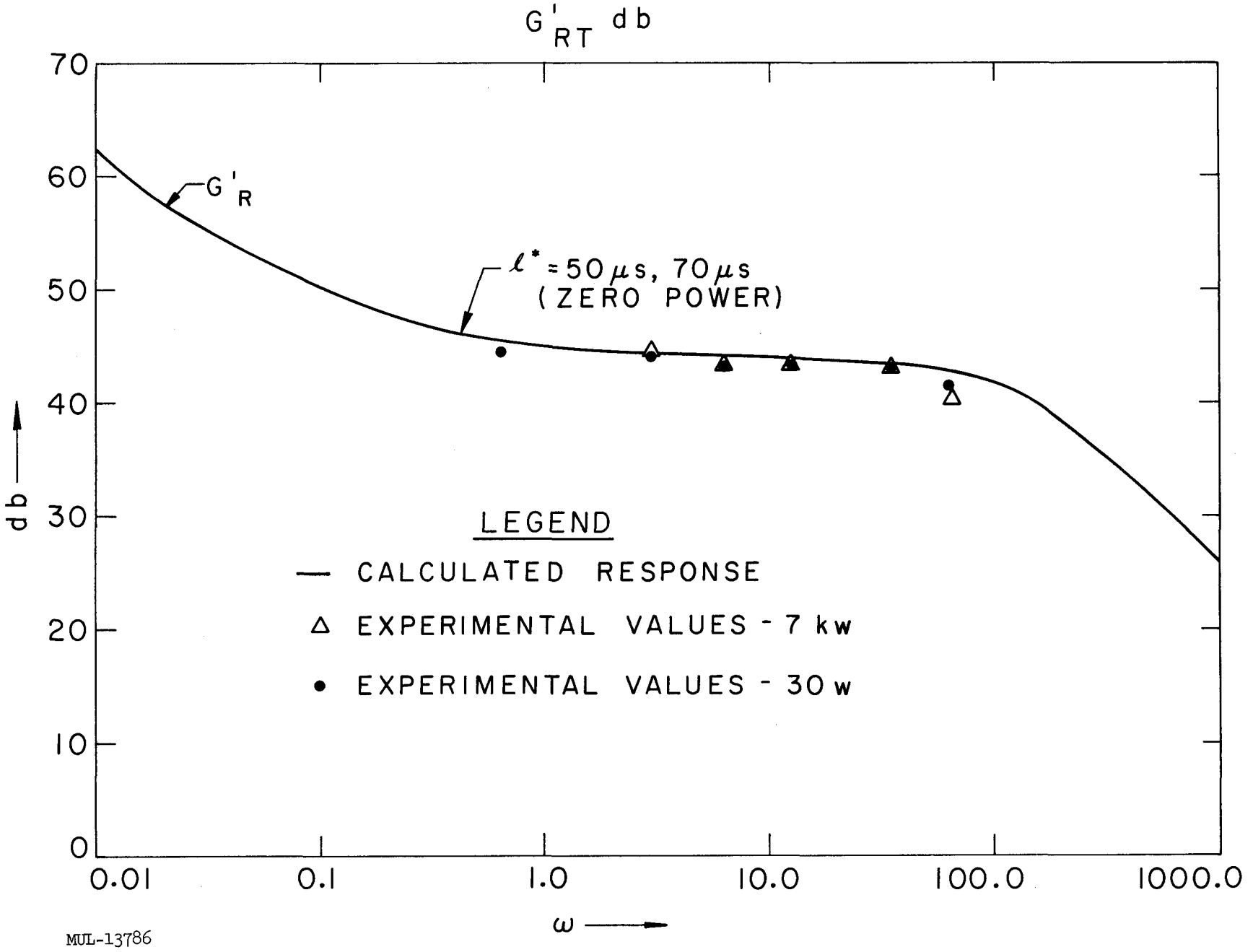

Fig. I-6. Plot of predicted and measured transfer function for Tory II-A-1 showing reactor phase angle as function of angular frequency.

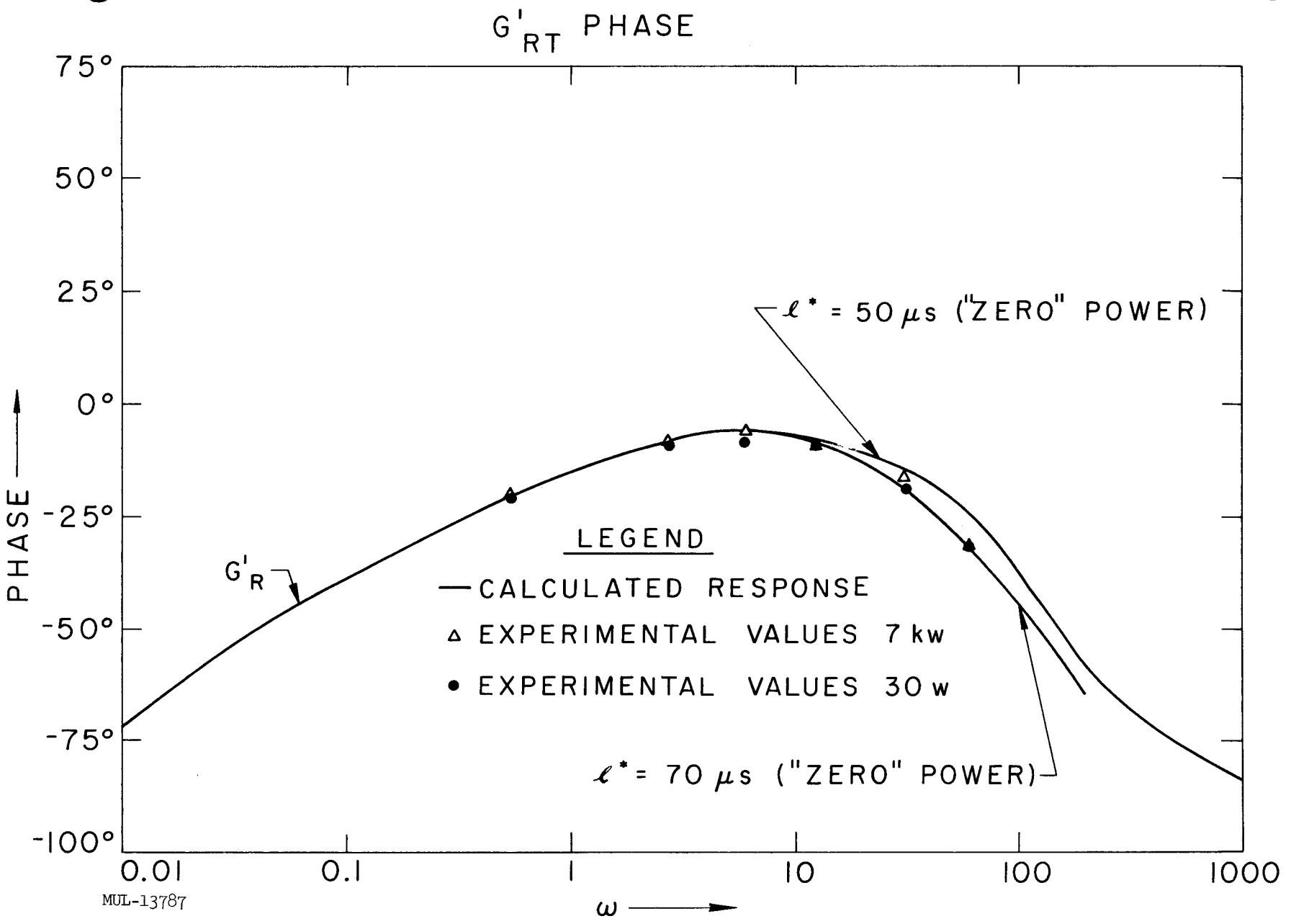

Fig. I-7. Plot of predicted and measured transfer function for Tory II-A-1 showing reactor gain as a function of angular frequency.

This entire series of events was reproduced the following day using a reactor simulation with actual hardware. It was decided on the basis of this information to repeat this run at a lower power level prior to the 40-Mw run.

May 5 Nuclear Run. During the low-power run of May 5, the compensated ion chamber used for control (P4) was positioned just below the core, so that the automatic power control loop could be closed at a low power level thus causing little additional site activation. The reactor was brought critical to a power of 180 watts under manual control. The transfer was then made to automatic log power control without any measureable power or period perturbations. In order to check stability of the power and period closed-loop systems, a rapid increase in power demand to 270 watts, then 1050 watts was scheduled by the nuclear operator. The system response is shown in Fig. I-8 and, as can be observed, both power and period control systems exhibit adequate stability. To check large-signal stability of the power loop, rapid decreases in power demand were programmed to 800 watts, then 180 watts. As seen in Fig. I-8, major corrections of the vernier rod and vanes were required, but the system brought the power level to the demanded value in a stable manner.

Based on the results of this test, it was decided to use automatic log power control during the intermediate and high-power portions of the 40-Mw run.

May 14 40-Mw Run. During this run, the reactor was brought critical and taken to approximately 400 kw under manual control. At this point the power control system was switched to automatic log power control using log power amplifier P1 for power level feedback. System stability was determined by means of positive and negative step changes in power demand before proceeding to higher power levels. The actual programs of power, flow, and temperature conducted are shown elsewhere in this report, so they will not be repeated here. Those items relating to the control systems which are considered to be of interest are itemized below:

1. Airflow rate was controlled throughout the run using AV-4 (6-in. pressure control valve) in the manual servo mode. The maximum flow rate attained was approximately 122 lb/sec.

2. Power level was controlled above 400 kw using automatic log power control. The system was stable and accurate at all power levels covered.

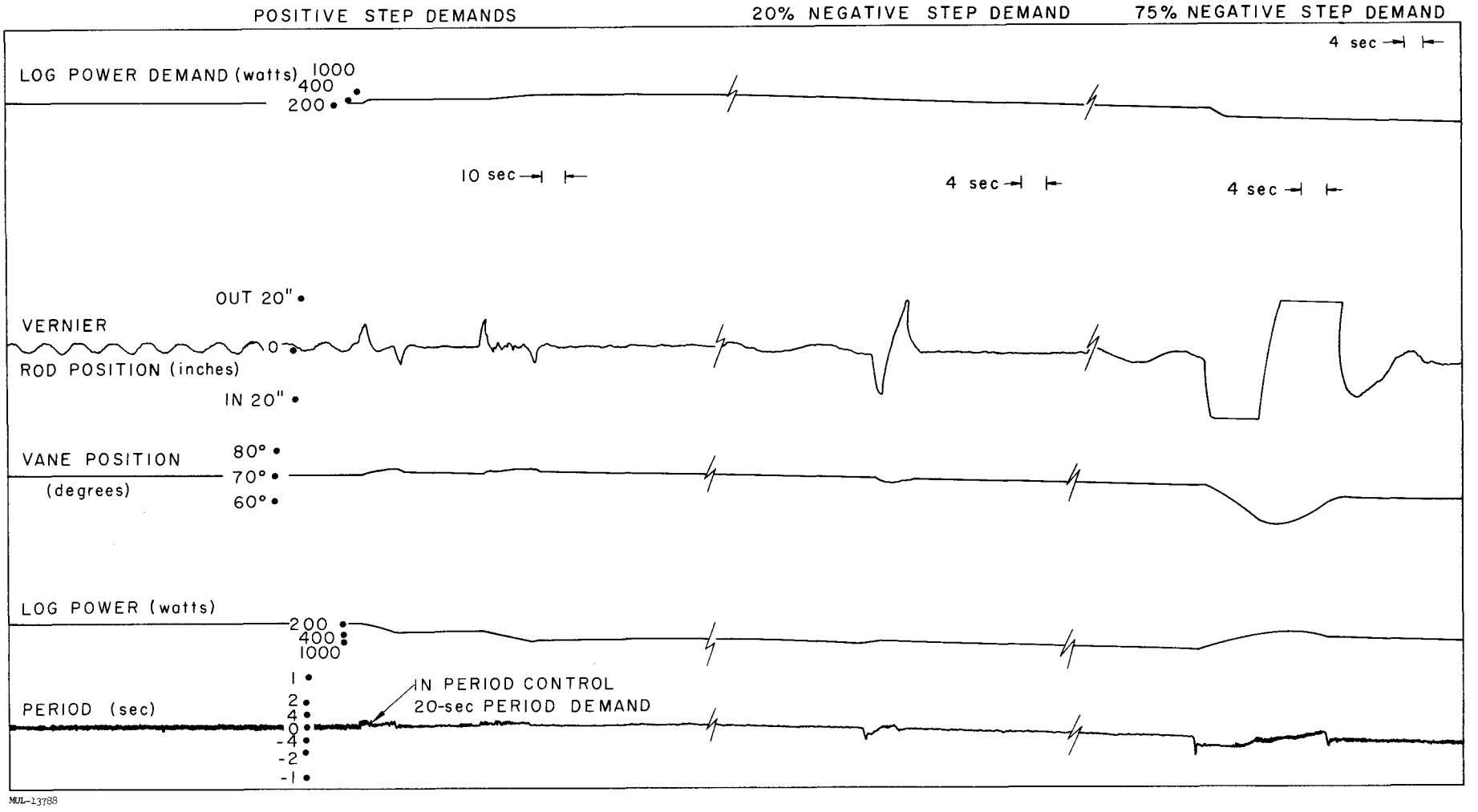

Fig. I-8. Power control system test data as recorded during first automatic control run (May 5, 1961).

3. Set points used during the run were as follows:

Power - Scram set point - 275 Mw
Reset set point - 137 Mw
Period - Scram set point - 1.1 seconds
Reset set point - 2 seconds

4. The reactor was shut down at the end of the run by means of an operator-initiated scram. This deviation from the planned operation was considered desirable because of the extremely slow shut down required in the automatic log power mode. The latter was caused by the slow decay of the 80-second delayed neutron group, with some gamma-n reaction noted also. Figure I-9 shows the test data as recorded during the high-power portion of the 40-Mw run.

Based on the experimental results gained in the above nuclear runs, we can conclude the following:

1. The automatic log power control system has ample stability margin and accuracy in both the large and small signal regions. The system stability margin does not change appreciably with reactor power level. It is concluded that this control mode can be used to control power level in a stable and accurate manner for power levels $\geq$ 100 kw (4 decade range above this value is possible).

2. The automatic inverse-period control provides accurate and stable control of reactor period for period demands $\leq$ 30 seconds for power levels $\geq$ 100 kw (4 decade range).

3. The dual-mode concept (power-period control combination) is a desirable method of reactor control, particularly when controlling the logarithm of power. Here a small demand voltage change appears as a relatively large power change.

4. The fast reset safety principle minimizes the probability of a false scram by allowing the operator to set scram levels quite high without jeopardizing safety considerations.

SYSTEM RELIABILITY TESTS

Life tests have been completed at Livermore on one vane actuator assembly and one rod actuator assembly. These tests included one million cycles of sine-wave excitation, 200 full-stroke fast resets, and 200 scrams on each assembly. The severity of these tests exceeds that of the Nevada Test Site

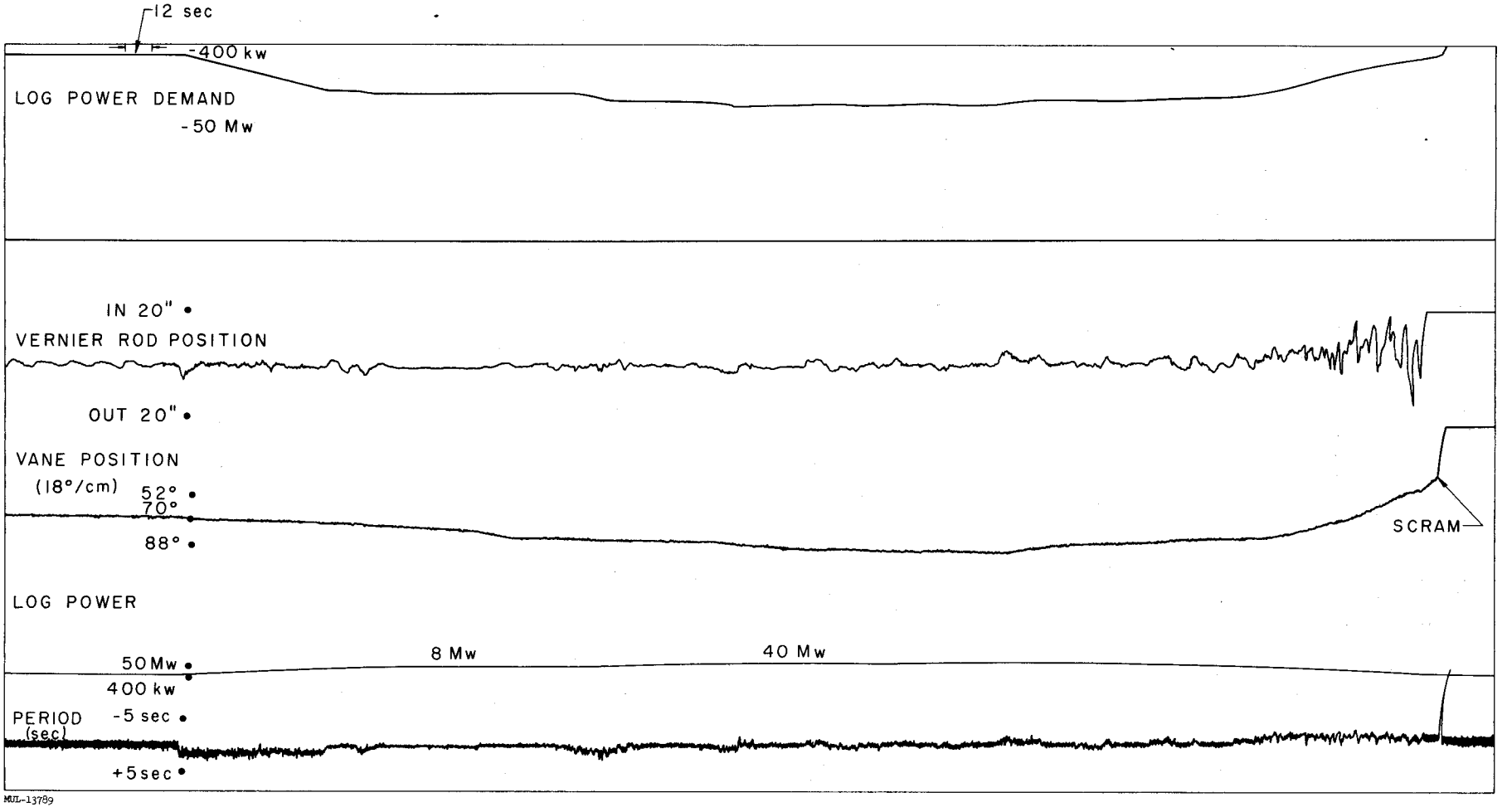

Fig. I-9. Power control system test data as recorded during May 14, 1961, 40-Mw run.

operating conditions by a wide margin. During these tests no major failures occurred, but slight deterioration of performance was evident.

The "on" time of the hydraulic actuator system at the Nevada Test Site to date totals 415 hours. This time includes 120 hours of automatic control, 180 hours of manual servo control, and 80 hours of manual override operation. This "on" time, during which there have been approximately 50 scrams, has been accumulated during system checkout, operator training, and actual test operations.

SECTION IV. ENGINEERING

TEST VEHICLE REPAIR

To qualify a test vehicle after the accident (see UCRL-6376), the second car was built up. Components that had been modified or available in a single set were transferred from the damaged car and repaired as required. A second set of parts was ordered through a supplier, have been delivered, and are in the final stage of installation on the first car.

DUCT INSPECTION AND REPAIR

Both sets of duct sections were inspected by radiographic and magnetic particle techniques in Nevada. The best set of hardware was retained at Nevada and used for the 40-Mw power nuclear run. The balance of the equipment that was in need of repair was sent to LRL. This included inlet diffuser forward, inlet diffuser aft, turning section, rake section, and nozzle. It was determined that the inlet diffuser aft and the rake section were beyond repair. In order to repair either of these sections it would be necessary to remove 75% of the welded area. The repair welding is accomplished by a neutral rod, Inconel A. The repaired area does not have the strength of the parent welds, however, it does have an elongation that permits it to distribute the strength; therefore there is a limit to the amount of weld that can be replaced. Because these parts could not be qualified by reworking, it has been necessary to rework the nozzle and aft diffuser that were used on the 40-Mw power run in Nevada.

PRODUCTION OF QUALIFIED V-BAND COUPLINGS

In the 40-Mw power run, the test vehicle was equipped with forged and cast clamps. The cast clamp connections were between the forward adapter/core vessel and turning section/nozzle. The recommendation of the Metallurgical Group is that cast clamps not be used for the higher power runs. Therefore, the manufacture of a new design, 16-shoe clamp is being expedited.

MARMAN CLAMPS

Results from the 40-Mw power nuclear run showed that stresses in the clamp connecting the exit nozzle to the turning section gradually rose to a peak of 100,000 psi at a time corresponding to the end of the airflow down ramp. The stress traces did not exhibit vibrational effects or correlate to the run profile. They show clear indication that the stresses were a result of thermal expansion of the flange into the clamp, which forced the clamp to spread apart. No appreciable stresses were recorded upstream of the core.

The torquing procedure on the exit nozzle/turning-section clamp was to seat the conoseal gasket with 400 ft/lb torque and then to loosen the clamp by rotating each bolt 150°. With this procedure it was possible to predict 80,000 psi stress in the clamp during the 40-Mw power run. A stress of 180,000 psi can be predicted for a high-power nuclear run with this same torquing procedure.

To reduce the magnitude of these stresses during a high-power run, the exit nozzle, turning section, and rake sections were painted with insulating paint. The effect of this paint is such that a thickness of 0.0075 inch reduces the predicted stress from 180,000 to 60,000 psi (see Fig. I-10). As a safety precaution in case the paint chips off, the couplings downstream of the core will be loosened 210° on each bolt. This allows for a predicted stress of 120,000 psi with no insulating paint on the surface.

HORNING

A pure-tone acoustic resonance at approximately 100 cps has been experienced during blow-down operation of the Tory II-A test vehicle at NTS. During the course of several blow-down runs from 9/29/60 to 1/11/61, the following information was deduced: (1) the horning occurred both with and without the aerodynamic grid in place; (2) horning occurred with both a straight and a canted nozzle; and (3) horning occurred both with and without the core

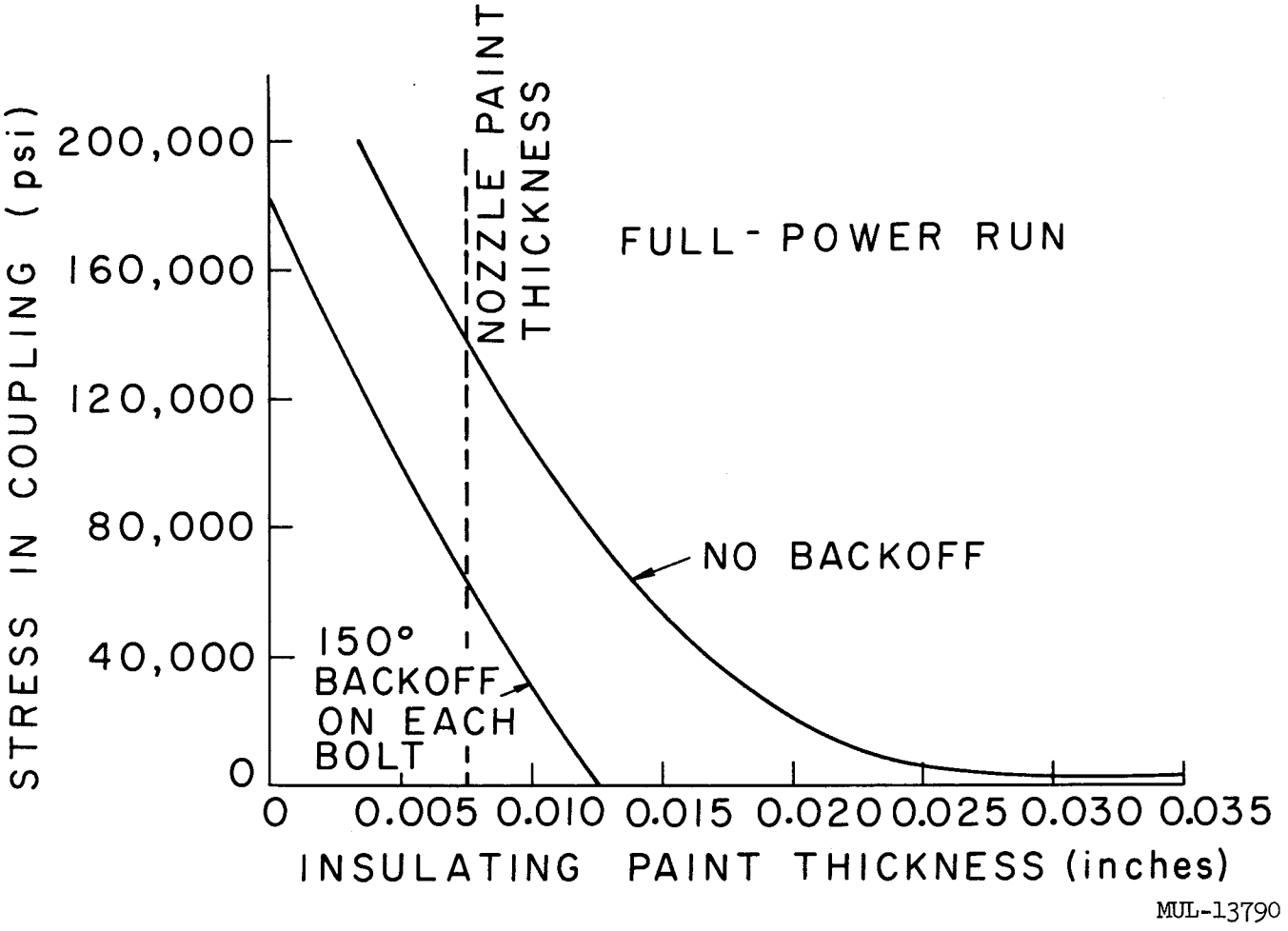

Fig. I-10. Tory II-A nozzle-coupling stress reduction due to the use of back-off and insulating paint.

in place. Resonance occurred over a range of total pressure upstream of the nozzle, Pt_4, between 1.15 and 2.20 atmospheres absolute. The nozzle choking point is at 1.4 atmosphere, absolute, thus the horning occurs both before and after the nozzle has choked. No duct vibration was associated with this horning, however, a static-pressure measurement at the nozzle throat indicated a ± 0.5 variation during horning at approximately one-half the acoustically observed frequency.

A scale model of the Tory II-A test vehicle ducting (diffuser, pressure vessel, turning section, and nozzle) has been operated under flow conditions similar to the checkout runs at Nevada. It has been demonstrated that the horning experienced in Nevada is entirely associated with the exit nozzle. The horning frequency was observed to scale inversely with the linear dimensions, as is to be expected with an acoustic phenomenon. It was found that a thin polyurethane sheet cemented to the wall of the converging portion of the nozzle eliminated resonance. Cutting off the diverging portion in increments did not affect the resonant frequency or intensity until three-fourths of the diverging portion had been eliminated, at which time the intensity diminished. The horning was stopped by eliminating the diverging portion of the nozzle.

A decision was made not to attempt to eliminate this acoustic resonance by modification of the nozzle, since there was no evidence of test vehicle vibration associated with the horning.

CHAPTER II. MATERIALS DEVELOPMENT AND PILOT PLANT ACTIVITIES

SECTION I. PROCESS AND MATERIALS DEVELOPMENT

I. MATERIALS STUDIES

A. BeO and BeO - UO_2

1. Growth of BeO Single Crystals

Very few crystals were grown from beryllium fluoride, sodium tungstate, and potassium hydroxide. However, many crystals were grown from lead fluoride and lead oxide.

Crystals were grown having either a tabular habit or an acicular habit. Crystals having a tabular habit were generally 3-5 millimeters long in the a-direction and one millimeter in the c-direction. It was found that in crystals having an acicular habit the needle axis and the crystallographic c-axis coincided. These crystals grew to a length of 3-5 millimeters in the c-direction, whereas growth in the a-direction seldom exceeded 0.5 millimeter. (Figures II-1, II-2).

2. Electrical Properties of BeO

The electrical conductivity of BeO is being determined as part of a general program to obtain transport data on oxide materials at high temperatures.

Measurements are being made on extruded samples, 97% of theoretical density, using a two-probe dc voltmeter-ammeter method, and a two-probe ac bridge method. Results from two samples illustrate that when log σ is plotted against $1/T$, the curve shows a kink separating two straight lines (Fig. II-3). The critical temperature is determined to be 1022°C at 4.6×10^{-9} $(\text{ohm-cm})^{-1}$. Values of conductivity range from 10^{-15} $(\text{ohm-cm})^{-1}$ at 200°C to 10^{-5} $(\text{ohm-cm})^{-1}$ at 1600°C. The activation energy for the low temperature or extrinsic conduction region is calculated to be 20 kcal/mole (0.87 ev). The activation energy for the high temperature or intrinsic conduction region is 58 kcal/mole (2.5 ev).

To determine the mechanism of conduction in BeO, the emf of the cell Pt/Fe, FeO/BeO/Ni, NiO/Pt was measured in thoroughly purified helium.

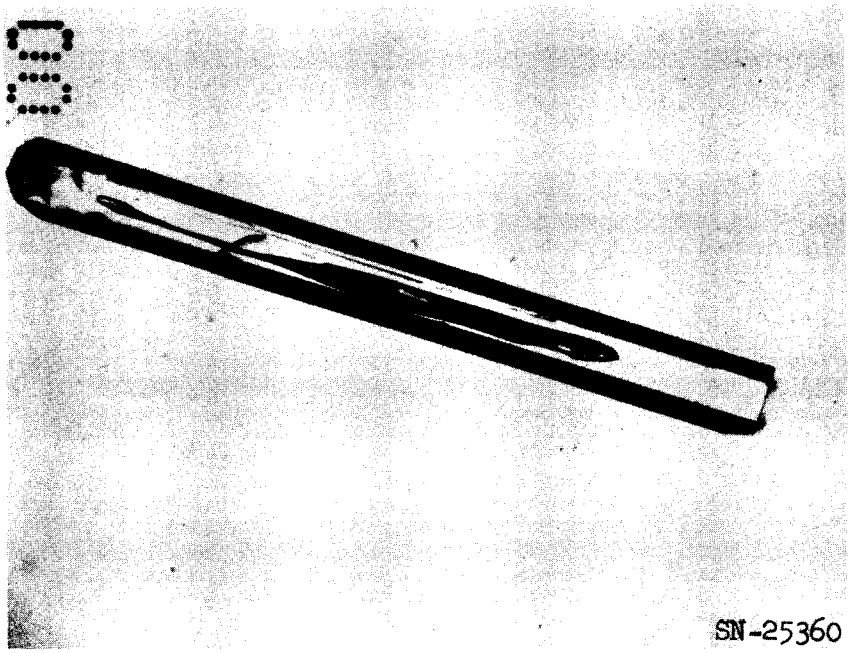

Fig. II-1. BeO single crystal.

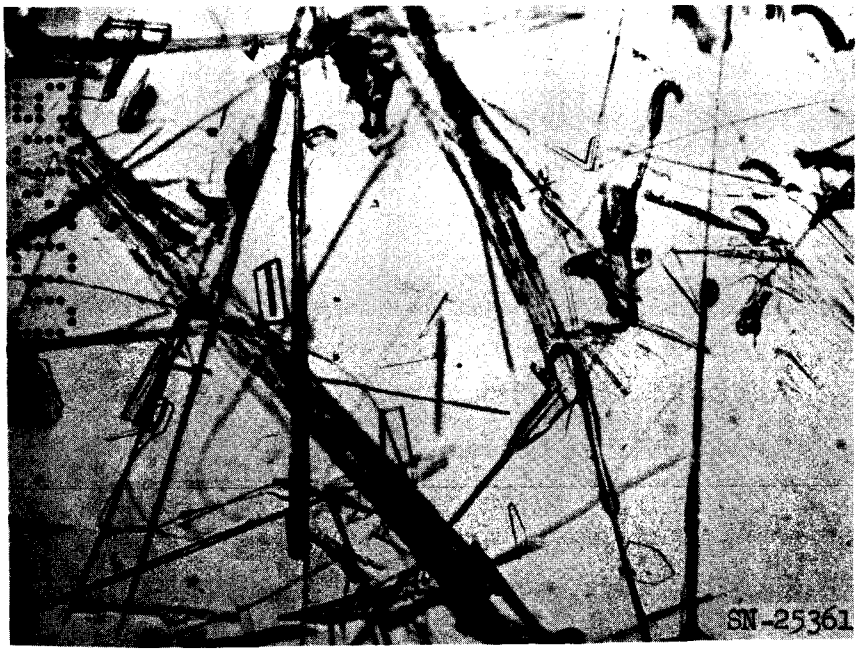

Fig. II-2. Growth of BeO single crystals.

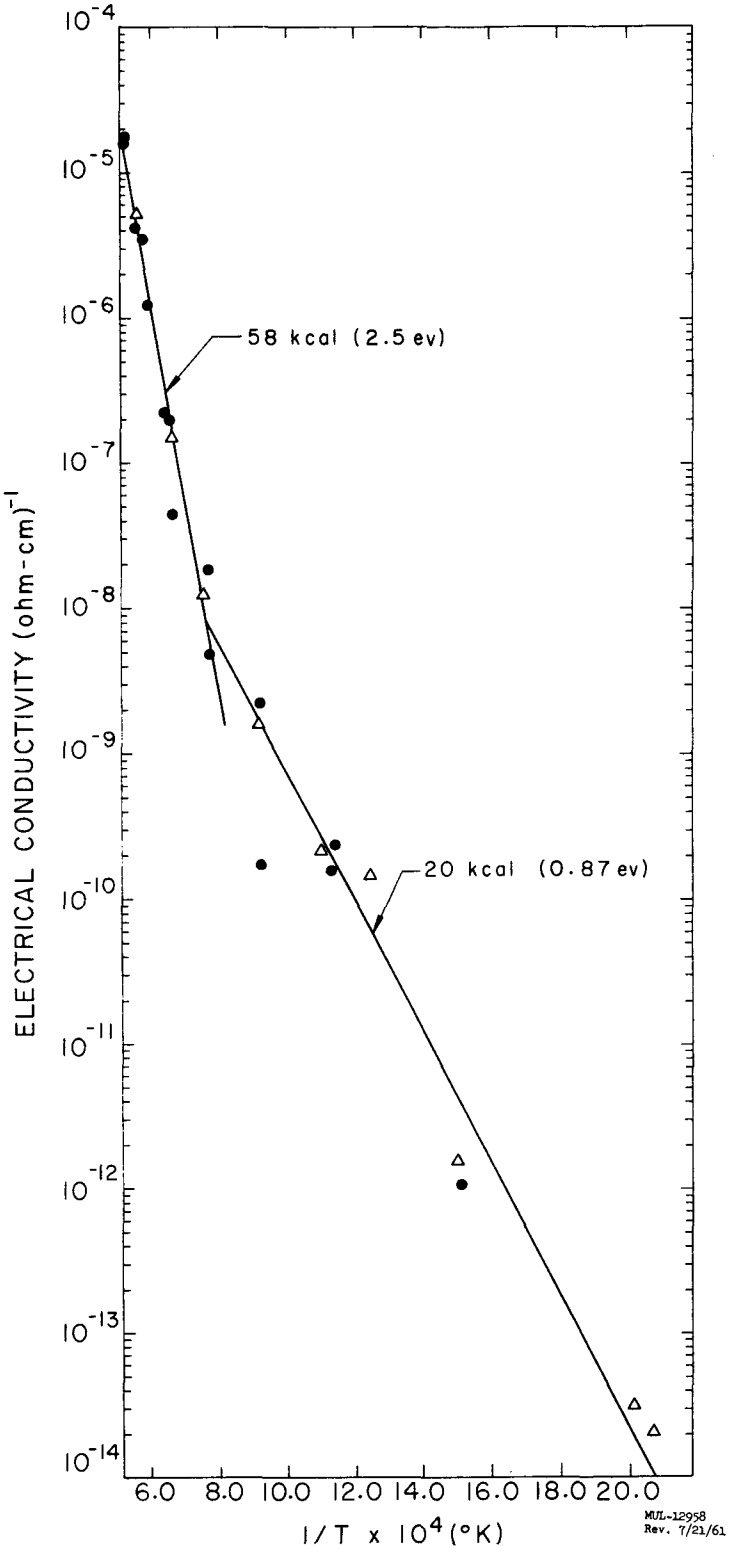

Fig. II-3. Temperature dependence of the electrical conductivity of polycrystalline BeO.

If BeO were a pure electronic conductor, the emf of the cell would be equal to zero. Actually the emf of the cell was found to be 0.100 ± 0.010 volts at 1075°C. An emf of 0.294 volts was measured by using a pure ionic conductor such as ZrO_2 (with 15 mole-percent CaO) in place of the BeO sample. Therefore, at least 34% of the current is simultaneously carried by ion migration at this temperature.

3. Sintering of BeO

The equipment for studying the sintering of BeO compacts was completed. The furnace can be controlled within ±2°C. The shrinkage of the compacts is followed by a transducer and recording system capable of a full-range sensitivity of 0.005 inch.

BeO compacts were prepared by pressing UOX powders at 6,000 psi and then sintering in air at 1320°C. The shrinkage was very rapid, with the initial stage (corresponding to approximately 4% shrinkage) complete within the first 30 minutes. A log $\Delta L/L$ versus log-time plot was not linear for the few samples examined. The shrinkages, as determined by measurements before and after sintering, agreed within 5% with those recorded by the transducer equipment. The period of time from the introduction of the sample into the hot zone until the system comes to thermal equilibrium is about 5 minutes. At these temperatures this represents a large portion of the initial stage which is not recorded. Modifications are now being made so that the time to equilibrium will be decreased to 30 seconds or less, thus making the equipment capable of following initial, intermediate, and final stages of sintering.

4. Infrared Study of Uranium Oxides

A preliminary study has shown the value of infrared techniques in analyzing the complex urania-oxygen systems. U_3O_7, α - U_3O_8, β - U_3O_8, and $UO_{2.6}$, along with the various UO_3 modifications, have given distinct absorption spectra.

5. Oxidation of Uranium Monocarbide

Despite uranium monocarbide's great potential as a fuel for high-temperature nuclear reactors, no data on its oxidation properties have appeared in the literature. For this reason, an oxidation study has been initiated.

The oxidation of uranium monocarbide can be categorized into at least three rather loosely defined temperature regions, 180°C to 280°C, 280°C to 370°C, and above 370°C, based on the oxidation product. Such a classification is uncertain, so further experimentation should provide better definition.

180°C to 280°C.

Only a few samples have been oxidized in this region, so the results are still inconclusive. So far, the oxidation products have been amorphous to x-rays and do not correspond to either UO_3 or U_3O_8 on a weight-gain basis. The kinetics suggest a diffusion mechanism since the weight gain versus time data fit Jander's equation.

280°C to 370°C.

At these temperatures, larger particles (70 to 140 mesh) are used to decrease the rate of oxidation. The oxidation product is a brownish-orange color and has been identified by x-ray as UO_3. Free carbon has also been confirmed as a reaction product by chemical analysis.

Weight-gain data require an additional reaction product, which could possibly be a condensed hydrocarbon produced by reaction with the water vapor in the air.

The oxidation curves fit either of the following kinetic equations quite well, except at higher percentages of oxidation:

$$\left[1 - (1 - R)^{1/3}\right] = k_1 t \,, \qquad (1)$$

$$\ln (1/1 - R) = k_2 t \,, \qquad (2)$$

where R is the fraction reacted at time t. Equation (1) requires the movement of an interface into a spherical particle. Since there is a large volume increase during oxidation which causes a breakup of the original particle, Eq. (1) does not provide a plausible mechanism. Using the first order equation, an activation energy of 28 kcal was found in this temperature region.

A puzzling feature of the oxidation was the type of UO_3 formed. Under apparently identical oxidizing conditions, the UO_3 was amorphous after one experiment and crystalline after another experiment.

Over 370°C.

Above this temperature the large exothermic effect causes the reaction to proceed very rapidly. The oxidation product is U_3O_8 with again the possibility of free carbon and condensed hydrocarbons being formed, although their presence has not been confirmed as yet. No attempt has been made to define the kinetics.

6. UO_2-O System

The question of the stability of the "$UO_{2.6}$ phase" as a phase distinct from the U_3O_8 phases has been investigated with several experiments in the high-temperature x-ray diffractometer. Previous work has shown that the x-ray powder patterns of the two phases are slightly different, although the differences are very subtle. The unit cells are based on the same hexagonal pseudo-cell. However, the b_0-axis of U_3O_8 is three times the pseudo-axis, whereas in $UO_{2.6}$ the b-axis is eight times. The composition of the $UO_{2.6}$ phase may vary from $UO_{2.54}$ to $UO_{2.64}$, and the variation is reflected in variable cell constants. The U_3O_8 may lose oxygen to about $UO_{2.62}$ with no apparent change in cell constants. No evidence has been presented to indicate an equilibrium exists between these two phases.

Samples of U_3O_8 heated above 400°C appear to be truly hexagonal. At least their b_0/a_0 ratio remains at $\sqrt{3/1}$ above this inversion temperature. Between 1200°C and 1300°C in air, the samples of U_3O_8 "recrystallize" on the platinum-ribbon heater. The rather poor x-ray patterns obtained from these crystals at the high temperature indicate that they are truly orthorhombic. Samples of U_3O_8 heated in a vacuum of 10^{-3} mm Hg behave the same as the air samples up to 500°C. Above 500°C they appear to lose O_2 and form an orthorhombic phase. Further heating to around 1000°C causes complete conversion to a cubic UO_{2+x} phase. Samples of the $UO_{2.6}$ phase, on the other hand, do not transform to a hexagonal phase when heated in a vacuum of 10^{-3} mm Hg. Instead, they appear to transform to a cubic UO_{2+x} at temperatures at least as low as 500°C. In contrast, the $UO_{2.6}$ does change to a hexagonal phase when heated in air to around 400°C, apparently gaining O_2 and becoming U_3O_8.

These preliminary experiments indicate that the $UO_{2.6}$ phase has a distinct one-phase field in the equilibrium phase diagram. The actual boundary line has not been located and some question still exists as to whether this phase change is of first or higher order because no region containing both phases has yet been observed.

7. Cr_2O_3 - UO_2-O System

Studies of the Cr_2O_3 - UO_{2+x} system have been carried out with 5 compositions ranging from 10 w/o UO_2 to 90 w/o UO_2 in 20 w/o increments. These samples were prepared by mixing and sieving the respective oxides,

followed by cold pressing into pellets. These pellets in turn were sintered either in air at 1200°C for approximately 50 hours or in helium at 1500°C for 2 hours. The x-ray results are tabulated in Table II-1.

It is apparent that the phase diagram in air is quite different from the one under inert conditions. The existence of a compound is indicated at about 78 w/o UO_2 - 22 w/o Cr_2O_3 since the unit cell a_0 = 5.078, b_0 = 11.702, c_0 = 4.861 indexes the x-ray powder pattern completely. The x-ray powder data on this phase are shown in Table II-2. A small (less than 50μ) crystal of the phase appeared to be a hexagonal bipyramid. Single-crystal studies in the precession camera indicate an orthorhombic crystal twinned as an interpenetrant triplet. Chemical analysis is being carried out. An attempt will be made to determine the U^{+4}/U^{+6} ratio by a coulometric technique.

Approximately 80 grams of the orthorhombic phase were incorporated into BeO and extruded. Several samples were heated in hydrogen at 1650°C for 5 hours, but, from x-ray and visual appearance, the samples appear to have lost the Cr_2O_3 phase, and the urania phase exists as UO_2.

Table II-1. Phases: Cr_2O_3 - UO_2.

Composition % w UO_2	Composition % w Cr_2O_3	Firing atmosphere	Firing temp °C	Firing time, hr	Phases present
90	10	Air	1200	53	x-phase + U_3O_8
		He	1500	2	UO_2 + Cr_2O_3
78	22	Air	1200	53	x-phase
70	30	Air	1200	53	x-phase + Cr_2O_3
		He	1500	2	UO_2 + Cr_2O_3
50	50	Air	1200	53	x-phase + Cr_2O_3
		He	1500	2	UO_2 + Cr_2O_3
30	70	Air	1200	53	x-phase + Cr_2O_3
		He	1500	2	UO_2 + Cr_2O_3
10	90	Air	1200	53	x-phase + Cr_2O_3
		He	1500	2	UO_2 + Cr_2O_3

Note: x-phase is an unknown phase, apparently a compound.

Table II-2. X-ray Diffraction Pattern for 78 w/o UO_2 - 22 w/o Cr_2O_3. (Fired in air 53 hours).

$Sin^2\theta$	"d" Value	Intensity	$Sin^2\theta$	"d" Value	Intensity
0.0119	7.08	VVW	0.1006	2.43_1	W-
0.0145	6.40	VVW	0.1102	2.32_2	W-
0.0174	5.85	W-	0.1171	2.25_2	W
0.0295	4.49	W	0.1222	2.20_5	W
0.0406	3.82	M	0.1318	2.12_3	W+
0.0527	3.36	S+	0.1408	2.05_4	M+
0.0637	3.05	S-	0.1572	1.95_2	S
0.0687	2.94	W-	0.1608	1.92_2	W
0.0876	2.60_4	S-	0.1679	1.88_1	W
0.0923	2.53_6	W+	0.1919	1.75_9	S

8. ZrO_2 - UO_2 - O_2 System

Samples of ZrO_2 and UO_2 were prepared with 5 compositions ranging from 10 w/o ZrO_2 (21 mole %) to 90 w/o ZrO_2 (95 mole %) in 20 w/o increments. The samples were mixed, sieved, and pressed into pellets. The pellets were heated in platinum boats for 22 hours at 1200°C in air. They were then crushed, sieved, repressed, and reheated for 38 additional hours at 1200°C. X-ray analysis indicated that the only phases present were U_3O_8 and monoclinic zirconia.

The samples were then sintered to a temperature of 1700°C for 30 minutes. The time between 1500 and 1700°C was about 2 hours. X-ray data are presented in Table II-3.

The data indicate that compositions near 50% w ZrO_2 (68 mole %) appear to form a compound. The unit cell is orthorhombic with a primitive lattice. Its cell constants are 5.384A, 5.282A, and 5.105A for a starting composition of 60 w/o UO_2 - 40 w/o ZrO_2 (nominal). These values are very close to the tetragonal cell of the UO_2 - in - ZrO_2 solid-solution. The nominal composition 50 w/o UO_2 - 50 w/o ZrO_2 also showed only one phase with slightly different cell constants, indicating possible solid-solution between this compound and the ZrO_2 or UO_2. Chemical analyses are being made to confirm the exact compositions.

Table II-3. X-ray Data for ZrO_2 - UO_2 - O_2 System.

(Samples heated in air to 1700°C for 30 minutes).

Nominal composition (ZrO_2/UO_2)		Phases present
w/o	m/o	
90/10	95/5	Monoclinic ZrO_2*
70/30	83.5/16.5	Weak U_3O_8 + strong orthorhombic ZrO_2 phase
50/50	68.6/31.4	Weak monoclinic ZrO_2 + strong orthorhombic ZrO_2 phase
30/70	48.5/51.5	Monoclinic ZrO_2†
10/90	21/79	U_3O_8

* Several unexplained lines.

† 30/70 sample unexplainedly appears to have changed composition with excessive loss of U_3O_8.

Visual comparison of the x-ray pattern of the orthorhombic phase with face-centered tetragonal patterns of U_3O_7 suggest that the orthorhombic phase is very nearly face-centered, i.e., those reflections which should be absent due to the face-centering appear only as very weak but definite reflections. The substitution of U for Zr atoms in the face-centered tetragonal ZrO_2 structure, on which the orthorhombic structure is based, is apparently not random, thus developing the lower symmetry. Whether the orthorhombic phase is a distinct phase, or a solid-solution with tetragonal ZrO_2 involving a higher-order phase change with respect to composition, is not yet clearly established.

Reheating powdered samples of the orthorhombic phase to temperatures above 900°C decomposes the phase to zirconia and U_3O_8. Samples heated at 900°C for 24 hours showed very little decomposition. At 1000°C, about one-half the sample appeared decomposed in 24 hours. At 1200°C, complete breakdown occurred in less than 5 hours.

B. Fuel Retention and Stability

1. Fuel Mixtures for Stability

Because BeO - UO_2 tubes made by our usual techniques showed structural instability when exposed to 1100-1250°C at high oxygen pressures (75 psia), attempts were made to develop more stable mixes.

Several techniques were used to solve the problem: "grog" and powder mixes, Al coating of the normal tubes, and third-component additions to mixtures of BeO - UO_2. During this period, ZrO_2 - UO_2 - BeO showed early promise, therefore our effort was concentrated on it. Other work has been done also, and is reported below.

A threefold attack was made on ZrO_2 - UO_2 - BeO: (1) A brief phase-diagram study was initiated (see above); (2) systematic ZrO_2 - UO_2 mixes of different ratios were made, exposed to oxidation, and examined; and (3) Zr was coprecipitated with U from solution on to slurried BeO powder in a simple modification of our normal "slurpitation" procedure for fueled tubes. The latter two approaches are described below, along with other (non-ZrO_2) approaches to the problem.

a. ZrO_2 - UO_2 - BeO Mixes

Since UO_2 and ZrO_2 are known to form solid solutions, an attempt was made to produce stabilized fuel tubes by mixing these in BeO. To avoid complications of changing the tube process as we now have it, the zirconia and urania were coprecipitated from zirconyl nitrate and uranyl nitrate on slurried BeO. Normal techniques were used up through the extrusion process. The starch burn-out temperature was initially raised from 1500°F to 1930°F and held for 4 hours. Further work indicated that starch burn-out temperatures of 1500°F are adequate. Therefore, all tubes made now are starch-burned at the lower temperature. Tubes of this mix (80X182), (80X204), and (80X205) have been made and tested in part for stability and fuel loss.

Tubes of mix (80X182) were sintered to 1600, 1650, 1700, 1750, 1800, and 1850°C. X-ray data and petrographic examination results are given in Table II-4.

Table II-4. UO_2 - ZrO_2 - BeO Tubes. (Mix 80X182).

Sintering temp °C	Density g/cc	Phases 1	2	3	BeO grain Size (μ)	Shape	Fuel grain Size (μ)	Shape	Pores
1600	3.23	BeO Hex	f.c.c. $a = 5.35_9$A	f.c.t. a = 5.167 c = 5.25_7A	0.5 - 2.5	--	Difficult to see		
1650	3.25	BeO Hex	f.c.t. a = 5.300 c = 5.33_2A	f.c.t. a = 5.183 c = 5.272A	1.5 - 2.0	Both elongate and equant grains. Rounded edges	Difficult to see		
1700	3.27	BeO Hex	f.c.t. a = 5.277 c = 5.325		≈3 - 25 Mode 5	Equant; angular	1/2 - 2.5	Elongate, triangular, faceted	
1750	3.27	BeO Hex	f.c.t. a = 5.277 c = 5.325		5 - 25 Mode 7 - 10	Equant; angular	*2 - 5	Elongate, irregular, circular (all 3 present)	Few
1800	3.27	BeO Hex	f.c.t. a = 5.277 c = 5.325		5 - 45 Mode 15	Equant; almost rounded	*0.5 - 7	Elongate, irregular, circular, (all 3 present)	Small, very few
1850	3.27	BeO Hex	f.c.t. a = 5.277 c = 5.325		5 - 50 Mode 20	Equant; almost rounded	*0.5 - 1 within BeO grain 2.5 - 5 grain boundary	Elongate, irregular, circular, (all 3 present)	Few

*Fuel distributed around BeO grains as well as within.

General Comment: All samples indicate a complete reaction between UO_2 - ZrO_2. Porosity is generally low for those samples where grain boundaries can be observed, i.e., where BeO grain size > 5μ.

The composition of the ZrO_2 - UO_2 - BeO is as follows:

1500 g Beryllia	87.25% w
69 g ZrO_2	4.91%
140 g UO_2	7.84%

with a mole ratio of approximately 58/42 mole percent zirconia to urania.

The tubes containing UO_2 and ZrO_2 (80X182) performed very well in every test so far. (See below).

Some tubes, sintered at 1600°C for 6 hours, were x-rayed after being subjected to 5 atmospheres O_2 pressure at 1250°C for 10 hours. There was a thin black layer on the outer surfaces which contained U_3O_8. The tube had a high modulus of rupture, however, indicating the element had not degraded because of this.

Mixes containing U^{235} have been made and are being fuel-loss tested at 1525°C and 1650°C (1 atmosphere O_2 pressure for 7 hours). Some tubes have been submitted for radiation damage studies and cycling effects.

b. Zirconia-Urania Mixtures

Components were reacted to give the following compositions:

ZrO_2 wt %	UO_2 wt %	ZrO_2 mole %	UO_2 mole %
20	80	35.4	64.6
30	70	48.4	51.6
40	60	59.4	40.6
50	50	68.6	31.4
60	40	76.7	23.3

All the values listed are nominal. Actual analyses of the reacted powders were somewhat lower in UO_2. The detailed results are being compiled and will be reported later.

The ZrO_2 - UO_2 powders were prepared by a coprecipitation from mixed nitrate-salt solutions with NH_4OH, followed by a filtration, washing, refiltration, drying, and calcining step prior to reaction of various portions at:

(a) 1250°C in air for a 3-hour soak,

(b) 1500°C in air for a 3-hour soak,

(c) 1600-1650°C in air for a 3-hour soak,

(d) 1700°C in air for a 1-hour soak,

(e) 1500°C in hydrogen for a 2-hour soak,

(f) 1700°C in hydrogen for a 2-hour soak.

These reaction products were crushed and screened through a 325-mesh screen and submitted for chemical analysis for uranium content, and for x-ray diffraction to establish the degree of completeness of reaction.

In summary:

(1) It appears that the minimum reaction temperature required for solid solution formation is 1500°C.

(2) At 1250°C, no solid solution formation was noted by x-ray diffraction.

(3) Comparable results were obtained from powder mixes and coprecipitated powders.

(4) Air reactions resulted in U_3O_8 - ZrO_2 solid solution and U_3O_8 formation, while hydrogen reaction led to UO_2 - ZrO_2 solid solution and UO_2 formation.

c. Ceria-Urania Mixtures

Mixtures were prepared of the following nominal compositions:

CeO_2 wt %	UO_2 wt %	CeO_2 mole %	UO_2 mole %
20	80	28.2	71.8
30	70	40.2	59.8
40	60	51.1	48.9
50	50	61.1	38.9
60	40	70.2	29.8

The CeO_2 - UO_2 powders were reacted in air at

(1) 1350°C for a 3-hour soak or,

(2) 1500°C for a 3-hour soak.

In both cases, complete solid solution formation resulted.

d. Fuel Mixtures in BeO

Based upon the analyses of the screened fuel powders, BeO bodies containing 6 w/o and 8 w/o UO_2 (nominal) were prepared for densification studies by cold-pressing pellets at 20,000 psi, prefiring in air at 900°C, and finally sintering at 1600-1650°C or 1750°C in hydrogen or air atmosphere

for a maximum period of three hours. The results indicate that the desired densification can be obtained by using the lower temperatures in hydrogen atmospheres. This is of interest for its potential effect on the microstructure and strength characteristics of the ultimate fabricated bodies.

e. Powder and Grog Mixes

Mixes were made in which urania was added to beryllia as a powder in the following ways:

a. The hard-grog mix (80X188). This material was a 50/50 w/o UO_2 - BeO mixture slurpitated and sintered to 1750°C/6 hours, then ground to -325 mesh. This was used as the fuel and then mixed into the BeO.

b. The soft-grog mix (80X189). This material was also a 50/50 w/o UO_2 - BeO mixture, but sintered to 1600°C/6 hours, then ground. This was the fuel addition to BeO.

c. The U_3O_8 mix (80X190). The U_3O_8 was obtained by heating -325 mesh UO_2 in air to 2300°F for 10 hours. The U_3O_8 was then mixed with BeO.

d. U_3O_8 intensive mix (80X192). This is the same as mix (80X190) except the beryllia and U_3O_8 were dry-blended in an intensified Y-blender for 24 hours rather than the 30 minutes normally used.

Tubes from these mixes were sintered at 1650°C, 1700°C, and 1750°C for 6 hours in a hydrogen atmosphere. Petrographic examinations and other data are shown in Table II-5.

An interesting observation is the extremely fine grain size of the 50/50 grog after sintering at 1750°C. Apparently the high urania concentration impeded BeO grain growth. This would be expected because there would be fewer BeO-to-BeO grain contacts in the presence of a large concentration of UO_2 grains.

Also noteworthy is the lower density (97.5) obtained when BeO plus grog was resintered to an 8% UO_2 content, compared to normal slurpitated mixes (generally 98.7 - 99.8% theoretical density).

Testing at 1150°C (4 hours, 75 psia O_2) indicated excellent stability insofar as post-test strengths were high, and no decreases in sonic moduli were observed (Table II-5). However, appreciable weight gains were observed, especially for the lower density tubes (e.g., + 0.3% for a 95% - dense tube). The U_3O_8 powder-mix tubes showed virtually no weight increases,

Table II-5. Powder and Grog Mixes.

Sample No.	Sintering temp °C 6 hours	BeO grain Size (μ)	UO_2 grain size (μ)	Laths	Pores	% Theoret. density	Percent shrinkage
Hard Grog + BeO							
80X188	1750	10-35 Modal 25-30	1-5	Some	Few 1μ	97.5	22.0
80X188	1700					97.0	22.0
80X188	1650					95.9	21.5
Soft Grog + BeO							
80X189	1750[a]	20-50 Modal 35	5-10	Some	Many < 1μ	97.3	23.0
80X189	1700					96.5	23.0
80X189	1650					95.1	22.3
U_3O_8 Mix + BeO							
80X190	1750	30-50 Modal 40	3-4	Some	Some < 1μ	98.6	24.4
80X190	1700					98.3	24.4
80X190	1650					97.4	23.8
Hard Grog Alone[b]							
500X170	1750[c]	< 5	1	Some	Many		

[a] The microstructure of this specimen resembled that of the Tory II-A-1 tubes.

[b] A grog is a material which has been sintered, then reground and mixed in with other powder.

[c] The fuel assumes a uniform shape, as in normal mix, as well as irregular shapes — filling interstices between grains corresponding to the general shape of grain boundaries before complete sintering.

but note that their densities were above 97% even at the low sintering temperature (1650°C). There is little or no correlation between post-test strength and sintering temperature. No samples were subjected to hot bend tests.

2. Pressure Testing

a. ZrO_2 - UO_2 Tubes

These tubes performed very well in the fuel instability range (1150-1250°C at 75 psia oxygen). Tables II-6 and II-7 contain the data to date.

Table II-6. Modulus of Rupture, Untested ZrO_2 - UO_2 - BeO Tubes.

Tube description	Sample number	Modulus rupture (4-point) (psi × 10^{-3})
All 80X205 fired in H_2 at 1700°C for 6 hours	62	20.7
"	63	23.9
"	65	27.1
"	43	30.8
"	52	33.1
"	38	33.6
"	45	34.0
		29.0 (Average)

The data presented in Table II-6 were intended to show the virgin strength of ZrO_2 - UO_2 tubes prior to testing. The strengths vary over a wide range (20,700 - 34,000 psi). The possibilities of temperature gradients during hydrogen firing will be examined in the future.

In Table II-7 the data are grouped into samples "hot-bend" tested, and those simply pressure tested. Tubes in both groups were tested simultaneously. Several uncoated 10% UO_2 tubes (results not tabulated) were run as test controls. Every control sample suffered radical loss in strength (final values 5,000 - 7,000 psi). The ZrO_2 - UO_2 - BeO tubes, on the other hand, show no ill effects from pressure testing alone and little effect from hot-bend testing except in the case of high loads (15,000 psi) at high temperatures (1400°C). Failure under these conditions is probably due to the ultimate strength of the material rather than fuel instability. Although current test results are still sparse, the following observations appear firm:

Table II-7. Fuel Stability Testing, BeO - ZrO_2 - UO_2 Tubes at 75 psia O_2.

Sample No.	Tube description	% UO_2 (chemistry)	Test temp (°C)	Time at temp (hr)	Bulk density before (g/cc)	Firing temp (°C)	% Weight[a] change	Flex. reson. ratio	Hot-bend[b] results (psi)	Mod. rupt. after testing (psi)
43-1	80X182	7.8	1150	4	3.27	1800	+0.02	1.00	UB-7400	26,200
45-3	80X182	7.8	1250	10	3.27	1800	+0.02	1.00	UB-7400	29,900
49-1	80X182	7.8	g	≈40	3.27	1750	No test	No test	B-7400[g]	30,400[c]
										32,300
53-4	80X182	7.8	1150	10	3.27	1750	+0.01	1.00	UB-10,000	No test
			1250	10[d]			No test	No test	B-15,000[e]	No test
55-3	80X182	7.8	1150	30[d]	3.27	1750	+0.02	1.00±0.03	UB-10,000	Still testing
58-2	80X182	7.8	1250	20[d]	3.27	1700	+0.03	1.00	UB-10,000	Still testing
60-6	80X182	7.8	1150	10	3.27	1700	+0.02	1.00	UB-15,000	Still testing
61-8	80X182	7.8	1250	10	3.27	1700	+0.02	1.00	UB-15,000	Still testing
62-11	80X182	7.8	1400	10	3.27	1750	No test	No test	B-15,000[f]	No test
43-2	80X182	7.8	1150	4	3.27	1800	+0.01	1.00	No test	33,600
49-2	80X182	7.8	g	≈40	3.27	1750	-0.05	1.00	No test	32,100
53-5	80X182	7.8	1150	10	3.27	1750	+0.02	0.98	No test	No test
			1250	10[d]			+0.04 (0.06)	1.00	No test	20,800
55-6	80X182	7.8	1150	30[d]	3.27	1750	+0.01	1.00±0.03	No test	Still testing
57-20	80X182	7.8	1150	10	3.26	1650	+0.02	No test	No test	44,600[h]
57-30	80X182	7.8	1150	10[d]	3.23	1600	+0.04	No test	No test	55,500
58-3	80X182	7.8	1250	20[d]	3.27	1700	+0.03	1.00	No test	Still testing
60-7	80X182	7.8	1150	10	3.27	1700	+0.02	1.00	No test	Still testing
61-10	80X182	7.8	1250	10	3.27	1750	+0.05	1.00	No test	Still testing
62-12	80X182	7.8	1400	10	3.24	1750	+0.01	1.00	No test	27,300[i]

[a] Total cumulative weight change in parenthesis.

[b] UB-Unbroken, B-Broken.

[c] Broken halves M.R. tested on 1-1/2-in. center.

[d] Testing in 10-hour increments. Cycled to room temperature in between.

[e] Sample broke after 2 to 5 hours at 1250°C. Total test time at 1150°C and 1250°C about 15 hours.

[f] Sample broke upon reaching 1400°C.

[g] Tested 1250°C/10 hours, cooled to 1150°C/10 hours, heated to 1400°C/10 hours, and cooled to room temperature. Hot-bend sample under 7400 psi broke sometime after 1400°C/2 hours.

[h] Black skin contains hexagonal U_3O_8 (x-ray diffractometer).

[i] 4-Point loading

MUL-13791

1. 80X182 tubes lose little or no strength under 75 psia O_2 for periods in excess of 10 hours from 1150°C-1400°C.

2. These tubes will support hot-bend loads of 10,000-15,000 psi for periods in excess of 10 hours at 1150°C and 1250°C.

An interesting feature which is being checked is firing temperature vs strength. Two samples (57-20 and 57-30) exhibited much higher strengths after testing than we are accustomed to seeing (44,600 and 55,500 psi). These samples were fired at 1650 and 1600°C respectively. A smaller BeO grain size could account for increased strength, which would warrant a lower firing temperature providing fuel-loss characteristics were not severely altered.

b. Grog and Powder Mixes

The details concerning the preparation of these mixes are given in another section of this report. Many of these mixes appeared stable in short-time tests.

Results of fuel-stability testing at 1150°C and 1250°C are given in Table II-8.

1. Grog Mix (-325-mesh BeO - UO_2 Grog)

Every specimen (18) withstood the tests at 1150°C and 1250°C. Performance was not a function of firing temperature (1650, 1700, 1750°C) or of weight gain in the 1250°C test. One sample (47-80X188-40) withstood a hot-bend load of 7,400 psi at 1250°C for 10 hours.

2. Grog Mix (100-mesh, and finer, BeO - UO_2 Grog)

This material, like the -325-mesh grog mix, showed little loss in strength after testing at 1150°C and 1250°C. The strengths were in general somewhat lower than the -325-mesh grog mix. Both mix techniques give much better stability than the normal slurry-mix process.

3. U_3O_8 Powder Mix

This material performed well at 1150°C regardless of firing temperature. Testing at 1250°C, however, indicated very poor strength retention for samples fired at 1750 and 1700°C. Samples fired at 1650°C did not exhibit a loss in strength at either 1150°C or 1250°C. The average (6 samples) densities were:

Table II-8. LRL Grog- and Powder-Mix Tubes at 75 psia O_2.

Sample description			Test temp (°C)	Test time (hours)	% UO_2	% Theoret. density	Resonance ratio before/after	% wt change	Mod. rupt. after	Sample remarks
Grog (-325M)	(41-80X188-2)	Fired 1750°C	1150	4	8.58	97.4	1.00	-0.01	32,400	
	(41-80X188-10)		1150	4	8.58	97.4	1.00	-0.01	33,200	
	(41-80X188-13)		1150	4	8.58	97.4	1.00	-0.01	34,200	
	(47-80X188-40)		1250	10	8.58	97.2	1.05	+0.01	33,500	Hot bend 7400 psi/10 hr
	(47-80X188-42)		1250	10	8.58	97.3	1.01	+0.05	24,800	
	(47-80X188-47)		1250	10	8.58	97.4	1.02	+0.03	23,600	
Grog (-100M)	(41-80X189-1)	Fired 1750°C	1150	4	8.60	97.1	1.00	-0.01	26,700	
	(41-80X189-3)		1150	4	8.60	97.2	1.00	-0.01	30,300	
	(41-80X189-7)		1150	4	8.60	97.0	1.00	+0.04	23,800	
	(47-80X189-5)		1250	10	8.60	97.2	1.00	-0.04	25,600	
	(47-80X189-9)		1250	10	8.60	97.2	1.00	-0.07	27,300	
	(47-80X189-11)		1250	10	8.60	97.1	1.00	-0.06	25,800	
(U_3O_8)	(41-80X190-13)	Fired 1750°C	1150	4	8.06	98.5	1.00	-0.01	25,000	Surface and center brown, no crazing
	(41-80X190-16)		1150	4	8.06	98.5	1.00	-0.01	25,300	
	(41-80X190-22)		1150	4	8.06	97.2	1.00	-0.02	26,800	
	(48-80X190-10)		1250	10	8.06	98.6	1.52	+0.19	2,700	Surface and section black, extreme
	(48-80X190-19)		1250	10	8.06	98.6	No res.	+0.19	2,700	crazing
	(48-80X190-34)		1250	10	8.06	98.6	1.57	+0.23	3,800	
Grog (-325M)	(43-28)	Fired 1700°C	1150	4	8.58	96.9	1.00	+0.02	33,200	
	(43-30)		1150	4	8.58	96.9	1.00	+0.03	38,500	Surface black, section brown with black
	(43-36)		1150	4	8.58	96.8	1.00	+0.03	35,000	ring, no crazing
	(47-31)		1250	10	8.58	97.1	1.01	+0.19	22,700	Surface black, section black, no crazing
	(47-32)		1250	10	8.58	96.8	1.01	+0.18	30,500	
	(47-35)		1250	10	8.58	96.9	1.02	+0.14	27,000	
Grog (-100M)	(43-80X189-25)	Fired 1700°C	1150	4	8.60	96.3	1.00	+0.07	29,300	
	(43-80X189-27)		1150	4	8.60	96.5	1.00	+0.05	31,900	
	(43-80X189-31)		1150	4	8.60	96.4	1.00	+0.05	26,900	
	(47-80X189-26)		1250	10	8.60	96.4	1.03	+0.26	22,800	
	(47-80X189-29)		1250	10	8.60	96.5	1.01	+0.23	24,300	
	(47-80X189-30)		1250	10	8.60	96.5	1.03	+0.24	24,200	
(U_3O_8)	(43-80X190-47)	Fired 1700°C	1150	4	8.06	98.2	1.00	0	31,200	
	(43-80X190-54)		1150	4	8.06	98.3	1.00	-0.01	30,500	
	(43-80X190-56)		1150	4	8.06	98.3	1.00	-0.01	33,500	
	(48-80X190-48)		1250	10	8.06	98.2	1.14	+0.17	No test	
	(48-80X190-53)		1250	10	8.06	98.2	1.15	+0.18	7,000	
	(48-80X190-55)		1250	10	8.06	98.2	1.06	+0.14	8,100	
Grog (-325M)	(43-80X188-22)	Fired 1650°C	1150	4	8.58	96.1	1.00	+0.10	31,600	
	(43-80X188-24)		1150	4	8.58	95.8	0.98	+0.15	35,600	
	(43-80X188-26)		1150	4	8.58	96.1	1.00	+0.17	29,900	
	(47-80X188-18)		1250	10	8.58	95.7	1.01	+0.29	24,600	
	(47-80X188-20)		1250	10	8.58	95.8	1.01	+0.28	27,700	
	(47-80X188-27)		1250	10	8.58	95.9	1.01	+0.31	27,600	
Grog (-100M)	(43-80X189-17)	Fired 1650°C	1150	4	8.60	95.0	1.00	+0.30	23,000	
	(43-80X189-18)		1150	4	8.60	95.0	1.01	+0.30	22,700	
	(43-80X189-21)		1150	4	8.60	95.1	1.00	+0.26	23,300	
	(47-80X189-14)		1250	10	8.60	95.0	1.03	+0.34	23,300	
	(47-80X189-20)		1250	10	8.60	95.0	1.02	+0.32	23,200	
	(47-80X189-23)		1250	10	8.60	95.0	1.02	+0.32	24,300	
(U_3O_8)	(43-80X190-38)	Fired 1650°C	1150	4	8.06	97.4	1.00	+0.01	31,100	
	(43-80X190-41)		1150	4	8.06	97.4	1.00	0	36,100	
	(43-80X190-43)		1150	4	8.06	97.5	1.00	-0.01	31,100	
	(48-80X190-37)		1250	10	8.06	97.2	1.00	+0.04	32,600	Surface black, section brown with black
	(48-80X190-42)		1250	10	8.06	97.4	1.04	+0.03	32,700	skin, no crazing
	(48-80X190-45)		1250	10	8.06	97.5	1.01	+0.01	29,500	
(U_3O_8) (24-hr dry mix)	(48-80X192-22)	Fired 1750°C	1250	10		98.5	1.25	+0.20	5,700	
	(48-80X192-33)		1250	10		98.5	1.20	+0.15	Cracked	
	(48-80X192-47)		1250	10		98.4	1.18	+0.11	5,500	

MUL-13792

1750°C - 98.3 ± 0.4
1700°C - 98.2 ± 0.2
1650°C - 97.4 ± 0.2

The explanation for the different behavior at these temperatures may be related to density or grain-size differences. Typical specimens have been submitted to petrography to elucidate this point.

c. LRL Uncoated Tubes

Table II-9 shows a series of LRL uncoated tubes of composition 2.5, 5.0, and 10.0% UO_2 which were tested at 1350°C for 4 hours under 75 psia oxygen. Tubes similar to the sample-13 series had previously been tested at 1250°C and 1150°C for 4 hours at 75 psia oxygen. These tests were reported in Quarterly Progress Report No. 7. The present tests were done to determine whether instability persists up to temperatures of 1350°C. Sample No. 13-32, containing 5 w/o UO_2, was hot-bend tested under 7500 psi at 1350°C. After ten minutes at test temperature, the alumina "load-transfer-rod" broke. The sample, however, was unaffected and no-load exposure was continued. The densities for all samples range from 98.8% to 99.6% of theoretical. Room-temperature modulus of rupture values after test indicated little loss of strength after testing at 1350°C for four hours, except for one 10% specimen (13-28). The balance of the data in Table II-9 are presented to elucidate the effect of composition between 5 and 10% UO_2.

In Table II-10 the data for all uncoated tubes are capsulated (information from Quarterly Report No. 7 also included). The salient features regarding the fuel instability of tubes prepared by the normal LRL process are:

1. Compositions of 2.5 to 5.0% UO_2 at 1150°C, 1250°C, and 1350°C have strengths ranging from 20,000 to 25,000 psi after testing; the 2.5% UO_2 tubes are the strongest (average strength 26,000 psi). In addition, two 5.0% UO_2 tubes withstood 7400 psi hot-bend load for 4 hours at 1150° and 1250°C.

2. Compositions from 6% to 10% UO_2 are not consistently satisfactory (the 6% tubes retained strength at 1250°C but not consistently at 1150°C). The 8% tubes (80X181) surprisingly withstood a 1250°C test, but showed erratic behavior at 1150°C. Tubes from batch 80X169 were poor at 1250°C.

Table II-9. Fuel Stability Tests — LRL Uncoated Tubes at 75 psia O_2.[a]

Sample No.	Tube description	% UO_2[b]	Test temp °C	Time at temp (hours)	% Theoret. density before test	% wt change	Flex. reson. ratio after testing	Mod. rupture after test (psi)
13-33	V-35 (Round - Tu)[c]	2.5	1350	4	98.8	-0.01	No test	27,400
13-34	V-35 (Round - Tu)	2.5	1350	4	98.9	-0.06	No test	25,800
13-35	V-35 (Round - Tu)	2.5	1350	4	98.8	-0.09	No test	30,900
13-36	V-35 (Round - Tu)	2.5	1350	4	98.8	-0.07	No test	27,300
13-29	50X156 (Hex - Tu)	5.0	1350	4	99.1	-0.09	No test	17,500
13-30	50X156 (Hex - Tu)	5.0	1350	4	99.1	-0.06	1.00	22,400
13-31	50X156 (Hex - Tu)[d]	5.0	1350	4	99.1	-0.11	0.99	22,400
13-32	50X156 (Hex - Tu)	5.0	1350	4	99.1	-0.10	1.00	23,800
13-25	100X151 (Hex - Tu)	10.0	1350	4	99.6	-0.17	No test	No test
13-26	100X151 (Hex - Tu)	10.0	1350	4	99.6	-0.14	No test	24,700
13-27	100X151 (Hex - Tu)	10.0	1350	4	99.5	-0.09	1.00	27,100
13-28	100X151 (Hex - Tu)	10.0	1350	4	99.6	+0.15	1.09	11,500
52-18	40X184 (Hex - Tu)	4.18	1150	10	98.5	-0.02	1.00	Not tested
52-21	40X184 (Hex - Tu)	4.18	1150	10	98.5	-0.03	1.00	26,900
52-26	40X184 (Hex - Tu)	4.18	1150	10	98.5	-0.02	1.00	17,700
52-24	50X185 (Hex - Tu)	5.20	1150	10	98.7	-0.02	1.00	19,900
52-41	50X185 (Hex - Tu)	5.20	1150	10	98.7	-0.02	1.00	20,600
52-53	50X185 (Hex - Tu)	5.20	1150	10	98.7	-0.02	1.00	20,600
52-24	60X186 (Hex - Tu)	6.19	1150	10	98.9	-0.03	1.00	19,500
52-31	60X186 (Hex - Tu)	6.19	1150	10	98.9	-0.02	1.00	25,200
52-45	60X186 (Hex - Tu)	6.19	1150	10	98.9	+0.14	1.25	8,800
52-15	70X187 (Hex - Tu)	7.26	1150	10	99.1	+0.19	1.26	6,100
52-19	70X187 (Hex - Tu)	7.26	1150	10	99.1	+0.18	1.22	8,500
52-27	70X187 (Hex - Tu)	7.26	1150	10	99.1	+0.14	1.08	16,200
52-67	80X181 (Hex - Tu)	8.36	1150	10	98.9	+0.01	1.01	20,400
52-75	80X181 (Hex - Tu)	8.36	1150	10	99.2	+0.05	1.01	8,600
52-99	80X181 (Hex - Tu)	8.36	1150	10	98.9	+0.04	1.00	14,300
44-4	40X184 (Hex - Tu)	4.18	1250	10	98.5	-0.03	1.00	20,900
44-30	40X184 (Hex - Tu)	4.18	1250	10	98.5	-0.02	1.00	23,600
44-39	40X184 (Hex - Tu)	4.18	1250	10	98.5	-0.01	1.00	20,900
44-23	50X185 (Hex - Tu)	5.20	1250	10	98.6	+0.02	1.00	21,700
44-26	50X185 (Hex - Tu)	5.20	1250	10	98.1	-0.03	1.00	23,200
44-45	50X185 (Hex - Tu)[e]	5.20	1250	10	98.7	-0.04	1.00	18,700
44-16	60X186 (Hex - Tu)[e]	6.19	1250	10	98.8	+0.07	1.00	29,300
44-29	60X186 (Hex - Tu)	6.19	1250	10	99.0	-0.02	1.00	21,600
44-37	60X186 (Hex - Tu)	6.19	1250	10	98.9	-0.01	1.00	24,500
44-16	70X187 (Hex - Tu)[e]	7.26 (7.24)	1250	10	99.0	+0.21	1.24	8,600
44-18	70X187 (Hex - Tu)[e]	7.26 (7.27)	1250	10	99.0	+0.25	1.22	6,800
44-25	70X187 (Hex - Tu)	7.26 (7.26)	1250	10	99.0	+0.23	1.26	6,400
44-72	80X181 (Hex - Tu)	8.36 (8.36)	1250	10	99.1	-0.01	1.00	32,500
44-79	80X181 (Hex - Tu)[e]	8.36 (8.33)	1250	10	98.8	+0.02	1.01	29,400
44-85	80X181 (Hex - Tu)[e]	8.36 (8.34)	1250	10	99.1	-0.03	1.00	37,000
63-255	80X169 (Hex - Tu)	8.1	1250	10	99.2	+0.20	1.16	7,100
63-257	80X169 (Hex - Tu)	8.1	1250	10	99.2	+0.20	1.11	6,600
63-267	80X169 (Hex - Tu)	8.1	1250	10	99.2	+0.25	1.20	6,600
62-276	80X169 (Hex - Tu)	8.1	1250	10	99.2	+0.19	No test	9,400
63-280	80X169 (Hex - Tu)	8.1	1250	10	99.1	+0.20	1.08	10,300
63-282	80X169 (Hex - Tu)	8.1	1250	10	99.2	+0.21	1.09	8,000
63-283	80X169 (Hex - Tu)	8.1	1250	10	99.2	+0.21	1.06	10,800

[a] Tests at 1350°C were brought up to temperature in 75 psia argon. All others were brought up in 75 psia oxygen.

[b] Values are nominal and are obtained from vault or batch composition. Values in parenthesis are chemical analysis.

[c] "Tu" refers to Tuballoy (U-238).

[d] Subjected to hot-bend load (7500 psi) for 10 minutes at 1350°C — alumina load-transfer rod broke.

[e] Tubes submitted to petrography.

MUL-13793

Table II-10. Summary of Fuel-Stability Tests — LRL Uncoated Tubes at 75 psia O_2.

Tube identification	% UO_2 [a]	Temp (°C)	Time [b] (hours)	No. samples tested	Average % theoret. density before testing	Average modulus [c] rupture after test (psi × 10^{-3})
V35 (Round - Tu) [d]	2.5	1150	4	4	98.7 ± 0.1	26.3 (21.1 - 30.2)
40X184 (Hex - Tu) [d]	4.2	1150	10	2 [e]	98.5 ± 0.1	22.3 (17.7 - 26.9)
50X156 (Hex - Tu) [d]	5.0 (5.2)	1150	4	4 [e]	99.2 ± 0.1	21.0 (18.0 - 23.7)
50X185 (Hex - Tu)	5.2	1150	10	3	98.7 ± 0.1	20.4 (19.9 - 20.6)
60X186 (Hex - Tu)	6.2	1150	10	3	98.9 ± 0.1	17.8 (8.8 - 25.2)
70X187 (Hex - Tu)	7.3	1150	10	3	99.1 ± 0.1	10.3 (6.1 - 16.2)
80X181 (Hex - Tu) [d]	8.4	1150	10	3	99.0 ± 0.1	14.4 (8.6 - 20.4)
100X160 (Hex - Tu) [d]	10.0	1150	4	4	99.7 ± 0.1	4.3 (3.6 - 4.7)
V35 (Round - Tu) [d]	2.5	1250	4	4	98.7 ± 0.1	27.0 (22.8 - 30.9)
40X184 (Hex - Tu) [d]	4.2	1250	10	3 [e]	98.5 ± 0.1	21.8 (20.9 - 23.6)
50X156 (Hex - Tu) [d]	5.0 (5.2)	1250	4	4 [e]	99.2 ± 0.1	21.0 (14.7 - 21.5)
50X185 (Hex - Tu)	5.2	1250	10	3	98.4 ± 0.2	21.2 (18.7 - 23.2)
60X186 (Hex - Tu)	6.2	1250	10	3	98.9 ± 0.1	25.1 (21.6 - 29.3)
70X187 (Hex - Tu)	7.3	1250	10	3	99.0 ± 0.1	7.3 (6.4 - 8.6)
80X181 (Hex - Tu)	8.4	1250	10	3	99.0 ± 0.1	33.0 (29.4 - 37.0)
80X169 (Hex - Tu) [d]	8.1	1250	10	7	99.2 ± 0.1	8.4 (7.1 - 10.8)
100X160 (Hex - Tu) [d]	10.0	1250	4	4	99.6 ± 0.2	5.5 (5.0 - 6.0)
V35 (Round - Tu)	2.5	1350	4	4	98.8 ± 0.1	27.9 (25.8 - 30.9)
50X156 (Hex - Tu)	5.0 (5.2)	1350	4	4	99.1 ± 0.1	21.5 (17.5 - 23.8)
100X160 (Hex - Tu)	10.0	1350	4	3	99.6 ± 0.1	21.1 (11.5 - 27.1)

[a] Values are nominal. Obtained from vault records. Values in parenthesis are wet chemical.

[b] Time at temperature.

[c] Ranges given in parenthesis.

[d] From Quarterly Report No. 7.

[e] One sample withstood 7400 psi hot-bend load throughout test.

3. Fuel instability at 1350°C does not appear serious, although the 10% UO_2 tubes did show rather large variations in modulus of rupture at this temperature. Both 1150°C and 1250°C seem to be equally severe from the standpoint of fuel instability, although some classes of tubes survived the 1250°C test. It is conceivable that the temperature is marginally within the fuel instability region reported previously.

d. Al-Coated Tubes

Table II-11 lists data for Al-coated LRL tubes tested at 75 psia oxygen. Test 27 was made to determine whether failure under hot-bend load was due to oxidation. The test furnace was first purged with argon at room temperature. The sample was then taken to test temperature under 75 psia argon. The furnace was depressurized to 1 atmosphere and repressurized to 75 psia oxygen, at which point the sample broke immediately. Coating designations (Nos. 4, 4A, 4B) are explained elsewhere. All are Al-paint dip coats with various amounts of kaolinite added.

The results indicate that, although Al-coated tubes (especially Nos. 4, 4A-2, and 4B) withstood the 1150° test in many instances, all tests of No. 4 coating failed at 1250°C. Note that in most recent tests, the test time has been increased from 4 to 10 hours. Yet to be proven are the 4A-2 and 4B type coatings at 1250°C for 10 hours. However, the greater stability of ZrO_2 - UO_2 fuels has caused reconsideration of Al coating.

e. Tory II-A-1 Tubes

Results for Tory II-A-1 tubes at 1150°C were reported in Quarterly Report No. 7. Further results are shown for 10-hour tests at 1250°C and 75 psia oxygen in Table II-12. Strength behavior was erratic and generally poorest at the higher concentrations. Modulus of rupture strengths for 4.93% UO_2 tubes range from 10,000 psi to 19,000 psi; for the 6.25% UO_2 tubes, strengths range from 16,000 psi to 21,000 psi; the 6.87 and 7.88% UO_2 samples had very low strengths ranging from 2,000 psi to 14,000 psi. Urania losses ranged about 1% (0.06 to 1.7%).

The previous observation (Quarterly Progress Report No. 7) that these tubes were more stable than LRL standard tubes at 1150°C fails to be true at 1250°C, where the Tory II-A-1 tubes showed poor stability.

Cycling tests were also run to simulate planned Tory II-A-1 conditions. Tubes containing a high concentration of UO_2 [Tory II-A-1 class 13

Table II-11. Al-Coated LRL Tubes at 75 psia O_2.

Sample No.	Tube description	% UO_2	Test temp °C	Time at temp (hours)	% Theoret. density before test	% wt change	Flex. reson. ratio after testing	Mod. rupture after test (psi)	Hot bend (7400 psi)
27-5	80X169 Coating #4	8.1	1150	0.25	99.8	0	1.00	24,300	No test
27-6	80X169 Coating #4	8.1	1150	0.25	99.7	No test	No test	No test	Note[a]
28-7	80X169 Coating #4	8.1	1250	10	99.8	+0.18	1.12	4,400	No test
28-8	80X169 Coating #4	8.1	1250	10	99.8	No test	No test	No test	Broke at 600°C
45-18	80X181 #4 Al Coating	8.36	1250	10	99.3	+0.04[b]		6,500	No test
45-41	80X181 #4 Al Coating	8.36	1250	10	99.4	+0.17[b]		4,700	No test
46-6	80X181 #4 Al Coating	8.36	1150	10	99.6	+0.05	No test	5,600	No test
46-25	80X181 #4 Al Coating	8.36	1150	10	99.4	+0.01	1.00	24,300	No test
50-9	80X181 #4 Al Coating	8.36	1250	10	99.3	+0.08	1.01	8,000	No test
50-13	80X181 #4 Al Coating	8.36	1250	10	99.3	+0.23	1.40	Cracked	No test
50-37	80X181 #4 Al Coating	8.36	1250	10	99.5	+0.32	1.34	4,100	No test
50-38	80X181 #4 Al Coating	8.36	1250	10	99.3	+0.20	1.18	6,400	No test
50-43	80X181 #4 Al Coating	8.36	1250	10	99.2	+0.08	1.02	6,400	No test
50-50	80X181 #4 Al Coating	8.36	1250	10	99.1	+0.03	1.00	20,000	No test
37-122	80X169 Al Coating	8.1	1150	4	99.4	+0.05	1.01	25,700	No test
37-124	80X169 Al Coating	8.1	1150	4	99.5	+0.07	1.02	14,500	No test
37-125	80X169 Al Coating	8.1	1150	4	99.4	+0.01	1.00	21,900	No test
37-116	80X169 Al Coating	8.1	No test	No test	99.4	No test	No test	23,100	No test
38-150	80X169 Coating 4A-1	8.1	1150	4	99.4	+0.07	1.07	8,700	No test
38-155	80X169 Coating 4A-1	8.1	1150	4	99.2	+0.10	1.08	8,800	No test
38-157	80X169 Coating 4A-1	8.1	1150	4	99.6	+0.01	1.04	15,300	No test
38-165	80X169 Coating 4A-1	8.1	No test	No test	99.2	No test	No test	27,200	No test
39-146	80X169 Coating 4A-2	8.1	1150	4	99.5	+0.01	1.00	22,200	No test
39-149	80X169 Coating 4A-2	8.1	1150	4	99.5	+0.06	1.03	17,700	No test
39-156	80X169 Coating 4A-2	8.1	1150	4	99.6	+0.01	1.00	17,600	No test
39-164	80X169 Coating 4A-2	8.1	1150	4	99.5	+0.05	1.00	24,900	No test
39-169	80X169 Coating 4A-2	8.1	No test	No test	99.6	No test	No test	17,100	No test
40-106	80X169 Coating 4B	8.1	1150	4	99.6	+0.01	1.00	24,700	No test
40-114	80X169 Coating 4B	8.1	1150	4	99.6	+0.01	1.00	24,600	No test
40-118	80X169 Coating 4B	8.1	1150	4	99.5	-0.04	1.00	24,800	No test
40-127	80X169 Coating 4B	8.1	No test	No test	99.5	No test	No test	26,100	No test

[a] Sample to temp in 75-psia argon, purged, switched to 75 psia O_2. Broke immediately.

[b] The ends of both tubes were bleached white after testing.

MUL-13830

Table II-12. Other Tubes (Tory II-A-1) at 75 psia O_2.

Sample No.	Tube description	Nominal % UO_2	Temp °C	Time hours	% Theoret. density before	% wt change	Flex. reson. ratio after testing	Mod. rupt. after test (psi)	% UO_2 loss by γ count	
35-1	Tory II-A-1, Class 2	4.93	1250	10	97.8	+0.12	1.05	19,900	0.77	
35-2	Tory II-A-1, Class 2	4.93	1250	10	97.8	+0.12	1.10	10,800	1.67	
35-3	Tory II-A-1, Class 2	4.93	1250	10	97.4	+0.06	1.05	15,500	1.05	
35-4	Tory II-A-1, Class 2	4.93	1250	10	97.3	+0.11	1.03	18,200	1.15	
35-5	Tory II-A-1, Class 7	6.25	1250	10	97.5	-0.04	1.04	20,900	1.64	
35-6	Tory II-A-1, Class 7	6.25	1250	10	97.1	+0.20	1.05	20,200	0.78	
35-7	Tory II-A-1, Class 7	6.25	1250	10	97.4	+0.05	1.04	16,900	0.81	
35-8	Tory II-A-1, Class 7	6.25	1250	10	97.5	+0.04	1.04	19,000	0.82	
35-9	Tory II-A-1, Class 9	6.87	1250	10	98.0	+0.05	1.09	14,400	1.73	
35-10	Tory II-A-1, Class 9	6.87	1250	10	97.9	+0.19	Not taken	2,400	1.06	
35-11	Tory II-A-1, Class 9	6.87	1250	10	97.8	+0.13	1.13	10,600	0.88	
35-12	Tory II-A-1, Class 9	6.87	1250	10	97.5	+0.21	1.12	8,100	0.62	
35-13	Tory II-A-1, Class 12	7.88	1250	10	97.4	+0.18	1.11	11,300	1.01	
35-14	Tory II-A-1, Class 12	7.88	1250	10	97.6	+0.13	1.11	14,000	1.40	
35-15	Tory II-A-1, Class 12	7.88	1250	10	97.5	+0.31	1.10	10,500	0.46	
35-16	Tory II-A-1, Class 12	7.88	1250	10	97.6	+0.25	1.11	6,100	0.76	
42-1	Core sample, hot-pressed plate No. 049360 (V-19, Zone F)	4.24	1150	4	98.9	-0.01	No test	27,200[a]		(Brown, no
42-2	" " No. 049360 (V-19, Zone D)	4.24	1150	4	98.2	-0.02	No test	26,100		(crazing
42-3	" " No. 049391 (V-82, Zone F)	6.01	1150	4	98.9	0	No test	6,900		(Brown, but
42-4	" " No. 049391 (V-82, Zone D)	6.01	1150	4	98.5	+0.01	No test	5,600		(crazed
42-5	" " No. 052500 (V-91, Zone F)	3.96	1150	4	97.2	-0.03	No test	26,900		(
42-6	" " No. 052500 (V-91, Zone D)	3.96	1150	4	99.9	-0.03	No test	26,500		(Brown, no
42-7	" " No. 051855 (V-98, Zone F)	5.40	1150	4	99.9	-0.03	No test	29,300		(crazing
42-8	" " No. 051855 (V-98, Zone D)	5.40	1150	4	98.5	-0.01	No test	30,400		(
42-9	Rectangular Hot Pressed Prisms - Annealed	5.0	1150	4	99.9	+0.11	No test	No test		(
42-10	Rectangular Hot Pressed Prisms - Annealed	5.0	1150	4	99.6	+0.10	No test	No test		(
42-11	Rectangular Hot Pressed Prisms - Annealed	5.0	1150	4	99.6	+0.12	No test	No test		(All samples
42-12	Rectangular Hot Pressed Prisms - Annealed	5.0	1150	4	99.6	+0.10	No test	No test		(black and
42-13	Rectangular Hot Pressed Prisms - Annealed	5.0	1150	4	99.7	+0.08	No test	No test		(badly cracked
42-14	Rectangular Hot Pressed Prisms - Annealed	5.0	1150	4	99.6	+0.12	No test	No test		(

[a] Broken on 3/4-in. centers.

MUL-13831

(8.27% UO_2)] were chosen, since previous testing indicated that high fuel concentrations were most likely to show oxidizing instability.

Testing condition and results are shown in Table II-13. All tubes displayed high modulus of rupture values after testing. The change in flexural resonance was slight, but does indicate some slight loss of strength during testing.

Fuel losses for all samples were small. The two samples (35-17 and 35-20) cycled 5 times to 1260°C in oxygen showed the highest losses (0.8% UO_2 by gamma counting).

A previous test made on class 13 tubes consisted in heating and cooling slowly (1-1/2 hours) under pressure (5 atm O_2) and holding at 1150°C for 4 hours. All four showed high strengths (24,000; 30,800; 33,100; and 26,100 psi).

Our conclusion is that the tubes withstood the tests satisfactorily. They should withstand similar Tory II-A-1 operations, subject to the limitations that the tests were carried out under laboratory conditions (i.e., free of thermal stress, radiation field, and flow conditions), and that the tubes represented only a small sampling of all the tubes in the core.

f. Hot-Pressed Plates

These specimens (Table II-12) were of two types. The first type were cores from hot-pressed plates intended for Tory II-A-2. These varied from 3.96 to 6.01% UO_2. These samples were satisfactory at 1150°C, 4 hours, 75-psia oxygen up to 5.4% UO_2. However, the 6.01% samples were crazed and had poor strengths after testing.

Rectangular hot-pressed prisms were also supplied (reputedly of 5% UO_2). These were purported to be hydrogen-annealed and expected to have good fuel retention. Interestingly, these all showed weight gains and had severe longitudinal cracks after testing. Consequently, strengths were not determined after test.

g. Tubes Containing Y_2O_3

Table II-14 shows a compilation of tests on tubes containing Y_2O_3 stabilized urania. The densities of all the tubes were consistently high (99.9% for the 6% UO_2 tubes). Weight gains varied from 0.08 to 0.39%. There did not seem to be any correlation between weight gain and modulus of rupture after testing. Modulus of rupture strengths ranged from 20,000 to 42,000 psi.

Table II-13. Tory II-A-1 Fuel Stability Tests.

Specimen No.[a]	% Theoret. density	% wt change	Flexural resonance before	Flexural resonance after	Ratio Rb/Ra (cycles) (sec)	Mod. rupt. (psi)	% Fuel loss (±0.1% by gamma count)	Testing conditions[b]	No. of cycles
35-17	97.8	-0.04	8735	8356	1.05	31,100	0.83	Heat in 1 atm O_2 to 1260°C in 10 min. Hold at 1260°C and 70-psig O_2 for 1 min. Cool in 1-atm O_2 to approx. 200°C in 10 min.	5
35-18	97.9	-0.01	8718	8448	1.03	29,100	0.02	Heat in 50-psig air to 1260°C in 12 min. Hold at 1260°C and 50-psig air for 1 min. Cool in 50-psig air to approx. 200°C in 10 min.	1
35-19	97.8	-0.02	8734	8500	1.03	32,700	0.05	Heat in 1-atm air to 1260°C in 10 min. Hold at 1260°C and 50-psig air for 1 min. Cool in 1-atm air to approx. 200°C in 10 min.	1
35-20	97.8	-0.04	8700	8395	1.04	28,900	0.81	Ditto sample 35-17	5
36-17	98.1	-0.01	8737	8383	1.04	23,300	0.16	Heat in 1-atm N_2 to 1150°C in 20 min. Flush and hold at 1150°C and 60-psig O_2 for 60 min. Flush and cool in 1-atm N_2 to approx. 200°C in 10 min.	1
36-18	97.8	-0.01	8639	8495	1.02	24,000	0.21	Ditto sample 35-17, except hold at 1100°C instead of 1260°C	5
36-19	97.1	-0.01	8702	8510	1.02	28,800	0.08	Sample aborted: attempted 350-psig air at 1150°C, developed leak at 150 psig and terminated test	1
36-20	97.8	-0.02	8688	8483	1.02	32,100	0.25	Heat in 1-atm air to 1100°C in 10 min; pressurize to 350-psig air in 2 min. Hold in 350-psig air for 1 min; depressurize to 1-atm air in 2 min. Cool in 1-atm air to approx. 200°C in 10 min.	5

[a] All tubes Tory II-A-1, Class 13, 8.27% UO_2.

[b] Temperatures are nominal ±25°C.

MUL-13832

Table II-14. Tubes Containing Y_2O_3 Stabilized UO_2 (75-psia O_2).

Test No.	Tube description	Test temp °C	% UO_2 [a]	% Theoret. density [b]	% wt change	Resonance ratio R-initial R-final	Hot-bend [c] results (7400 psi)	Modulus rupture after test psi	Flexural resonance before testing (cycles/sec)
20-1	6BF116-45	1150	6.0 ---	99.9	+0.10	1.00	Unbroken (4 hr)	20,000	7224
6-11	6BF116-57	1150	6.0 (6.14)	99.9	+0.10	1.00	No test	36,600	7157
6-12	6BF116-56	1150	6.0 (6.13)	99.9	+0.09	0.99	No test	35,400	7195
6-13	6BF116-53	1150	6.0 (6.12)	99.9	+0.10	1.00	No test	34,200	7184
6-14	6BF116-74	1150	6.0 (6.12)	99.9	+0.09	1.00	No test	35,700	7178
20-2	6BF116-32	1150	6.0 ---	99.9	+0.10	1.00	No test	17,400	7248
9-11	6BF116-40	1250	6.0 (6.08)	99.9	+0.15	0.99	No test	19,500	7174
9-12	6BF116-59	1250	6.0 (6.15)	99.9	+0.39	0.99	No test	21,400	7152
9-13	6BF116-68	1250	6.0 (6.11)	99.9	+0.20	0.99	No test	20,500	7173
9-14	6BF116-69	1250	6.0 (6.14)	99.9	-0.20	1.00	No test	21,600	7252
32-1	10BF116-A22E30	1150	10.0	99.2	+0.08	1.00	Unbroken (10 hr)	20,400	5505
32-2	10BF116-A22E13	1150	10.0	99.1	+0.08	1.00	No test	21,500	5459
29-4	10BF116-A22E38	1250	10.0	99.1	No test	No test	Unbroken (10 hr)	No test	5549
29-11	10BF116-A22E8	1250	10.0	99.1	No test	1.00	No test	20,400	5510

[a] Values in parenthesis are chemical analysis, other values are nominal values.

[b] Values based on chemical analysis when available. Theoretical density of 6% and 10% are 3.245 g/cm^3 and 3.424 g/cm^3, respectively.

[c] Sample 29-4 was broken after test completion when furnace blew.

MUL-13833

In every case, the resonance ratio was 1.00, which indicated little change in structural integrity during the test.

Two specimens (10% UO_2) withstood the hot-bend test (7400 psi, 3-point bend) for 10 hours at 1150°C and 1250°C.

3. Fuel-Loss Testing

Fuel loss was measured as a function of atmosphere (air and oxygen) and temperature (1525°C and 1650°C) at several fuel loadings (6.58% to 8.22% UO_2), and at a constant time of 7 hours (Table II-15). A flow rate of 0.0086 cfm (0.24 liter/minute) of dry gas was used, giving one furnace-atmosphere change once every five minutes. The furnace was purged with dry air before the samples were introduced into the furnace and for 10 minutes before the samples were removed. After the samples reached test temperature (seven minutes after entry), the test atmosphere was turned on.

The results are not yet complete, but so far indicate:

1. Fuel loss, by gamma count, agrees well with that determined by weight loss.

2. Losses at 1645-1650°C were all 68-77% in oxygen.

3. Losses at 1525°C were 6-7% for the 6.58% UO_2 loaded material and 2.5-4% for the 8% UO_2 loading.

4. At 1650°C the loss was roughly proportional to the oxygen partial pressure, i.e., about five times higher for oxygen than for air. This is not necessarily true at times other than 7 hours, nor at lower temperatures.

5. At 1525°C the fuel loss for BeO - UO_2 containing ZrO_2, a 2% loss by weight determination, was about the same or somewhat lower than for BeO - UO_2 alone (2 - 4% loss) at the same composition (7.5-8.2% UO_2).

6. At 1650°C the fuel loss in oxygen of BeO - UO_2 containing ZrO_2 was less than half that for BeO - UO_2 alone.

7. Strength was not markedly reduced even after 70% fuel loss. The two low-strength values, 12,600 and 8,900 psi, accompanied low fuel losses and may have been caused by cracking while the samples were changing temperature in the instability region (1050-1250°C). This was not observed in the case of the lower fuel loadings (6.58% UO_2), which is consistent with their greater stability.

Table II-15. Fuel Loss vs Temperature and Atmosphere (7 hours Duration).

Sample No.	% UO_2	Atm flow cfm	Test temp °C	Fuel loss: Weight loss (%)	Fuel loss: Based on wt %	Fuel loss: Change in gamma count %	Modulus of rupture psi	
209-658-114-31-1209-7	6.58	0.0086 O_2	1520	0.420	6.38	6.36	24,100	
1209-20	6.58	0.0086 O_2	1525	0.499	7.58	7.72	24,100	
1209-29	6.58	0.0086 O_2	1645	5.02	76.3	71.3	20,200	
1209-44	6.58		Untested - modulus of rupture only				24,400	
1209-55	6.58	0.0086 Air	1645	0.947	14.4	14.16	Not determined	
1209-63	6.58	0.0086 O_2	1645			67.6	Not determined	
209-658-117-31-1209-95	6.58	0.0086 O_2	1520	0.398	6.05	5.65	24,400	
1209-102	6.58	0.0086 O_2	1525	0.430	6.53	6.09	26,900	
1209-111	6.58	0.0086 O_2	1645	5.05	76.8	71.2	22,600	
1209-122	6.58		Untested - modulus of rupture only				29,600	
1209-136	6.58	0.0086 Air	1645	1.18	17.9	17.9	Not determined	
1209-141	6.58	0.0086 O_2	1645			67.5	Not determined	
211-815-121-31-1211-9	8.15	0.0086 O_2	1521	0.211	2.59	3.37	29,000	
1211-20	8.15	0.0086 O_2	1540	0.264	3.24	3.65	12,600	
1211-27	8.15	0.0258 O_2	1520	0.300	3.68	4.20	28,300	
1211-30	8.15	0.0086 O_2	1645	6.40	78.5	75.0	Not determined	
212-822-123-31-1212-10	8.22	0.0086 O_2	1540	0.239	2.91	3.31	8,900*	
1212-23	8.22	0.0086 O_2	1521	0.169	2.01	2.64	41,900	
1212-31	8.22	0.0258 O_2	1520	0.212	2.33	3.00	33,000	
1212-44	8.22	0.0086 O_2	1645	6.45	78.5	74.4	Not determined	
V 36 - 17	7.5	0.0086 O_2	1650	6.20	82.7	U^{238} Unable to count		
V 36 - 20	7.5	0.0086 O_2	1650	6.28	83.7	U^{238} Unable to count		
V 36 - 19	7.5	0.0086 Air	1650	1.02	13.60	U^{238} Unable to count		
V 36 - 22	7.5	0.0086 Air	1650	1.20	16.00	U^{238} Unable to count		
80X182-1	7.85	0.0086 O_2	1520	0.160	2.04	U^{238} Unable to count	Contains approx. 4.9 w/o ZrO_2	
80X182-2	7.85	0.0086 O_2	1520	0.161	2.05	U^{238} Unable to count	Contains approx. 4.9 w/o ZrO_2	
80X182-3	7.85	0.0086 O_2	1641	2.37	30.2	U^{238} Unable to count	Contains approx. 4.9 w/o ZrO_2	
80X182-4	7.85	0.0086 O_2	1641	2.50	31.8	U^{238} Unable to count	Contains approx. 4.9 w/o ZrO_2	

* Specimen appeared laminated after testing.

MUL-13834

4. Determination of UO_2 Concentration by Gamma Counting

Data have been compiled which relate UO_2 content (U-235), as determined by wet chemistry, with gamma counting. Assuming that the gamma count of a tube is proportional to the concentration and the weight of the tube, and inversely proportional to the density, then the following equation can be written:

$$\gamma_{ct} = K(\text{conc.})W/\rho ,$$

where W is the weight, ρ is the density, and K is a constant whose value is a function of sample and counter geometry. If BeO exhibits no shielding effect, then a plot of (conc.) vs $\gamma_{ct} \times \rho/W$ should yield a straight line which goes through the origin. This is shown to occur in Fig. II-4. Also, some vacuum-annealed tubes for which gamma-count and wet-chemistry data were available are also shown. These points fall slightly below the curve, but it should be pointed out that they were counted on different shelves than the other specimens and had to be corrected to the same shelves as the standard samples. Three-inch lengths of the original specimens have been retained for use in calibrating different shelves and different specimen lengths. Data are listed in Tables II-16 and II-17.

5. Corrosion Blowpipe

A summary of six samples run in the blowpipe is given in Table II-18. All of the samples but one were coated with from one to three coats of aluminum paint, but these coatings were later considered ineffective. Sample 109-L-3 was recoated with one coat of aluminum paint No. 4, and earlier coatings disregarded.

Thermal stresses were induced in samples 109-L-2 and 3. The SiC heater temperature was 1550°C at the start of the test of sample 2. During the run the SiC oxidized, giving low optical readings. The final heater temperature was at least 1750°C, giving a corresponding maximum tensile stress of about 8300 psi in the sample. For sample 3 the SiC temperature was limited to 1500°C, which gave a maximum tensile stress of about 3800 psi. These tensile stresses (σ_θ) were located along the base surface of the tube, tangential to the bore diameter; along this same surface axial stresses (σ_z) have the same value. The predominant effect in the samples reported appears to be damage — oxidation (black color), crazing, and loss of strength (modulus of rupture) — due to thermal stresses. Weight and gamma-count changes do not form a pattern. The aluminum-paint coatings do not appear to be effective in the presence of thermal stresses.

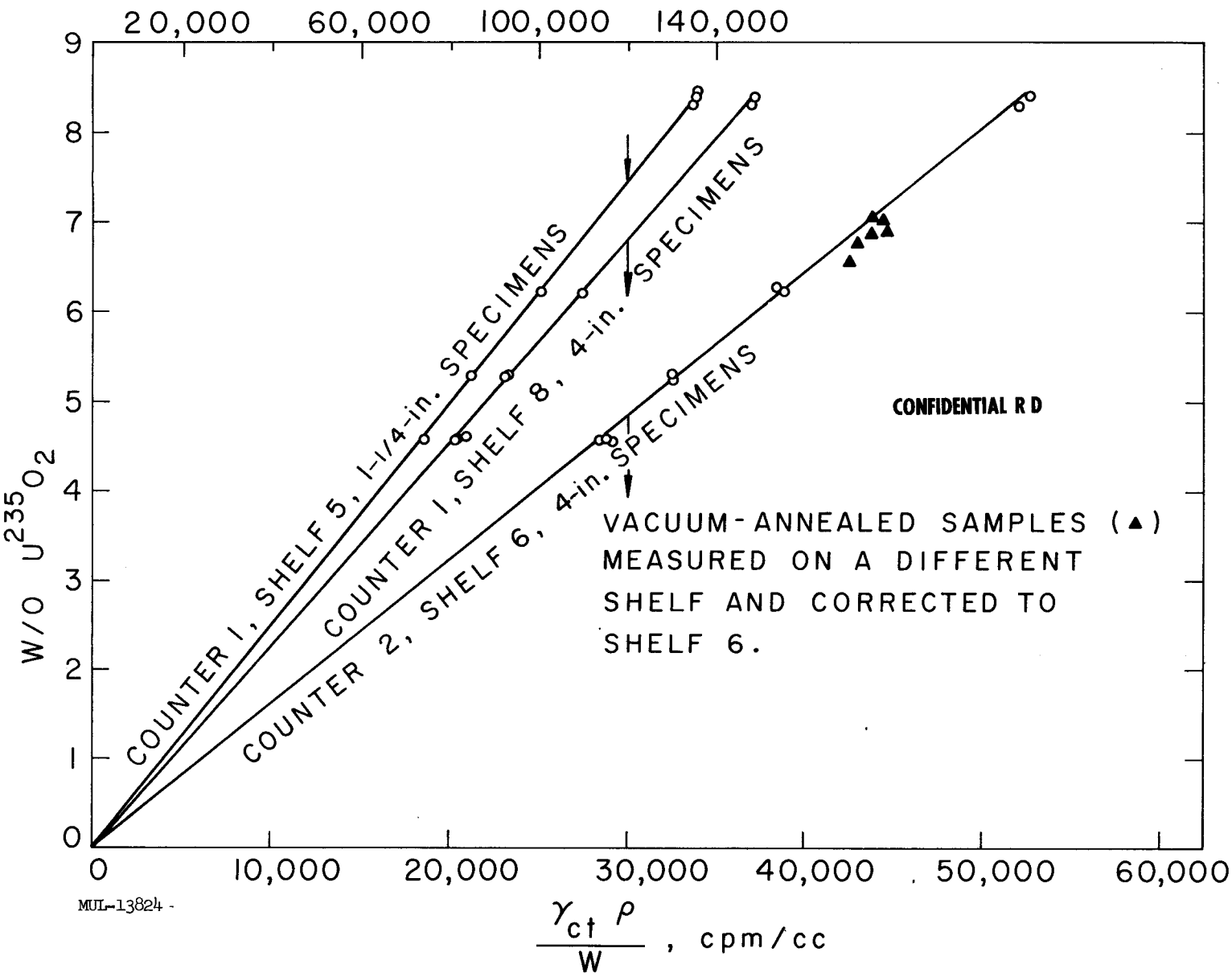

Fig. II-4. $U^{235}O_2$ concentration as a function of gamma count.

Table II-16. Determination of UO_2 Concentration by Gamma Counting of U^{235}

Sample No.	w/o UO_2*	ρ, g/cc	% Theoret. density	Specimens cut to 4-inch lengths: Counter No. 1, shelf 8 — γ Count cpm	$\frac{\gamma ct\ \rho}{W_1}$ (cpm)/(cc)	Specimens cut to 4-inch lengths: Counter No. 2, shelf 6 — γ Count cpm	$\frac{\gamma ct\ \rho}{W_1}$ (cpm)/(cc)	Specimens cut to 1-1/4-inch lengths: Counter No. 1, shelf 5 — γ Count cpm	$\frac{\gamma ct\ \rho}{W_1}$ (cpm)/(cc)
1043B-47									
1	4.60	3.048	97.9	55,820	20,280	79,160	28,760	63,948	73,860
2	4.61	3.056	98.2	55,893	20,290	79,214	28,760	64,158	74,080
67	4.60	3.063	98.4	56,045	20,540	79,348	29,080	64,278	74,150
3	4.59	3.022	97.1	55,837	20,120	79,020	28,470	63,798	73,110
1040E-40									
10	5.28	3.084	98.6	64,500	23,123	91,180	32,690	74,052	84,890
17	5.30	3.081	98.5	63,702	23,090	91,107	32,670	72,463	84,850
8	5.28	3.081	98.5	63,160	23,140	89,326	32,723	71,909	84,680
4	5.29	3.086	98.6	64,092	23,130	90,795	32,764	72,794	84,650
1049J-11									
55	6.24	3.099	98.3	75,264	27,300	106,454	38,610	86,317	99,710
71	6.24	3.106	98.6	76,035	27,430	107,500	38,780	86,771	99,950
1	6.23	3.102	98.4	76,340	27,400	108,122	38,800	87,444	99,950
26	6.25	3.105	98.52	76,034	27,450	107,925	38,970	86,548	99,900
13Q									
1	8.32	3.180	99.3	106,427	36,810	150,404	52,020	121,700	134,250
2	8.43	3.181	99.3	105,656	37,000	149,810	52,460	121,200	135,190
3	8.40	3.184	99.4	105,255	37,080	149,153	52,540	120,578	135,380
4	8.42	3.182	99.3	105,974	37,100	149,796	52,450	121,100	135,140

* Determined by wet chemical analysis. Accuracy = ±0.5%.

MUL-13835

Table II-17. Determination of UO_2 Concentration by Gamma-Counting Vacuum-Annealed Samples.

Sample No.	w/o* UO_2	Annealing conditions: Time hr	Annealing conditions: Temp °C	% UO_2 loss	ρ g/cc	Counter No. 2, shelf 6: $\frac{\gamma \text{ ct } \rho}{W}$	Counter No. 2, shelf 6: $\frac{\text{cpm}}{\text{cc}}$
1109-136	6.96	0.5	1800°C	0.301	3.139	43,970	
1109-126	7.04	0.5	1800°C	0.02	3.137	44,400	
1109-235	6.93	2	1900°C	5.92	3.146	44,470	
1109-159	6.93	2	1900°C	6.98	3.146	43,590	
1109-256	6.78	4	1900°C	15.95	3.142	43,000	
1109-148	6.57	4	1900°C	16.25	3.145	42,500	

* By wet chemical analysis. Accuracy = ± 1%.

Sample X-151-7 had an air flow of 62.4 scfm, equal to reactor flight conditions. This gave a supersonic shock wave downstream from the sample, and a pressure drop at that point of from 285 to 32 psia. This resulted in loss of flow control, and the shock wave broke the air-stream thermocouple. When the flow was reduced to about 85% of reactor flow (52 scfm, all other samples) all velocities were subsonic, flow control was good, and downstream pressures were usually about 235 psia.

A high-pressure thermal-stress furnace has been constructed. The unit will develop thermal stresses (σ_θ) up to 15,000 psi tension in standard fueled tubes at all reactor operating temperatures, with a moderate velocity air flow at all pressures up to 400 psia. Bore temperatures are determined by optically sighting down the length of the tube. Calibration runs show maximum errors of about ± 25°C at 50 psia increasing to ± 100°C at 300 psia. These maximum errors will vary stresses by only ± 1000 psi, but the problem of correlating stress effects with a given test temperature still exists.

C. Protective Coatings

1. Al Coatings

Several additions to Al paint-dip coats were tried, in addition to the Al paint coat itself:

No. 4	9.2 w/o	kaolinite,	balance	Al paint
No. 4A-1	6.6 w/o	kaolinite,	balance	Al paint
No. 4A-2	1.7 w/o	kaolinite,	balance	Al paint
No. 4B	3.3 w/o	kaolinite,	balance	Al paint

Table II-18. Corrosion Blowpipe Results.

Sample	% UO_2	Density g/cc	Density % Theoret.	Coating	Test conditions: Pressure psia	Temp °C	Air flow scfm	Dew point °F	Time, hours
Lot X-151									
29	5.3	3.09	98.9	None	285	1160	52	-48	2
3	5.3	3.09	98.9	1 coat Al paint*	285	1160	52	-60	2
7	5.3	3.09	98.8	1 coat Al paint*	285	1100	62	-61	0.5
Lot 109-L									
1	6.86	3.14	99.3	1 coat Al paint*	285	1170	52	-80	4
2	6.86	3.14	99.3	2 coats Al paint*	285	(1200 inside (1218 outside	52	-76	2
3	6.86	3.14	99.3	1 coat Al paint #4	285	(1160 inside (1169 outside	52	-80	1.5

* These coatings were not considered good coatings — see text.

Sample	ΔUO_2 % by wt	ΔUO_2 % by γ count	Results: Density g/cc	Thermal stress, (σ_θ) max tension, psi	Modulus of rupture, psi (post-test)	Crazed	Appearance
Lot X-151							
29	-0.5	†	3.09	0	18,000	No	Solid brown, dark surface, no apparent damage
3	-0.1	†	3.09	0		No	Solid brown, no apparent damage
7	-0.1	†	3.09	0	17,500	No	Solid brown, no apparent damage
Lot 109-L							
1	-0.8	-1.2	3.14	0	23,300	No	Solid brown, no apparent damage
2	-0.3	-1.4	3.04	8,300	2,900	Yes	Black throughout, badly crazed, few isolated brown areas
3	-0.3	0	3.14	3,800	4,400	Yes	Black throughout with a few isolated brown areas, some crazing

† U-238 — no counts taken.

MUL-13836

Tubes containing 8% UO_2 were dip-coated and tested for instability (Table II-11). The test results were erratic for the No. 4 coats at 75 psia and 1150°C, but all "failed" at 1250°C (10 hours), i.e., post-test strengths of about 5000 psi (see pressure testing). Furthermore, No. 4 Al coats showed erratic behavior in other tests carried out as follows: tubes were heated up to 1150°C in 15 minutes in 75-psia oxygen, then kept at 1150°C for 1.5 hours and 5 hours, respectively (2 samples). Weight changes were negligible and the tubes were integral after testing. However, two other samples cracked after 8 and 22 hours, respectively, at 1350°C, after being heated up (26 minutes) to temperature in 75-psia oxygen. Furthermore, weight loss was 0.5%, indicating appreciable fuel loss (0.5/0.08 = 6% UO_2, ignoring oxidation to U_3O_8).

It is believed that these coatings are not reliable enough, although No. 4B coating, which showed good stability in 3 out of 3 tubes at 1150°C testing, have not been exposed to 1250°C. The trend seems to indicate that low or zero concentration of kaolinite is best.

2. Vapor Phase Al_2O_3 Coating

An eight-percent UO_2 (U-235)-BeO tube, four-inches long, was completely coated with Al_2O_3. Coating thickness was figured on a weight-gain basis and averaged about 0.7 mils on the i.d. and 0.15 on the o.d. Visually, (near the tube ends) the i.d. coat appeared as dense, crystal clear, and uniform. The o.d. coat had some areas which appeared powdery and less dense. Experimental work has indicated that this powdery appearance is inferior in imperviousness and adherence to the dense vitreous coats.

This tube, an adjacent BeO and an 8% UO_2 (U-235)-BeO control tube, were weight-loss tested in wet air (94°F dew point) for four hours. Approximately three inches of each tube were in a constant-temperature zone of 1530°C with the other inch in a gradient (end at about 1490°C).

Both weight change and visual observation of sections through the tested tubes indicated that the one coated with Al_2O_3 showed UO_2 oxidation to about the same degree as the U-235 control. The o.d. coating did not uniformly cover the specimen. Apparently, portions of the thin coat (0.2 mil) and its powdery areas offered little or no protection.

An improved apparatus for vapor-depositing Al_2O_3 on the o.d. of BeO-fueled tubes has been made and calibrated for operation. Coatings plated with this equipment are more dense and vitreous appearing over the entire tube surface with no powdery-like areas present. Improvement has also been made in i.d. coating as evidenced by this same dense-vitreous appearance which seems uniform over the entire i.d.

Photomicrographs of vapor-deposited Al_2O_3 on the i.d. of an 8% UO_2 - BeO tube were made. The Al_2O_3 coating, when deposited during a half-hour period, varied in thickness between 0.4 and 0.6 mils over the 4-inch length. It was single crystal in thickness and polycrystalline along its length and width. Grain boundaries in the coating appear to exist at, and protrude out from, the grain boundaries in the tube.

D. Mechanical Properties

1. Compressive Creep

Recent work has been directed towards establishing creep stress laws for LRL BeO-10 w/o UO_2. A test selected to clarify the nature of the creep stress law at 2500°F has been completed (specimen L-144). The creep rate at 5500 psi correlates with the linear portion of the curve (Fig. II-6 — Quarterly Report No. 7). The conflicting results from specimens L-144 and L-103 (6000 psi test) have been scrutinized, but no discrepancies could be found. Additional data obtained from future creep tests employing the change-of-temperature and change-of-stress technique will be used to establish which test is valid.

Three tests selected to reveal the nature of the stress laws at 2600°F and 2700°F are reported below along with the data for specimen L-144.

Specimen	Percent UO_2	Density % theoret.	Temp °F	Stress psi	Secondary creep rate in/in/hr
L-144	10	98.8	2500	5500	3.28×10^{-4}
L-113	10	99.0	2600	1500	2.05×10^{-4}
L-115	10	99.0	2700	1500	6.01×10^{-4}
L-153	10	99.0	2700	3000	10.9×10^{-4}

2. High-Strength Extruded Rods

Two samples of BeO extruded rods sintered at 1500°C (outside organization) were examined for chemistry and microstructure. These rods were samples which exhibited very high moduli of rupture (70,000 psi in 3-point bend test). The analytical results indicate that the major difference between these bodies and standard UOX powder is that the former contains about 0.1% of magnesium. Densities were 2.93 and 2.85 g/cm^3.

The microstructural results obtained for two samples from different rods showed the following:

Sample I. The equant, angular BeO grains vary in size from 7-28 μ with a modal size of approximately 7 μ. There are two different impurities in this sample. One is black opaque material, 3-15 μ in size and equant to tabular in shape. It constitutes about 0.8% of the sample. The other impurity appears grey in transmitted light, is about 10 μ in size and appears to be isotropic or have very low birefringence. Pores make up about 4-5% of the material. (Density = 2.85 g/cm^3 or 95%.)

Sample II. The BeO grains are equant and angular with a modal size of about 7 μ. No impurities were observed within the sample. Porosity appeared very low, about 0.8%. (Density = 2.93 g/cm^3 or 97.6%.)

3. Thermal Stress

Five steady-state thermal-stress runs on BeO have been completed using the washer-shaped samples, 3/4-in.-o.d. × 1/4-in.-i.d. × 3/4-in.-long. Four samples are tested at a time so that the results in Table II-19 give an indication of the sample statistics.

The stress was applied in a linear fashion on a one-minute cycle. The data indicate the materials parameter $\sigma k/E\alpha$ is decreasing up to at least 2550°F.

Table II-19. Thermal Stress Resistance of BeO.

Sample No.	ρ (g/cc)	No. samples cracked	T_{mean} °F	T_{mean} °C	Q (watts/inch)	Stress, psi *(calc)
8	97.09	3	2067	1130	230	21,800
5	- -	3	2540	1393	156	18,470
32	- -	0	2550	1398	116	13,750
26	97.09	4	2550	1398	203	24,070

$$\sigma_t\ *(\text{calc}) = \frac{E\alpha\, Q \ln (r_2/r_1)}{4\pi k}$$

for $r_2/r_1 = 3$

$$\sigma_t = \frac{0.0874\ E\alpha Q}{k}$$

E. Sintering Study on 8-w/o Fueled Tubes

The purpose of this investigation was to observe the density change with temperature during the sintering operation. A possible useful application would be to improve the slip-dip application of refractory coatings to protect the fuel element from water attack at high temperatures.

Tubes containing nominally 8-w/o UO_2 were used. The methods of adding the fuel were (1) by standard slurpitation, and (2) mixing of powders.

These fuel elements were extruded and starch-burned at the usual temperature (1500°F). The sintering temperature was varied from 1500°C/6 hours to 1850°C/6 hours. Results of the sintering curves are shown in Table II-20.

In another study, tubes were fired in hydrogen and their shrinkages observed (using a cathetometer) as temperatures increased. The total heating time was 4 hours from room temperature to 1750°C in each case, with a linear time-power input. The tubes subjected to this study all contained 8% UO_2. 80X182 contained zirconia; 80X190 was a powder mix; and 80X182 was a normal slurpitated mix. Results are shown in Figs. II-5, II-6, and II-7.

Table II-20. Sintering of BeO-8% UO_2 vs Temperature.

Sample No.	Sintering temp °C (6 hours)	UO_2 grain size(μ)	BeO grain size(μ)	Laths	Pores	% Theoret. density	% Shrinkage
80X181							
G	1500	< 0.5	5	Some	-	81.0	21.87
F	1550	< 0.5	5	-	-	80.0	22.00
C	1600	< 1.0	4	Some	-	92.2	24.50
E	1650	0.7	5	Some	Few	97.9	25.38
D	1700		5-25	-	Few	98.4	25.88
C-1*	1750	0.7-0.5	5-25	Some	Few	98.7	26.25
A*		0.7	5-35	-	Few	98.8	26.25
B*		0.7	10-25	-	Few	99.0	26.13
Standard	1750	0.7	5-10	Many	Few	99.0	26.13

*Samples: A Was fired to 1800°C, held for 1 hour; cooled to 1650°C and held for 5 hours.
B Was fired to 1650°C, held for 5 hours, raised to 1800°C and held for 1 hour.
C-1 These tubes were first sintered to 1600°C/6 hours, then refired to 1750°C/6 hours.

Several observations stand out:

1. Densification is not high until 1650-1750°C is reached.
2. Tubes may be fired at 1600°C and then resintered at 1750°C with little or no adverse effect on the ultimate density.
3. Tubes fired at 1800°C/1 hour and then at 1650°C/5 hours showed no improvement in density compared with the normal sintering procedure.

Tubes of known density will be made and coated with refractory oxides, then resintered to mature the coating and the fuel element simultaneously.

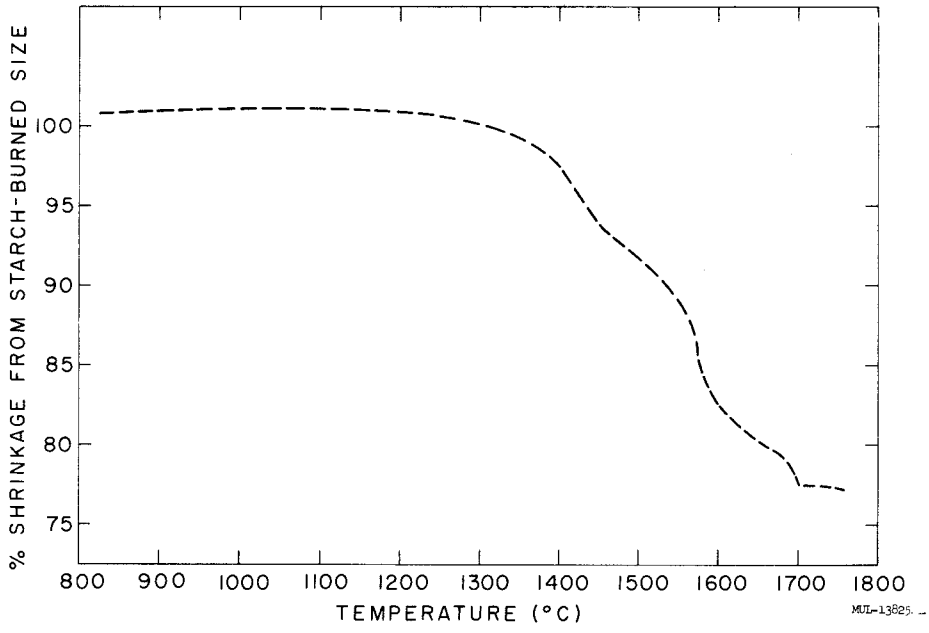

Fig. II-5. Shrinkage vs temperature, sample 80X182-2 (contains ZrO_2). Starch-burned density 1.35 g/cc; sintered density 3.27 g/cc; total shrinkage 26.6%. Heating time: 4 hours from room temperature to 1750°C.

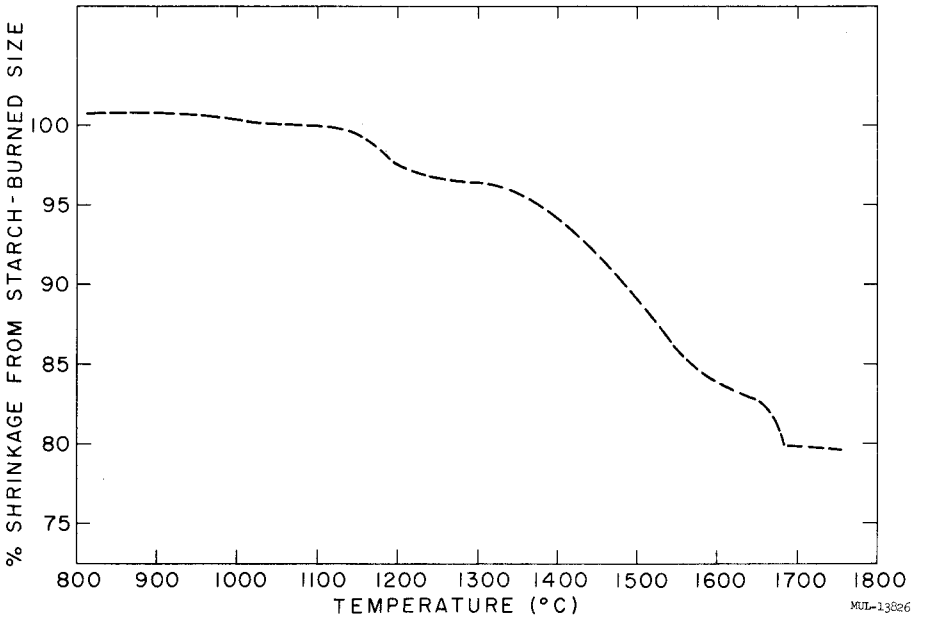

Fig. II-6. Shrinkage vs temperature, sample 80X190-2 (powder mix). Starch-burned density 1.47 g/cc; sintered density 3.12 g/cc; total shrinkage 23.0%. Heating time: 4 hours from room temperature to 1750°C.

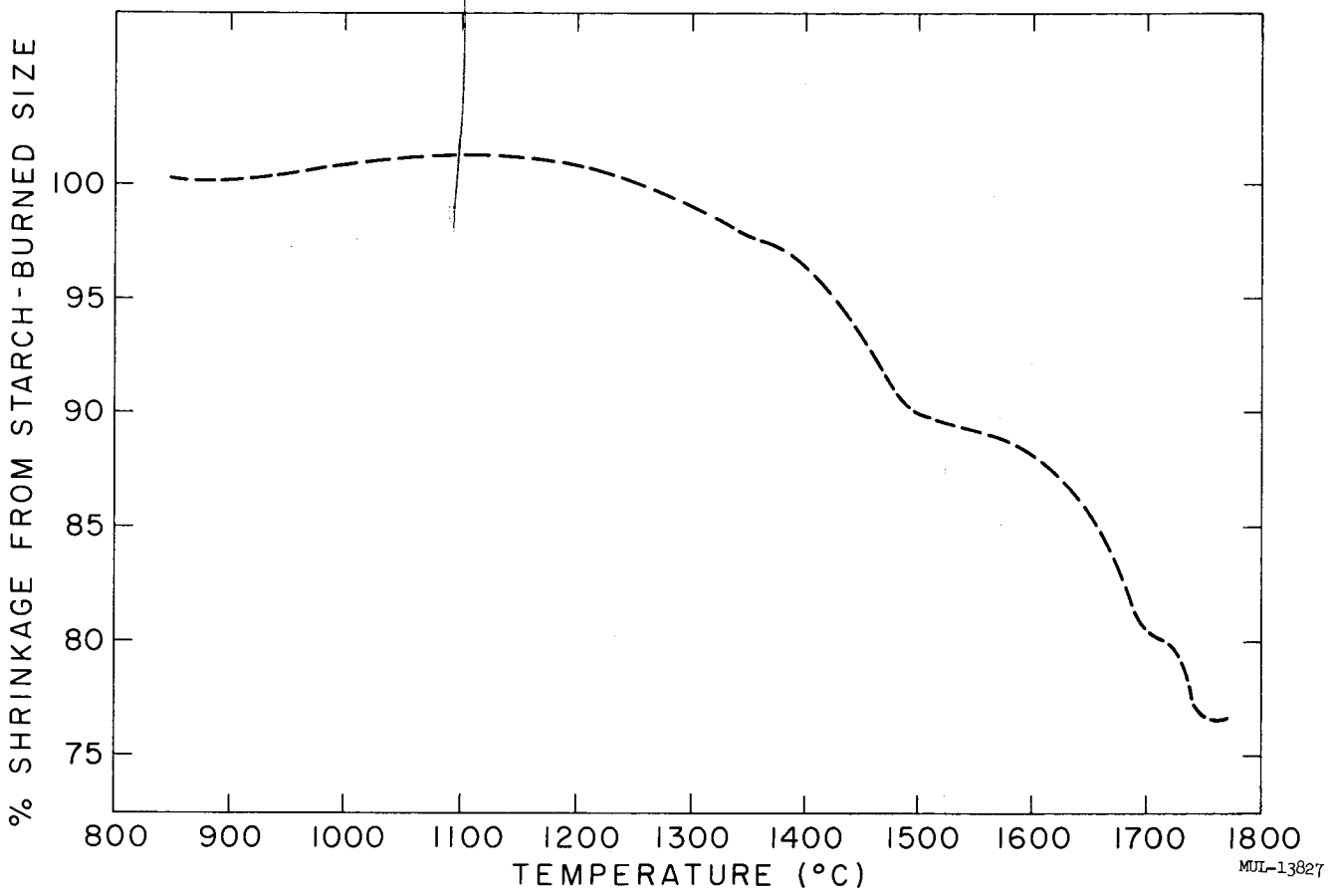

Fig. II-7. Shrinkage vs temperature, sample 80X181 (normal mix). Starch-burned density 1.35 g cc; sintered density 3.18 g cc; total shrinkage 26.0%. Heating time: 4 hours from room temperature to 1750°C.

II. FUEL-ELEMENT FABRICATION FACILITY

A. General

Since the last quarterly report, approximately 800 fueled tubes have been submitted for inspection. These represent about 57 percent of the material initially fed to the process. Of the tubes sent to inspection, 73 percent were acceptable in radiograph and zyglo, except for end defects. (End defects were discounted because most of the tubes were not cropped before inspection.) Thus, about 42 percent of the total material enetering the process emerged flaw-free. About 20 percent of the original material enetering the process was never extruded; it was scrapped as extruder plugs. Recognizing this, one notes that slightly over 50 percent of the material actually extruded was finally reported as flaw-free.

A sizeable number of these tubes were also dimensionally acceptable, although close dimensional control was not an immediate objective of these extrusions.

Dimensional data indicate that the final sintered-tube cross section is highly predictable. Camber is a different matter. Straightening can be realized in sintering, within limits. In general, the straighter the green tube, the straighter the sintered tube. Green tubes so curved that they will barely accept a 3/16-in.-diameter mandrel will not sinter to acceptable cambers when current sintering methods are used.

Quality improvement is primarily attributed to two factors:

1. improvement of the mixing-precipitation step; and
2. the use of a die with lands carefully radiused at the exit end.

Process details follow.

B. Raw Materials

The mixing system has long been recognized as inadequate. However, it is now realized that it also is a major source of tube flaws. This has to do with the "dispersability" of the BeO powder. A survey of tube inspection results indicated that tubes made from certain lots of BeO contained far fewer low-density inclusions than those from other lots. This correlates with the bench-top observation that some lots of BeO are more difficult to disperse than others. Two approaches to this problem have been taken: first, changes in the mixing process, to be discussed in the next section; second, elimination of the dispersal problem by obtaining wet BeO mud, prior to the drying step, from the supplier. This material is on order.

C. Mixing-Precipitation

An interesting correlation emerged from a study of tube inspection results. (See Fig. II-8.) There were no extrusions in the shaded area. This implies that inclusions in the tube wall are a major contributor to surface flaws (zyglo inspection). Clean mixes as well as good extrusion and firing practices, are prerequisite to good tube surfaces.

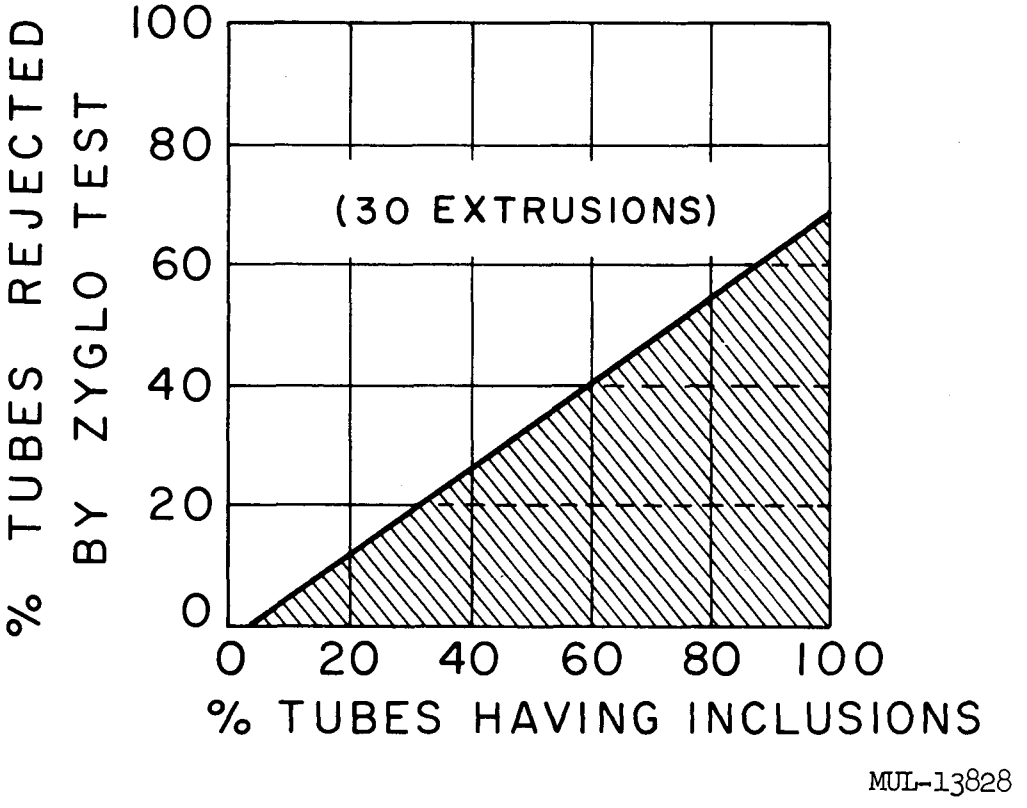

Fig. II-8. Surface flaws vs rejectable inclusions.

A bench-top mixing operation was installed in which BeO powder can be slurried and the dispersion observed until it is smooth. This, coupled with vibratory screening of all batches through 50-mesh screens, has consistently produced batches with very low inclusion levels.

The bench-top mixer has now been supplanted by a new mix-tank configuration which resulted from mixing studies made in a Lucite tank. The new baffle and paddle design produces good mixing and shear in the long mix tanks.

Three batches of co-precipitated $Zr(OH)_4$-$(NH_4)_2$ U_2O_7 (53.2 and 46.8 mole percent ZrO_2 and UO_2 respectively) in a BeO slurry were prepared and calcined at 1000°F for subsequent extrusion and evaluation. No serious difficulty was encountered in preparing this material using the normal procedure and mix line. However, filtration times were increased by a factor of 2 to 3. Clogging of the filter in the filtrate-to-waste line took place more rapidly than had been previously noted; however, this was only a qualitative observation. At this time we have no information on degree of dispersion or final concentration of ZrO_2. This concentration is suspect due to hydrolysis of the zirconyl nitrate, resulting in loss as colloidal material.

D. Tungsten Kilns

The tungsten-kiln operation has developed very well. One kiln (JC 2) is now on a fully automatic, cam-controlled cycle. The operation is very simple and stable. No difficulties are foreseen in placing and maintaining these kilns in operation. Each unit can sinter about 1000 tubes per week on a round-the-clock schedule.

Kiln furniture from the first unit is holding up well without serious distortion of the straightening grooves after repeated firings.

E. Extrusion and Drying

1. Summary

During the quarter covered by this report, work has continued on designing an extruder which will fabricate tubes that are both straight and free from die-caused defects (transverse and longitudinal cracks).

2. Spider

Two spider designs have been checked. The original spider was thick webbed and had a tapered center section to seat the mandrel; this formed a decompression area in the entrance angle. The new spider is thin webbed; the webs extend only one-half the distance through the spider and have a roughened surface at the material interface. This spider is used in conjunction with a straight-shanked mandrel and a die holder with a 90° rather than a 120° included entrance angle.

3. Mandrels

The original mandrel design tapered into the spider, whereas the new spider design takes an untapered mandrel. Two major varieties of the latter type mandrel have been fabricated. A short mandrel has a relieved length at about 1/2 inch, whereas a long type has a relieved length of about 3.4 inch. The purpose of the long mandrel is to bridge the gap between the end of the die and the belt. A number of experiments have also been made to determine the best kind of relief for the mandrel. Originally, the relief was given a nominal radius, but with the first of the untapered mandrels, the practice was initiated of giving the relief a 0.012-inch radius. Another experimental mandrel had the relief in the form of a taper of 1° 22" for about 1/2 inch. This mandrel was intended for use with a die having a similarly tapered flare.

A number of experiments were made to determine the best relationship between the die relief and the mandrel relief. The variable relationship was effected by placing one or more accurately sized shims between the die and the die holder, thus moving the die relief in its relation to the mandrel relief.

4. Die Holder

Along with the newly designed spider, a redesigned die holder has been put into use. In this die holder, the included entrance angle is 90° rather than 120°. It was hoped that the smaller angle would result in a more uniform flow pattern with a material-metal flow interface rather than a material-material interface. It is felt that the thixotropic nature of the material allows the nonflowing

portion in the entrance throat to set up, but due to the frictional drag of the material which is moving, occasional layers of hardened material would be fed into the stream and cause uneven flow patterns through the die.

5. Conveyor

It has been demonstrated that the position of the receiving end of the conveyor (which is a hinged bridge) must be so aligned with the extrusion axis that the tubes drop onto the conveyor belt. Straight tubes have been made when the conveyor axis was as much as 1/16 inch below the extrusion axis. If the relationship is reversed, the tubes dish badly as they move down the belt.

6. Cutter

A deep cut into the extrusion results in: (a) momentarily stopping the flow of the extrusion on the mandrel; (b) generating chips and scrapings of material behind the cutter; and (c) creating an upset which nearly doubles the wall thickness for 1/8 inch at one end of the tube. A light cut leaves the tubes connected at the takeoff end of the conveyor, which creates stresses in the soft undried length on the conveyor, as well as making separation and takeoff extremely difficult. Therefore, unless otherwise noted, all experiments mentioned in this report were made using a moderately deep cut, so that the tubes were separating about 15 feet down the conveyor from the extruder.

A cutter which uses a scoring cut across two opposed flats was tried in place of the iris cutter, but was found to be unsatisfactory in that tubes thus scribed were very difficult to separate, and were found to be severely cracked transversely.

7. Dryer

Voltage input into the side heaters along the conveyor has been dropped from 190v to 150v. This has resulted in a more nearly uniform longitudinal temperature distribution along the conveyor.

T. C.	Location from takeoff end	190v setting	150v setting
1	4 ft	72°F	72°F
2	16 ft	250°F	210°F
3	25 ft	310°F	250°F
4	34 ft	110°F	110°F

This change should be in the proper direction, since the tubes are dried in a more uniform temperature distribution and are not subjected to nearly as sharp a shock as they travel down the conveyor. Ideally, the tubes should enter a drying cycle at low temperature and high humidity, with the two parameters being slowly reversed as the tube dries (with the moisture traveling from the interior to the exterior along fine capillary pores) until final drying is accomplished at high temperature and low humidity.

8. Binder Burnout

A programmed binder-burnout cycle has been developed with hold levels at temperatures of 350-400°F (water and glycerine out); 1080°-1120°F (organic burnout) and 1450°F for completion of burnout. The cycle requires twenty-four hours.

A series of experiments was run using nonfueled BeO to evaluate extrusion and drying techniques. After extrusion and pre-drying in the conveyor drier, tubes were dried for several hours at 200°F in the starch-burning ovens. They were then examined visually for defects using fluorescent dye under ultra violet light (usually about 36 tubes were examined from an extrusion).

9. Entrance Angle, Spider

One experiment was run at the beginning of this period in which the new spider and entrance angle (90°) were compared with the old design (120° included angle). The following results were obtained on the runs made:

120° style - 86.5%, 83.5% acceptable,

90° style - 83.5% acceptable.

Extrusion pressure averaged 100-200 psi higher for the 120° style.

10. Mandrel – Short vs Long

The short mandrel ends about 1/2 inch from the end of the die; this leaves a gap of about 3 inches between the end of the mandrel and the belt conveyor. The long mandrel is designed to end just beyond the point where the idler-wheel radius fairs into the conveyor bed, thus bridging the gap. Results were:

Long - 80%, 93% acceptable,

Short - 57%, 70% acceptable.

11. Location of Mandrel and Relief

Experiments were performed to determine the optimum relationship between material release from the die and that from the mandrel. The following data might imply that the material may be released from the mandrel either before (minus) or after (plus) die release, but not simultaneously with die release; these data are inconclusive, however (see Table II-21.)

12. Plug Gauges

A setup was put together consisting of die 1D12A-1 (0.391R), mandrel 1HO3A-0, the 90° entrance-angle die holders, and an accurate plug gauge to check out centering of mandrel in die. Surface flaws were at a low level, but even with this matched set of die parts, camber continues to be a problem.

13. Cutter

Varying the depth of cut from light to heavy showed the following:

Percent Surfaces O.K.

	X1205	X1206	X1207	X1208
Light cut	88%	92%	92%	92%
Heavy cut	88%	84%	96%	96%

Table II-21. Location of Mandrel in Die.

Mandrel	Die	Shim (in.)	Relationship (+) = mandrel downstream (-) = mandrel upstream	Results (% acceptable)
Short	1/16-in. -R (0.391R)	0	+0.048	92%; 100%
		0.033	+0.015	47%; 71%
		0.048	0	33%
		0.051	-0.003	100%
		0.063	-0.015	98%; 95%
		0.078	-0.030	71%; 97%
		0.111	-0.063	95%
Long	1/16-in. -R (0.391R)	0	+0.055	100%
		0.033	+0.022	91%
		0.051	+0.004	94%
		0.078	-0.023	91%
		0.111	-0.056	88%
1FO5A-0	1/16-in. -R (0.391R)	0	+0.055	97%
		0.018	+0.037	69%; 100%
(Long, w/radiused relief)		0.033	+0.017	97%; 100%; 100%; 100%
		0.048	+0.002	100%; 94%; 100%;
		0.051	-0.001	94%; 93%
		0.078	-0.028	97%; 100%; 97%
		0.111	-0.061	86%; 86%
1FO5A-0	0.005-in. -R (0.400R)	0	-0.004	80%; 8%
		0.018	-0.022	25%; 39%
		0.033	-0.037	80%; 28%; 95%
		0.051	-0.055	6%; 29%
1GO5A-0	0.395R	0		72%
(Long w/tapered relief)	(tapered relief)	0.018		55%
		0.033		53%
		0.051		5%

Additional results:

Dies using the 0.391 die with a 1/16-in. radius – 86%; 83%; 68%; 98%; 88%; 88%; 84%; 92%; 92%; 96%; 96%; 92%; 100%; 92%; 96%; 92%; 94%; 100%; 92%. Others have already been indicated under "Mandrel Experiments."

Dies using the 0.395 die with the 0.005-in. flare – 58%.

Dies using the 0.397 die with a 1/16-in. radius (this die was not radiused as accurately as the 0.391R die) – 8%; 78%; 61%.

The last two results were obtained after the die had been reworked.

Dies using the 0.400R die, with a hand-honed 0.005-in. radius – 94%. Other experiments are reported under "Mandrels."

SECTION II. GENERAL CHEMISTRY

A. Stability of Fueled Tubes in High-Pressure – High-Temperature Environments

The cracking region for untreated 7.29 wt percent OyO_2 hex tubes extends from 1000°C to about 1300°C at 5 atm O_2, and 1040°C to 1230°C at 0.21 atm O_2. It is somewhat larger for these hexes than for untreated 7.5 wt percent OyO_2 round tubes. Although the extent of the cracking region was not determined for tubes with other loadings (3.53, 5.0, 6.175, 7.89, and 8.03 wt percent) results with these tubes indicate that the critical concentration is about 5 wt percent. Tubes showing a weight change of +0.013 percent or greater were cracked; those showing a change of -0.02 percent or less were uncracked. With the development of stabilized fuel tubes, the problem of cracking is no longer of crucial importance.

B. Measurement of Thermal Diffusivity

1. Equipment

Two pieces of equipment are now in operation for measuring thermal diffusivities. One is essentially a room-temperature device ($T \approx 150$°C), and has been described previously (UCRL-5925, p. 136). The newer apparatus is designed to operate at temperatures up to about 1800°C, and is currently being checked out. Test measurements on standards of Ta, Mo, and Fe are now under way. This equipment is much the same as the room-temperature model, but has a tungsten helix furnace which allows the sample to be heated. The heat source is a molybdenum block, with a heating element of molybdenum wire wound on Al_2O_3 insulation. The system can be evacuated to approximately 10^{-5} mm Hg.

2. Correction of Experimental Results

In the course of developing the room-temperature diffusivity apparatus, two effects have been encountered which are difficult to eliminate experimentally and impractical to compensate for analytically. These are

radiation of heat from the sample, and local cooling of the heat source upon initial contact with the sample.

Loss of heat by radiation during a run both changes the shape of the time-temperature curve and prevents the sample from attaining the temperature of the heat source. Since the radiation loss is proportional to the area of the sample, for samples of constant length, the radiation loss effect can be correlated with the sample diameter.

Local cooling always takes place initially when the cold sample is placed against the heat source. The severity of the cooling for a specific material is dependent on the mass of the sample, so, again for samples of constant length, the effect can be correlated with the sample diameter.

The following graphical method has been found satisfactory for correcting the combined effect of radiation loss and source cooling, but gives no insight into the relative importance of the two effects. The curves shown in Fig. II-9 were constructed from experimental data using the apparatus with iron and molybdenum as standards, where:

α = thermal diffusivity, cm^2/sec

$\alpha_{rel} = \alpha_{calc}/\alpha_{true}$

$$\alpha_{calc} = \frac{-0.933\ L^2}{\Delta t} \log_{10}\left(\frac{T_{LO} - T_{50}}{T_{LO} - T_{10}}\right) \qquad (1)$$

L = length of sample in cm

Δt = time in seconds for sample to change in temperature from 10% to 50% of the "level-off" temperature

T_{10} = 10% of "level-off" temperature

T_{50} = 50% of "level-off" temperature

T_{LO} = "level-off" temperature

To calculate a α value for an unknown material, a Δt measurement is made with the equipment. Next, α_{calc} is obtained from Eq. (1). The third step involves successive approximations carried out in the following way: using the curves from Fig. II-9, α_{calc} is located on the family of curves for the particular diameter and α_{rel} read; $\alpha_{calc}/\alpha_{rel}$ then gives "α_{true}", which is

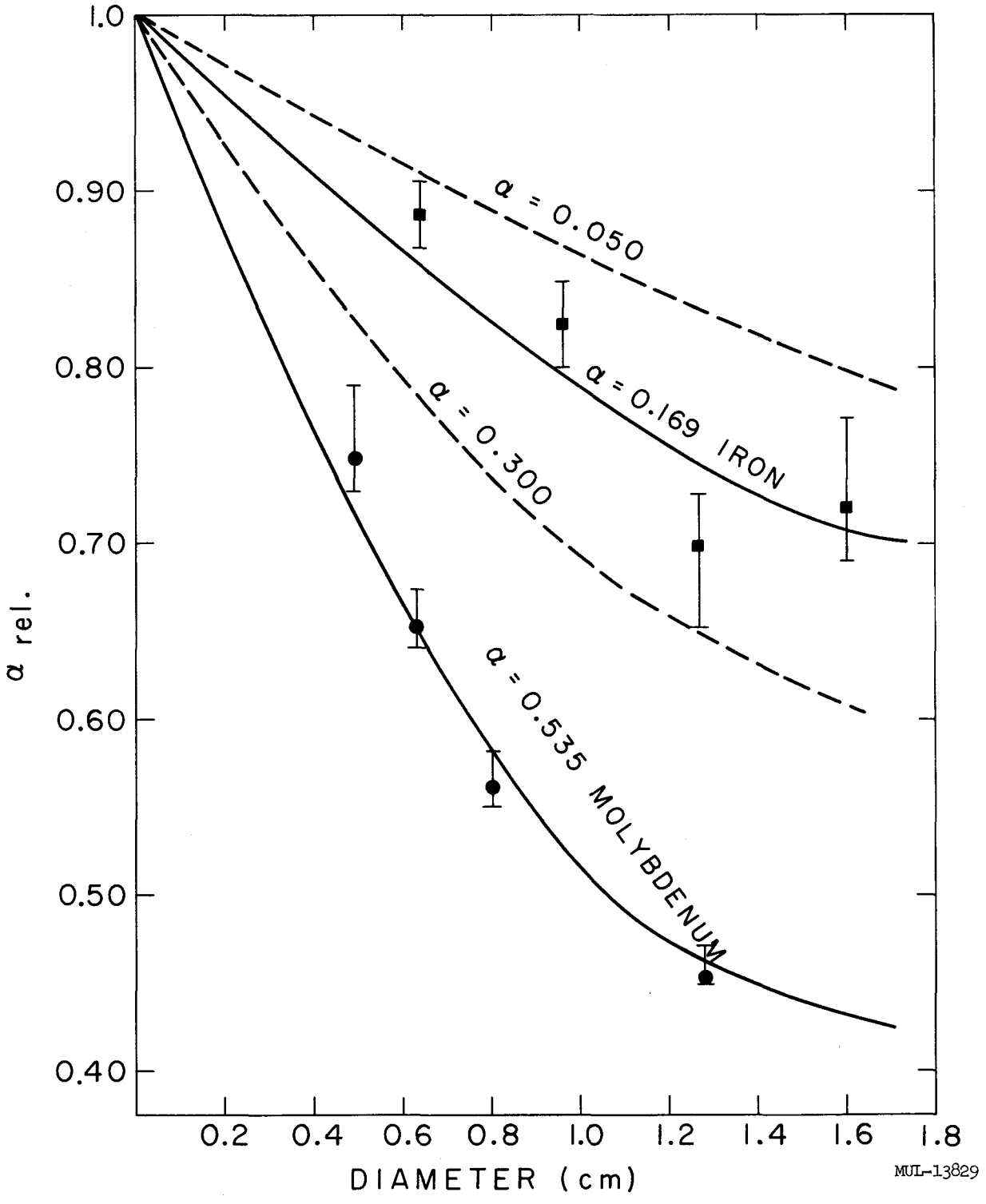

Fig. II-9. Thermal diffusivity correction curves.

the first approximation; "α_{true}" is then used with the curves in place of α_{calc}, and the procedure repeated. Three such approximations are usually sufficient to bring convergence.

In Table II-22 are given the results of a number of measurements of thermal diffusivity at about 150°C.

Table II-22. Thermal Diffusivity Measurements.

Material	L	D	Run No.	Δt(sec)	Ave Δt(sec)	α_{calc} (cm^2/sec)	α_{true} (cm^2/sec)
Vanadium	3.23 cm	0.815	1	33.0			
			2	29.8	31.4	0.071	0.081
			3	31.3			
Scandium	3.50	0.97	1	40.60			
			2	41.10	41.1	0.070	0.082
			3	40.30			
			4	42.55			
Niobium alloy: 10% Ta, 10% Mo, 80% Nb	3.59	1.29	1	19.50			
			2	19.03	19.3	0.19	0.28
			3	19.26			

C. Oxidation of Hafnium

Differences in oxidation behavior of weight-change measurements on hafnium in air at temperatures between 700°C and 1200°C were observed to depend on the type of treatment the sample had received prior to testing. Samples which were annealed and pickled, to remove surface contamination, were characterized by an initial linear oxidation followed by a parabolic rate law. This behavior is thought to be representative of the pure metal, and is similar to the behavior shown by high purity Cr. Samples which were untreated except for cleaning with an organic solvent showed anomalous behavior in that higher oxidation rates were observed at lower temperatures. Part of this phenomenon may be explained by the presence of strain below 900°C, and also by contamination in the surface. Further work will be done to characterize

the oxidation behavior of Hf under more controlled conditions of specimen purity and environment.

D. Estimation of S°_{298} from High-Temperature Enthalpy Data

High-temperature enthalpy data have been received* for several carbides, borides, silicides, nitrides, and oxides for which the corresponding low-temperature heat capacity data are as yet undetermined. As values of S°_{298} are needed for equilibrium calculations from thermodynamic data, the following method for estimating this parameter has been developed. The method fits an equation to the high-temperature enthalpy data. The equation is then extrapolated to 0°K (-273°C), and the S°_{298} obtained.

For a refractory of empirical formula $A_m B_n$, one may write:

$$C_p = R\sum_{1}^{3} D\left(\frac{\theta}{T}\right) + R\sum_{4}^{3(m+n)} E\left(\frac{\theta}{T}\right) + \sigma T$$

The first two terms of this expression result from Born's lattice theory, while the last term attempts to take account of $C_p - C_v$ and is also consistent with the Born-Brody theory of high-temperature heat capacity. An empirical selection of two characteristic temperatures and σ is usually enough to fit the experimental enthalpy data over the entire range of measurement. After making the fit, one may integrate each of the terms in this heat capacity equation to obtain S°_T and from

$$S^\circ_{298} = S^\circ_T - (S^\circ_T - S^\circ_{298})$$

obtain an estimated standard entropy. Some results of such calculations are given in Table II-23. The values were obtained by using an IBM 709 program which carried out the necessary computations by successive approximations.

---

* Private communication from J. L. Margrave, Dept. of Chemistry, University of Wisconsin.

Table II-23. Comparison of Estimated S°_{298} Values with Experimental Values.

Compound	S°_{298}(estimated)	S°_{298}(experimental)
AlN	4.3 e.u.	4.8 e.u.
C (pyrographite)	1.2	1.37 (graphite)
CeO_2	15	14.9
CeS	13	-
CrB_2	11	-
HfB_2	15	-
Mg_3N_2	18	-
Mo_3Si	26	25.4
$MoSi_2$	13	-
TaB_2	15	-
TaC	10	10.1
WSi_2	24	-
ZrB_2	12	-
ZrC	7.8	-

E. Preparation of Magnesium Uranate

Mixtures of powders of MgO and U_3O_8 were made up to give the following compositions: $2MgO \cdot UO_{2.67}$, $MgO \cdot UO_{2.67}$, $MgO \cdot 2UO_{2.67}$, and $MgO \cdot 3UO_{2.67}$. The samples were heated in Al_2O_3 crucibles in air to 1200°C for 6 hours. They were then furnace cooled, crushed, blended, and reheated to 1200°C for an additional 6 hours.

The first two samples were yellow-brown in color and the last two were green. X-ray diffraction analysis showed the first two samples to be predominantly the $Mg(UO_2)O_2$ phase reported by Zachariesen [Acta Cryst 7, 788 (1954)]. The last two were mixtures of $Mg(UO_2)O_2$ and U_3O_8.

F. Hot-Pressed BeO-Fuel Preparations

In an attempt to produce fueled BeO bodies stable to high pressures of oxygen at high temperatures, several mixtures of BeO with various fuels were vacuum hot-pressed into 1-in.-diameter, 9/16-in.-high cylindrical pieces. It was found that BeO (UOX) could be successfully hot pressed in graphite dies to greater than 95% theoretical density by pressing at 1475°C and 3500 psi for 30 minutes. The use of the hot press makes it convenient to prepare samples in the laboratory which are comparable to those made by production techniques.

Mixtures of BeO with -200-mesh powders of U_3O_8, $MgUO_4$, UBe_{13}, and $U_{0.4}Zr_{0.6}Be_{13}$ were made up equivalent in fuel to 7.5 wt percent UO_2 in BeO. Before pressing, these mixtures were blended overnight in a "V" blender with polyethylene balls added to aid the blending. The $U_{0.4}Zr_{0.6}Be_{13}$ was prepared by hot-pressing a mixture of UBe_{13} and $ZrBe_{13}$ in a Mo-lined graphite die at 1575°C and 3500 psi for 30 minutes. X-ray diffraction analysis showed the resulting product to be about 90 percent single phase.

Pressings of U_3O_8 in BeO were not uniform. The outer edges of the pressings appeared very dense with orange, brown, and black-brown reduction products of U_3O_8 present in layers around the edges. The central portion of the pieces had a black, grainy appearance. Slabs cut from this center section disintegrated when heated to 1150°C in air. It was concluded that vacuum hot-pressing to high densities is probably impossible without reduction of the U_3O_8.

A pressing of $MgUO_4$ in BeO made at 1450°C was uniformly dense throughout, but again the outer edges of the piece contained a layer of red-brown reduction products. Tests were made on slabs cut from the black center section of the piece. At 1150°C and 5 atm O_2, a slab of the material gained 0.03% in 2 hrs. In a 2-hour test at 1500°C, the sample stuck to the Al_2O_3 support, apparently because of spinel formation at the points of contact. The piece could not be weighed, but did not look badly oxidized, nor did it have any apparent flaws.

Pressings of UBe_{13} in BeO and $U_{0.4}Zr_{0.6}Be_{13}$ in BeO at 1525°C and 3500 psi resulted in uniform pieces with densities 97% theoretical. Tests at 1150°C and 5 atm O_2 resulted in severe oxidation and spalling with the UBe_{13}-BeO pieces. The $U_{0.4}Zr_{0.6}Be_{13}$ in BeO showed much more promising behavior. The results of several tests are given in Table II-24.

Table II-24. Oxidation of $U_{0.4}Zr_{0.6}Be_{13}$ in BeO.

Sample	Test conditions		Total time tested (hrs)	% wt change
	P_{oxygen}	T°C		
C 125-1	60 psig	1300	4	+ 0.2
	"	"	8	+ 0.4
	"	"	12	+ 0.47
	"	"	27	+ 0.58
C 125-2	60 psig	1300	4	+ 0.22
	"	"	8	+ 0.35
	"	"	12	+ 0.35
	"	"	27	+ 0.46
C 125-3	60 psig	1500	2	+ 0.5
	"	"	8.25	+ 0.9
	"	"	14.5	+ 1.2
C 126-1[a]	60 psig	1150	2.33	+ 0.1
	"	"	18	+ 0.33

[a] C 125 and C 126 were different pressings.

G. Oxidation-Resistant Coatings for Unstabilized Fueled Tubes

Oralloy-loaded BeO-fueled tubes were successfully coated with a Ca-Al-Mg-O composition. Coated tubes have withstood the conditions of temperature and oxygen pressure which ordinarily crack high-loaded, unprotected tubes. (A more detailed discussion of the conditions causing the cracking phenomenon is presented earlier in this report.)

The coatings were applied in thicknesses of approximately 4 microns by spraying or dipping in a water suspension. The composition of the coating consisted of a mixture of CaO, Al_2O_3, and MgO, in the molar ratios of 54.1: 32.6: 13.4. Application has been made on fired 6.175-percent Oralloy hex tubes cut into 3/8-in. lengths. The coated tubes were heated to 1375-1400°C for a period of 1 to 2 hours in an atmosphere of flowing Ar. The results of a number of tests are given in Table II-25.

Table II-25. Test Results.

Sample	Preparation T°C	Preparation time	Pretreatment T°C	Pretreatment time	Test conditions T°C	Test conditions time	Results
1	1375	1 hr			1150	7 hr	No cracks
2	1375	1			1250	1	Cracked
3	1375	2			1250	1	No cracks
4	1375	1			1150	1	No cracks
5	1400	1			1250	1	No cracks
6	1375	1	100°C H_2O	8 hr	1150	1	No cracks
7	1375	1	1450 air (1 atm)	16-1/2 hr	1150	1	No cracks

All tests were made under 60 psig O_2.

For sample 1, examination of a thin section with a polarizing microscope indicated no microcracking had occurred in the BeO - UO_2 body. This particular sample had been subjected to two successive heatings. No cracking occurred during the first hour, so a subsequent 6-hour run was performed. There was some evidence of movement of the UO_2 phase into the coating to form a phase which is thought to be $CaUO_4$. Very little oxidation to U_3O_8 occurred, and the area near the coating was not greatly depleted by the coating or by the high-temperature oxidation treatment. No detectable weight change was noted during the testing except for sample #2, which showed cracking after 1 hour at 1250°C and 60-psig O_2. Apparently the firing time during coating application was insufficient to form a satisfactory coat, because

sample #3, which was fired 2 hours rather than one, showed no cracks. The same results can be obtained by shorter firings at higher temperatures, as shown by sample #5.

Since a very fluid liquid is formed above the liquidus temperature (about 1300-1350°C), the performance of the coated tube at higher temperatures may be limited by this effect rather than by cracking. Testing at higher temperatures is now in progress. In the case of sample 7, a prolonged exposure in 1 atm air above the liquidus temperature caused no detectable weight change. A subsequent test under "cracking conditions" resulted in no cracks. This behavior is significant, in that appreciable diffusion of the coating undoubtedly took place, with no deleterious effect on the resistance of the coating to penetration.

It is hoped that the coating may also provide resistance to the hydrolysis of the BeO. None of the components of the coat is reported to be carried by high-temperature water (UCRL-1831, 1952). One would, therefore, expect little loss of BeO, at least until the liquidus temperature is reached. Hydrolysis experiments will be done if the coats prove otherwise satisfactory.

H. Spinel Coatings on $BeO-UO_2$ Tubes

As previously reported, the rate of growth of the alumina-containing layer on LRL tubes is very much slower than that reported by a supplier. A supplier's tube of the type used in Tory II-A was subjected to the same coating procedure that had been previously used for an LRL tube. Whereas the initial rate of buildup on the LRL tube was about 0.18 microns/hr, the initial rate for the supplier's tube (Class 5-0) was 1.13 microns/hr. In both cases the rate becomes parabolic.

Various methods of bypassing the time-consuming chrysoberyl-layer formation were tried. These were:

1. Application of the alumina by dipping the tube in an alumina slurry of various liquids, followed by sintering in vacuo and/or hydrogen.

2. Application of the alumina as above, then firing with MgO rods either during and/or following the initial sintering of the alumina.
3. Dipping the tube in solutions of various aluminum salts, then decomposing the salt followed by sintering of the alumina.

The coatings produced with these methods were, in various combinations, all unsatisfactory. It was also apparent that having the alumina in contact with the BeO surface did not cause a more rapid buildup of chrysoberyl than is possible using the sapphire rods as in the supplier's method. Apparently the nature of the tube determines the kinetics of the chrysoberyl formation rather than the rate of alumina transport through the gaseous phase to the surface.

CHAPTER III. HOT BOX

PRELIMINARY RESULTS OF HIGH-TEMPERATURE BARE U^{235}-C CRITICAL ASSEMBLY MEASUREMENTS*

A survey has been completed of the influence of temperature upon the critical buckling of bare-graphite enriched-uranium assemblies in the Lawrence Radiation Laboratory's Hot Box high-temperature critical facility.[1] The survey covered the whole range of carbon-to-uranium-235 molar ratio available in Hot Box, for temperatures between 45°F and 1205°F. The lowest ratio, 1185, required more than 90% of the total inventory of both 4-mil and 2-mil fuel elements,[2] and the highest ratio, 21,690:1 (18 times the lowest), involved the largest assembly that can presently be stacked on the low-mass table. Preliminary results of the survey are given in Table III-1.

The C/U^{235} ratios are taken from the amount of graphite per lattice unit and the amount of U^{235} present in the associated foils; no corrections have been made for foil self-shielding or flux depression. All dimensions are room-temperature measurements, and the heights include 2.5-in. for the contribution of the base layer, low-mass table, and floor. The poison of the neutron source container[3] was present in the center of the assembly for all criticality determinations. The volume-average density of the graphite, including flow passages and control voids, was 1.48 g/cm^3. The graphite contained 5 ppm boron-equivalent moderator poison. The measured thermal expansion of Hot Box graphite (grade CS-312) in the vertical and horizontal directions is shown in Fig. III-1. Room-temperature critical heights and the critical temperatures of overstacked assemblies were determined by means of standard Hot Box experimental procedures.[4]

The numbers in the table, while of preliminary nature and subject to minor revision, are of sufficient accuracy to allow comparison with machine

---

* This discussion also appears in an unclassified Report UCRL-6504.

[1] See UCRL-5483.

[2] See UCRL-5334.

[3] See UCRL-6329.

[4] See UCRL-6329.

Table III-1. Preliminary Results of Hot Box Bare Graphite Assembly Survey.

Uncorrected C/U^{235}	T_c (°F)	H (in. at R. T.)	L × W (ft at R. T.)	Fuel element lattice	
1185	60	50.3	4 × 5	4-mil foils - 2-in. spacing	(Top view) 4 4 2 2 4 4 4 2 2 4 4 4 2 2 4 4 4 2 2 4 Location of foil thicknesses
1185	850	52.5	4 × 5	2-mil foils - 1-in. spacing	
2370	45	59.2	4 × 5	4-mil foils - 4-in. spacing	
2370	950	65.5	4 × 5		
2370	1620*	69.5	4 × 5		
7150	85	61.0†	6 × 6	2-mil foils - 4-in. spacing	(Top view) 8 8 8 8 8 8 4 4 4 4 4 4 8 8 8 8 8 8 8 8 8 8 8 8 4 4 4 4 4 4 8 8 8 8 8 8 Location of foil spacings
7150	1110	72.5†	6 × 6	2-mil foils - 8-in. spacing	
8940	50	62.0	6 × 6	2-mil foils - 5-in. spacing (where 4 above)	
8940	880	74.5	6 × 6	2-mil foils - 10-in. spacing (where 8 above)	
14440	79	61.5	8 × 8	2-mil foils - 12-in. spacing	
14440	723	69.5	8 × 8		
14440	1060	73.5	8 × 8		
16850	52	68.8	8 × 8	2-mil foils - 14-in. spacing	
16850	961	84.5	8 × 8		
21690	46	78.8	8 × 10	2-mil foils - 18-in. spacing	
21690	557	89.5	8 × 10		

Average 2-mil foil wt = 123 g oralloy (93.2% U^{235}) with 105 g SS-347 cladding.
Average 4-mil foil wt = 246 g oralloy (93.2% U^{235}) with 105 g SS-347 cladding.
Average graphite density = 1.48 g/cm^3; a 12- × 24-in. graphite area is associated with each foil.
*Extrapolated from a 1205°F experiment.
†This experiment had, in effect, an extra 2.41 kg of SS-304 per kg of oralloy, not in the oralloy flux depression.

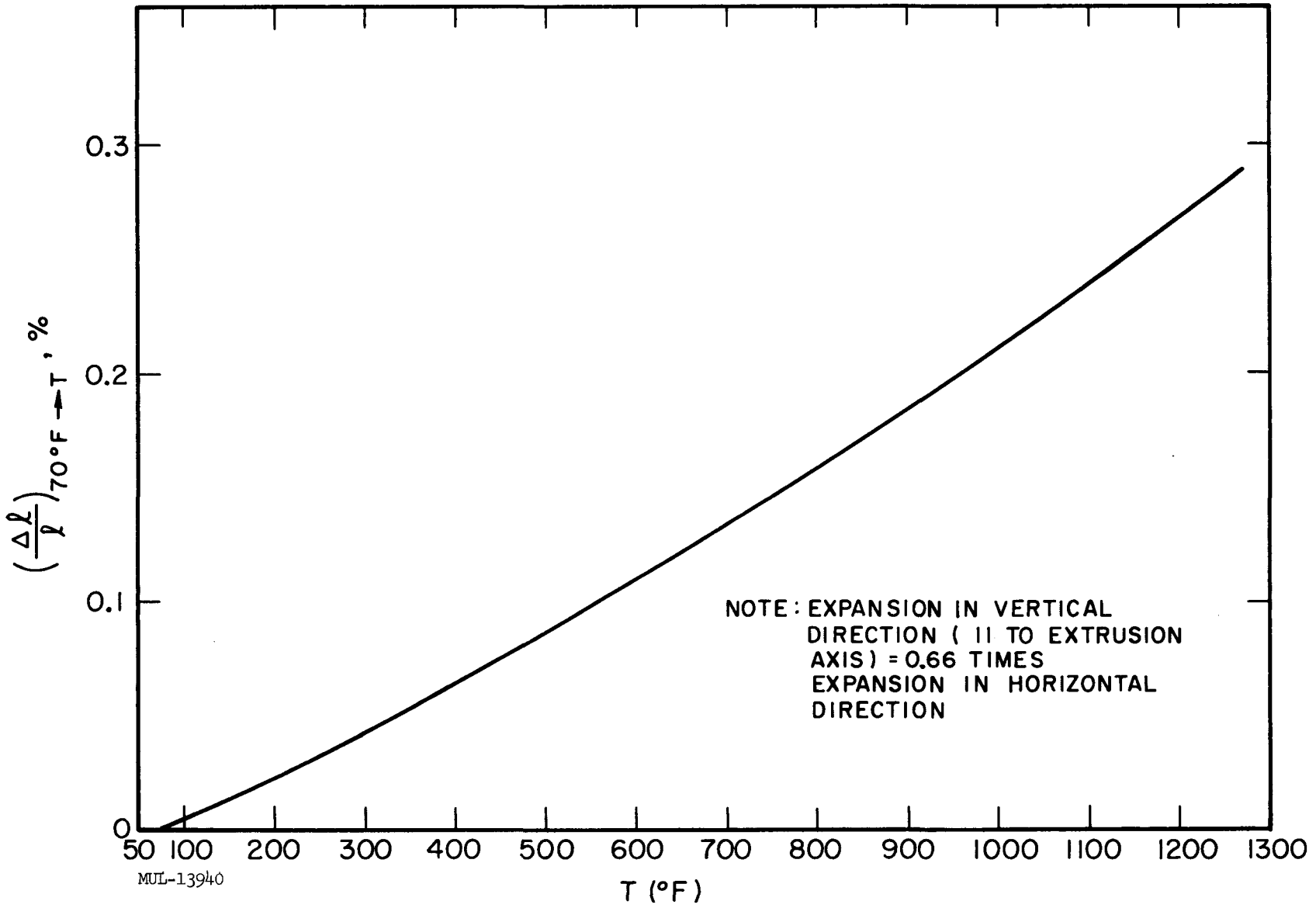

Fig. III-1. Linear thermal expansion of Hot Box graphite in horizontal direction (perpendicular to extrusion axis) as measured by LRL autographic dilatometer.

calculations of the differential effect of temperature. A difference in buckling between the assembly critical at room temperature and the assembly critical at an elevated temperature for each C/U^{235} ratio has been calculated from the room-temperature dimensions given in the table. The fractional change in buckling and the associated change in temperature give the fractional rate of change of buckling with temperature for each experiment. This quantity is plotted in Fig. III-2 against the median temperature between room temperature and the elevated critical temperature in each case. It is seen that, for the two C/U^{235} ratios where two high temperature experiments were done, the absolute value of $(B^2/B^2)/T$ decreases with T. Using this information on the variation of this quantity with temperature, we can evaluate it at one temperature for all values of the C/U^{235} ratio. Figure III-3 is a plot of the value of $(B^2/B^2)/T$ at 500°F vs C/U^{235} ratio. (The experimental results are not pertinent to homogeneous systems until corrected for foil self-shielding and the often-ignored variation in foil self-shielding with temperature.)

A series of Zoom-code[5] calculations for the actual Hot Box experiments will be undertaken soon. A more complete description and analysis of the experiments will be issued in a later report.

---

[5] See UCRL-5682.

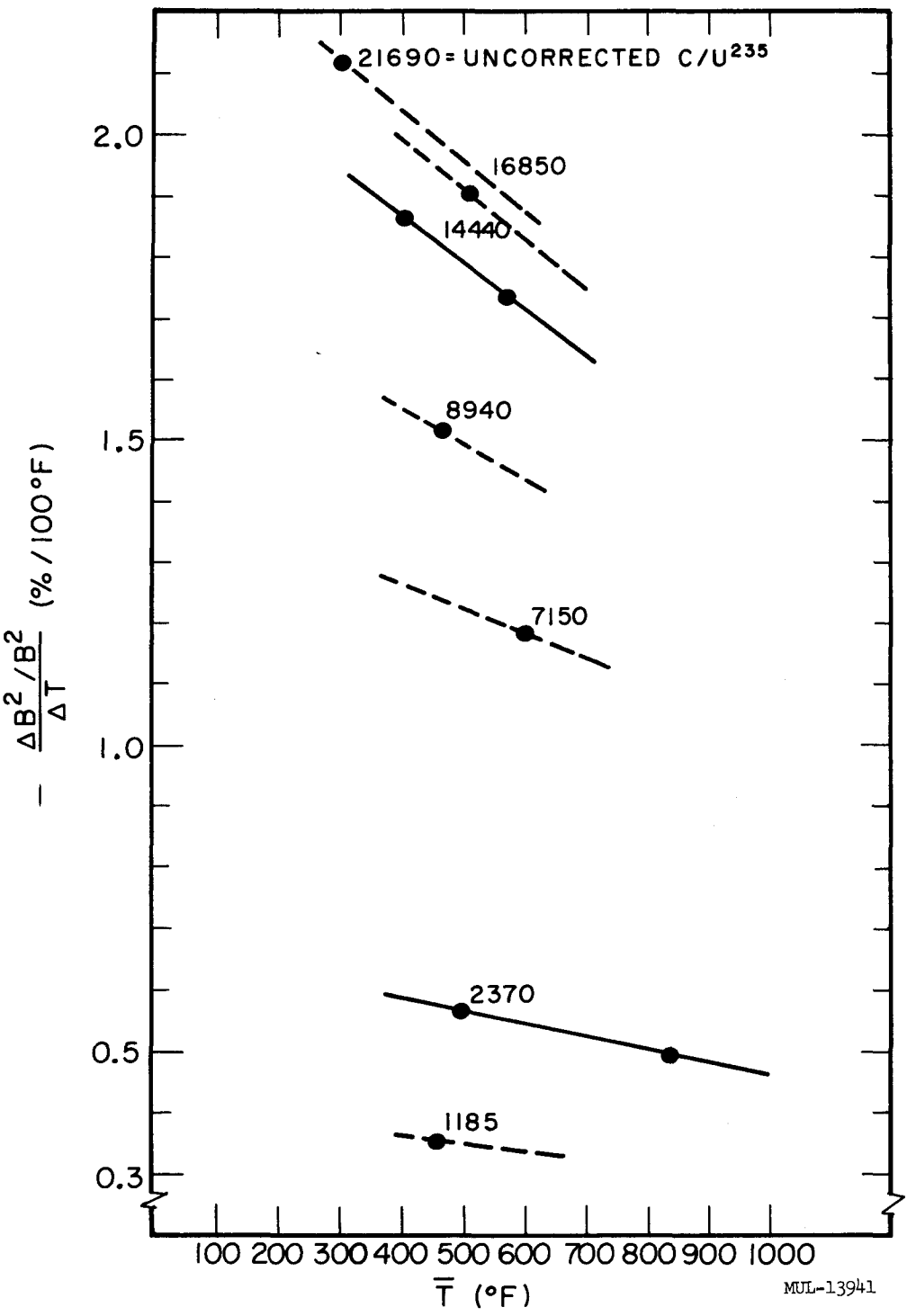

Fig. III-2. Auxiliary plot of measured values of $(\Delta B^2/B^2)/\Delta T$ vs temperature at center of measured range (to obtain value at 500°F). $\Delta T = T_c - T_o$, $\overline{T} = (T_c + T_o)/2$.

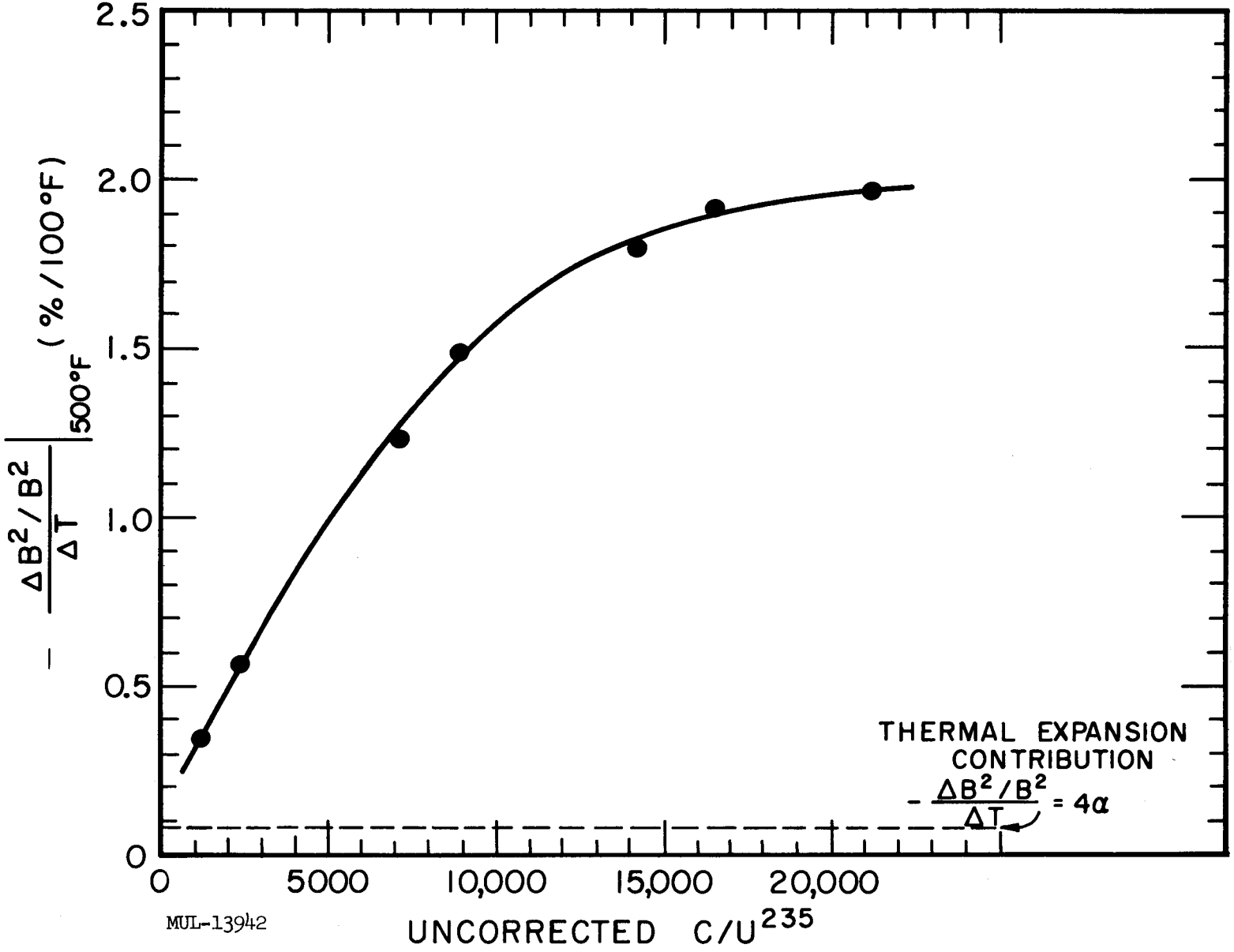

Fig. III-3. Variation of $(\Delta B^2/B^2)/\Delta T$ at 500°F vs C/U^{235} ratio.

CHAPTER IV. TORY II-C

SECTION I. NEUTRONICS

CRITICAL MASS OF TORY II-C

Angie calculational results on the Tory II-C reactor configuration having a side-support structure and control-rod holes are discussed in this section, as well as an interim statement on critical mass.

The neutronic description of the reactor configuration as it existed in May, 1961 is described below. The configuration treated here does not contain any control rods. The side-support-structure worth and control-rod-hole worth were both found using Angie calculations. The effect of the front support structure and the rear base plate were estimated using Zoom calculations.

The more important parameters used in the calculations are:

Dimensions

Core length (cold)	50.7 in.
Core radius (cold)	23.625 in.
Side reflector thickness (cold)	3.00 in.
Front reflector thickness (cold)	10.00 in.
Rear reflector thickness (cold)	2.00 in.
Rear base-plate thickness (cold)	1.00 in.
Front support-structure thickness (cold)	9.00 in.
Side support-structure thickness (cold)	1.875 in.
Average temperature	1277°C

Fractional linear expansion, all dimensions 1.272 percent

Volume fractions:

Core (not including effect of control rod holes):

Fueled BeO	0.43327
Unfueled BeO	0.03935
Tie tubes	0.00447
Void	0.52291

Front reflector:	
Unfueled BeO	0.40077
Beryllium metal	0.04903
Tie tubes	0.00447
Void	0.54573
Rear reflector:	
Unfueled BeO	0.47262
Tie tubes	0.00447
Void	0.52291
Side reflector:	
Unfueled BeO	0.9121
Tie tubes	0.006025
Void	0.081875
Side support structure:	
713-C	0.13220
R-41	0.08144
Ha-C	0.18837
Void	0.598
Rear base plate:	
F-48	0.381
Void	0.619
Front support structure:	
Ha-C	0.25
Void	0.75

Fueled and unfueled BeO was assumed to be at 98 percent theoretical density. Two-thirds of all tie tubes were of René-41, the remainder were of Hastelloy R-235. The tie tubes were distributed uniformly (smeared) throughout the core region according to the number actually present in the core. The remainder were distributed uniformly throughout the side reflector.

Base Problem

The base calculation employed the best set of cross sections available at the present time (self-shielded and resonances

where appropriate). The fuel mass (OyO_2) was set at 50 kg. The fuel was distributed throughout the core such that the radial power profile is flat to within ±5 percent over the major portion of the core length. Also, the axial power profile is flat in the forward half of the core. This base calculation does not consider the effect of a side support structure, the control rod holes, the rear base plate, or the front support structure. The calculated multiplication constant for this reactor (hot) was:

$$k_{eff} = 1.0304$$

Side Support Structure

The materials and thicknesses (equivalent) used in the side support structure are:

Materials	Thickness
Hastelloy 713-C	4.98 g/cm^2 - 0.63 cm
René - 41	3.20 g/cm^2 - 0.388 cm
Hastelloy C	8.02 g/cm^2 - 0.897 cm
	16.2 g/cm^2 - 1.915 cm

The side support structure region thickness is 4.7625 cm.

The first treatment of the side support structure involved smearing the three materials given above within the region specified. No material was smeared from or into the side reflector. In this sense, we call this treatment discrete. This treatment is neutronically justifiable due to the closeness of the transport cross sections (which, in diffusion theory, determines extrapolation distance) in value.

The discrete treatment yielded a reactivity increase, in terms of effective multiplication factor charge, of

$$\Delta k_{eff}/k_{eff} = 0.044 .$$

The change in the radial power profile may be seen in Fig. IV-1. At the core-reflector interface there is about a 20% increase in power. Spread in power is about 5%. A gentle rise in power from the core center to radial edge of about 7.5% will be reduced to 4% when gamma heating is included.

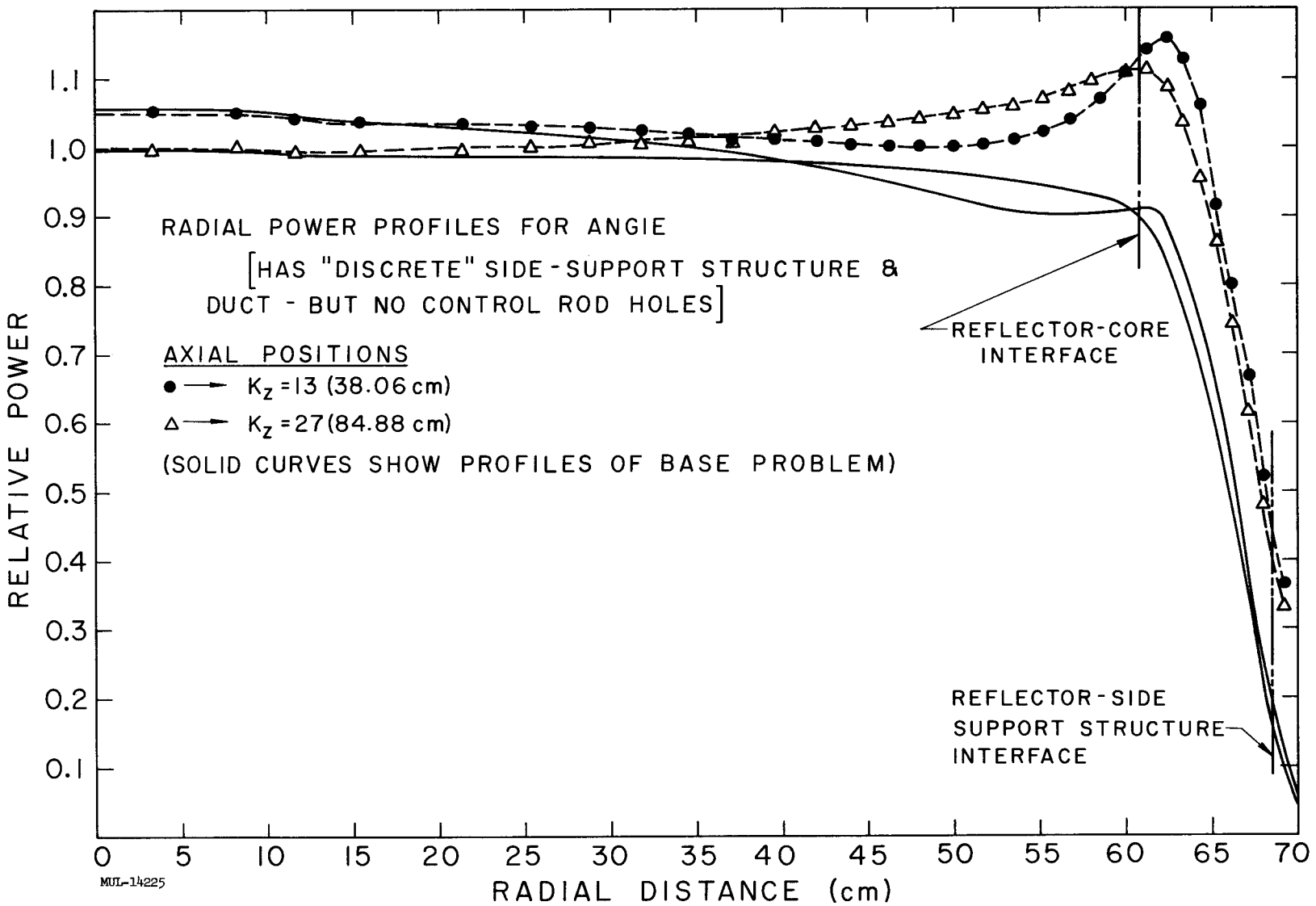

Fig. IV-1. Power profiles versus radial distance.

Control Rod Holes

A calculation involving a consideration of both side support structure and control rod holes has been made. The total reactivity increase (the base problem AR52) is:

$$\Delta k_{eff}/k_{eff} = 0.031 .$$

We may thus assign to the holes a reactivity change of:

$$\Delta k_{eff}/k_{eff} = -0.013 \qquad \text{(control rod holes)} .$$

This calculation was a radial-axial (RZ) calculation wherein the holes were represented by a reduction of core material (both fuel and moderator) in the annular cylindrical shell in which they fell. All 14 holes were included. The additional tie-rod material was taken into account. The effect of the holes on the radial power profile is negligible (less than 2%).

Front Support Structure

The front support structure for Tory II-C consists of beams of Hastelloy C of 2-in. × 9-in. cross section which have an approximate porosity of 0.5. The beams are placed with their center lines having a 4-in. separation (a 2-in. gap between beams). The resultant porosity is 0.75. Since the support structure covers so little of the core's cross-sectional area, most of the neutrons escaping the front face of the forward reflector will "stream" down the void channels and thus never "see" the front support structure.

To adequately treat the effect of the front support structure on reactivity, in the absence of an analytical treatment or experimental estimation of the effect of streaming, three one-dimensional (axial) calculations were made using quarter-density Hastelloy C smeared to thicknesses of 9 inches, 5 inches, and 2 inches. The greatest effect on reactivity of these calculations (i.e., 9-in. case) was $\Delta k/k = 0.008$. Fission traverses on the Tory II-A-1 reactor (which has a similar front support structure) indicate that a conservative estimate of the equivalent thickness is about 0.4 inches. Accordingly, this estimate will provide a reactivity increase of

$$\Delta k_{eff}/k_{eff} = 0.001 .$$

The effect of the front support structure on axial power is negligible. Our 0.4-inch equivalent thickness estimation will provide about a 2% gain in power at the front reflector-core interface.

Rear Base Plate

A rear base plate of F-48 (niobium alloy) having a volume fraction of 0.381 was attached to the core in a calculation made by Zoom. This addition will provide a reactivity increase of:

$$\Delta k_{eff}/k_{eff} = 0.002.$$

Effect of Camber

It is currently planned that the BeO fueled and unfueled tubes be ground, with an allowable camber of 0.5 mils. On the other hand, if camber of the unground tubes can be kept within 2 mils, the decision may be to eliminate the grinding step. If we assume the 2-mil camber, and further assume no cancellation in the stacking process, we may realize a 0.45% increase in radial dimension and an accompanying 0.9% decrease in reactor material density. This maximum effect has been calculated by Zoom to give a reactivity decrease of

$$\Delta k_{eff}/k_{eff} = 0.006.$$

Ground tubes are expected to give a reactivity decrease of

$$\Delta k_{eff}/k_{eff} = 0.0015.$$

Other Reactivity Changes

Three factors causing a change in effective multiplication factor considered earlier are:

1.	Neutron streaming: (Behrens' method)	$\Delta k_{eff}/k_{eff} = -0.010$
2.	Xenon poisoning: (10-hr mission)	$\Delta k_{eff}/k_{eff} = -0.025$
3.	Fuel burnup: (10-hr mission)	$\Delta k_{eff}/k_{eff} = -0.001$
		-0.036 .

To this list we must add the k_{eff} margin necessary to place the hot reactor on a 5-sec period during startup. This is crudely estimated to be:

4. $\Delta k_{eff}/k_{eff} = 0.005$ (startup) .

It was recently recommended that the power in the outer ring of fuel tubes be reduced by 27.1% to avoid undue thermal stress. This ring occupies 2.47% of the core cross-sectional area.

Angie and Zoom calculations indicate that 6% in fuel equals 1% in k_{eff}. A further Zoom calculation shows that 1% in fuel equals 1.02% in power in the core peripheral region. Thus, 1% in power equals 0.0817% in k_{eff} in this region where the fuel importance is only 0.50. A 27.1% power change in 2.47% of the core is a 0.67% over-all power change. The reduction in k_{eff} due to this power decrease is

$$\Delta k_{eff}/k_{eff} = -0.0005 .$$

Conclusion

The various items contributing to or reducing the effective multiplication factor may best be summarized by the following table:

Item	$\Delta k_{eff}/k_{eff}$ Contribution	$\Delta k_{eff}/k_{eff}$ Reduction
Side support structure	0.0437	
Control rod holes		-0.0125
Front support structure	0.001	
Rear base plate	0.0021	
Camber		-0.006
Neutron streaming		-0.010
Xenon poisoning		-0.025
Fuel burn-up		-0.001
Fast period startup		-0.005
Core-edge power reduction		-0.0005
	0.0468	-0.0600

Total deficit

$$\Delta k_{eff}/k_{eff} = -0.0132$$

Our base problem had

$$k_{eff} = 1.0304 .$$

Thus $k_{excess} = 0.0172 = 1.72\%$.

In terms of fuel, this is 10% or 5.0 kg. Thus, critical mass = 45.0 kg of OyO_2 .

CRITICALITY ADJUSTMENTS

Experience with Tory II-A has shown that criticality adjustment is necessary when dealing with prototype reactors. In this report we present several methods of adjustment, some of which lend themselves to the final stages of construction, others require complete disassembly.

Tie-Tube Adjustment

Two materials are being considered for tie-tube fabrication; René-41 and Hastelloy R-235. The "normal" core configuration calls for one-third of all tie tubes to be made of Hastelloy and two-thirds of René. By replacing all René tie tubes by Hastelloy, we may raise k_{eff} (effective multiplication factor) by 4.2%. Conversely, replacing all Hastelloy tie tubes by René lowers k_{eff} by 2%.

Unfueled Central Cylinder

Unfueled BeO tubes of small bore may be placed in the central region of the core to either increase or decrease k_{eff}, depending on the cross-sectional area of the region. Bear in mind that here the BeO density is twice that of the fueled tubes. For a radius of 2-1/4-in., a maximum Δk_{eff} increase is 0.35%. The "break-even" radius is 4-5/8-in. Beyond this radius Δk_{eff} becomes increasingly negative.

Stainless Steel Exterior "Skin"

A gain in k_{eff} may be obtained by placing sheets of stainless steel (SS-304) completely around the reactor exterior to the side support structure and duct. A 1-in. sheet is found to increase k_{eff} by 1.62%. (In order to obtain the proper extrapolation length, the stainless steel was expanded such that the macroscopic transport cross section matched that of the side support structure. Calculations have shown that Σ_{tr} of the side support structure is roughly the same as that of the side reflector.) One inch of stainless steel alters the power profile by about 6%.

$U^{238}O_2$ Fueled Tubes in the Forward Reflector

When all of the large-bore tubes in the forward reflector are fueled with 10% (by weight) $U^{238}O_2$, there is a resultant 1.92% decrease in k_{eff}. This decrease is slightly due to the loss of BeO and mainly due to the neutron absorption by U^{238}. The axial power profile changes considerably. The forward fuel tubes would operate at a power level of 70% of normal.

Five Percent Fuel Loading Limitation

At the front of the core, the fuel loading approaches 7% by weight as we near the core-side-reflector interface. At the interface the loading does not drop below 5% for the first 20% of the core length. Radially, the high-loading region occupies 40% of the cross-sectional area at the front core face. On the conventional radial-axial loading chart, the high-loading region occupies a triangular region in the front exterior corner.

If we impose a limit of 5% by weight fuel loading, calculations reveal an almost negligible 0.1% drop in k_{eff}. The axially integrated power profile changes shape such that a decrease at the interface is compensated for by an increase centering around 45-cm radius. A two-to-three percent dropoff in integrated power is therefore realized at the core periphery. The integrated power profiles are plotted for reactors without the side support structure.

Half-Inch Extension of Side Reflector into the Core

By increasing the thickness of the side reflector by half an inch

at the expense of core material, we may increase k_{eff} by 1.77%. Here, the fuel weight percentages are maintained constant in their respective zones, thereby implying a reduction in fuel mass. (The reflector is roughly twice as dense as the core.) If we now vary the fuel loading such as to again attain the original power profile, a net k_{eff} of 2.4% is realized.

On the other hand, weight-percent fueling may be lowered overall to maintain the original k_{eff}. If this is done, the maximum weight percent drops from about 7% to about 5.5%.

Five-Inch Front Reflector Change Holding Total Reactor Length Constant

If we add 5 inches to the forward reflector, reducing the core length by the same amount, we may reduce k_{eff} by 2.2%. Conversely, adding 5 inches to the core and reducing the forward reflector length by the same amount, raises k_{eff} by only 0.8%. In neither case was the fuel loading in any region altered, except in the effected regions adjacent to the forward reflector. In the first case, 5 inches of the core was simply "chopped off" leaving the remainder unchanged; in the second case a 5-inch extension of the first region was added on which had the same fuel loading. In both cases, the fuel mass changes by about 16%, since the loading is quite high at the forward end of the core. The axial power profile is profoundly affected (±40%) at the forward end.

Beryllium-Metal Side Reflector

All BeO (96% theoretical density) was replaced by solid Be metal (having the appropriate side reflector porosity). For the standard 3-inch (cold) side reflector there is a k_{eff} gain of 0.38%. Further calculations reveal the following equivalence:

1-in. Be = 1.017-in. BeO (in the side reflector),
where $\rho(Be) = 1.85\ g/cm^3$; $\rho(BeO) = 2.89\ g/cm^3$.

Beryllium Metal in the Core

As an academic exercise, one may compare the neutronic aspect of beryllium metal as a replacement to BeO in the core. Zoom calculations show that total replacement increases k_{eff} by 11.2%. If we compare moderating

ratios (i.e., $\xi \Sigma_{sc}/\Sigma_a$) of Be metal and BeO, we find that Be is 1.27 times as good a moderator as BeO. This is roughly a factor of 2 too high and is hence only good as a very crude estimation. A slowing-down power (i.e., $\xi \Sigma_{sc}$) ratio yields 1.236, again a factor of 2 too high. Through Zoom we may, however, establish the following calculated equivalences:

$$1\ cm^3\ Be = 1.112\ cm^3\ BeO,$$

$$1\ g\ Be = 1.77\ g\ BeO,$$

$$1\ atom\ of\ Be = 0.642\ molecules\ of\ BeO,$$

where $\rho(Be) = 1.85\ g/cm^3$; $\rho(BeO) = 2.95\ g/cm^3$.

Exchange of Fueled Tubes for Unfueled Tubes of Small Bore

One percent of all fueled tubes were replaced by unfueled BeO tubes of 0.087-inch bore. Each small-bore tube has double the cross-sectional area of "normal" fueled tubes, and thus a 1% replacement by the small-bore tubes amounts to a 1% increase in BeO area. From results of Zoom problems we calculate that the k_{eff} change resulting from such a replacement will be a 0.61% increase.

Conclusion

Using the methods of adjustment presented here, k_{eff} may be raised or lowered with various degrees of difficulty. Some methods are useful in final adjustment of core criticality, while others require various amounts of disassembly. In tabular form the methods and effect on k_{eff} are listed below:

Method	K_{eff} Increase	K_{eff} Decrease
Tie-tube adjustment	4.2%	2.0%
Unfueled BeO central cylinder	0.36% max	varies
One-inch exterior stainless steel	1.62%	----
10% by weight $U^{238}O_2$ in fwd refl.	----	1.92%
5% by weight fueling limit	----	0.10%
Half-inch extension of s. ref. into core	1.77% → 2.47%	----
Five-inch change in fwd. refl.	0.8%	2.17%
Beryllium-metal side reflector	0.38%	----
Beryllium-metal core moderator	----	11.2%
Fuel tube exchange	0.61%	----

ANGIE CALCULATIONS OF A HIGH-TEMPERATURE BeO CRITICAL EXPERIMENT

Introduction

Some critical experiments were recently reported (UCRL-6329) which were performed on bare BeO assemblies at the Hot Box facilities (UCRL-5483). The experiments were primarily involved with measuring the critical length at room temperature and at 515°C of an assembly with an effective BeO density of 2.73 g/cm^3 and a gross BeO/U^{235} molar ratio of 556:1. Calculations of these assemblies were performed on the Angie code (UCRL-6076) with a detailed description in two dimensions of the fuel loading and cruciform gaps in order to more accurately evaluate our calculation of nuclear temperature effects.

Description

The geometrical description used in Angie is shown in Fig. IV-1a. Only those space points which are at the boundary of a region are shown. Region 6 consisted of as many regions as there were fuel foils (62 foils in the cold configuration and 66 foils in the hot configuration). Each fueled region was a homogenized mixture of a fuel element and the material within approximately 0.5 inch of either side of it. Self-shielding factors appropriate to 4-mil-thick foils in a lattice spacing of 1 inch were applied to the fuel. The proper amount of fuel for each region was determined from the experimental loading charts (UCRL-6329). The cruciform gaps were initially treated by conserving graphite mass and smearing the adjacent graphite uniformly through the gap area. This will be discussed in more detail later. The BeO in regions 4, 5, and 6 had transfer coefficients in groups 5 through 14 which were appropriate for the average flux in each region, assuming the flux to have the functional form E^n, where E is the neutron energy. From previous calculations on similar assemblies, the proper n value was determined (UCRL-5740), and from this n the proper $\mu^{i-1, i}$ was determined. The values of n used were -0.93 for region 4, -0.965 for region 5, and -0.91 for region 6. In calculating thermal expansion effects, the coefficients of thermal

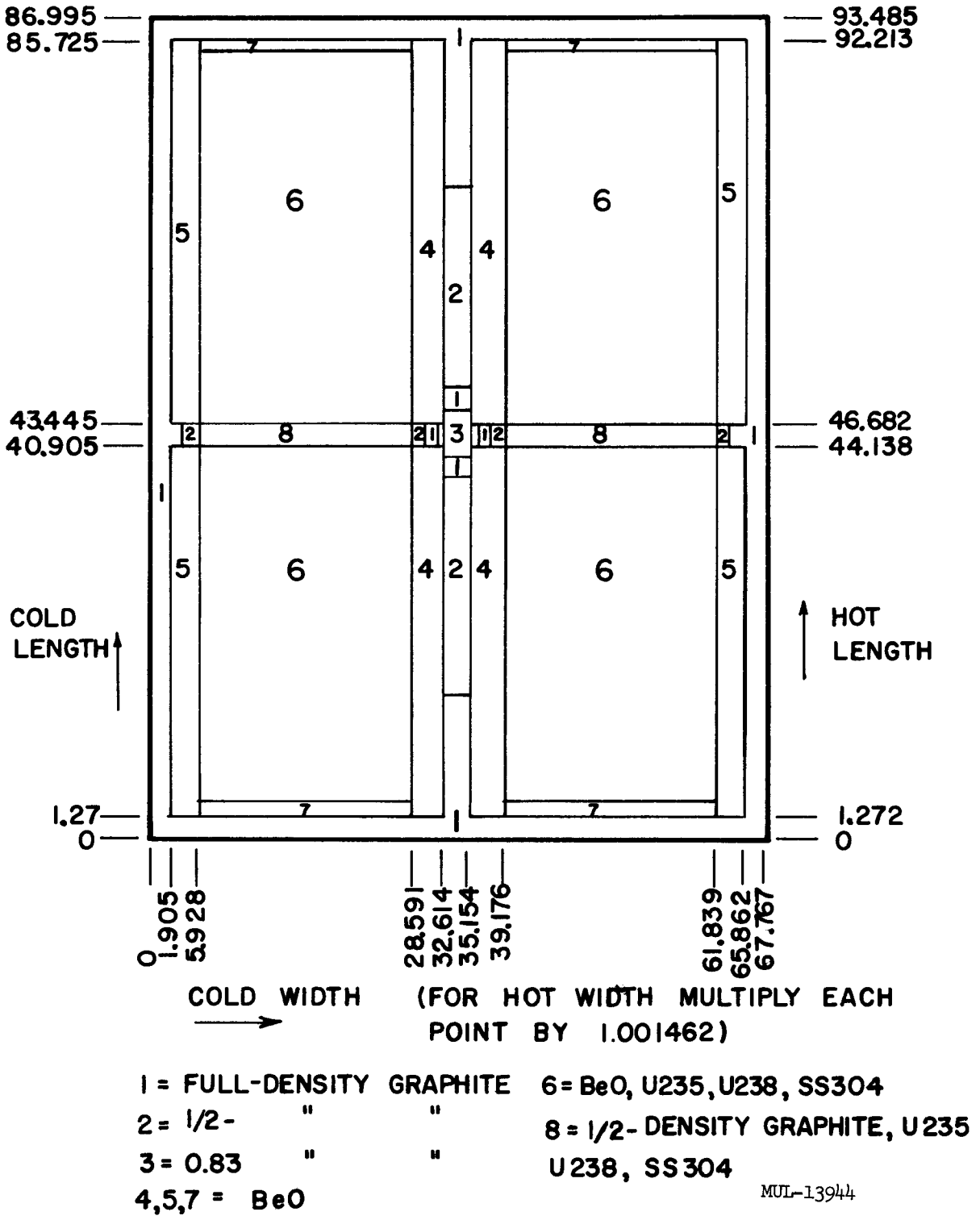

Fig. IV-1a. Description of BeO Hot Box (Angie).

expansion used were 4.5×10^{-6}/°F for BeO, and 1.8×10^{-6}/°F for graphite. It was assumed that the length and width expansions were due to graphite, and the height expansion was due to BeO. This assumption and its effects will be discussed later.

Results

Table IV-1. Criticality Calculations.

Temp (°C)	K_{eff}	Comments
27	1.0017	Room-temperature assembly
515	0.9938	High-temperature assembly

The critical K_{eff} of the hot assembly was obtained from Fig. IV-2, a plot of K_{eff} vs neutronic temperature at the points 27°C, 377°C, and 727°C. Comparison of the results of Table IV-1 shows an inconsistency of 0.0079 in K_{eff} calculations. It is of interest to determine if the cause of this inconsistency lies in the calculational procedures or if it is due to experimental uncertainties.

The experimental uncertainty in the critical length of ±0.2 inch gives an uncertainty in the room temperature K_{eff} of ±0.0016; however, the experimental uncertainty in ΔK_{eff} between room-temperature criticality and hot criticality is far less than this because the hot criticality was merely an extension of 1 inch of BeO and fuel to each end of the room temperature criticality. The principle experimental uncertainty in ΔK_{eff} between hot and cold criticality is in the thermal expansion of the hot criticality, especially in the width expansion. If the BeO blocks were stacked flush against the center cruciform, the width would have expanded like BeO, instead of like graphite as was assumed in the above calculations. This would have resulted in $\Delta K_{eff} = -0.002$ for the hot criticality. In the experimental criticality, no special attention was given to the positioning of the blocks with respect to the cruciform, however, it is most probable that none or very few of the blocks were against the cruciform. Any correction for this expansion effect would increase the inconsistency in the calculated results.

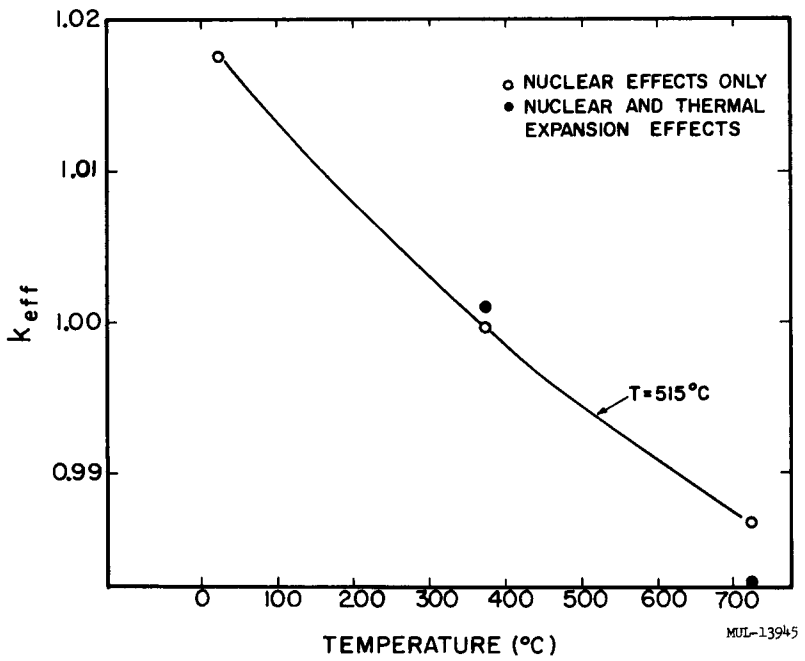

Fig. IV-2. Angie calculations of temperature vs K_{eff} for the hot assembly configuration.

A less important experimental uncertainty which contributes to the inconsistency is the uncertainty in supercriticality of the room temperature criticality. This amounts to a ΔK_{eff} of ± 0.0008. A minor correction of $\Delta K_{eff} = -0.0003$ should be applied to the room temperature calculations to account for the difference between "room temperature" in the calculations (27°C) and the experimental "room temperature" (32°C). Clearly, the experimental uncertainties cannot account for the calculated inconsistency. Therefore, the calculations do not properly treat the temperature effect on K_{eff}.

The sources of the temperature effect may be separated into two kinds, neutron transfer-coefficient changes (nuclear effects), and geometry changes (thermal-expansion effects). Calculations of the nuclear effects were performed at 27°C, 377°C, and 727°C (circled points, Fig. IV-2). In these problems the geometry and thermal expansion were held constant at the proper value to represent a temperature of 515°C and only the material transfer coefficients were changed. Calculations of both nuclear and thermal expansion

effects were performed at 377°C and 727°C (x points, Fig. IV-2). With this information, the nuclear temperature coefficient of reactivity and the thermal-expansion temperature coefficient of reactivity were computed (Table IV-2).

Table IV-2. Calculated Temperature Coefficients of Reactivity.

$(\Delta\rho/\Delta T)$ Nuclear	-4.63×10^{-5}/°C over range 27°C → 727°C
$(\Delta\rho/\Delta T)$ Nuclear	-3.92×10^{-5}/°C over range 377°C → 727°C
$(\Delta\rho/\Delta T)$ Thermal expansion	-1.67×10^{-5}/°C over range 377°C → 727°C
$(\Delta\rho/\Delta T)$ Thermal expansion and nuclear	-5.59×10^{-5}/°C over range 377°C → 727°C

The effect on the calculation of void spaces in the cruciform was determined by the technique in which the voids were filled with various densities of graphite, and K_{eff} calculated for each case (Fig. IV-3). From previous experiments on similar assemblies, it has been determined that the extrapolation of the tangent to the curve of K_{eff} vs void density at a point between 0.75 and 1.5 times graphite density gives the corrected curve of K_{eff} vs void density. The difference in Fig. IV-3 between the calculated curve at half-density graphite and the linear extrapolation is a measure of the error in K_{eff} due to the improper treatment of the void. For the room temperature criticality this was $\Delta K_{eff} = -0.0106 \pm \frac{0.0081}{0.0041}$, and for the hot criticality, $\Delta K_{eff} = -0.0101 \pm \frac{0.0077}{0.0038}$. This would contribute $\Delta K_{eff} = +0.005 \pm \frac{0.0004}{0.0003}$ to the inconsistency of temperature calculations discussed before. Adding the correction for the void to the room temperature calculation results in a corrected $K_{eff} = 1.0123$. This value is approximately 1% higher than previous calculations on similar Spade criticalities that did not contain voids (see UCRL-5740).

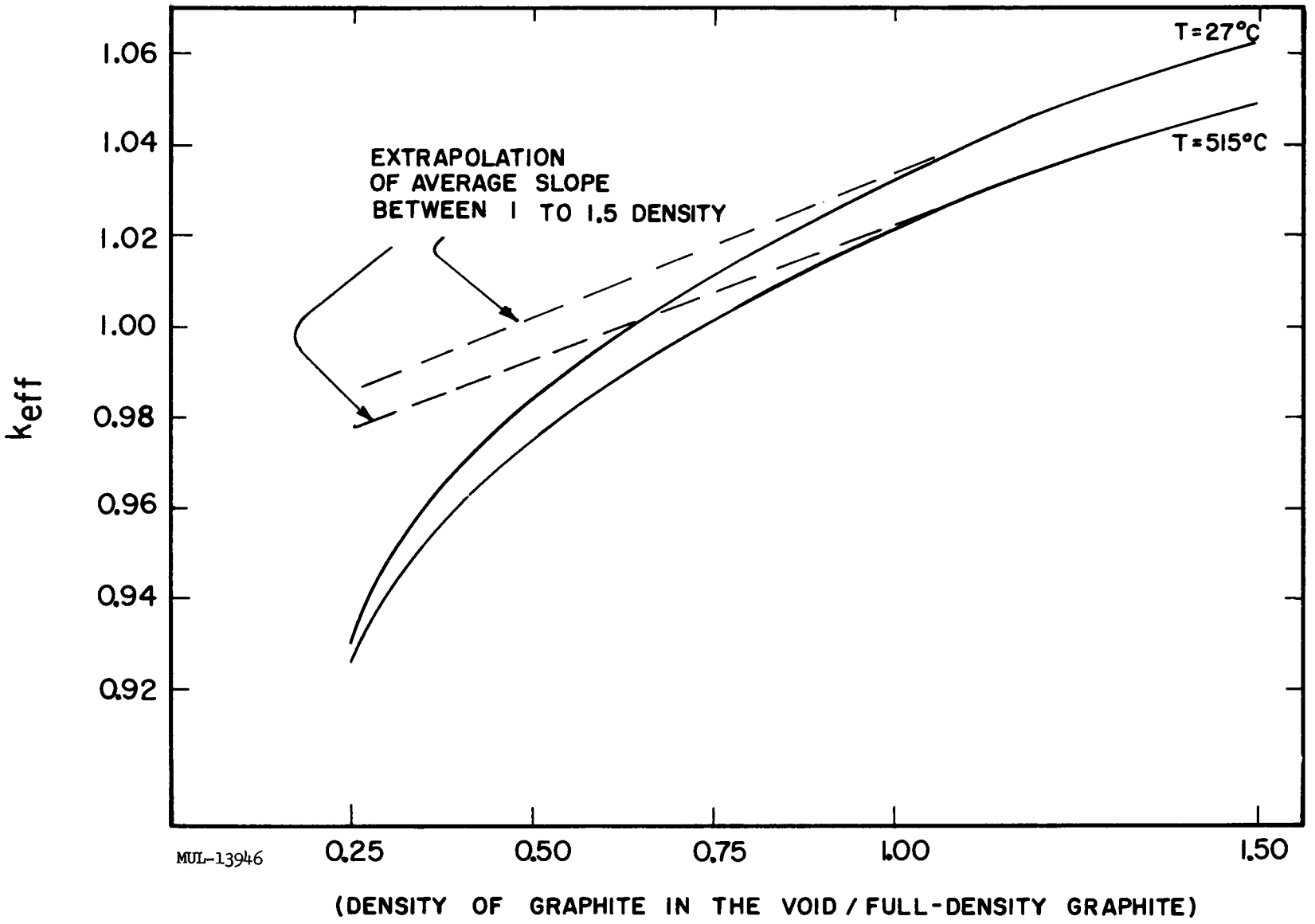

Fig. IV-3. Density of graphite in the void vs K_{eff} at T = 27°C and T = 515°C.

Including the above discussed uncertainties and corrections, the calculated inconsistency between the hot criticality and the room temperature criticality is a ΔK_{eff} of 0.0080 with possible extreme variations of + 0.0042 and - 0.0022. This inconsistency can be attributed solely to the nuclear effect, since the geometric (thermal expansion) effect can be calculated to a much higher degree of accuracy. The total calculated nuclear temperature effect is ΔK_{eff} = 0.0241 (Fig. IV-2). From this the error of 0.0080 ΔK_{eff} must be subtracted, leaving 0.0161 ΔK_{eff} as the proper nuclear temperature effect that should have been calculated to agree with the experiments. In other words, the calculated nuclear temperature effect on K_{eff} is too large by a factor of 1.50 with possible extremes of + 0.26 and - 0.33. The calculated effects can also be discussed in terms of critical length; however, it should be noted that additional uncertainties are introduced in the conversion factor from K_{eff} to length. The calculated nuclear temperature effect on critical length is therefore an increase of 3.13 in. ± 0.19 in., which is 1.04 in. $^{+0.63 \text{ in.}}_{\pm 0.32 \text{ in.}}$ too large.

In some previous experiments with graphite moderated oralloy systems, this relative error in the temperature effect was found to be about 2 in./11.5 in. (C/U^{235} = 8700 molar ratio) and about 2 in./10 in. (C/U^{235} = 14114 molar ratio) which indicates that our treatment of nuclear effects by the heavy-gas model is better for systems with larger moderator/fuel ratios. This is reasonable, since the calculation of the nuclear effect is based on a Maxwellian thermal neutron spectrum, which is a better approximation for thermal systems than for fast systems.

Conclusion

Although the absolute K_{eff} for the room temperature system is about 1% above unity and in rough agreement with previous Spade critical measurements, there is a sizeable error in the temperature effects. This error, due to nuclear effects, is an over-prediction of 0.80% (ΔK_{eff}) in a calculated ΔK_{eff} of 2.41% for the temperature change from 27°C to 515°C. An equivalent statement is that the calculated nuclear temperature effect on K_{eff} is too large by a factor of $1.50 \, ^{+ 0.26}_{- 0.33}$. The error in nuclear effects arises

principally from the assumptions of the scattering kernel and the neutron spectrum. Techniques are presently being developed to approximate the spectrum much more accurately.

NEUTRONIC STUDY OF HAFNIUM CONTROL RODS IN A SPADE REACTOR

Introduction

A series of experiments has been conducted to measure the reactivity worth of various metals as a function of their thickness. Among these experiments were three relating to hafnium which constitute the basis of this discussion.

Eighteen group cross sections and transfer coefficients for hafnium have been formulated for input to the two-dimensional, multigroup, neutron diffusion code-9 Angie [see UCRL-5913 and Nuclear Sci. and Eng. 8, 226 (1960)]. The results of the neutronic calculations employing this code are herein compared to the experimental results.

Neutron leakage calculations have been made for each of these experiments and are discussed. Two methods have been used to calculate the leakage, both employing edit quantities from the code. The equivalence of these two methods is demonstrated.

Method 1. Direct calculation of leakage from neutron balance consideration, knowing total reactor power and non-fission capture rate. It was seen that a poison rod enhanced leakage from the system.

Method 2. Integration of leakage over the reactor surface using the 18 energy group fluxes.

Experiment

The measurements were made in a Spade critical assembly, an unreflected, BeO-moderated oralloy system with dimensions 24 × 24 × 20-in. having a 24 × 1 × 1/8-in. slot through the center of the assembly. A moderator-to-fuel (BeO-to-U^{235}) molar ratio of 247 was achieved with a BeO density

of 2.86 g/cc and a fuel lattice of 8-mil-thick foils at a 1-in. spacing. The assembly was built up of BeO blocks measuring 6 × 6 × 1 in. with a 0.015-in.-deep, 5.375-in.-wide groove cut in one face to accommodate the fuel in the form of 5.25-in^2 foils. [Nuclear Sci. and Eng. 8, 221 (1960)].

With the hafnium sample fully inserted in the slot, an Omnitron was used to pulse the reactor. The reactivity worth of the sample was then determined by measuring the rate of decay of the neutron population in the reactor (private communication D. E. Kroft to E. Goldberg, December 2, 1960).

Neutronic Input Data

The cross sections and transfer coefficients for Oralloy and beryllium oxide, as well as the energy group limits, the neutron fission spectrum, and the Oralloy self-shielding corrections for this BeO/U^{235} = 247/1 Spade assembly are those in general use at this laboratory. They have previously been published (see UCRL-5913) and are not duplicated here.

The hafnium 18 energy-group absorption cross sections and self-shielding factors have been previously calculated at this laboratory by the "ROE" method using the 9 Sophist II code (KAPL-1241). In these calculations the 1/v portion of the absorption cross section was eliminated. Consequently these 1/v contributions have been added to the resonance contribution after applying a self-shielding factor appropriate to the hafnium thickness under consideration. The un-self-shielded 1/v portion of the cross section was taken to be 105 barns at 2200 m/s.

As presented to the code, the hafnium and beryllium oxide were treated as a uniform mixture smeared through twice the actual slot width, the densities having been adjusted accordingly. This eliminates the nondiffusion region which otherwise exists between the hafnium and the walls of the slot.

In calculating the individual $\overset{i}{R}f_a$ (T) by the "ROE" method using the 9 Sophist II code, resonance scattering has been neglected on the assumption that it is very small compared to the absorption; i.e., $\Gamma_n \ll \Gamma_\gamma$. An upper limit to the error involved in neglecting resonance scattering may be determined as follows: One first specifies that all neutrons with energy at

(or very near) the resonance energy which suffer a scattering collision within the foil are degraded in energy to such an extent that they are effectively removed from the resonance, and hence are denied the possibility of absorption due to that resonance. While this is not an exact model of the situation which actually occurs, it represents a reasonable upper limit in the case of a narrow resonance.

It can be shown that the $R^i f(T)$ calculated by the code (neglecting resonance scattering) is equivalent to $R^i f(T')$ with resonance scattering treated as specified above, where T and T' are related by $T' = (\Gamma_\gamma/\Gamma)T$.

This enables one to use the results of the ROE calculations to find the contribution to $^i\sigma_a$ due to resonance scattering. This procedure was carried out for the hafnium problems studied. The errors so found, representing as they do an upper limit, were small (i.e., $< 5\%$) so that the neglect of resonance scattering in this particular calculation is justified.

Flux Depression

The artificial flux depression which occurs in the multigroup codes may be explained as follows: The typical resonance is very narrow compared to the width (1.15 lethargy units) of the energy groups in the resonance region. Neutrons at or near resonance energy will, upon passing into the hafnium sheet, either be absorbed or will pass through. If they pass through and are then scattered back into the hafnium, they will generally have been degraded below the energy of that resonance.

In assigning an effective resonance absorption cross section to an energy group of the code, it is necessary to spread a narrow resonance throughout the group. This causes a flux depression in the group because several scatters are required to traverse the group, which leads to an absorption rate that is too low for the narrow resonance.

One can compare the group fluxes within the hafnium from the Angie calculations in the perturbed case, with the fluxes in the same region in the unperturbed case (no hafnium present) to determine a flux depression factor. This has been done for the most extreme case considered (i.e., 97.9-mils hafnium). The ratio of the (i-1)st to the i^{th} group flux in the perturbed

and unperturbed problems were found to differ by about 3.5% in the lower energy (i.e., higher cross section) groups. This was considered too small an effect to warrant a change in the group cross sections.

Results

The results of the calculations involved in this study are presented in Table IV-3 and Figs. IV-4 and IV-5.

The experimental worth (dollars) was converted to K_{exp} (col. 2) from a knowledge of the reactivity and worth of a one-inch height change in the Spade assembly. This procedure precludes the necessity of determining β_{eff} (the effective fraction of the neutrons liberated which are delayed), although it does imply a particular value of β_{eff}. (This value, $\beta_{eff} = 0.00871$, must be considered as preliminary.)

In col. 3 are listed the effective multiplication factors as calculated by the code. These are compared with the experimentally determined values in the manner indicated in col. 4.

A further comparison of calculated to experimental results is given in Fig. IV-4 where the change in the effective multiplication factor is plotted versus the hafnium thickness. The uncertainty of $(\Delta K)_{calc}$ stems from a probable error of about 0.001 in K as calculated by 9 Angie. For $(\Delta K)_{exp}$, the probable error is based on a 7% estimated error in measuring the reactivity and a 2% error in measuring the neutron decay rate after pulsing the assembly.

The fission rate (i.e., total power) and the neutron capture rates (total and in hafnium alone) are listed in cols. 5, 6, and 7, respectively. These values result from the Angie edit values after correction for the distribution factor $\frac{c}{H} \cos \frac{\pi d}{c} z$ and normalized to the same total power for all experiments.

Column 8 has been added for use in calculating control-rod heating due to neutron absorption. Here $\overline{K} \equiv K$ (average) and the other symbols are self-explanatory. It is presented for $\Delta K/\overline{K}$ determined by both experiment and calculation for comparison.

Column 9 lists the results of leakage calculations from both the neutron balance method and from integrating the leakage over the surface. (Calculation of leakage by integrating over the surface was performed only

Table IV-3. Criticality, Leakage, and Capture Calculations.

1	2	3	4	5	6	7	8	9	10	11	12
T Hafnium thickness (mils)	K_{exp} eff. mult. factor (experiment)	K_{calc} eff. mult. factor (calc)	$\frac{K_{exp} - K_{calc}}{(\Delta K)_{exp}}$	F Fission rate	C Neutron capture rate (total)	$(C)_{HF}$ Neutron capture rate in hafnium	$\frac{(\Delta C/F)_{HF}}{(\Delta K/\overline{K})_{exp}}$ $\frac{(\Delta C/F)_{HF}}{(\Delta K/\overline{K})_{calc}}$	L Neutron leakage rate	L/F Neutrons leaked per fission	KL/F Neutrons leaked per parent fission	$\Delta L/\Delta C$
0 (Base problem)	0.9942	0.994445	----	100	16.2575	----	----	133.703 (133.701)	1.337	1.330	----
32.0	0.9836	0.980272	0.311	100	17.4494	1.342	1.252 0.935	136.134	1.361	1.334	2.040
65.3	0.9760	0.973816	0.121	100	18.0260	2.000	1.082 0.954	137.238	1.372	1.336	1.999
97.9	0.9716	0.969339	0.102	100	18.4417	2.477	1.077 0.969	138.001 (138.048)	1.380	1.338	1.968

MUL-14119

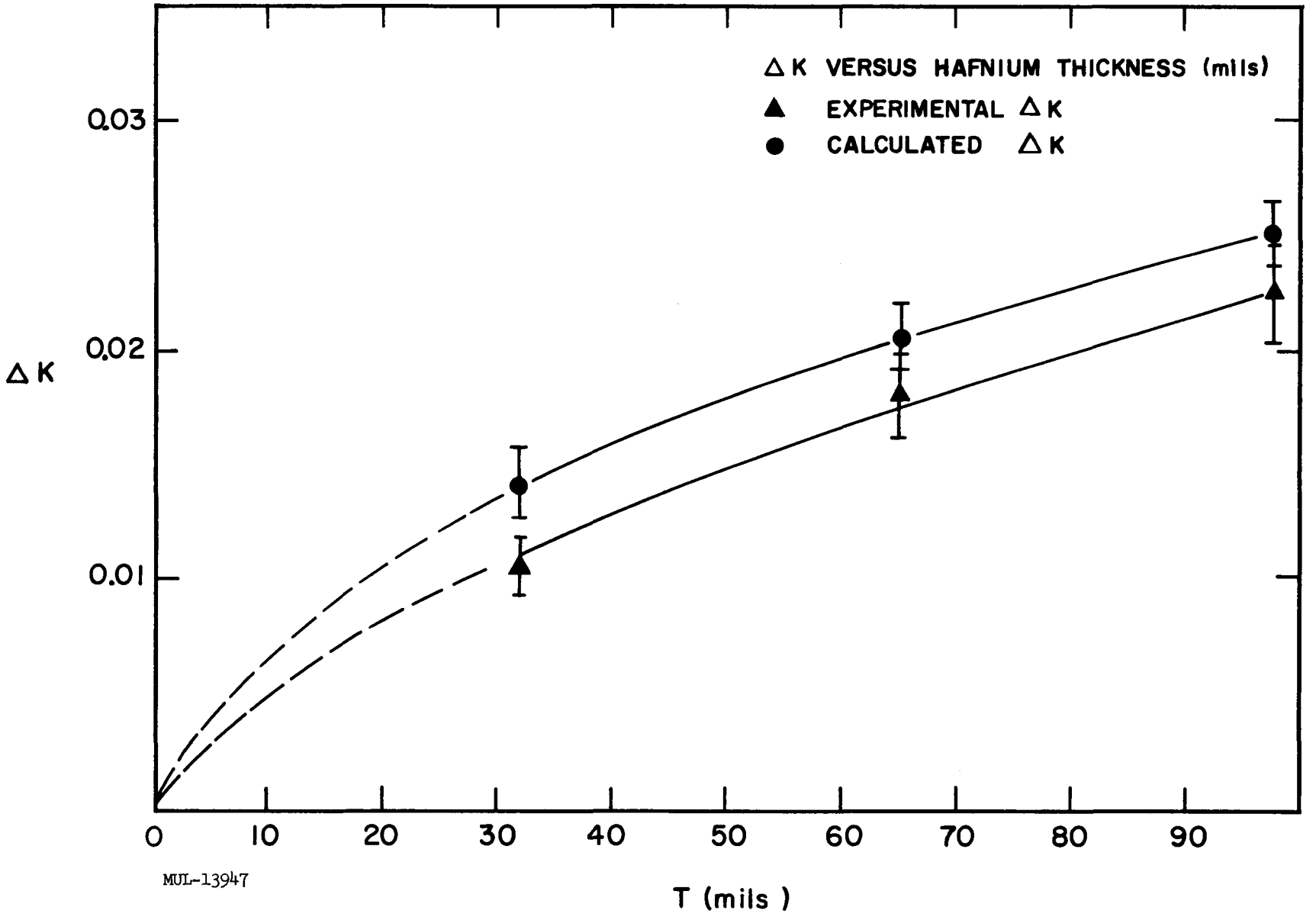

Fig. IV-4. ΔK vs hafnium thickness.

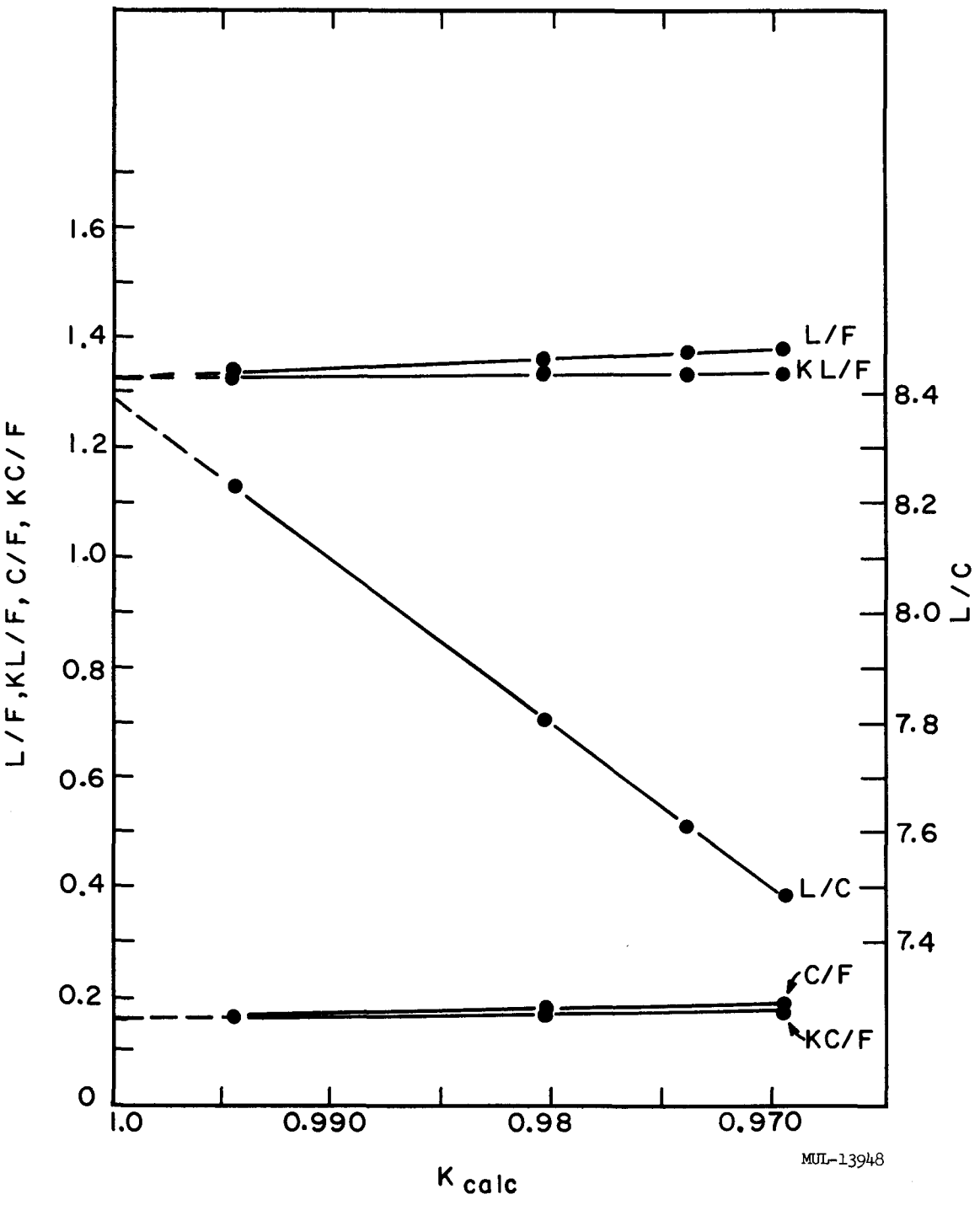

Fig. IV-5. Leakage and captures per fission vs K_{calc}, and leakage per capture vs K_{calc}.

for the base problem and the 97.9-mil hafnium problem and these are denoted in col. 9 by parentheses.) A careful integration was made in the base problem by fitting a cosine curve to the Angie flux values along the median line of each surface to within a few centimeters of the edge, and then assuming a linear fit from there to the boundary. The relative leakage between the perturbed and the base problems was calculated by integrating relative power over the surface, this being an easier task than integration of leakage. This yielded a value of 1.0325 which, when applied to the leakage rate in the base problem, gives a value of 138.048 for leakage rate in the perturbed problem. The excellent agreement between the two methods would seem to verify the accuracy of the "neutron balance" method.

The number of neutrons leaked per fission (L/F) and the number of neutrons leaked per parent fission (KL/F) are listed in cols. 10 and 11, respectively. Angie solves for the eigenvalue K, and by requiring that ν/K neutrons be liberated per fission, reduces the actual subcritical system to a hypothetical critical system. Thus, L/F may be taken as the neutrons leaked per fission if ν/K neutrons were liberated per fission, in which case the reactor would be critical. On the other hand, KL/F gives the number of neutrons which leak of those ν neutrons which are liberated per parent fission. It ignores the neutron population present at the time K is changed, in order to find the leakage per fission from those neutrons subsequently liberated. No particular significance is implied in the quantity KL/F except that it does remove some of the effect of subcriticality from the number of neutrons leaked per fission.

Column 12 documents the fact that addition of a poison rod increases leakage loss, if criticality is regained by adjustment of ν.

In Fig. IV-5 are presented graphically some of the values from Table IV-1, in addition to captures per fission (C/F) and captures per parent fission (KC/F).

Conclusions

The relatively good agreement (Fig. IV-4) between ΔK_{exp} and ΔK_{calc} – they differ by about 0.003 for the three hafnium thicknesses

considered — affords a measure of confidence in the derived cross sections. Further, it lends justification to the neglect of resonance scatter and artificial flux depression. However, the values of $(K_{exp} - K_{calc}) \div \Delta K_{exp}$ in col. 4, Table IV-1, indicate the desirablilty of further refinement of those cross sections.

Calculation of the leakage by use of the neutron balance approach is valid, rapid, and undoubtedly more accurate than the laborious integration of leakage over the reactor surface. The only requirement is that total power and capture rate are calculated and edited by the code. The reactor shape, the materials, and whether a bare or reflected assembly is considered, are immaterial in application of the neutron balance approach. If the code produces accurate values for the effective multiplication factor and for fission and capture rates, then an accurate value for the leakage rate is obtained.

Calculations also showed that, for a centrally located control rod, $\Delta K/\overline{K} = -0.010$ resulted from absorption of 0.0095 ± 0.0002 neutrons per fission in the rod. This value applies to rods worth up to $\Delta K/\overline{K} = -0.023$.

COUPLING EFFECTS BETWEEN CONTROL RODS

The relative worth of control rods was studied using the Angie diffusion code and an X-Y geometry. Perturbations of the multiplication factor and of local power density were noted due to the central 12 control rods. An approximately correct distribution of control rod locations was assumed, all rods being placed on a 21.116-cm average radius. Control rods were represented by superposition of a hafnium resonance cross section on a background of fueled and unfueled BeO. The poison content was selected to depress the multiplication factor by approximately 1% per one rod.

Results of this study are shown on Fig. IV-6. It can be seen that the relative worth of control rods remains quite constant up to 6 uniformly spaced rods. Coupling effects become noticeable with a greater number of rods. One of twelve inserted rods is worth only 87% of that value which would be realized if it existed alone in the reactor. Also, given a total number of only 4 rods, a slight enhancement of control rod worth is observed. However, this

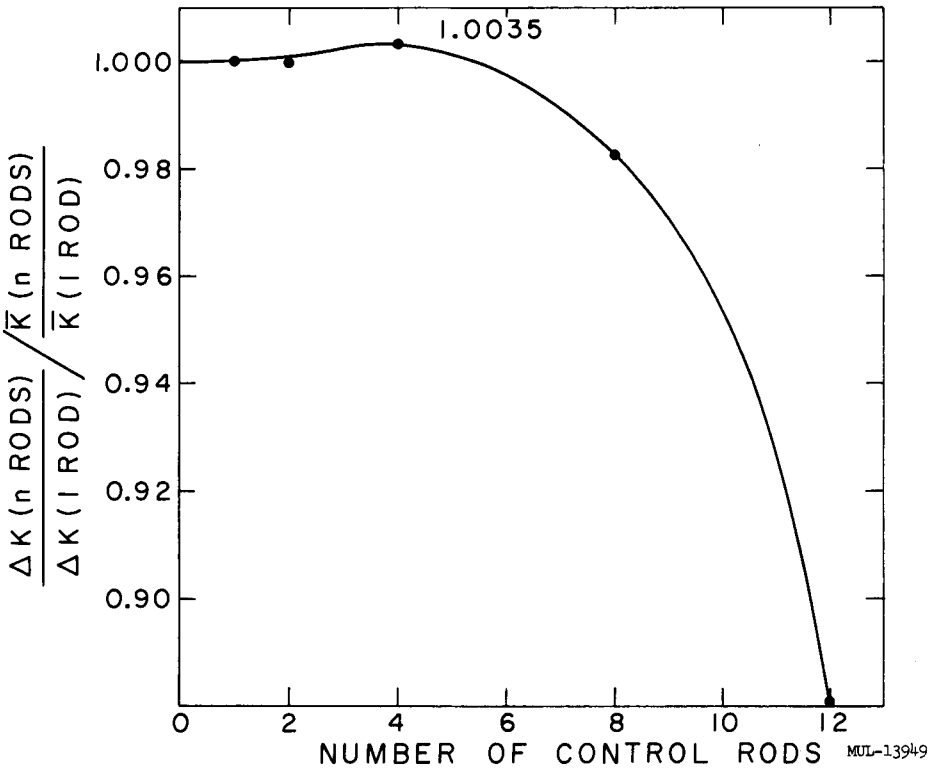

Fig. IV-6. Relative worth of control rods.

enhancement is very small, i.e., 0.4%. This study was performed by representing control rods by a square and by a cruciform geometry. Both representations render results which are quite alike.

THE EFFECT OF CONTROL RODS ON RADIAL POWER PROFILE

Control rods within the active core necessarily have a profound effect upon the radial power density. This is clearly seen on Fig. IV-7 where the percent change in local power density due to the insertion of twelve control rods is noted. The same representation of control rods in machine codes, as mentioned before, was used. This effect depresses the power at the core center by 12.4% and causes a 10.4% increase of power near the periphery. In the immediate vicinity of the control rod itself, the depression of the power profile is, of course, greatest; it is as much as 20%. In the presence of 12 control rods, equally spaced

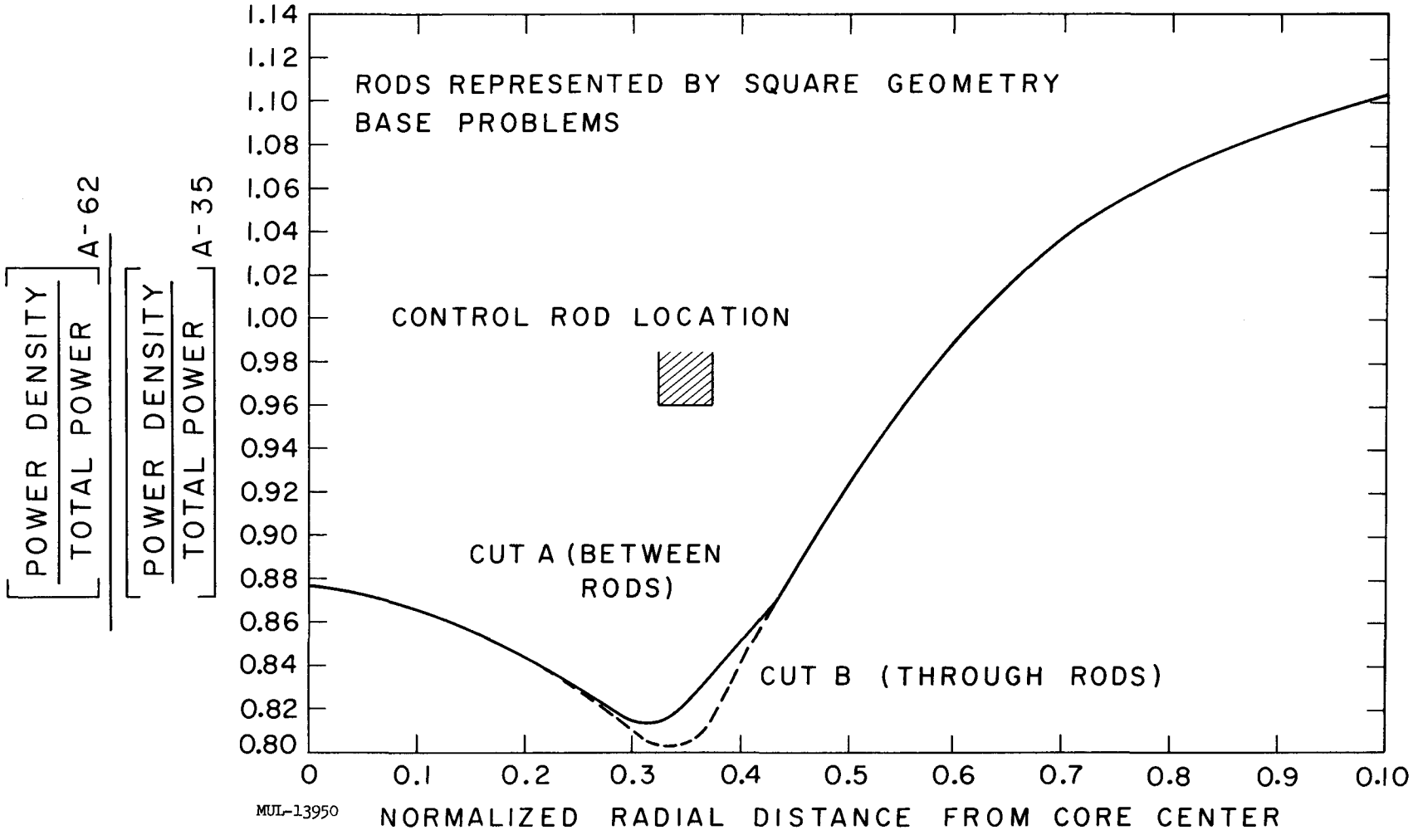

Fig. IV-7. The effect of control rods on average power density (normalized to problem without control rods and to the total power).

about the core center, the rods are sufficiently close to each other to render a radial power profile between rods which is only slightly different from that through any one rod. This power profile is marked by the dotted line on Fig. IV-7. A 2-dimensional plot of isopowerlines is shown on Fig. IV-8. A cruciform geometry for control rods affects the power very much like the square-shape representation.

It must be stressed that the study on coupling effects and radial power density perturbations was made by an appropriate use of the hafnium resonance only. The background material was fueled BeO, etc., as mentioned. Calculations are in progress where the local removal of fueled BeO and the insertion of tension-tube materials and control rods is studied, to render the absolute worth of control rods for the Tory II-C reactor.

SUMMARY OF TORY II-C NUCLEAR HEATING VALUES

A. Summary of Results

The reappraisal of the total gamma-energy source and a more accurate evaluation of the spatial gamma-ray absorption intensity distribution in the Tory II-C reactor has brought about a revision of the Tory II-C nuclear heating values published to date. As a result, in order to arrive at a closer approximation of the heating realized by Tory II-C components after a 10-hour steady operation, it was found that the gamma component of each heating value published had to be enhanced by approximately 10%. Since gamma heating generally contributes from 30% to 80% to the total heating of nonfueled components, the net effect on the total heating will be an increase of approximately 3% to 8% for the 10-hr steady operation (or 90% fission product gamma saturation) case. A revised summary of the maximum peak nuclear heating of Tory II-C components published to date is given in Table IV-4.

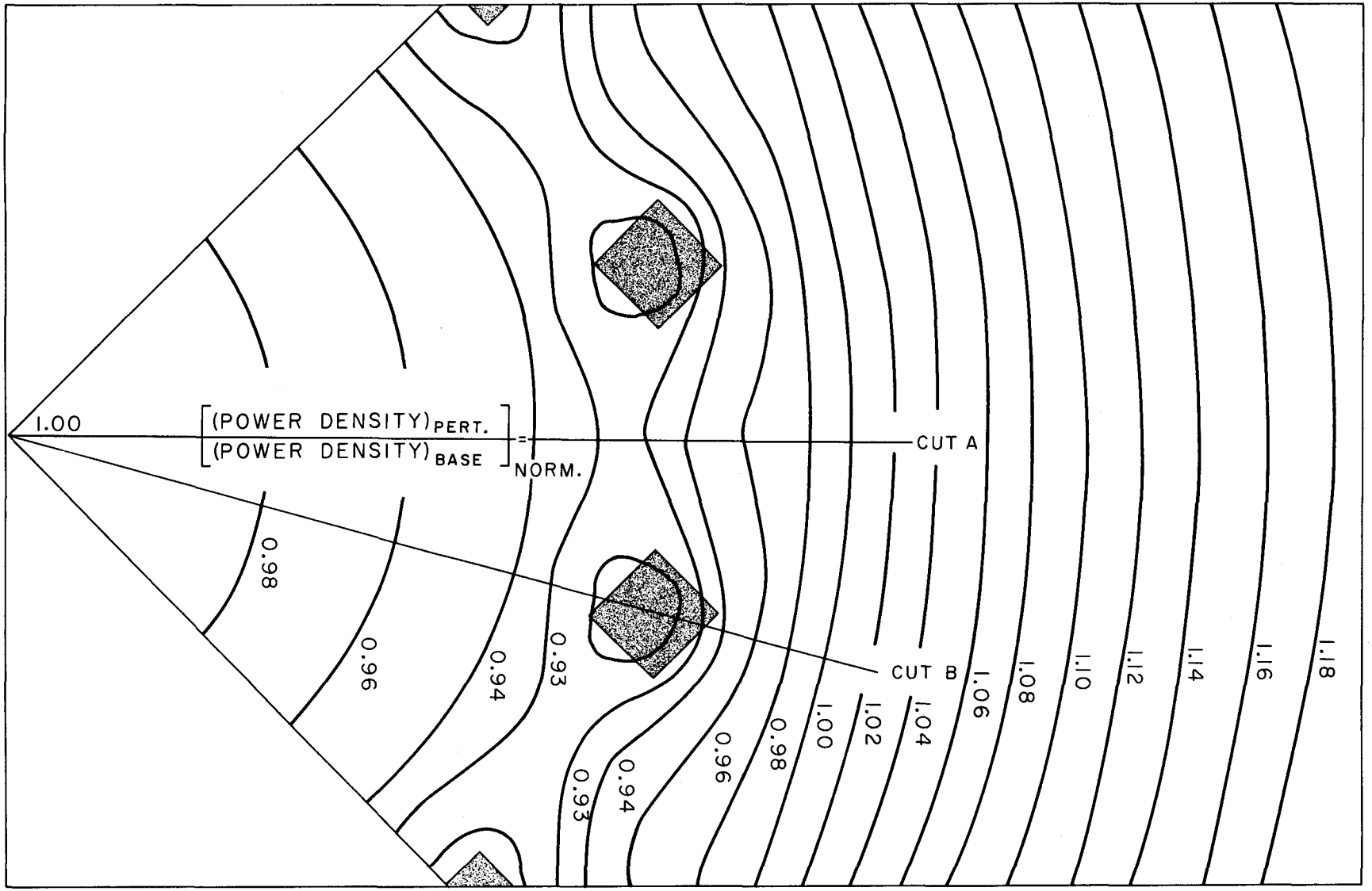

Fig. IV-8. Effect of control rods on average power density in problem with radially varied fueling (normalized to problem without rods and to power at core center).

Table IV-4. Summary of Revised Peak Nuclear Heating Values for Tory II-C Components (Mw/ft^3 of Full-Density Component Material per Mw/ft^3 of Average Core Power Density at 90% Fission Product Saturation).

Component		Peak Values of Respective Components				
		Gamma	(n, γ)	(n, n)	Beta	Total
Tie rods at R=0	R-235	0.6705	0.249	0.0241	--	0.9436
	René 41	0.6785	0.504	0.0241	--	1.2066
Hafnium control rods	80-mil Asterisk-shaped	1.132	1.151	--	--	2.283
Side support structure	Pressure pads	0.0811	0.0251	0.0029	--	0.1091
	Buggy springs	0.051	0.0166	0.0025	--	0.0701
	Aft duct	0.0425	0.0267	0.0023	--	0.0715
Unfueled BeO inserts[a]		0.1975	--	0.05	0.023	0.2705
Side reflector	Inner boundary	0.085	--	0.026	0.023	0.134
	Outer boundary	0.0244	--	0.006	0	0.0304

[a] Unfueled BeO tubes surrounding the tie rods.

B. Summary of Calculations

1. Re-evaluation of the Total Gamma Source in Tory II-C.

The gamma-energy source in a reactor consists of prompt fission gammas, fission product decay gammas, and gammas which are the result of neutron capture in the reactor medium, or (n, γ) gammas. Because of the time dependence of fission product decay gammas, the total gamma energy released per fission will increase from an initial value at start-up to a maximum value at time infinity. This maximum value in the case of Tory II-C is about 1.64 times the initial start-up value. To illustrate, Table IV-5 lists the gamma-energy yield per fission at various times of operation.

Table IV-5. Gamma-Energy Yield per Fission.

Time after start-up	0	2 min	10 hr	∞
% Fission product saturation	0	50%	90%	100%
Prompt fission gammas	7.925	7.925	7.925	7.925
Fission product decay of gammas	0.	3.492	6.286	6.984
Neutron capture in fuel	1.445	1.445	1.445	1.445
Neutron capture in tie-rods	1.634	1.634	1.634	1.634
Total yield	11.004	14.496	17.290	17.988

All previous gamma heating calculations were based on a 14.75-Mev/fission gamma-energy source (which was applicable to the Tory II-A case). For any of the four considered Tory II-C cases, the gamma heating values should be corrected by multiplying them by the ratio of the newly calculated gamma-energy yield to the one considered before (i.e., 14.75-Mev/fission). For the considered times after start-up these ratios are:

Time after start-up	Source yield correction
0	0.746
2 min	0.9828
10 hr	1.1722
∞	1.2196

2. Appraisal of the Spatial Gamma-Ray Absorption Intensity Distribution in Tory II-C.

It has so far been assumed that, given a homogeneous medium with a uniform source distribution, the gamma heating in the geometric center of the core assumes the same value as that calculated for an infinite medium. However, for Tory II-C average core composition and dimensions, it is seen that the value of gamma heating does not attain that of an infinite medium at the geometrical center.

Using the analytical expression derived in Chapter 22 of J. R. Stehn's The Physics of Intermediate Spectrum Reactors, for the gamma-ray absorption on the axis of a cylindrical source region given by Eq. 22.139, it was calculated that the gamma absorption intensity in the center of a cylindrical core with L = 2R and an average gamma-energy absorption coefficient of 0.041 cm^{-1} (which was calculated by Trikl code* for the average II-C composition) is 0.94. Since the spatial gamma-ray absorption intensity distribution used in the past was normalized to unity at the center of the core, and since this distribution was derived from the same analytical considerations, the correction factor of 0.94 applies throughout the core.

To summarize: The combined effect of the source and geometry corrections results in a gamma heating correction factor of 1.102, or an effective increase of the gamma heating component by 10.2%, for the case of a 10-hr steady operation.

3. Nuclear Heating of Tory II-C Hafnium Control Rods.

Nuclear heating calculations have been performed for the latest proposed control rod design which has six 80-mil-thick by 1/2-inch blades arranged in an asterisk configuration.

In order to obtain more accurate control rod heating values, a simplified Monte-Carlo code, Yogi, has been written, checked out, and employed during this quarter. This code computes, in a reasonable amount of

---

* See UCRL-6376.

IBM-7090 computer time, values for the magnitude of control rod heating by gamma radiation generated in the medium surrounding the control rod, as well as gammas generated by the (n, γ) process in the control rod itself. Secondary electrons produced by gamma radiation were not traced in the initial version of the code; the code was modified however, and it was found that when the electrons produced in Compton collisions were followed, their energies being linearly decreased along their paths, no change in heating value was observed, within statistics.

Gamma heating calculations were done for fully inserted control rods considering a 90% fission product gamma-saturation level (corresponding to a 10-hour steady operation). The results obtained from the Yogi Monte-Carlo code were applicable to the considered geometric configuration (i.e., 80-mil asterisk-shaped rod) without due regard paid to the surrounding 30-mil Hastelloy R-235 control rod shell. The shielding effect of the Hastelloy shell on the control rod was evaluated by means of the Trikl code (see UCRL-6376, p. 92) by incorporating the shielding effect of the Hastelloy shell in the photoelectric cross sections of the hafnium. This shielding factor can be shown to be proportional to the exponential integral of the second order E_2 (μx), where (μx) is considered to be the photoelectric mean free path in the 30-mil Hastelloy shell. The net effect of the Hastelloy shell on the hafnium control rod external gamma heating was found to be about 10%.

It is presently intended that the control rods used during high-power operation will have the minimum required reactivity for reactor control. The (n, γ) heating calculations were based on a neutron absorption capacity per hafnium rod corresponding to this minimum required reactivity swing. This implies 0.0127 neutrons/fission captured per rod (see UCRL-6376, p. 92). The absorbed energy fraction of gammas generated in an asterisk-shaped control rod was determined by the Yogi Monte-Carlo code to be 25.5%.

SECTION II. TORY II-C CONTROLS

SUMMARY

The Tory II-C controls effort has centered on (1) the development of the high temperature actuation system and associated control components, and (2) the servo laboratory facility which will be used to test and evaluate these systems and components.

During this quarter, the development of the high-temperature actuation system has progressed through the high-temperature checkout stage at one contractor's facility and has reached the high-temperature checkout stage at another contractor's facility. Each of these developmental programs appears promising.

An accurate analog of the electropneumatic actuation system has been completed at LRL and is being used to analyze and refine component design and system performance.

DEVELOPMENT OF 1200°F ELECTROPNEUMATIC ACTUATION SYSTEM

Model 1240 Test and Evaluation

This section summarizes the progress toward development of a prototype high-temperature (1200°F) and radiation resistant electropneumatic control rod positioning system. This prototype is called the Model 1240 actuator, and is applied in a simple closed-loop system shown schematically in Fig. IV-9. A condensed drawing of the components exposed to elevated temperatures and high radiation is shown in Fig. IV-10.

The major problem areas encountered during specified room and high-temperature tests are:

1. The servo valve, in its present configuration, cannot tolerate large temperature differentials between ambient and supply air.
2. The carbon motor gear side plates have limited life at both room and high temperature.
3. The linear feedback transducer failed completely.
4. Both snubber springs failed at high temperature due to lack of spring lubrication.

Below are summarized all significant results determined during room and temperature testing of the Model 1240, comparing actual performance to specified performance where results are available.

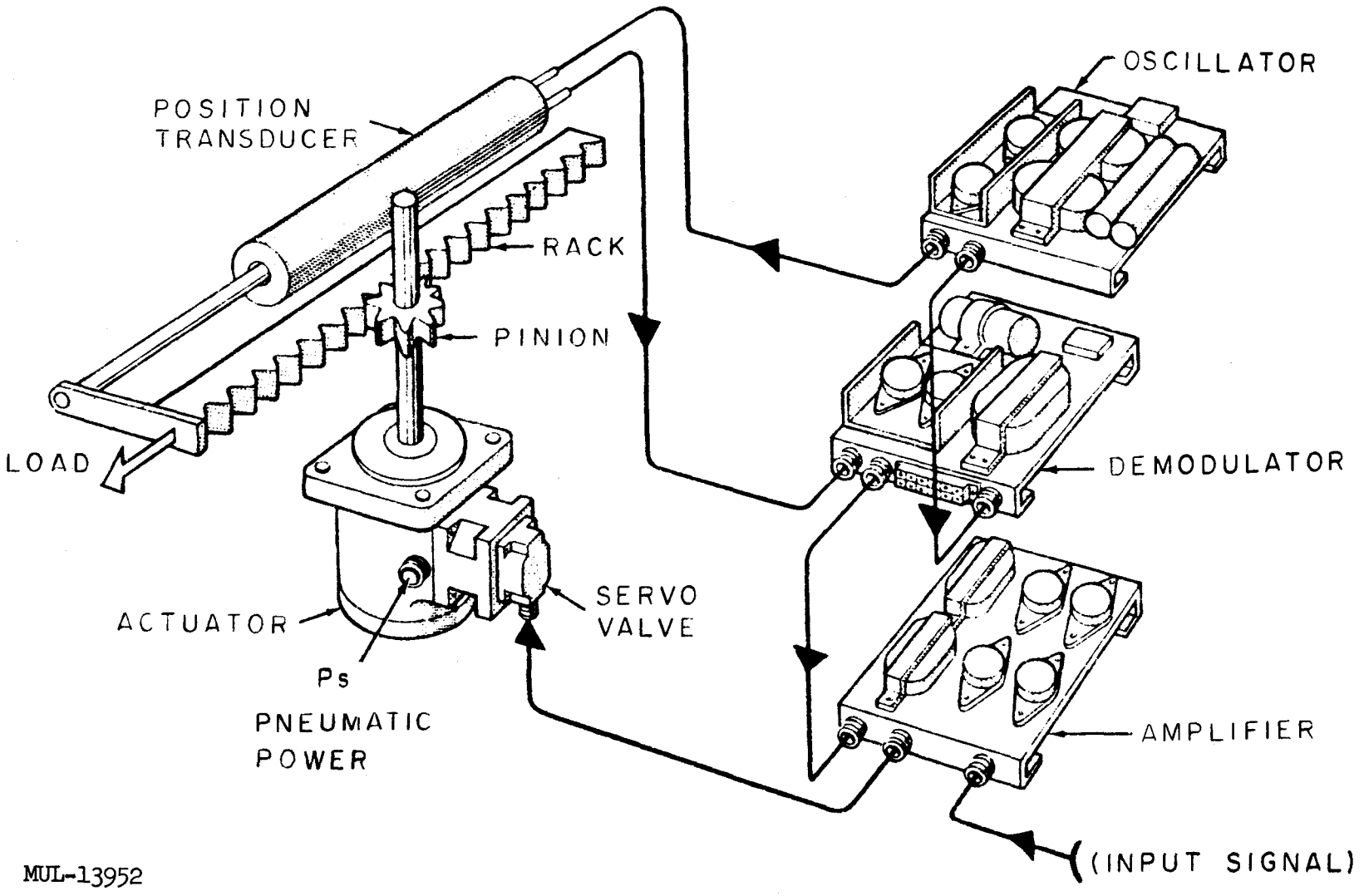

Fig. IV-9. Schematic of Model 1240 regulating-rod control system.

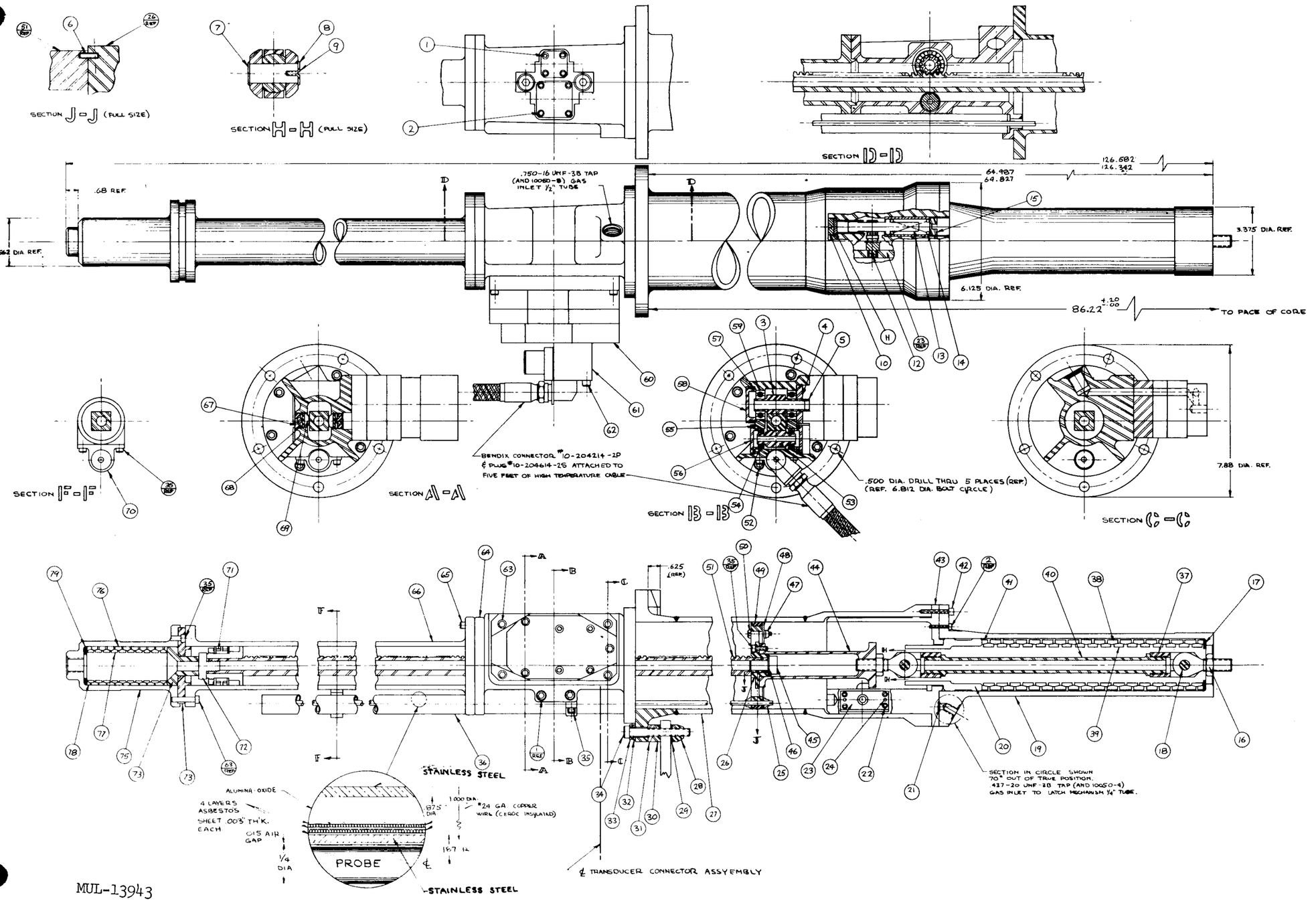

MUL-13943

ITEM	NO. REQ'D	CODE	PART NO.	PART NAME
79	1	B	2670-003-167	LOCATOR
78	2	B	2670-003-137	SPRING - END RING
77	10	B	2670-002-136	SPRING - INNER RING
76	9	B	2670-003-135	SPRING - OUTER RING
75	1	D	2670-003-149	SPRING HOUSING
74	1	B	2670-003-153	PLUNGER
73	1	B	2670-003-152	PILOT PLATE
72	1	B	2670-003-173	STOP
71				
70	1	B	2670-003-182	GUIDE TRANSDUCER
69	4	B	2670-003-154	SIDE SUPPORT
68	4	A	2670-003-179	WASHER SIDE SUPPORT
67	4	A	2670-003-177	LOCK - SIDE SUPPORT
66	1	D	2670-003-142	FORWARD GUIDE TUBE
65	6	B	2670-003-142-1	CAPSCREW - HEX. SOC. HD. .3125-18 UNC
64	1	E	2670-003-141	TRANSMISSION HOUSING
63	10	B	2670-003-142-2	CAPSCREW - HEX. SOC. HD. .3125-18 UNC
62	4	B	2670-003-123	CAPSCREW - HEX. SOC. HD. .250-20 UNC
61	1	D	6641-002-104	HIGH TEMP. PNEUMATIC VALVE
60	1	D	2670-003-110	PNEUMATIC MOTOR MODEL 1240
59	2	~	STOCK	
58	1	B	2670-002-131	BEARING RETAINER
57	1	A	2670-003-187	SPACER - BEARING RETAINER
56	2	B	2670-003-129	BEARING RETAINER
55	2	A	2670-003-188	SPACER - BEARING RETAINER
54	2	~	STOCK	
53	1	B	2670-002-138	ROLLER
52	5	B	2670-003-190-1	CAPSCREW - HEX. SOC. HD. .375-16 UNC
51	1	C	2670-003-140	GEAR RACK
50	5	B	2670-003-195-1	SCREW - HEX. HD. MACH. .190-32 NF
49	1	C	2670-003-158	BEARING
48	1	C	2670-003-160	RETAINER
47	5	~	STOCK	ESNA NUT - .190-32 NF # 1802-02
46	1	A	2670-003-197	WASHER
45	1	B	2670-003-196-1	CAPSCREW - HEX. SOC. HD. .5625-12 UNC
44	1	C	2670-003-161	EXTENSION
43	1	D	2670-003-145	LATCH HOUSING
42	8	B	2670-003-192-3	CAPSCREW - HEX. SOC. HD. .3125-18 UNC
41	2	B	2670-003-134	SPRING - END RING
40	1	C	2670-003-163	CLEVIS ROD
39	16	B	2670-003-133	SPRING - INNER RING
38	15	B	2670-003-132	SPRING OUTER RING
37	2	C	2670-003-162	CLEVIS
36	1	~	STOCK	COLLINS LMT-97904 TRANSDUCER
35	11	B	2670-003-191-1	CAPSCREW - HEX. SOC. HD. .250-20 UNC
34	5	B	2670-003-189-1	CAPSCREW - HEX. SOC. HD. .375-24 UNF
33	5	B	2670-003-156	SPHERICAL WASHER
32	5	B	2670-003-155	SPHERICAL WASHER
31	1	C	2670-003-183	PLATE - CONVEX
30	1	C	2670-003-184	PLATE - CONCAVE
29	5	~	STOCK	FLAT WASHER (.375 SCREW) 300 SERIES SST
28	5	~	STOCK	ESNA NUT .375-24 UNF-2B # Z 1200-064
27	1	E	2670-003-144	APT GUIDE TUBE
26	1	C	2670-003-159	BEARING HOUSING
25	2	~	STOCK	ESNA NUT - .250-28 UNF # Z 1200-064
24	2	B	2670-003-175	DOWEL PIN
23	1	B	2670-003-149	LATCH PLATE
22	4	B	2670-003-193-1	CAP SCREW HEX. SOC. HD. .190-24 NC
21	1	~	STOCK	'K' SEAL - HARRISON # 12130
20	1	C	2670-003-166	LARGE SPRING PLUNGER
19	1	D	2670-003-157	HOUSING, LARGE SPRING
18	2	A	2670-003-185	ROD END ALTERATION
17	1	A	2670-003-176	SPACER SPRING
16	2	~	STOCK	HEX JAM NUT .625-18 UNRF 3B 300 SERIES SST
15	1	B	2670-003-150	LATCH PISTON STOP
14	1	B	2670-003-148	LATCH SPRING
13	1	B	2670-003-147	LATCH PISTON
12	1	B	2670-003-146	LATCH SECTOR
11	1	A	2670-003-186	PLUG - SEALING
10	1	B	2670-003-151	LATCH PISTON PLUG
9	2	B	2670-003-196	CAP SCREW - FL. HD. SOC. .190-24 NC
8	2	B	2670-003-165	CLEVIS WASHER
7	2	B	2670-003-164	CLEVIS PIN
6	1	~	STOCK	ESNA # 79-028-125-0375 ROLL PIN
5	1	A	2670-003-180	SPACER GEAR
4	1	A	2670-003-181	NUT - RETAINING
3	1	C	2670-003-139	DRIVE GEAR
2	8	B	2670-003-191 3	CAP SCREW HEX SOC. HD. .250-20 UNC
1	8	B	2670-003-191 2	CAP SCREW-HEX SOC. HD .250-20 UNC

Fig. IV-10. High-temperature components of Model 1240 regulating-rod control system.

Table IV-6 shows, in summary, reliability information on the high-temperature electropneumatic servo valve used in the Model 1240. The servo valve, which is the most critical component in the system, has performed quite well except for its intolerance to temperature differentials. If the temperature difference between the valve body and spool exceeds 100-200°F, the valve will not operate properly. A correction program is presently being conducted to eliminate this discrepancy.

Table IV-7 shows a summary of actuator performance characteristics determined during room-temperature and high-temperature testing. In general, the Model 1240 meets the specified dynamic performance. Table IV-8 shows a summary of known reliability information relative to the high-temperature motor. Table IV-9 gives a summary of reliability information on the entire Model 1240 actuation system including (1) servo valve, (2) high-temperature motor, (3) rack, pinion, and simulated load, (4) position transducer, and (5) amplifier with connecting cable. Table IV-10 shows a summary of problem areas revealed thus far during operation of the system. Possible solutions and action items are indicated where known.

The Model 1240 actuator is shown in exploded form in Fig. IV-11 prior to assembly and test. Figures IV-12, IV-13, and IV-14 show several views of the Model 1240 motor before high-temperature test. Figures IV-15 and IV-16 show the actuator system being prepared for high-temperature test at the contractor's facility. Figure IV-17 shows the motor-servo valve combination following test at 1200°F. Figure IV-18 shows an exploded view of the motor following high temperature test.

During June 1961, the Model 1240 actuator is undergoing vibration tests at the contractor's facility.

Compensation Network Analysis

A complete signal flow representation network-operational-amplifier circuit used in the prototype system has been developed and reduced to transfer-function representation by digital techniques. These results substantiate the approximation approach by showing negligible interaction between the compensation critical frequencies (complex) in the neighborhood of those used in compensating the prototype servo.

RAHS Actuator Development

This alternate approach to the high-temperature actuator problem is being pursued by a contractor, but with the Tory II-C application in mind.

The contractor is attempting to establish feasibility of a system similar to the Model 1240, but which utilizes a nutating-disk motor in place of the gear motor. A drawing of the nutating-disk motor is shown in Fig. IV-19. Figures IV-20 and IV-21 show photographs of an early high-speed prototype, while Fig. IV-22 shows a photograph of the RAHS.

The nutating-disk motor approach shows promise for high-temperature operation, as has been demonstrated with a "4-inch" actuator model over a two-year span. This actuator has been run successfully at 1220°F for over 40 hours, and at 1600°F for two hours. The RAHS development, utilizing all of the same basic concepts, has yet to be run at temperature, although a small version of the RAHS servo valve has been operated for several hours in performance tests with the "4-inch" actuator.

The principle variations of the RAHS actuator from the Model 1240 are:

1. Scram is accomplished through the motor-transmission path by means of pneumatic shifting.
2. Pneumatic snubbing is used rather than spring snubbing.
3. No outboard rack supports (other than those integral with motor) are required.
4. Variations within the existing unit to accomplish shim-rod-actuator specifications are possible.

Table IV-6. Summary of Reliability of High-Temperature Servo Valve.

Test	Time at room temp	Time at high temp	Remarks
Total time at high temp of valve before preliminary high-temp test of actuator		9.7 hr over 1000°F (3.75 hr over 1200°F)	Time over 1000°F without disassembly and adjustment - 5.3 hr. Time over 1200°F without disassembly and adjustment - 3.6 hr.
Preliminary performance tests of actuator	1 hr	7 min 1200°F 1 hr-37 min 1000°F (17 min cyclic)	Valve was initially operating erratically; corrected by applying large rapid-input signal to valve at full pressure.
Acceptance test	6 hr-17 min (1 hr-51 min cyclic)	1000°F 3 hr-29 min (1 hr-38 min cyclic)	New torque-motor valve malfunctioned; found to be dirt in pilot stage - valve cleaned and reassembled.
	2 hr-31 min (1 hr-14 min cyclic)	5 hr-5 min 1000°F (1 hr-26 min cyclic)	Test terminated
Total	9 hr-48 min	20 hr	

Table IV-7. Actuator Performance Characteristics.

Item	Specified	Room temp Q(0)	1000°F
Dynamic response 90° phase shift	15 cps 1000 psig	10 cps 700 psig	15 cps 100 psig
Saturation velocity	Greater than 60 in/sec at 1000 psig	Not available	166 in/sec
Position resolution	± 0.02 in.	± 0.015 in.	± 0.030 in.
Scram time	40 inch 25 sec at 1000 psig	0.38 sec, valve hard over	Not available
Transient response	Equal to or less than 12% of demand step or 0.01 inch, whichever is greater	0.14 step overshoot 0 0.69 step " 32% 1.23 step " 32% 9.1 step " 11%	0.13 step overshoot 0 0.6 step " 0 1.04 step " 0 8.05 step " 30%
System stiffness	Capable of holding 20-lb load within resolution with continuous 69-lb axial load at 1000 psig	10,000 lb/in.	Not available
Linearity	± 5% of stroke over temp range of operation	Not available	Not available
Full stroke displ, time under servo cont.	Less than 0.75 sec	Not available	0.4 sec
Relative stability	Gain margin 6 db or more, phase margin - 50° or more	Not available	Not available

Table IV-8. Summary of Reliability of 1240 High Temperature Motor.

Test	Time at room temp	Time at high temp	Remarks
Open-loop cyclic reliability test	1 hr-14 min	(1 hr-11 min) 1200°F, 1 hr-24 min 1000°F	Motor had new bearings and carbon wear plates and gears were re-electrofilmed. After test was completed, the motor was disassembled and all parts were found in good condition.
Preliminary performance tests of actuator	1 hr	7 min 1200°F, 1 hr-37 min 1000°F (17 min cyclic)	Motor was re-assembled using all the original parts. Motor failed during 400°F operability test in cool-down cycle. Drive gear rubbed against housing, tearing silver plate loose - causing motor to bind up.
Acceptance test	4 hr-3 min (1 hr-14 min cyclic)	1 hr-37 min 1000°F (37 min cyclic)	New bearings and carbon wear plates were put in motor, gears were re-electrofilmed and center section was re-silver-plated. Carbon wear plates replaced.
	2 hr-51 min (1 hr-14 min cyclic)	3 hr-45 min (1 hr-50 min cyclic)	Carbon wear plates replaced.
Demonstration	1 hr-4 min (37 min) cyclic	1 hr-30 min 1000°F 1 hr-17 min (37 min cyclic) 1000°F, 25 min 1000°F	Motor disassembled for inspection on carbon plate; showed signs of wear (0.001-in.) - re-assembled.
	100 scram 2 hr		Tests terminated
Total	12 hr-12 min	11 hr-42 min	

Table IV-9. Summary of Reliability of 1240 Actuator.

Test	Time at room temp	Time at high temp	Remarks
Room-temperature life	3 hr-21 min (cyclic)		No friction load - room temp 1240 motor used. After test was completed, actuator was disassembled and parts examined for excessive wear - parts in good condition, rack and pinion re-electrofilmed, actuator re-assembled with original parts.
Preliminary performance test of actuator	1 hr	1000°F	Electrical cable to torque motor failed.
	15 min	7 min 1200°F	Transducer failed - aft wear ring replaced.
		1 hr-37 min 1000°F (18 min cyclic)	Motor failed during cooling cycle - actuator and motor disassembled - all carbon parts show signs of erosion with exception forward wear ring and piston rings - snubber springs locked.
Acceptance test	2 hr-49 min (37 min cyclic)	1000°F 9 min	All bearings and carbon parts replaced with new parts - rack and pinion, ring springs, spring housing re-electrofilmed - new torque motor.
	1 hr-14 min (37 min cyclic)	1 hr-28 min (37 min cyclic)	Transducer failure - small snubber spring locked, latch mechanism not functioning - removed, valve electrical connector replaced. Force gain down. Carbon motor plates replaced.
	2 hr-14 min (37 min cyclic)	1 hr-52 min (51 min cyclic)	Valve malfunction - transducer failure, room-temp transducer used to close loop.
	37 min (cyclic)	1 hr-53 min (49 min cyclic)	Carbon motor plates replaced.
Demonstration	1 hr-4 min	1 hr-30 min	Large snubber spring locked. System had tendency to go unstable.
Demonstration		1 hr-17 min (cyclic) 25 min + scrams	
	100 scrams 2 hr		Motor disassembled and inspected, ring springs greased, latch mech. greased.
			Tests terminated
Total	14 hr-34 min	10 hr-18 min	

Table IV-10. Major Problem Areas Revealed by Prototype Actuator Operating Experience to May 1, 1961

Component or characteristic	Problem	Possible solution	Action being taken
(1) LVDT position transducer	No tolerance to thermal gradients, leads open, structural failure.	Mechanical design to allow differential expansion, support leads.	Contractor redesign with supplier fabrication contractor elevation.
(2) Servo valve	Erratic operation, may be dirt, pilot stage leakage, temperature difference between gas and body.	Improve pilot stage filter. Improve seals.	Redesign study by contractor.
(3) Motor bearings	Large radial clearance and poor radial stability cause high leakage and allow gear tooth-center section contact. Possible cause of carbon wear due to skew.	Minimize radial load-deflection requirements by capping external leakage; use pre-loaded, angular contact, thermally compensated bearings.	Small gear bearings are capped. Contractor investigating total bearing capping.
(4) Motor carbon plates	Excessive wear increases leakage passages.	Pressure balance motor, avoid bearing skew, improve wear characteristics. Restrain axial gear play.	
(5) Buffer spring	Locks in compressed position.	Improve lubricant design.	Lubricant investigation by contractor.
(6) Latch	Sticks	Improve lubricant. Increase clearances.	Lubricant investigation by contractor.
(7) Electrical cable and connector	High contact resistance. Shorts to shield and between leads at elevated temperature.		
(8) Combined mechanism friction, including load friction simulator	Time-temperature variation changes performance characteristics.	Increase servo static and dynamic stiffness. Reduce friction.	Valve-motor design optimization and compensation redesign for improved electro-pneumatic components by LRL.

Fig. IV-11. Model 1240 actuator disassembled prior to test.

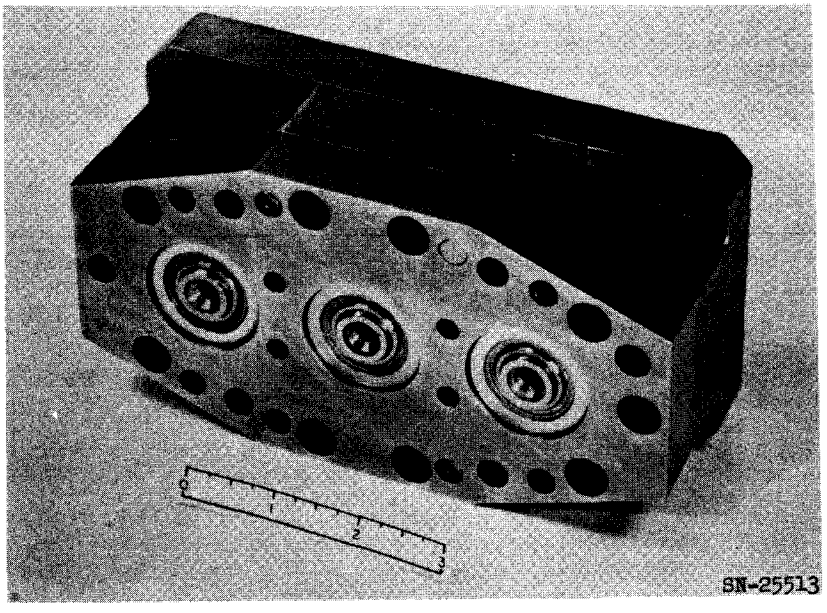

Fig. IV-12. Model 1240 motor, servo-valve end (before high-temperature test).

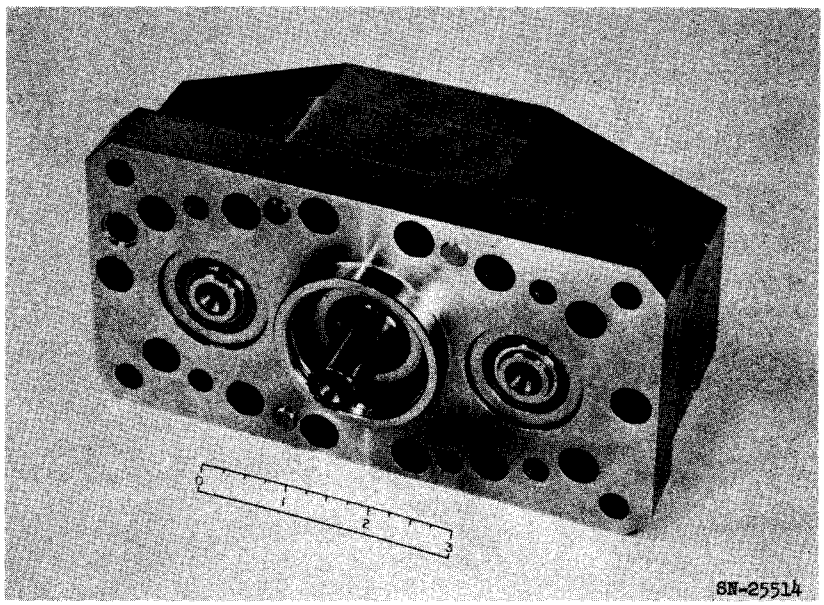

Fig. IV-13. Model 1240 motor, output end (before high-temperature test).

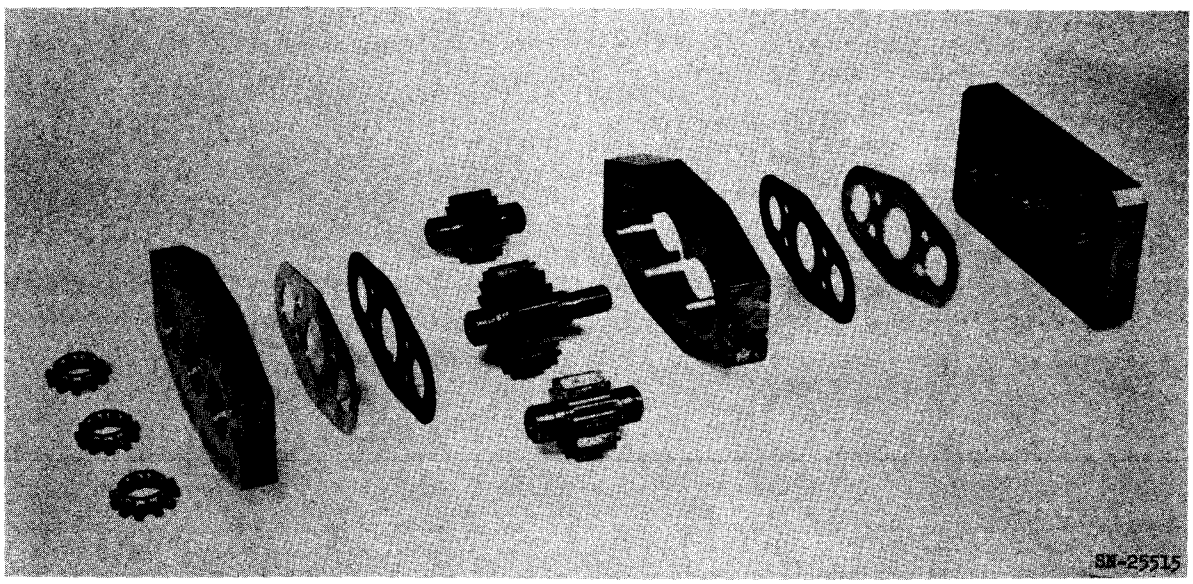

Fig. IV-14. Exploded view of Model 1240 motor (prior to high-temperature test).

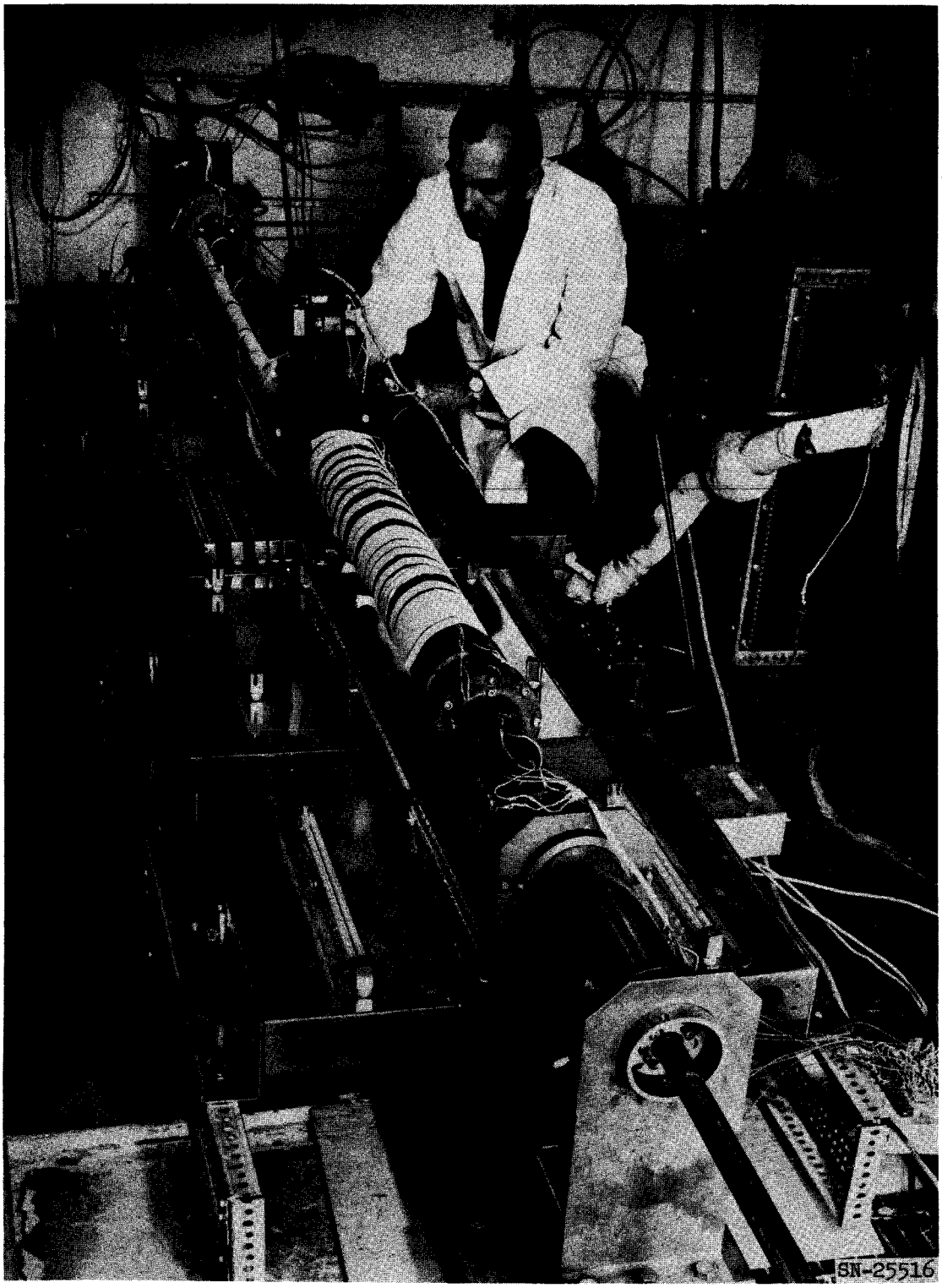

Fig. IV-15. Model 1240 actuator system being prepared for high-temperature test.

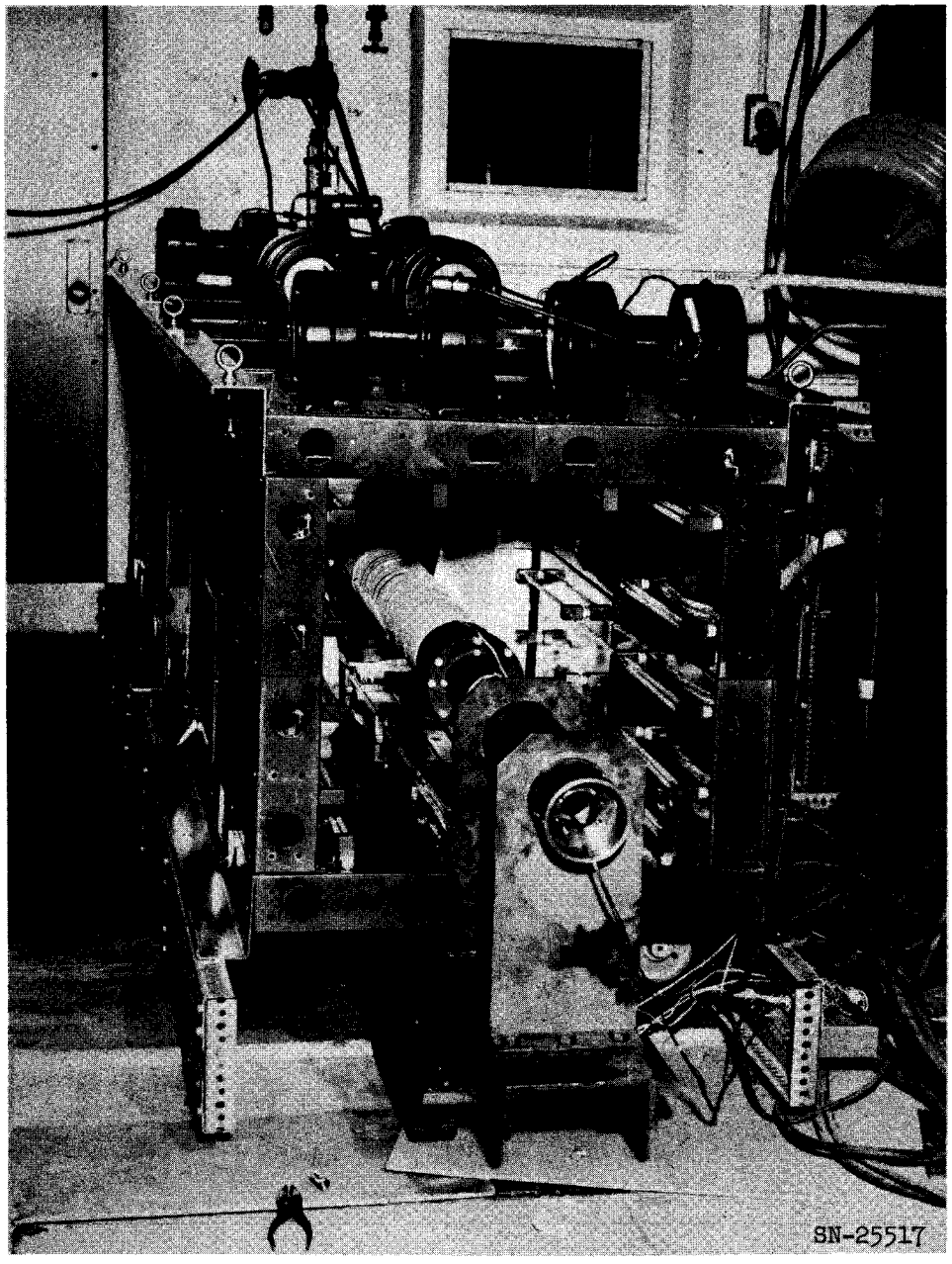

Fig. IV-16. Model 1240 actuator system in quartz-lamp oven ready for high-temperature test.

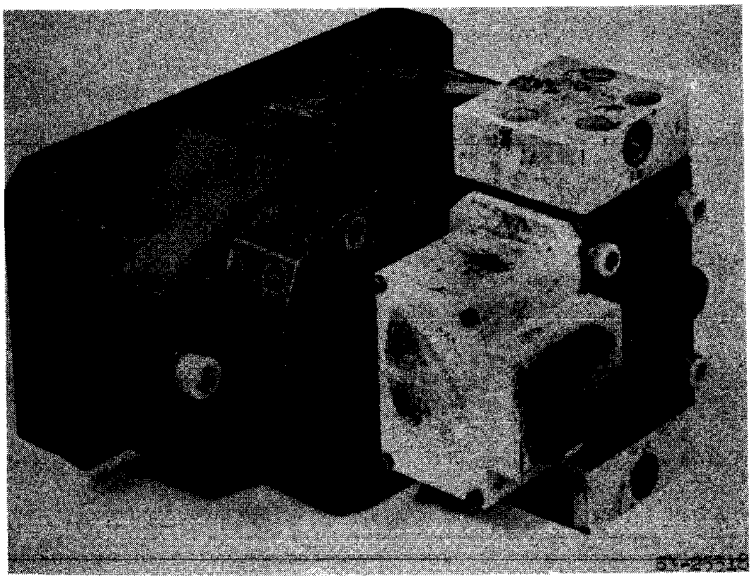

Fig. IV-17. Model 1240 servo valve and motor after 1200°F test.

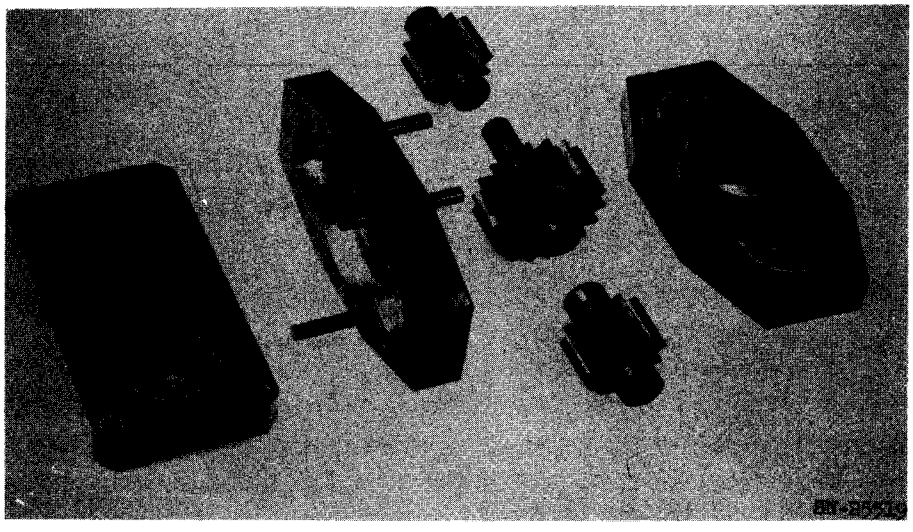

Fig. IV-18. Exploded view of Model 1240 motor after 1200°F test.

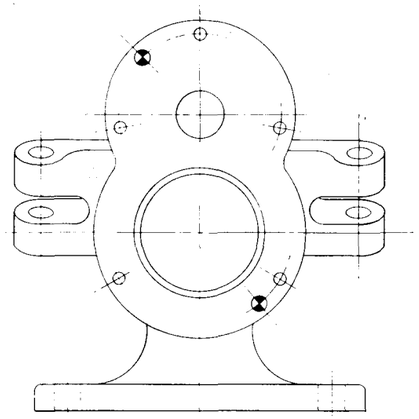

SECTION B-B
WITH ALL MATING PARTS REMOVED

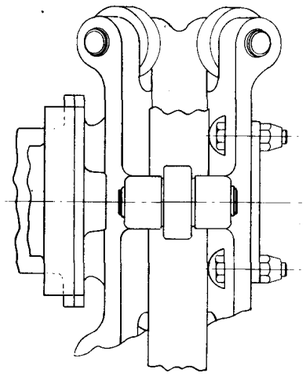

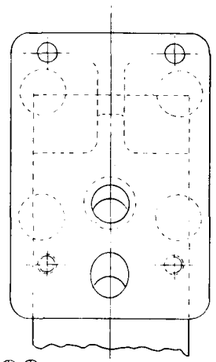

VIEW C-C
CONTROL VALVE MOUNTING FLANGE

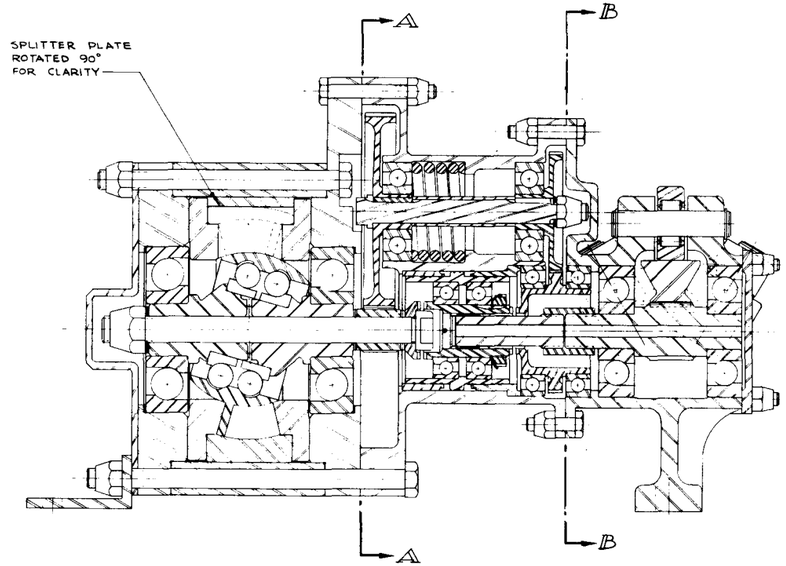

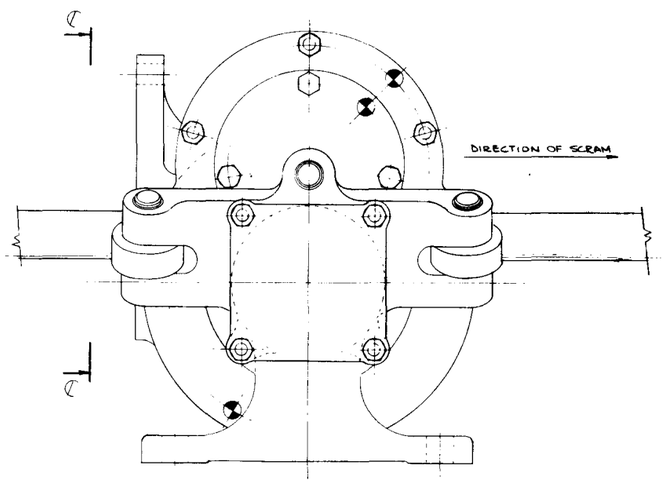

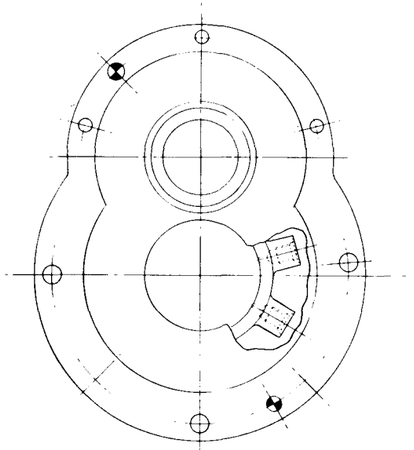

SECTION A-A
WITH ALL MATING PARTS REMOVED

MUL-12964
Rev. 8/2/61

Fig. IV-19. Nutating-disk motor of RAHS high-temperature actuator development.

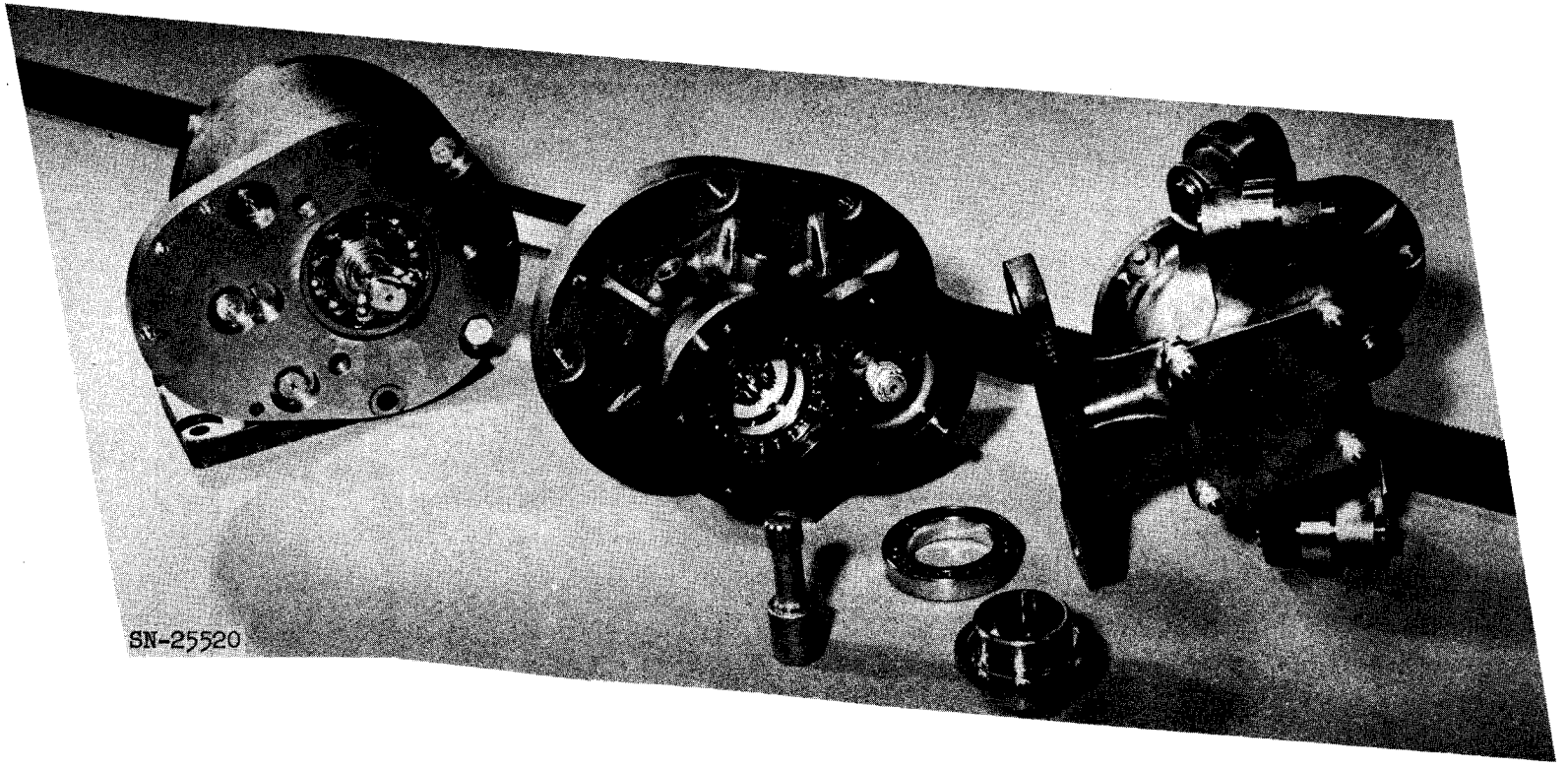

Fig. IV-20. Major components of high-speed nutating-disk motor (left-hand view).

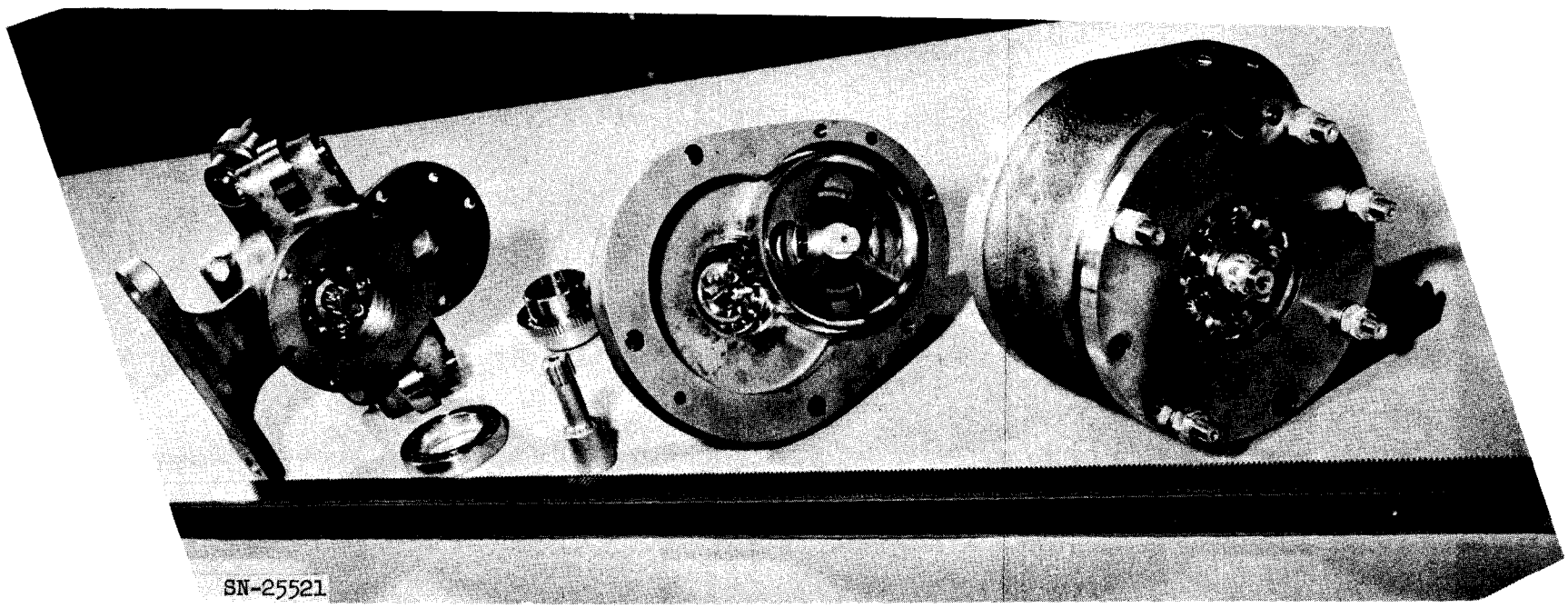

Fig. IV-21. Major components of high-speed nutating-disk motor (right-hand view).

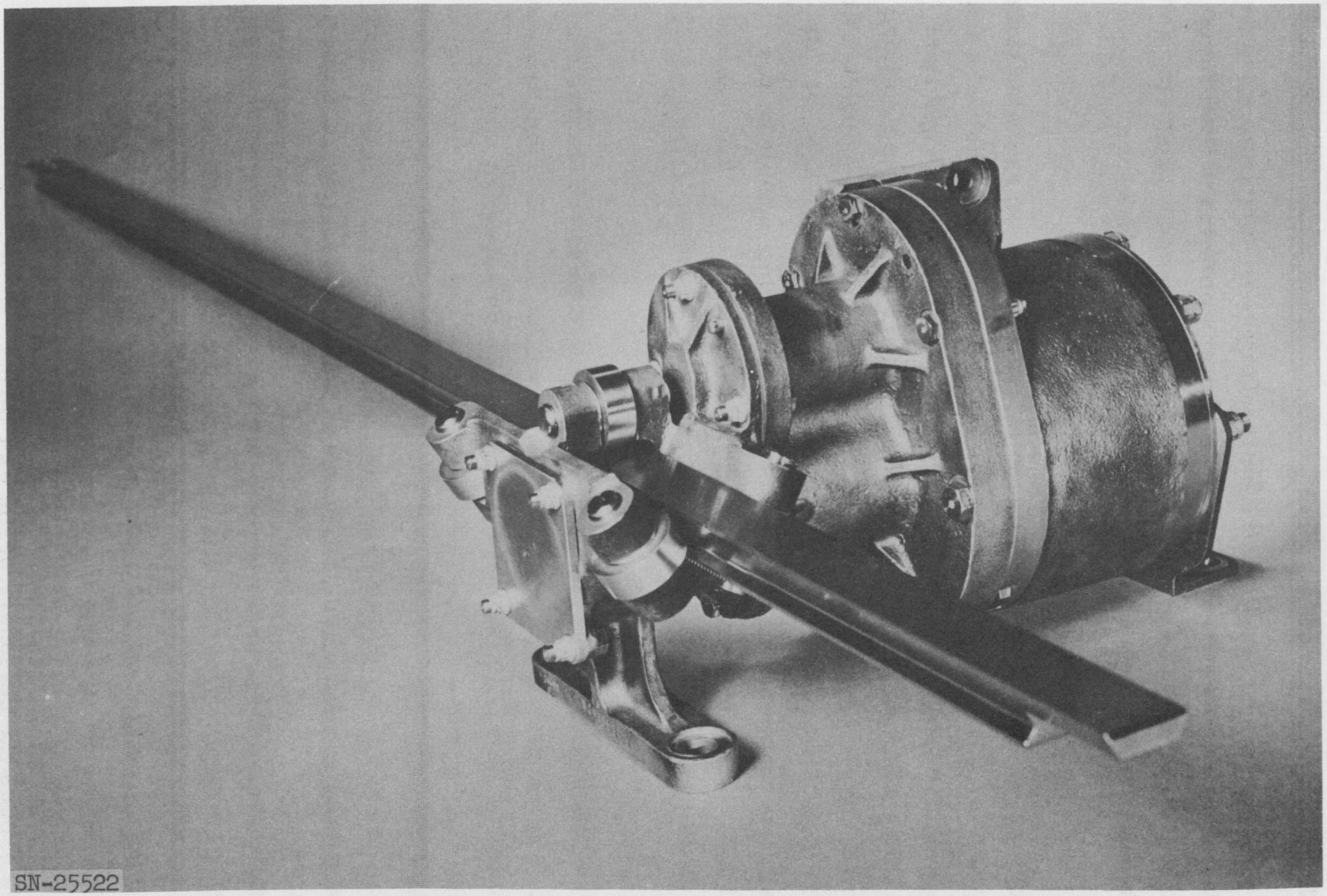

Fig. IV-22. RAHS actuator assembly shown in bread-board version.

SECTION III. ENGINEERING

DUCT MATERIAL EVALUATION

It has been decided to fabricate the entire Tory II-C duct from a single material, Hastelloy C. This decision was based on the philosophy that if one material were used we could undertake a material development program, and thus the fabrication technology would be applicable to the entire job.

MOBILE SUPPORT SYSTEM

The vehicle and the trucks for the mobile support system are soon to be released for fabrication. The main duct support structure has received a number of redesigns in an attempt to satisfy opposing criteria, i.e., rigidity to prevent vibrations and flexibility to permit thermal growth while maintaining axial symmetry. It is felt that the present flange design is stiff enough to eliminate eccentricities. Work is in progress on a retractable duct support. It appears feasible to combine this requirement with fixturing capable of permitting axial rotation of the duct without removal from the car. The vehicle brakes have been approved and are being fabricated.

HORNING

Scale models (1/24th and 1/48th) of the Tory II-C test vehicle ducting have been operated under flow conditions similar to the Tory II-C operational range. An acoustic horning has been experienced which appears to be quite different from that noticed with the Tory II-A vehicle and model. For the Tory II-C model a high-frequency (about 1500 cps) acoustic pure tone occurs under flow conditions for which the nozzle is choked. The horning persists under all flow conditions for which the nozzle is choked (e.g., P_{t4} 220 psi, the Tory II-C design point). No subsonic resonance has been experienced. In the Tory II-A system, the noise is entirely associated with the exit nozzle; in the Tory II-C it appears that the noise is generated in the external flow field. This acoustic resonance is sensitive to flow conditions in the immediate vicinity of the nozzle throat. Vanes external to the nozzle and a 1/8-in. rod transverse to the flow located from zero to four diameters downstream of the nozzle eliminate horning. Horning was also eliminated by drilling several "bleed" holes around the periphery of the exit throat. Polyurethene sheet cemented in the diverging portion also eliminated horning.

REACTOR DESIGN

Figure IV-23 (a, b, c, and d) is an assembly drawing of the Tory II-C reactor. Procurement of all major structural components is proceeding on the basis of this design. The general features of the reactor were described in a previous Pluto Quarterly Report.

A change in the basic unit cell size has resulted in a more favorable base block arrangement and front support grid design. The basic unit cell cross section consists of 37 groups of 7 fuel elements each, for a total of 259 fuel elements. The grouping is hexagonal, with the central seven tubes removed to make a passage for the tie rod. The 12 fuel elements surrounding the tie rod are replaced by unfueled tubes which run cool to provide a thermal shield. The transition from each group of seven fuel-element holes to one large hole in the base block is accomplished by using two BeO inserts. The periphery of the two inserts exactly replaces the periphery of a cluster of 7 tubes. The upstream insert continues the seven flow passages and feeds them through a funneling arrangement into one large hole in the downstream insert. This hole matches the base block hole.

One of the main reasons for having large holes in the base blocks is that coating application is simpler, thus the coated part is more reliable. However, exit air from the side reflector is sufficiently cool to make small holes feasible from the standpoint of coating integrity. For this reason the reflector tubes are brought down to the base block and exhausted through separate small holes.

A major change was made in the front support grid design. With the unit cell arrangement described above, it is possible to use a series of straight beams to collect the upstream end of the tie rods. Each beam will be made from a 2-inch-thick plate of Hastelloy C placed on edge and drilled for cooling flow passage. Ends of each beam will be fitted into a continuous ring where the load transfer is accomplished, without reliance on welded or bolted fastening. Stresses and deflections in this type of structure can be predicted accurately.

TIE RODS

Tubing Fabrication Development

Several different fabrication methods were evaluated during the past six months. The purpose was to establish vendors that can manufacture usable Hastelloy R-235 and René 41 thin-wall small- and large-diameter tubing.

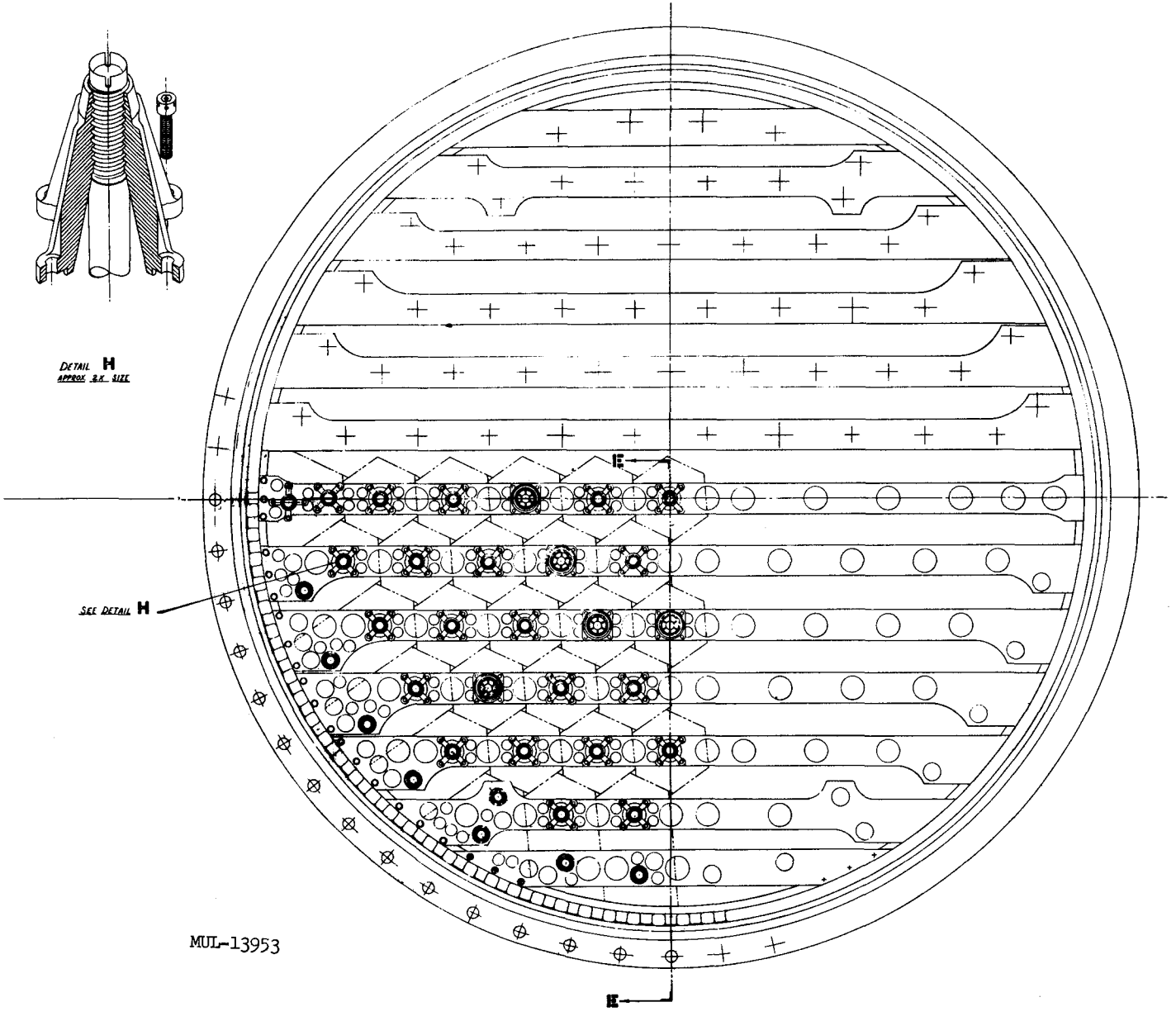

Fig. IV-23a. Reactor assembly.

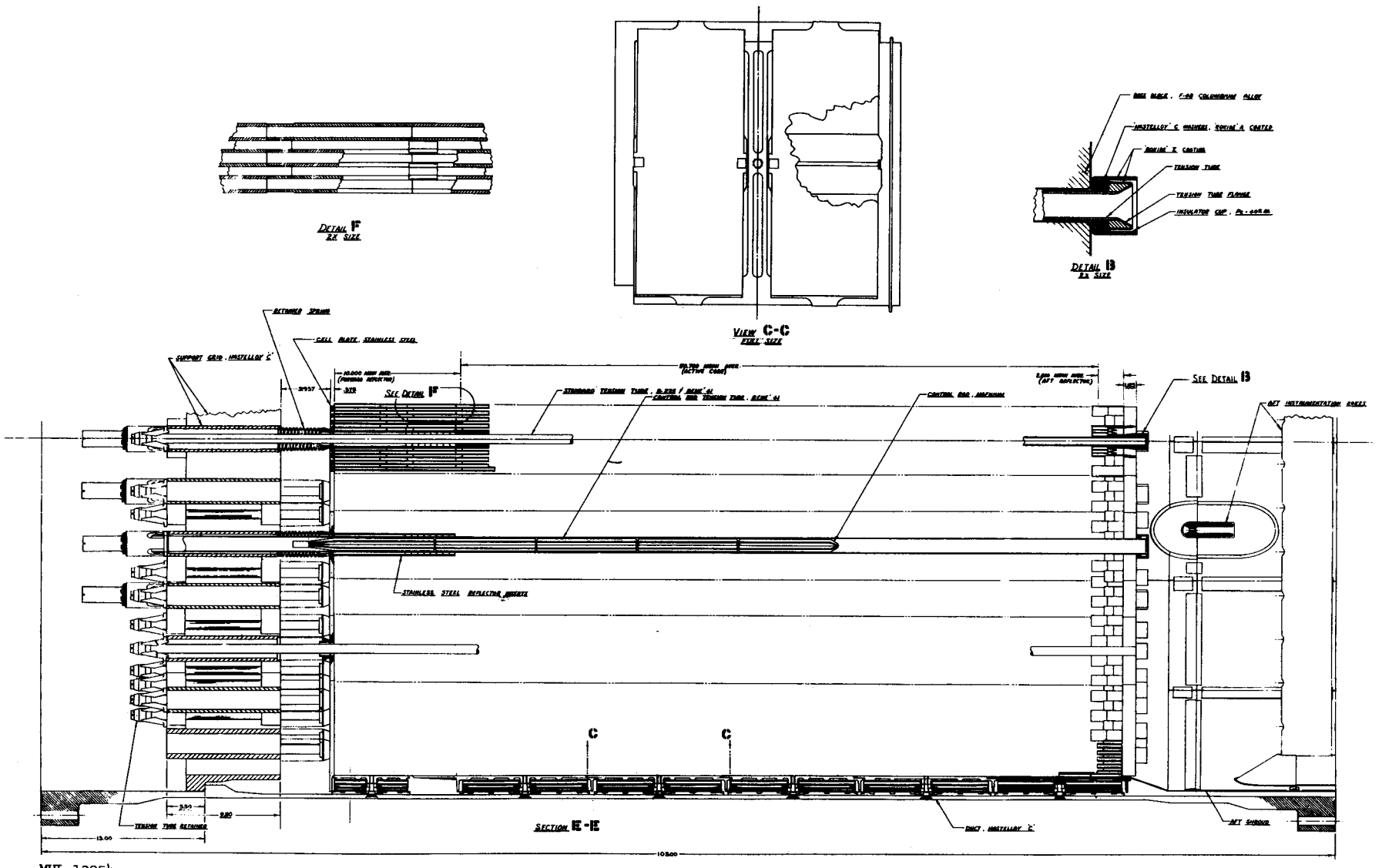

MUL-13954

Fig. IV-23b. Reactor assembly.

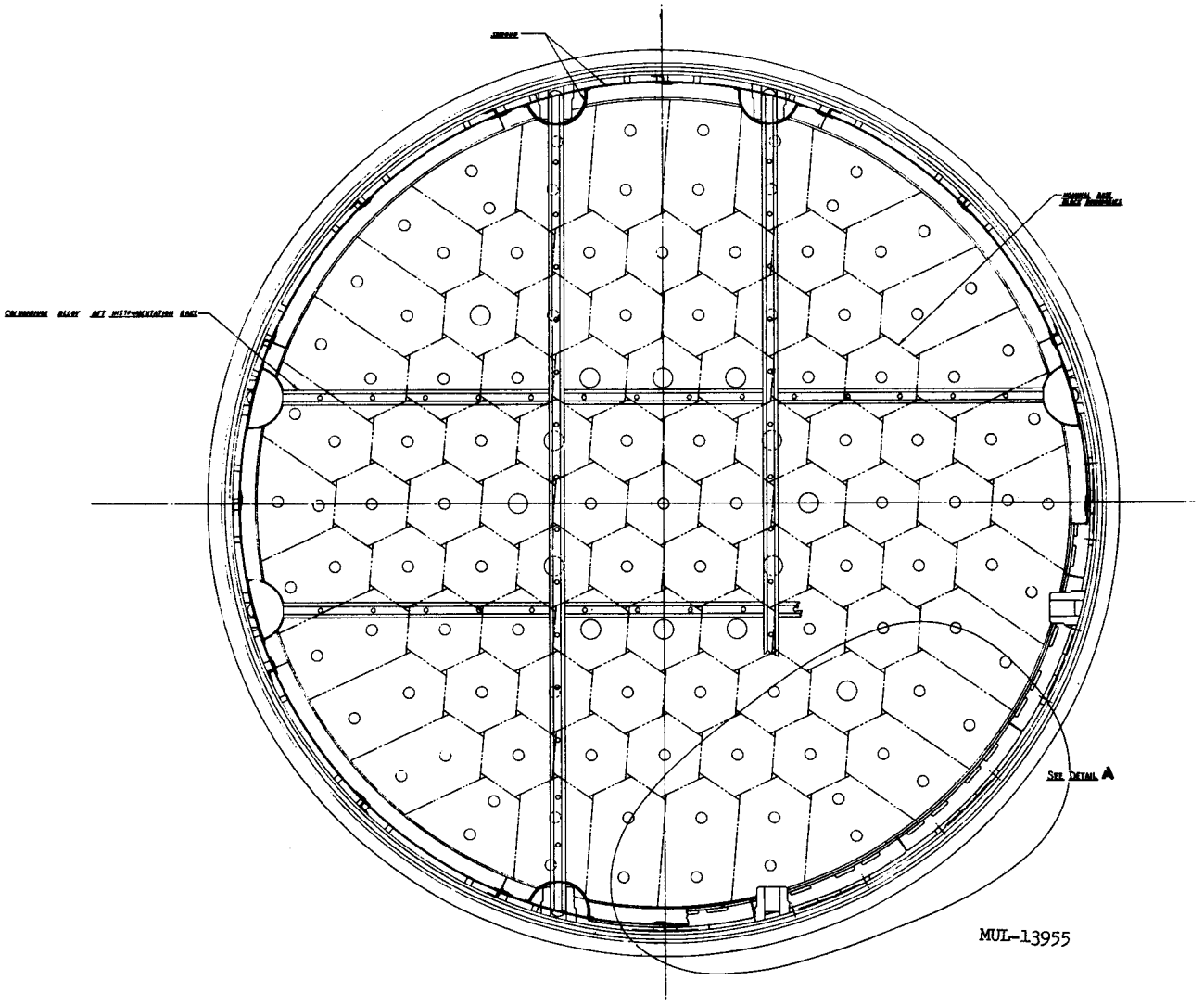

Fig. IV-23c. Reactor assembly.

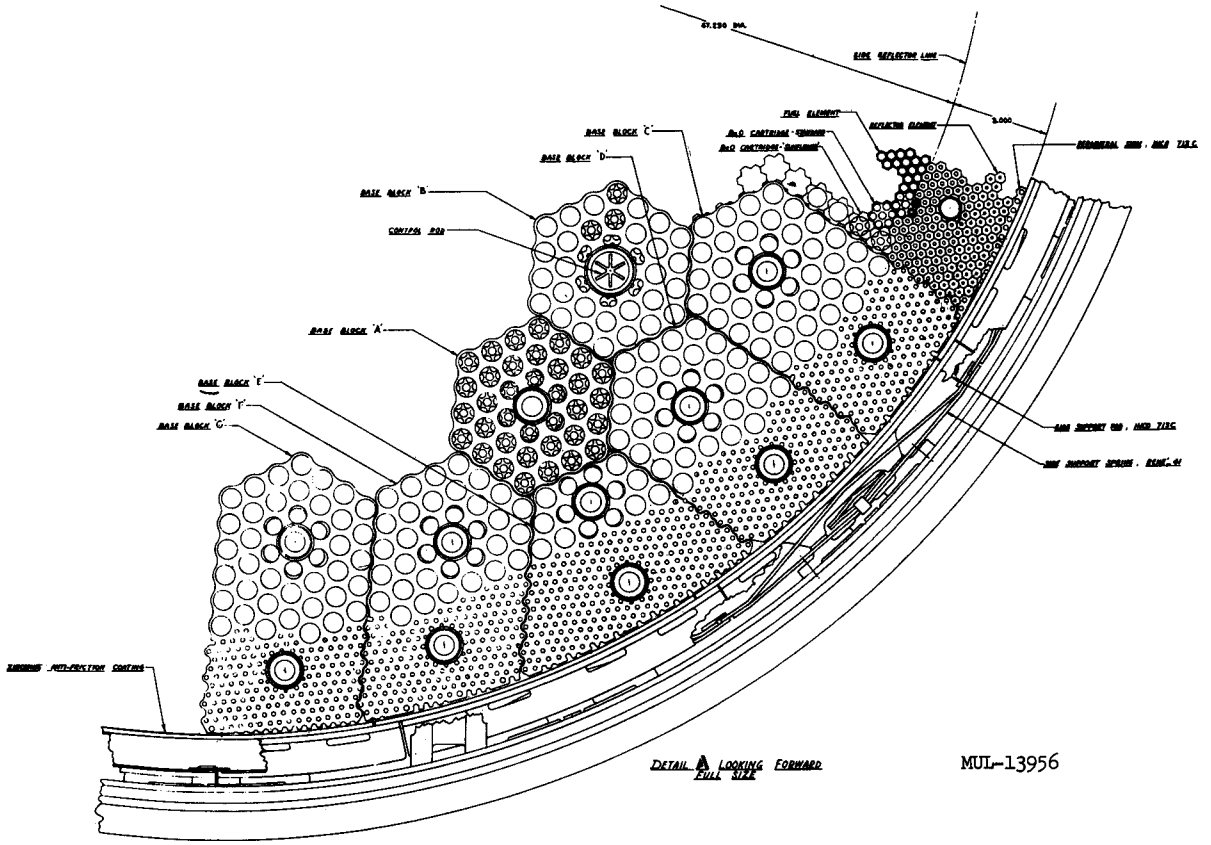

Fig. IV-23d. Reactor assembly.

Results have been encouraging, and it has been shown that crack-free tubing can be made, provided proper annealing and proper cold working are performed in each step of the process. Detailed fabrication specifications have been prepared and reactor quantities of tubing are now on order.

Figure IV-24 shows the results of an ultimate-strength tensile test on a piece of control rod tubing of 1-1/4-in. o.d. and 0.030-in. wall thickness. This tubing was fabricated by forming the sheet metal, welding, and drawing to final size. The small amount of cold work in the weld during sizing does not cause cracking. The ultimate breaking stress in this test was 112,000 psi at 1400°F. Elongation was 9% over a 2-inch gage length.

Aft-Flange Temperature Analysis

Figure IV-25 shows the temperature distribution of the aft flange which transfers the load from the base plate to the tension tube. The zirconia insulation formerly used has been replaced by a series of aluminum-oxide-coated Hastelloy-C washers. This has solved the problem of high thermal stresses in a brittle material by use of a ceramic-coated ductile metal which can deform plastically under thermal or point-lead stresses.

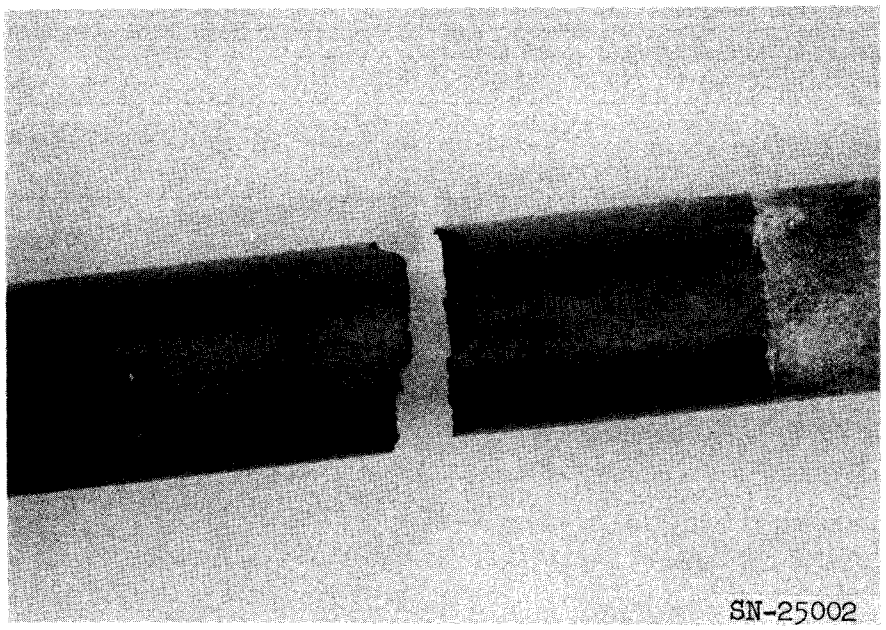

Fig. IV-24. Tensile fracture of control-rod tension tube. R-235 material in aged condition. 1-1/2-in. o.d., 0.030-in. wall thickness.

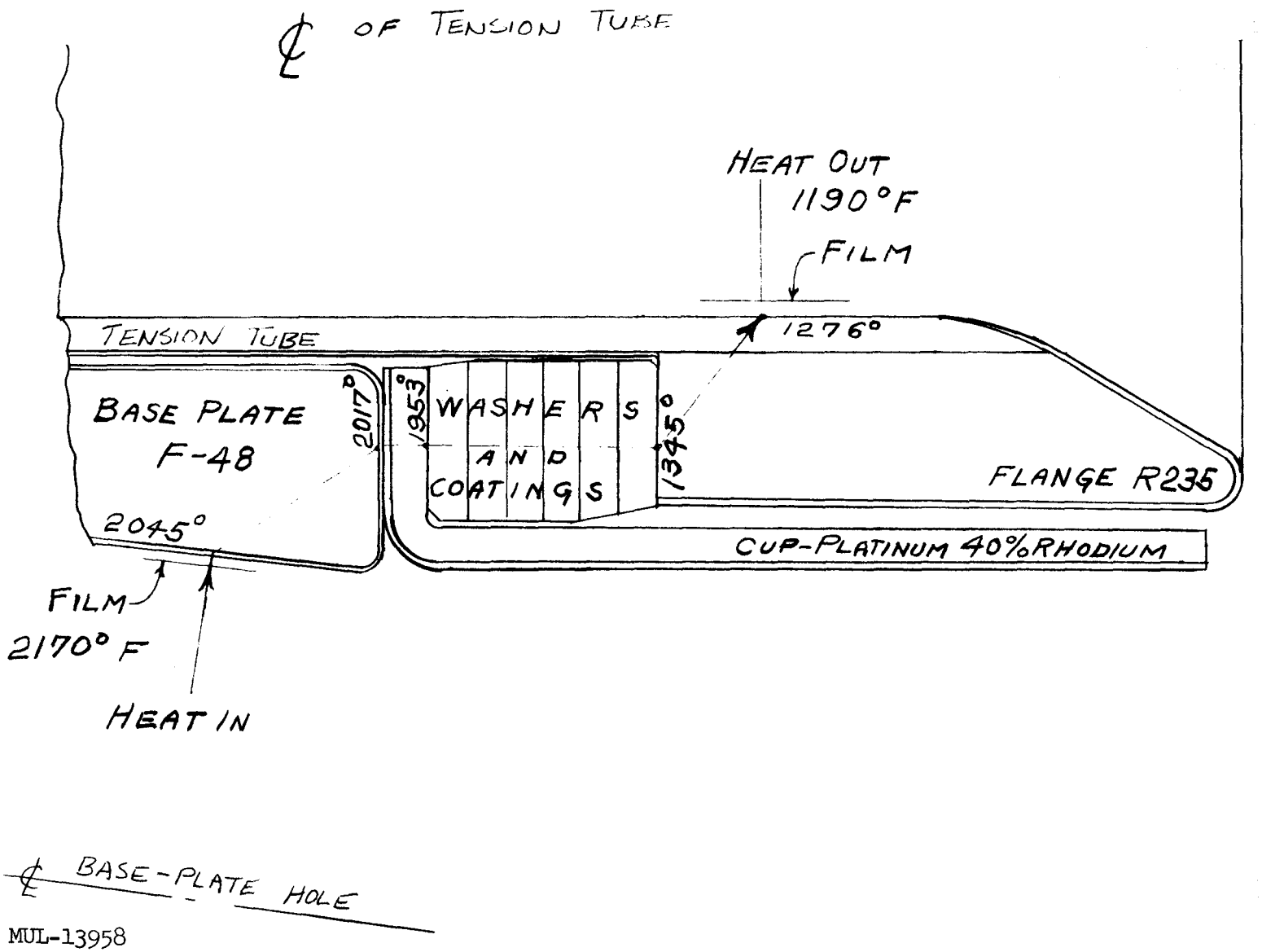

MUL-13958

Fig. IV-25. Temperature distribution of tension tube aft flange attachment.

Brazing Development

Figure IV-26 shows the results of an ultimate-strength test on the aft-end brazed joint at 1400°F. The break occurred in the tubing, not in the braze, thus obtaining 100% joint efficiency. This is typical of all tests which have been performed on this joint detail. The joining alloy is vendor's J-8100 brazed at 2150°F in vacuum for five minutes. Two subcontractors are brazing test assemblies to determine optimum setups, times, and temperatures. Joint evaluation utilizes ultrasonic, x-ray, fluorescent dye-penetrant, and metallographic techniques.

Figure IV-27 shows a 100 × photomicrograph of a typical braze using this alloy.

Figure IV-28 shows the LRL vacuum-brazing equipment used in initial development and for brazing test assemblies.

Front Attachment Design

The primary requirements of the fitting attaching the tie rod to the forward support beam are adequate strength and ease of remote disassembly. The resulting design is based on aerotype threads cast in Inconel 713C. This provides for assembly simplicity and gives a low stress-concentration factor of 1.5 in the thread roots.

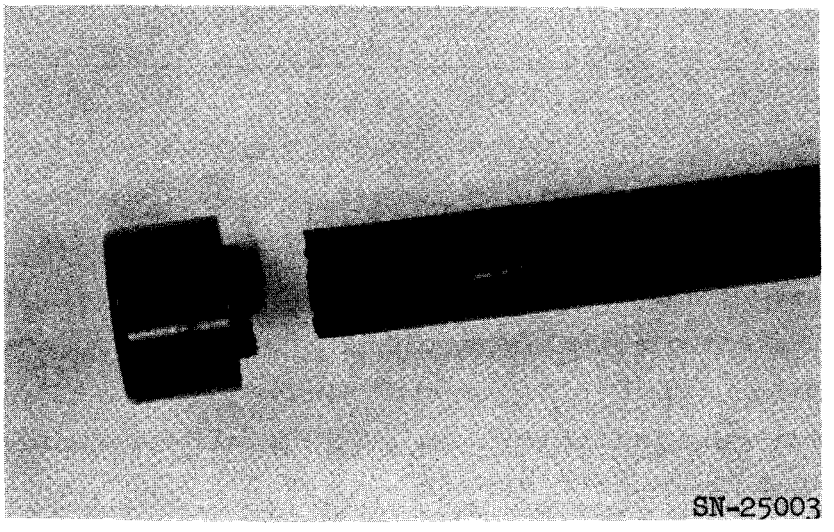

Fig. IV-26. Ultimate strength test of tension tube aft brazed joint at 1400°F. R-235 tubing and flange. J-8100 brazing alloy.

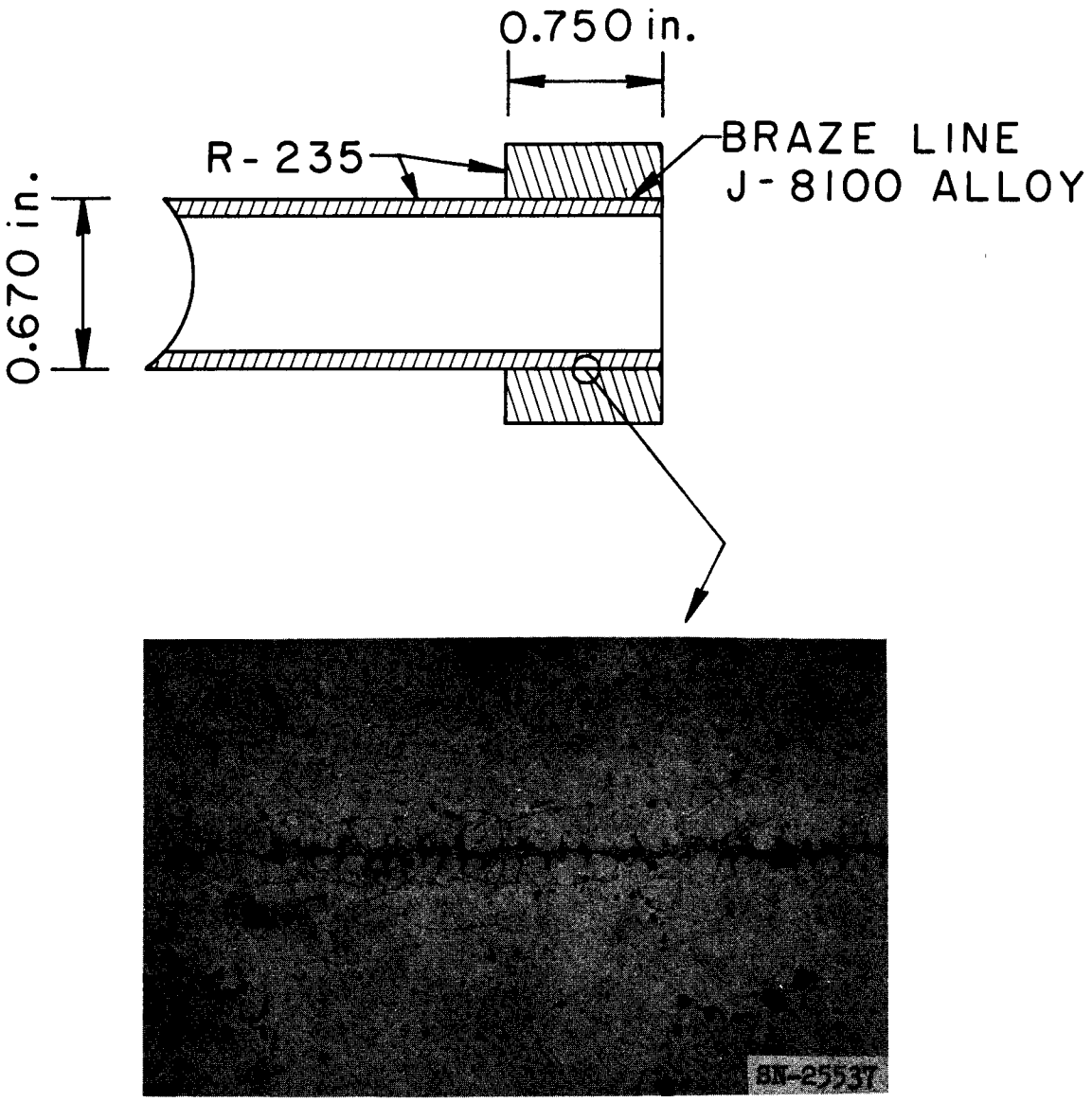

Fig. IV-27. Photomicrograph of tension tube aft brazed joint. Tube and flange are R-235. Brazing alloy is J-8100.

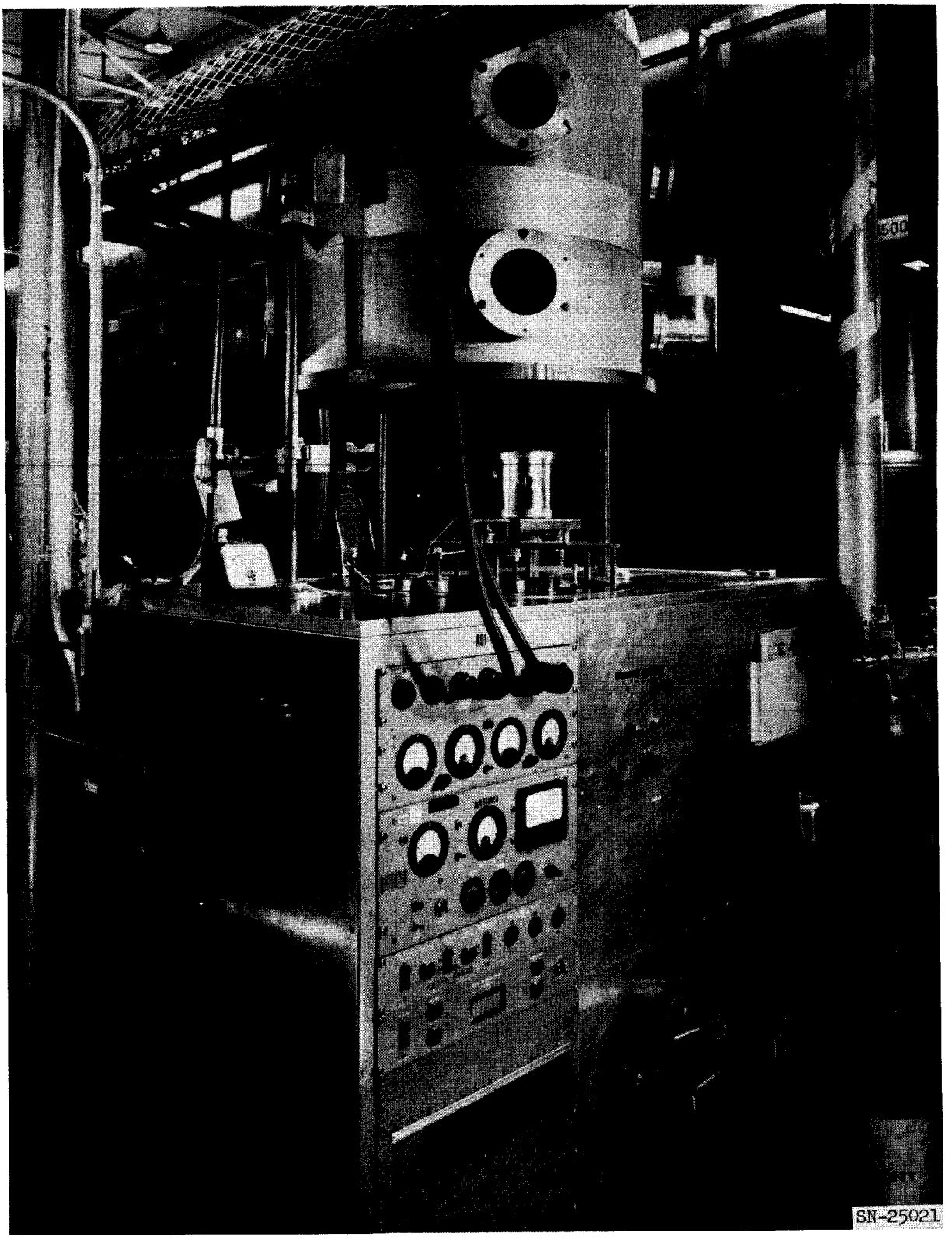

Fig. IV-28. Vacuum-brazing equipment at LRL.

Figure IV-29 shows the front support fastener attached to the standard tie rod. The guaranteed minimum ductility of the as-cast material is 5%.

R-235 Creep Testing

To confirm LRL test data, a subcontract for creep-testing R-235 has been carried out. The data have been plotted on Larsen-Miller coordinates and are shown in Fig. IV-30.

CONTROL RODS

Oxidation of Hafnium

Oxidation studies were conducted on hafnium in air at elevated temperatures and pressures in the equipment shown in Fig. IV-31. Atmospheric oxidation testing was conducted in a Marshall furnace.

Before testing the specimens were ultrasonically cleaned and pickled in a $HF-HNO_3 - H_2O$ bath to give a uniform surface. They were placed in holders of either alumina, Hastelloy R-235 or René 41, then brought up to temperature and pressure as shown in Table IV-11, and held for 3 hours.

The oxidized specimens were evaluated as follows:

1. Weight gain per unit surface area was computed for each specimen to determine the amount of oxidation of the hafnium under each environmental condition.
2. Superficial hardness tests were performed to determine if the surface hardness was dependent on the amount of oxidation.
3. Room-temperature bend tests were performed on the specimens after exposure to determine the effect of oxidation on ductility. The specimens were placed in a die and bent around a radius of 3 times the specimen thickness. The crosshead movement rate was 0.06-inch per minute until the specimen failed or until the included bend angle of the specimen was less than 90°.

The results of the bend test, superficial hardness test, and weight gain per unit surface area are shown in Table IV-11. Figure IV-32 is a photograph of some of the specimens. The superficial hardness tests show a random effect, or no trend, with respect to test temperature, pressure, or holder material.

From weight-gain data, it appears that above 1700°F the oxidation rate increases sharply with temperature. This may be seen from the curves

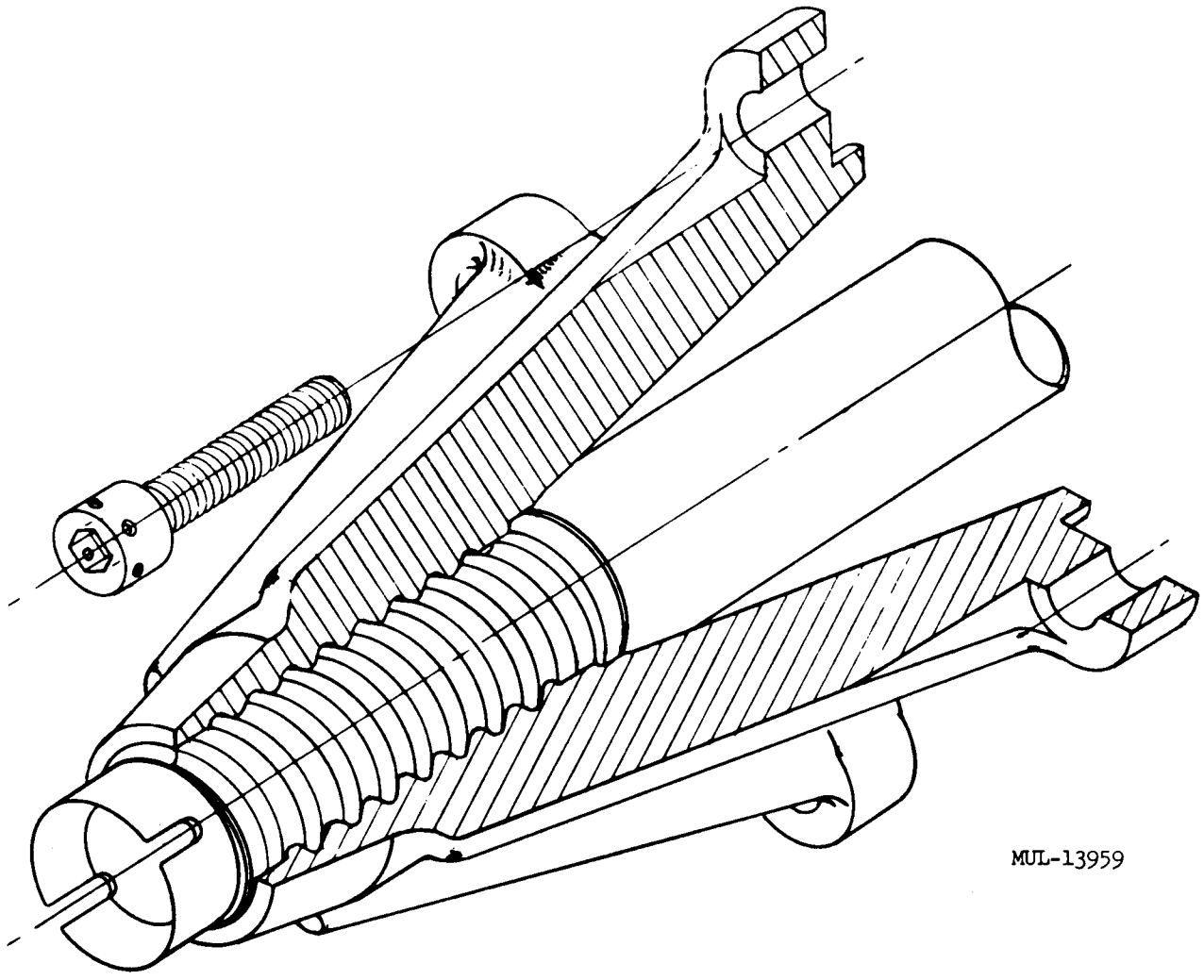

Fig. IV-29. Tension tube forward attachment.

MASTER RUPTURE CHART

Alloy HASTELLOY R235	C 0.13	Temp.	Stress	Time	Elong.	P
Test	Fe 10.20	°F	1000 PSI	Hours	%	
Heat	Cr 15.50	1200	101.2	5.72	1.3	
Vendor	Ni BAL.	1200	108.2	6.85	1.5	
Requestor	Co 0.77	1200	104.0	2.51	1.7	
Date	Mo 5.50	1200	106.4	5.85	1.4	
By	W -	1400	57.1	3.30	1.7	
	V -	1400	60 4	5 60	2.4	
Temp.	Ti 2.51	1400	61.3	4.43	1.7	
T.S.	Al 1.90	1400	65.5	4.25	1.8	
Y.S.	Mn 0.01	1600	29.0	5.84	-	
Elong.	Si 0.09	1600	31.0	9.50	1.6	
R.A.		1600	28.9	10.00	3.3	
Charpy		1600	44.6	10.00	2.2	

Treatment: SOLUTION TREAT @ 2025°F 45 min Remarks:
AIR COOL, AGE @ 1400°F 2 hrs 15 min, AIR COOL

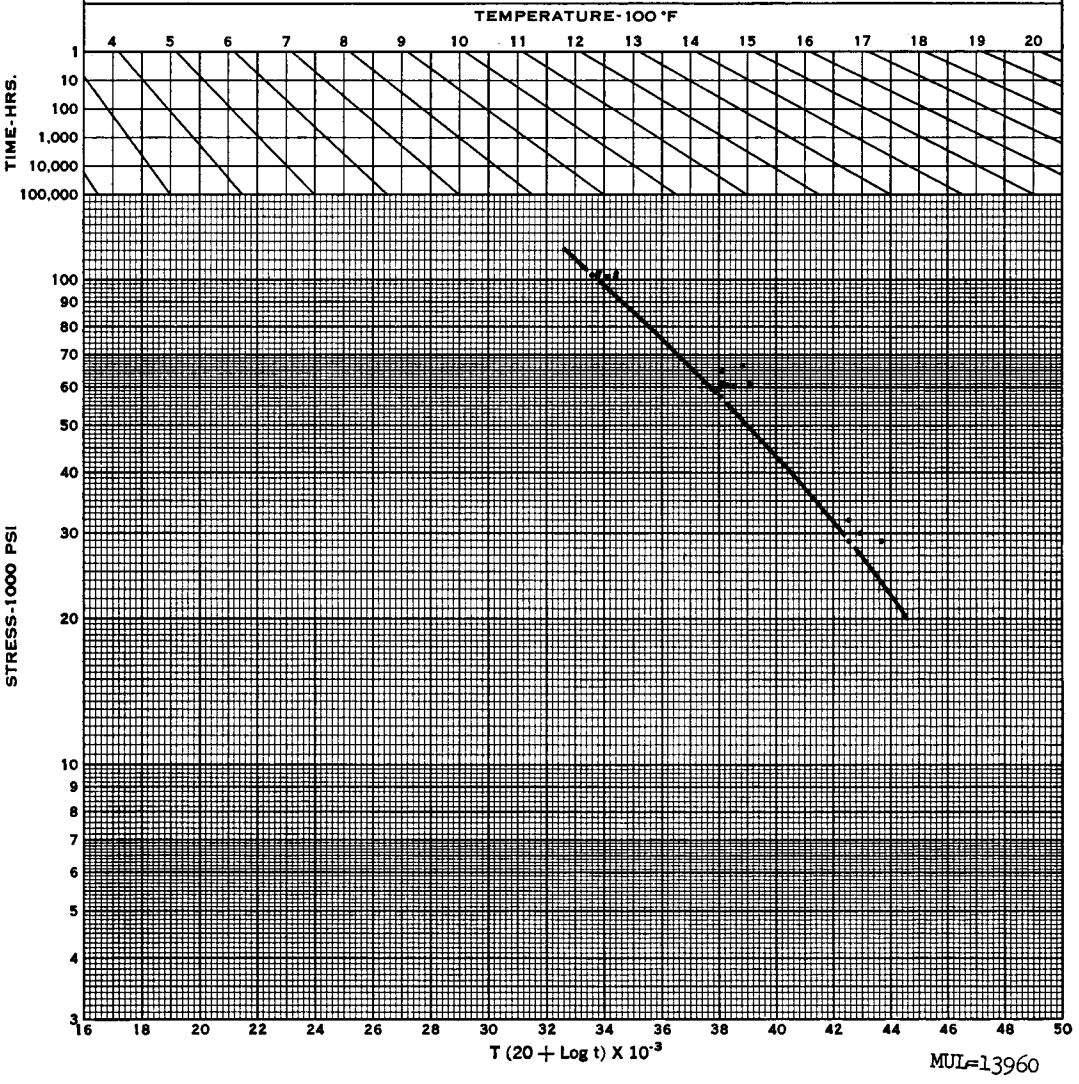

Fig. IV-30. Creep rupture of R-235.

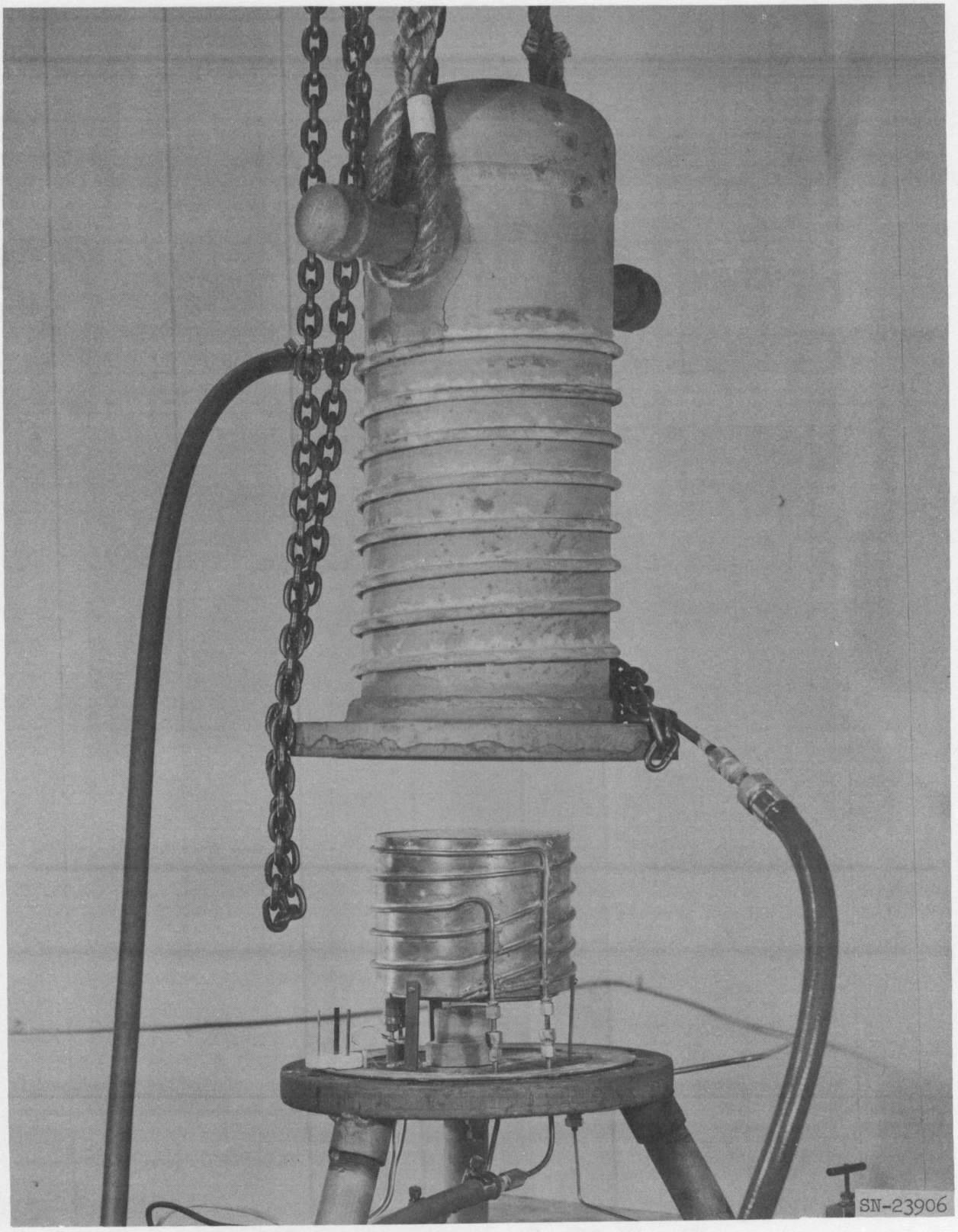

Fig. IV-31. High-pressure furnace facility.

Table IV-11. Results of Hafnium Oxidation Tests.

Specimen No.	Test temperature °F	Test pressure	Holder material	Test facility	Weight gain unit surface oven milligrams/cm^2	Superficial hardness	Bend breaking load	Bend angle
1	NT	NT	NT	NT	NT	88.2	N	84°
2	1500	1 atmos	Al_2O_3	M	0.73	86.0	N	88.5°
3	1500	200 psi	Al_2O_3	P	1.53	88.5	N	86.5°
4	1600	1 atmos	Al_2O_3	M	1.21	88.2	N	88
5	1700	1 atmos	Al_2O_3	M	1.75	87.8	N	88.5
6	1500	200 psi	R-235	P	1.31	88.0	N	85
7	1750	200 psi	R-235	P	11.2	76.9	8.4	173
8	1500	200 psi	René 41	P	0.87	88.2	N	87
9	1750	200 psi	René 41	P	5.14	91.7	21.0	167.5
10	1500	200 psi	Al_2O_3	P	1.30	87.5	N	86.5
11	1500	200 psi	Al_2O_3	P	1.52	89.0	N	86.5
12	1500	1 atmos	Al_2O_3	P	1.22	88.0	132.8	108
13	1800	1 atmos	Al_2O_3	M	9.80	85.0	27.6	173.5
14	1800	1 atmos	Al_2O_3	M	5.15	93.0	24.4	175

NT - not tested

N - did not break

M - marshall furnace

P - pressure furnace

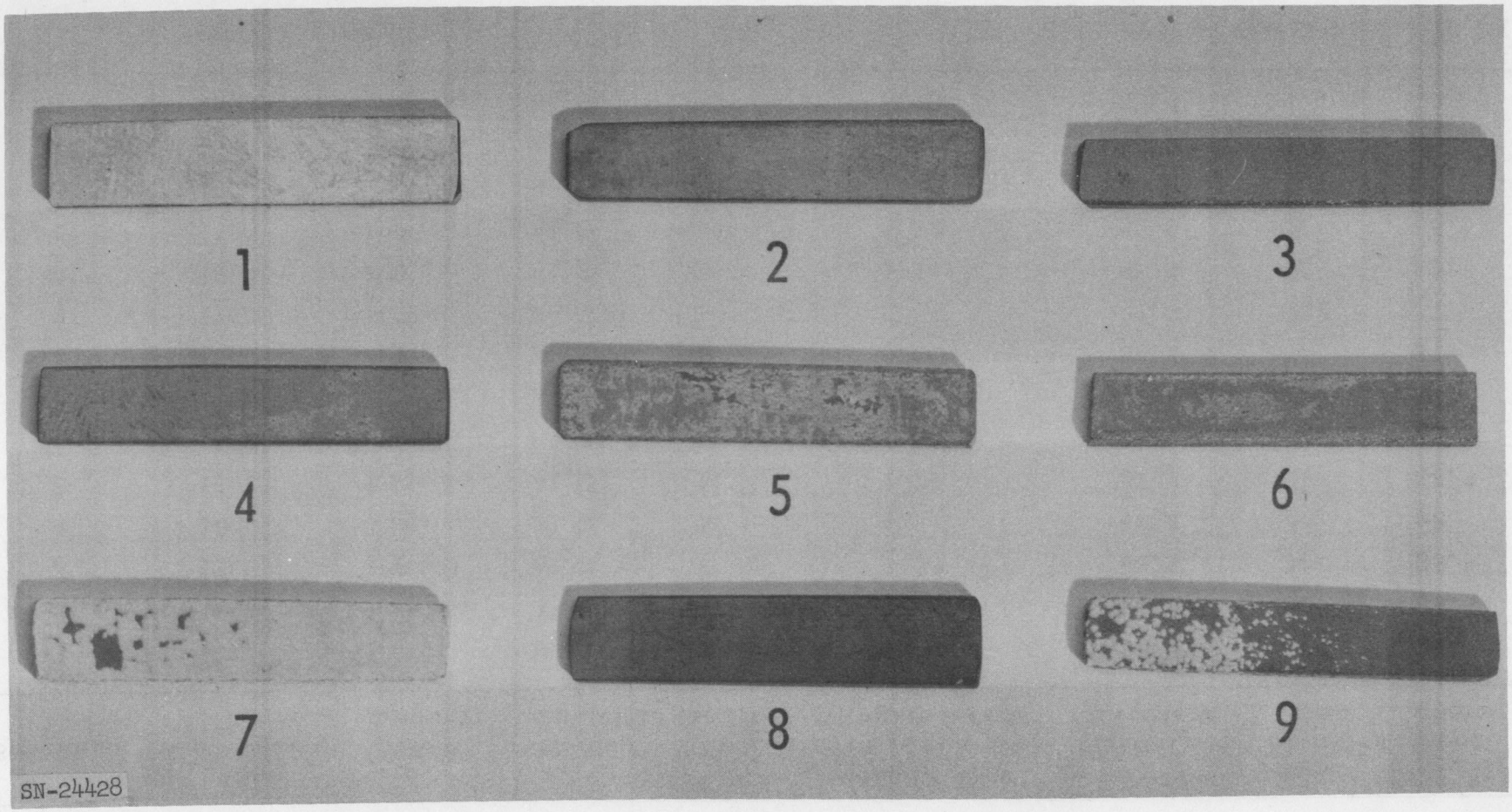

Fig. IV-32. Hafnium specimens after oxidation exposure. Refer to Table IV-2 for details.

of Fig. IV-33. Increased pressure increases oxidation rates somewhat, although there are not enough data here to reveal a quantitative effect. There was no marked increase in oxidation rate by using Hastelloy R-235 and René 41 holders over using alumina holders at 1500°F; however, above 1700°F the alloy holders seem to increase the oxidation rate.

BASE PLATES

Fabrication

Two machining blanks which meet LRL material specifications have been produced by a supplier. These pieces were cross-rolled from the extruded bar pictured in the previous Pluto Quarterly Report. One step in the cross-rolling operation is seen in Fig. IV-34. Machining blanks produced by this process are shown in Fig. IV-35. A test part machined from one of the blanks is pictured in Fig. IV-36. This part will be coated and subjected to testing in a high-temperature and high-pressure flow environment.

Mechanical Properties

Tensile tests have been made on five different source pieces of wrought F-48 plate material. A description of the five source pieces is given in Table IV-12. Short-time ultimate and yield strengths, creep rupture strength, and modulus of elasticity were determined up to 2500°F. Complete results of all testing are given in Tables IV-13 through IV-21, and Figures IV-39 through IV-44. Typical test specimens, typical failures, and some of the test equipment used to obtain these data are pictured in Figures IV-45 through IV-50.

Room-temperature ductility of material from source piece No. 1 is shown in Fig. IV-37. The three small bend bars pictured here were taken in the same plane and as close together as possible. As noted in Table IV-12, this material has been extruded 4:1 from the cast billet, followed by a 2200°F stress relief. Greater ductility can be expected after more work is put into the metal by cross-rolling.

One attempt was made to press-forge a cast billet of F-48. Forging direction was parallel to the billet axis. A reduction of 44% was accomplished in the initial pressing, however, an intolerable amount of edge cracking occurred. Figure IV-51 shows the billet after upset. The cracks ran in to a depth of 1/4 in. and caused a weight loss of 22% on clean-up machining.

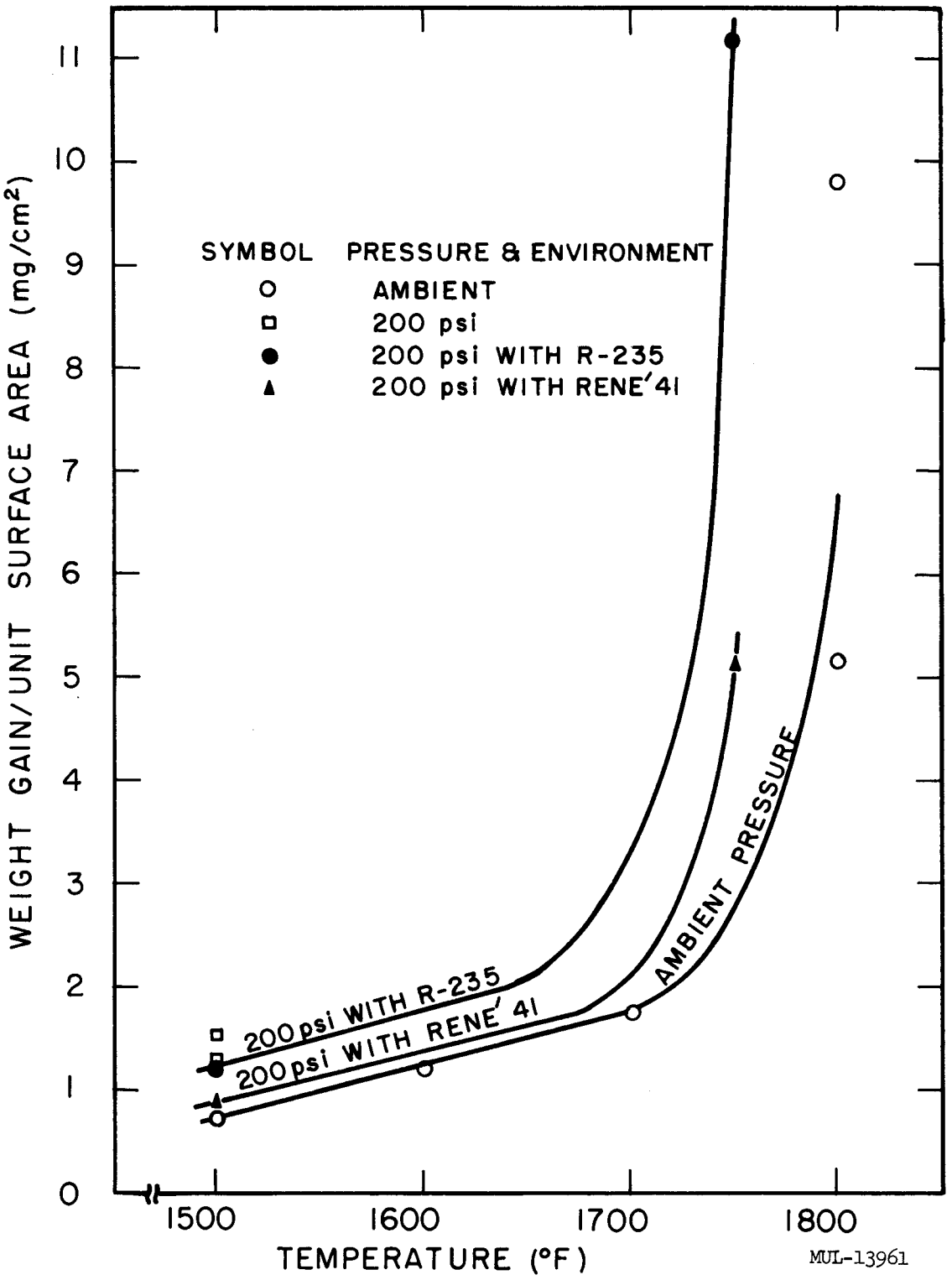

Fig. IV-33. Weight gain per unit surface area for hafnium held at temperature for three hours.

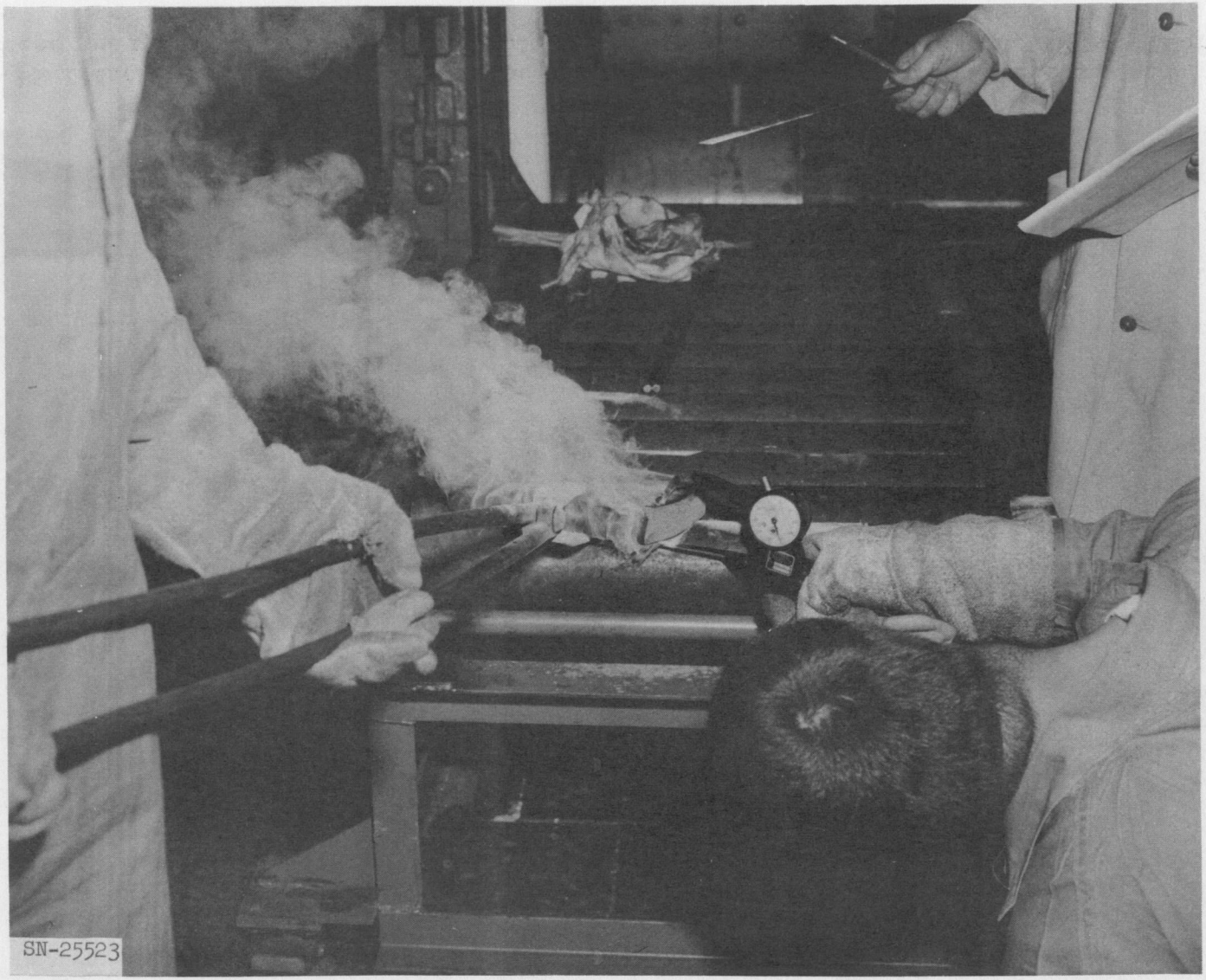

Fig. IV-34. Cross-rolling extruded bar to produce plates shown in Fig. IV-35.

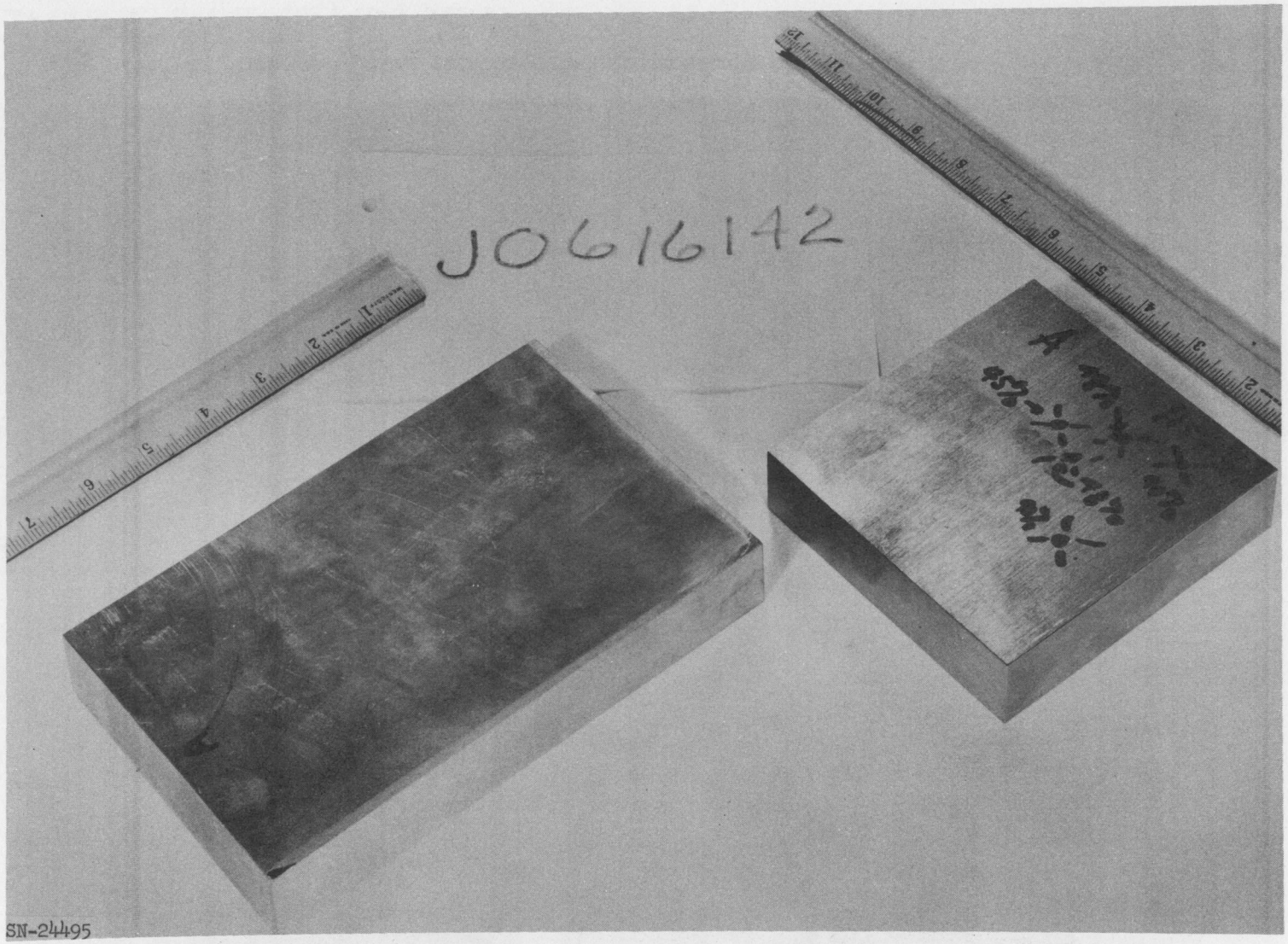

Fig. IV-35. Machining blanks of F-48 produced by the same process as for source piece No. 3 of Table IV-12. Sizes are typical for Tory II-C base plates. Material meets LRL specification for Tory II-C application.

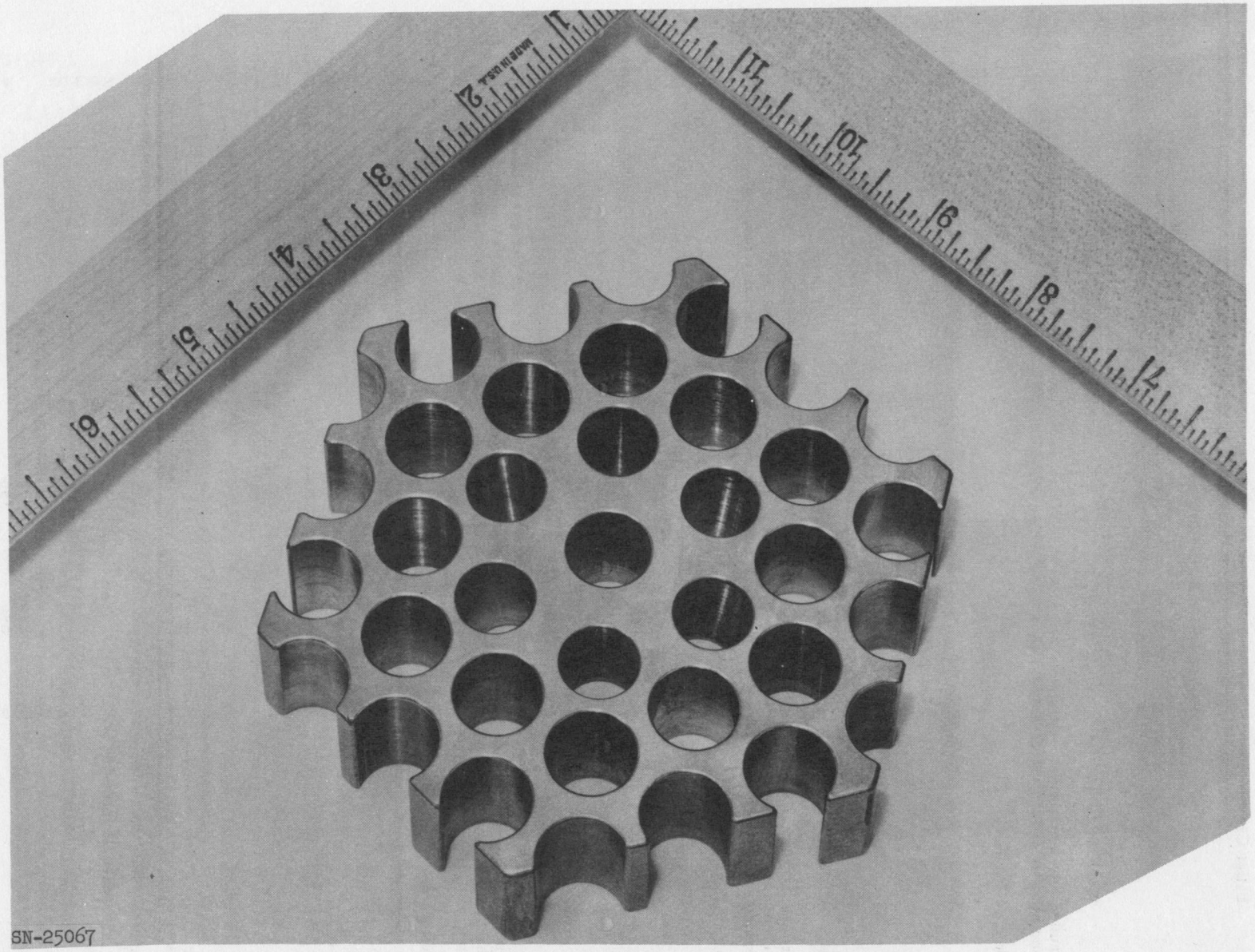

Fig. IV-36. Base plate for Tory II-C unit cell, test-machined from the small blank of Fig. IV-35. Similar in detail to final Tory II-C parts.

Table IV-12. Description of F-48 Source Pieces.

Source Piece No. 1: (see Fig. IV-37 - a, b, and c)

Billet Chemistry:

	Top	Bottom
W	15.7	15.3 w/o
Mo	5.2	5.2
Zr	0.99	1.10
O	210	150 ppm
C	443	320
N	13	57

Work History:

Extruded at approximately 4:1 reduction from a 5-in.-diameter billet. Extruded bar dimensions approximately 4 in. × 1-1/4 in. (fully rounded edges). Annealed one hour at 2200°F after extrusion.

Source Piece No. 2:

Billet Chemistry:

	Top	Bottom
W	15.6	15.7 w/o
Mo	4.6	4.8
Zr	0.97	0.99
O	180	270 ppm
C	320	430
N	41	85

Work History:

Extruded at approximately 3.1:1 reduction from a 5-in.-diameter billet. Extruded bar dimensions approximately 4-1/4 in. × 2-1/4 in. A piece 5-1/2-in. long was removed from the bar and press-forged by a "nibbling" operation (1-in. bite per nibble) from 2-1/4-in. thick to 1-1/4-in. thick. Annealed one hour at 2200°F after forging.

Source Piece No. 3:

Billet Chemistry:

	Top	Bottom
W	15.6	15.7 w/o
Mo	4.6	4.8
Zr	0.97	0.99
O	180	270 ppm
C	320	430
N	41	85

Work History:

A second piece 5-1/2-in. long was removed from the extruded bar described under Source Piece No. 2. This piece was cross-rolled from 2-1/4-in. thick to 1-1/4-in. thick. Rolling temperature was 2300-2500°F for each of 6 to 7 passes. Annealed one hour at 2200°F after rolling.

Source Piece No. 4:

Billet Chemistry:

From one analysis on the finished piece:

W	12.4 w/o
Mo	3.9
Zr	1.0
O	109 ppm
C	232
N	36

Work History:

Extruded at approximately 3:1 reduction from a 4-1/2-in.-diameter billet. Extruded bar dimensions approximately 3 in. × 1-1/2 in. Bar was press-forged from 1-1/2 in. down to 1-1/8-in. thickness as it was cooling down from the extrusion operation.

Source Piece No. 5: (see Fig. IV-38)

Billet Chemistry:

	Top	Bottom
W	13.8	14.5 w/o
MO	4.7	4.8
Zr	0.92	0.98
O	210	190 ppm
C	290	330
N	17	37

Work History:

Extruded at 2.1:1 reduction from 3.9-in.-diameter billet. Extruded bar dimensions approximately 2-7/8 × 1-1/2 in. Bar was taken to a press forge immediately after extrusion, where half the length (29 in.) was reduced from 1-1/2 in. to 1-1/4 in. in thickness by a "nibbling" operation. Extrusion temperature 2600-2700°F. Forging temperature 2100-2400°F.

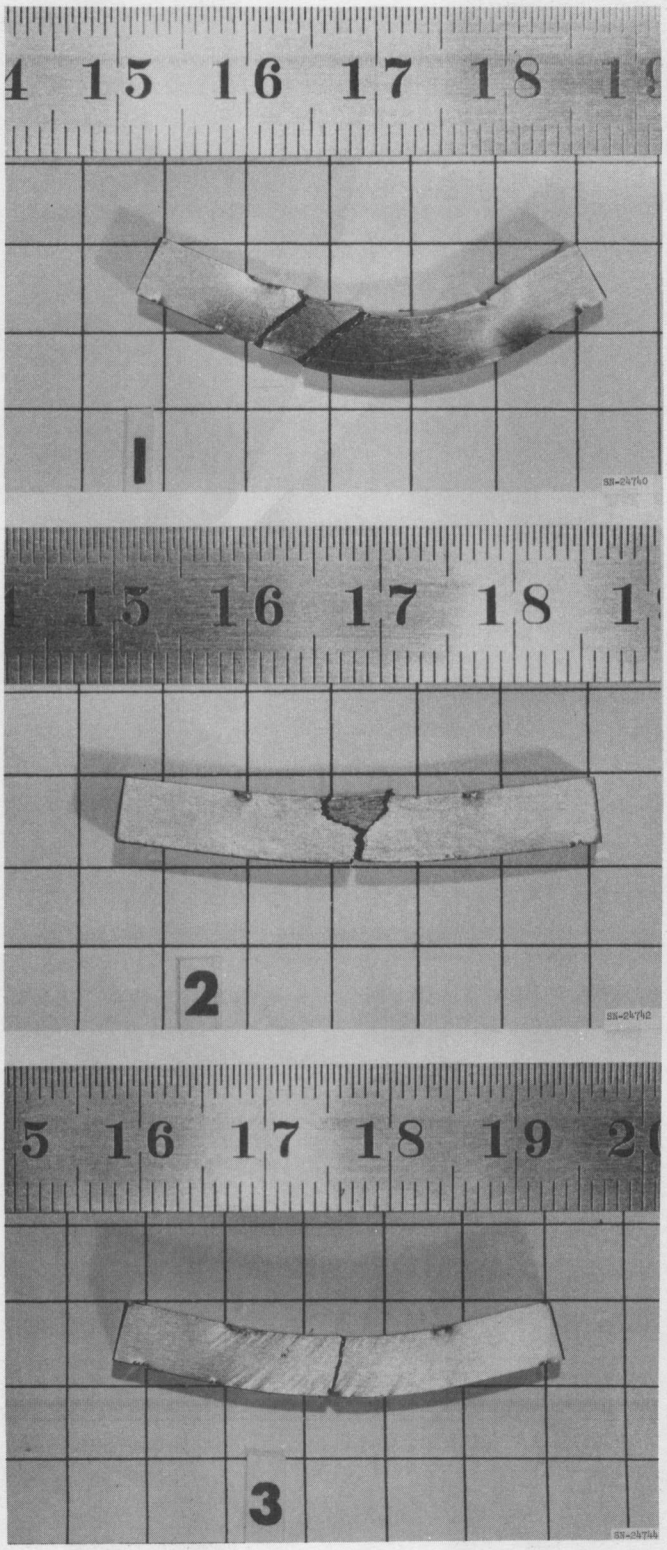

Fig. IV-37. Room-temperature bend tests of F-48 material. Removed from source piece No. 1 of Table IV-12. (1) longitudinal, (2) transverse, (3) 45°.

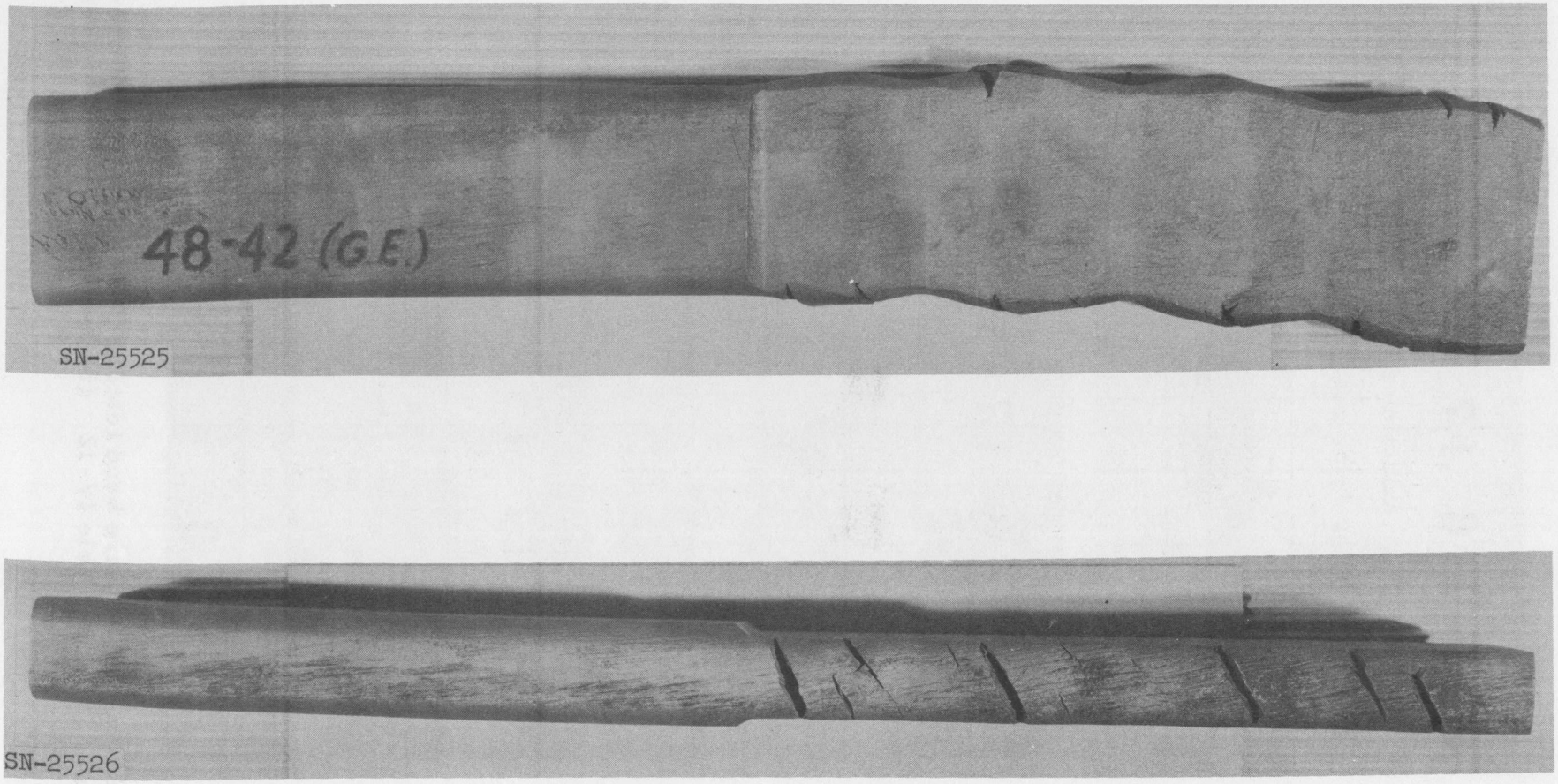

Fig. IV-38. Extruded and press-forged bar of F-48, extrusion ratio 2.9:1, extrusion temperature 2700°F. A top view of the bar is shown at the top, an edge view at the bottom.

Table IV-13. Tensile Properties of F-48 Source Piece No. 1 Obtained at LRL. (Pinned-end specimens coated for oxidation protection and tested in air. Induction heating 3-in. gage length.)

LRL specimen designation	Test temp	Testing direction relative to extrusion direction	Yield strength (ksi)			Ultimate strength (ksi)			Ultimate elongation (%)		
			0.005	0.05	0.5	0.005	0.05	0.5	0.005	0.05	0.5
37[b]	R.T.	Parallel	96.7			109.7			4.7		
38[b]	R.T.		99.5			114.5			2.0		
1[b]	R.T.	Transverse	100.0			113.8[c]			3.0		
2[b]	R.T.		102.5			117.0[d]			2.0		
3[b]	R.T.		97.0			112.2[c]			2.5		
4[b]	R.T.		96.0			110.5[c]			2.2[e]		
5[b]	R.T.		98.2			111.7[d]			1.9[e]		
6[b]	R.T.		101.0			113.3[d]			1.9[e]		
T-24	1000°F	Parallel					80.2			7.7	
T-22	1000°F						78.3			5.7	
T-2	1000°F						78.0			6.0	
T-33	1600°F	Parallel					63.5			3.3	
T-5	1600°F						66.9			3.0	
T-34	1600°F					68.3			3.0		
T-19	1600°F		59.0			64.9			2.3		
T-29	2200°F	Parallel	50.0			52.9			6.3		
T-4	2190		49.6			54.8			4.6		
T-12	2225			52.2			56.1			4.6	
T-15	2203			52.3			56.1			4.6	
T-8	2200				53.3			59.2			5.6
T-13	2198				55.0			61.2			5.6
T-10	2380°F	Parallel	38.2			40.9			7.7		
T-34	2375		42.7			45.0			9.3		
T-11	2365			43.5			46.0			8.7	
T-32	2385			48.5			51.3			4.0	
T-6	2365				42.9			48.4			7.7
T-28	2375				41.8			46.5			9.7
T-18	2490	Parallel		39.5			42.6			11.0	
T-3	2500			43.6			46.9			8.0	
T-16	2560		32.0			34.1			12.0		
T-23	2565		32.0			34.5			8.3		

[a] Strain rate, per min.
[b] Tested without coating.
[c] Strain rate = 0.015 per min.
[d] Strain rate = 0.15 per min.
[e] Broke out of gage length.

Table IV-14. Tensile Properties of F-48 Source Piece No. 1 Obtained in Three Laboratories. (Strain rate = 0.005 per min.)

Testing laboratory	Test equipment	Type of specimen	Testing direction relative to extrusion	Testing temp	Yield strength (ksi)	Ultimate strength (ksi)	Ultimate elongation (%)
LRL	Induction heating in air	Pinned end. Coated for oxidation protection 3-in. gage length.	Parallel	R. T.	96.7	109.7	4.7
					99.5	114.5	2.0
			Transverse[a]		100.0	113.8	3.0
					97.0	112.2	2.5
					96.0	110.5	2.2
			Parallel	2200	50.0	52.9	6.3
					49.6	54.8	4.6
Outside	Vacuum furnace with radiant heating	Button-head specimen 0.160-in. diam in gage length. 1-in. gage length.	Transverse	R. T.	94.4	108.0	6
					92.3	98.0	3
					86.2	90.3	2
					100.1	115.1	3
				2200	24.6	36.2	12
Outside	Vacuum furnace with electron-beam heating	Threaded-end specimen. $\frac{1}{4}$ - in. diameter in gage length. 1-in. gage length.	Parallel	R. T.	102.3	117.0	7.0
					---	90.2[b]	--
			Transverse		103.1	116.1	5.0
					101.4	115.0	3.0
					---	63.2[c]	1.0
			45°		96.2	102.6	2.0
					---	44.4[c]	--
			Parallel	2200	50.1	56.6	23.0
					41.1	45.9	23.0
			Transverse		51.5	53.2	20.0
			45°		44.6	52.6	23.0
					40.7	50.5	23.0

[a] LRL transverse specimens were tested at 0.015 per min strain rate.
[b] Specimen failed in threads.
[c] No indication of plastic yielding.

Table IV-15. Tensile Properties of F-48 Source Piece No. 2.

Testing laboratory	Testing temp (°F)	Testing direction relative to extrusion	Position of specimen in source piece	Yield strength (ksi)	Ultimate strength (ksi)	Ultimate elongation (%)
Outside	R. T.	Parallel	Top	95.8	117.0	9.0
			Bottom	89.6	103.5	9.0
		Transverse	Top	95.5	110.6	10.0
			Bottom	91.8	94.0	3.0
		45°	Top	94.5	109.2	9.0
			Bottom	81.2	91.1	3.0
	2200	Parallel	Top	36.7	43.5	16.0
			Bottom	42.6	44.6	15.0
		Transverse	Top	38.1	42.6	10.0
			Bottom	24.0	27.9	17.0
		45°	Top	42.3	53.8	16.0
			Bottom	39.3	46.7	16.0
Outside	R. T.	Parallel	-Not Recorded-	96.0	116.9	15.0
				93.0	116.9	15.0
		Transverse		98.5	114.4	7.0
				96.5	111.9	5.0
		45°		90.7	106.2	7.6
				97.9	115.5	7.0

Notes: Tests performed at outside laboratories; 1-5/8-in.-long button-head specimens with 0.160-in. diam in gage length.

Tests in vacuum using radiant heating strain rate: 0.005 per min.

Table IV-16. Tensile Properties of F-48 Source Piece No. 3.

Testing laboratory	Testing temp (°F)	Testing direction relative to extrusion	Position specimen in source piece	Yield strength (ksi)	Ultimate strength (ksi)	Ultimate elongation (%)
Outside	R. T.	Parallel	Top	89.5	107.5	8.0
			Bottom	93.9	115.2	17.0
		Transverse	Top	96.0	108.7	10.0
			Bottom	89.8	93.7	3.0
		45°	Top	91.5	99.6	8.0
			Bottom	83.9	98.9	6.0
	2200	Parallel	Top	40.6	45.1	14.0
			Bottom	43.2	48.3	25.0
		Transverse	Top	45.3	50.6	10.0
			Bottom	46.0	50.9	21.0
		45°	Top	25.8	33.7	6.0
			Bottom	47.6	49.1	16.0
Outside	R. T.	Parallel	-Not Recorded-	96.0	118.6	18.0
				97.5	122.4	12.0
		Transverse		93.0	117.9	15.0
				94.9	120.4	12.0
		45°		100.8	111.9	2.1
				97.0	116.9	11.0

Note: See table IV-15.

Table IV-17. Tensile Properties of F-48 Source Piece No. 4.

Temp (°F)	Direction rel. extrusion	0.2% Yield strength (ksi)	Ultimate strength (ksi)	Elongation (%)
R. T.	Parallel	123.2	130.5	3
		120.6	133.9	5
		117.2	126.6	2
		121.6	130.1	4
	Transverse	117.0	122.7	3
		125.2	128.3	2
		115.2	117.1	2
	45°	135.2	123.4	4
		132.1	134.6	2
		121.8	126.6	2
2200	Parallel	25.9	29.0	20
		32.5	37.7	33
		26.2	33.8	16
		28.7	33.5	12
	Transverse	26.6	29.9	13
		31.9	38.4	7
		31.4	35.8	8
		35.2	39.8	4
	45°	36.5	30.1	20
		32.2	36.0	18
		27.1	34.7	12

Notes: Tests performed at outside laboratory.
1-5/8-in. long button-head specimen with 0.160-in. diameter in gage length.
Tested in vacuum using radiant heat.
Strain rate = 0.005 per min.

Table IV-18. Creep Properties of F-48 Source Piece No. 1.

Test direction	:	Parallel to extrusion.
Specimen	:	Pinned-end with 2-in. uniformly heated gage length. Coated for oxidation protection.
Heating	:	Induction heating in air.
Temperature measurement	:	L & N optical pyrometer and Shaw two-color pyrometer.
Testing laboratory	:	LRL

Temp (°F)	Stress (ksi)	Time to rupture (min)	Time to 1% creep (min)
2100	40	1080	520
	45	758	480
	46	186	148
	46	103	56
2300	33	676	270
	36	670	338
	40	140	75
	40	114	87
	40	95	64
2350	32	107	54
	35	124	65
	35	97	62
	35	300	--
	40	69	--
	40	43	--
	42	55	--
	44	10	--
	45	3	--
	45	6	--
2400	30	654	370
	40	19	8
2500	27	295	75
	30	113	48
	30	85	45
	30	74	35
2580	25	42	17
	30	4.5	2.5

Table IV-19. Modulus of Elasticity from F-48 Source Piece No. 1.

Testing laboratory	Temp (°F)	Testing direction relative to extrusion	Modulus of elasticity (psi)
LRL	R. T.	Parallel	16.1×10^6
			17.4
		Transverse	18.2
			16.3
			15.8
			16.4
			15.1
		Average E = 16.5×10^6 psi	
Outside	R. T.	Parallel	16.2
			18.5
		Transverse	16.6
			16.4
		45°	16.9
			18.2
		Average E = 17.1×10^6 psi	

Table IV-20. Hardness Traverses of Short-Time Tensile Specimens.

Source Piece No. 1.

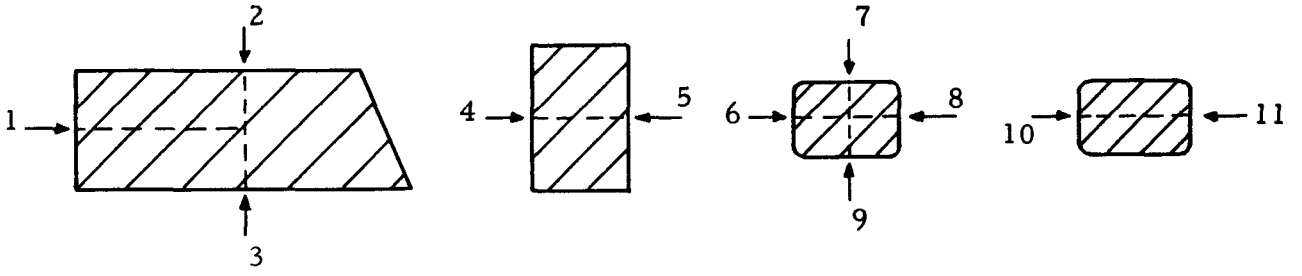

End of spec. No. T-29. Represents as-coated material

As-rec'd. material

Test section of spec. No. T-29. Represents as-tested material at 2200°F.

Test section of spec. No. T-4. Represents as-tested material at 2200°F.

Knoop hardness numbers

Traverse No.	Distance from edge, mils									
	1	2	4	6	8	10	25	50	Cent.	Avg.
1	291	305	313	305	307	316	295	300	293	303
2	310	295	293	310	300	307	325	325	313	308
3	287	307	310	316	300	300	295	338	325	308
4	260	298	280	307	293	300	287	295	288	290
5	267	274	267	274	270	272	285	288	272	274
6	288	293	293	295	293	291	298	288	298	293
7	278	288	260	287	285	287	288	265	298	282
8	313	310	295	300	313	300	298	295	298	302
9	295	295	293	287	298	305	345	293	298	296
10	288	307	295	291	300	305	300	293	288	297
11	300	285	295	298	295	288	280	295	293	296

Table IV-21. 2200°F Tensile Properties of F-48 Source Piece No. 5. (This material is shown in Fig. IV-37).

Specimen code: A - Extruded, longitudinal.
B - Extruded and press-forged, longitudinal.
C - Extruded, transverse.
D - Extruded and press-forged, transverse.

Specimen	Ultimate strength (psi)	0.2% Yield strength (psi)	% Elong. 1-in.	% Ra
A-3	56,400	50,700	18.0	75.0
A-4	55,800	49,200	16.0	79.0
B-3	59,200[a]	49,700	7.3	8.5
B-4	62,200	49,700	18.0	75.0
C-3	57,200	52,200	10.0	11.4
C-4	57,700[a]	53,200	7.0	29.0
D-3	44,300[a]	39,000	2.7	10.8
D-4	51,800[a]	43,300	0.0	2.0

[a] Fractured in or near radius.

It is believed that the cracking is due to the large reduction attempted. The material moved easily at the 2700°F forging temperature, requiring 800 tons to accomplish 44% reduction of the 5-in.-diameter billet. It is expected that edge cracking could be avoided by lowering the reduction per pass, annealing between passes, and providing oxidation protection (such as a molybdenum can) throughout the forging operation.

Press-forging for billet breakdown offers no advantage over extrusion in producing Tory II-C base plates. Therefore, no further attempt will be made to develop a forging process.

Coating Reproducibility Studies

The development of a protective coating for the base plates has progressed to a point where a satisfactory coating has been obtained. The process specification for this coating has been "frozen" and a programmed series of reproducibility studies begun. Concurrent with the reproducibility studies, laboratory work is being continued to improve the coating further.

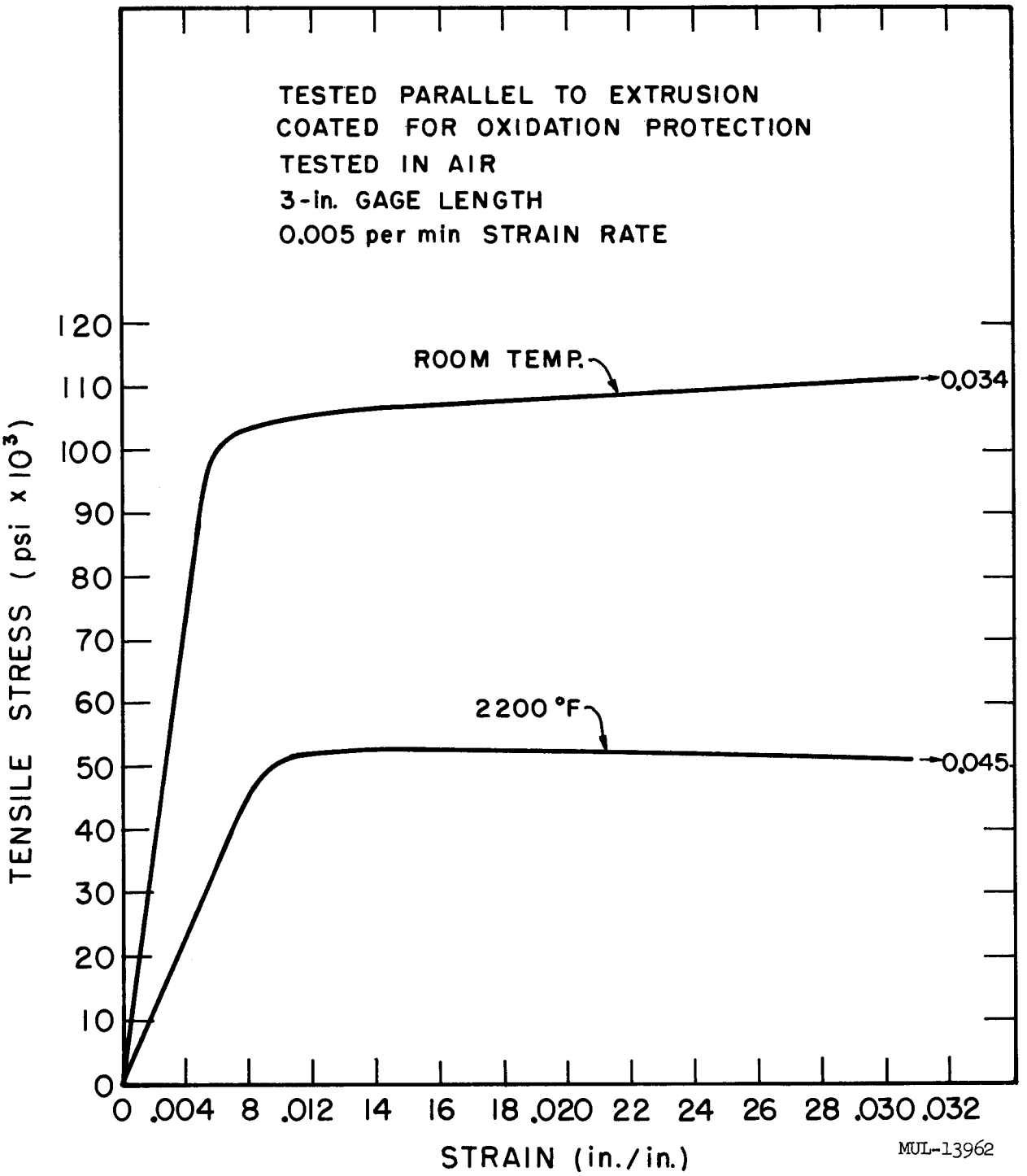

Fig. IV-39. Typical stress-strain curves for F-48 source piece No. 1 (see Table IV-12).

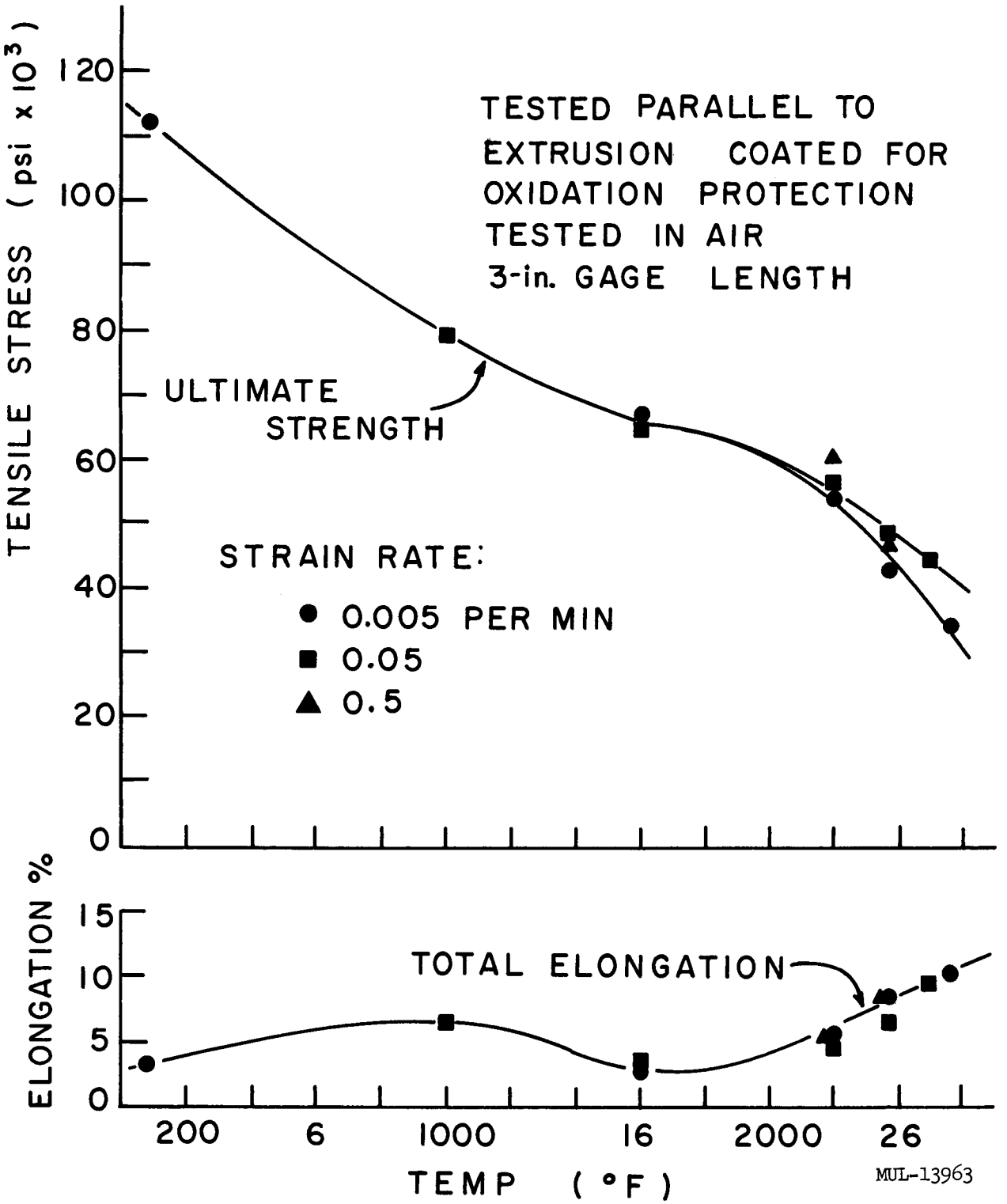

Fig. IV-40. Ultimate tensile strength and total elongation for F-48 source piece No. 1. Coated and tested in air.

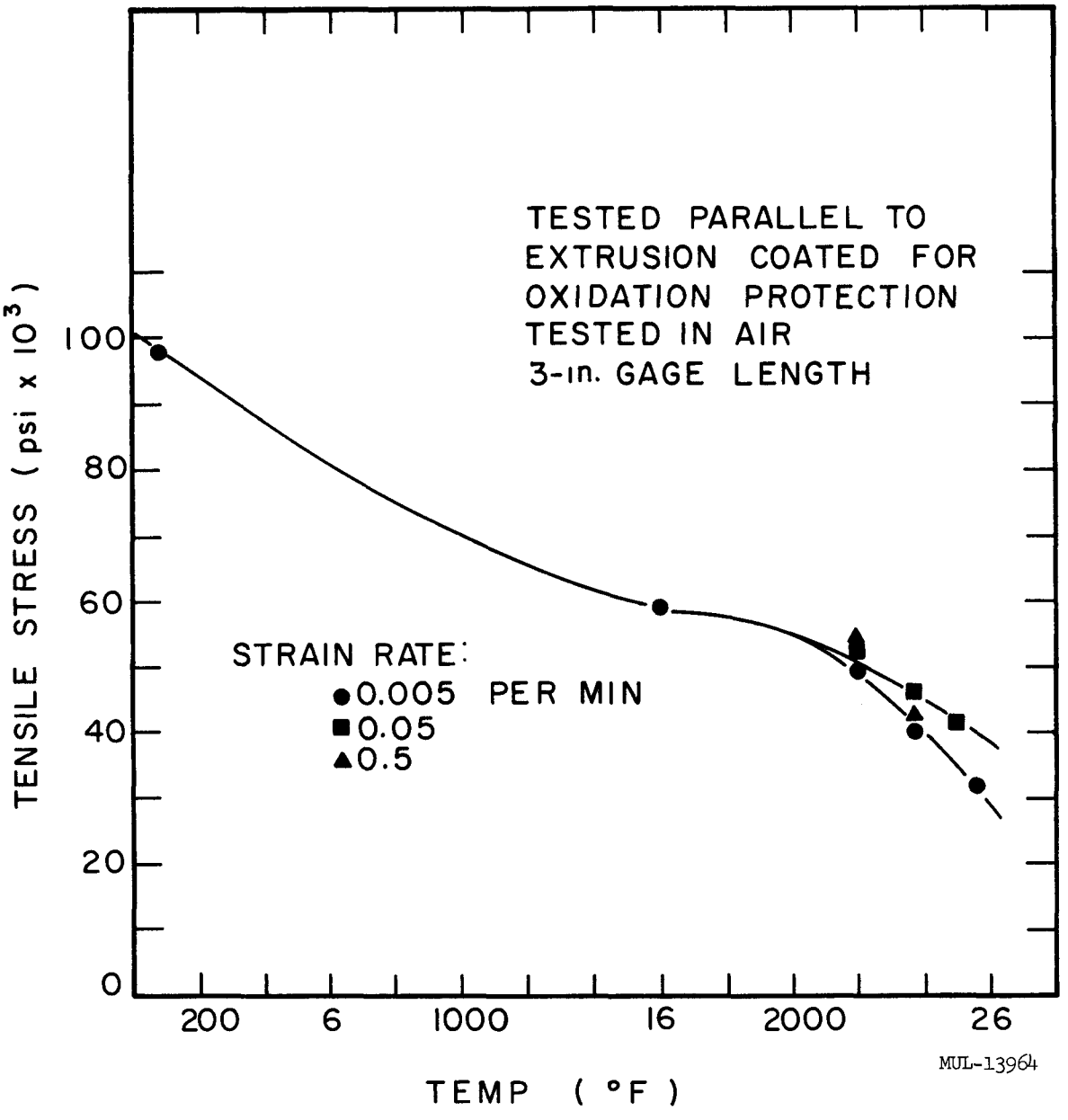

Fig. IV-41. 0.2% yield strength for F-48 source piece No. 1.

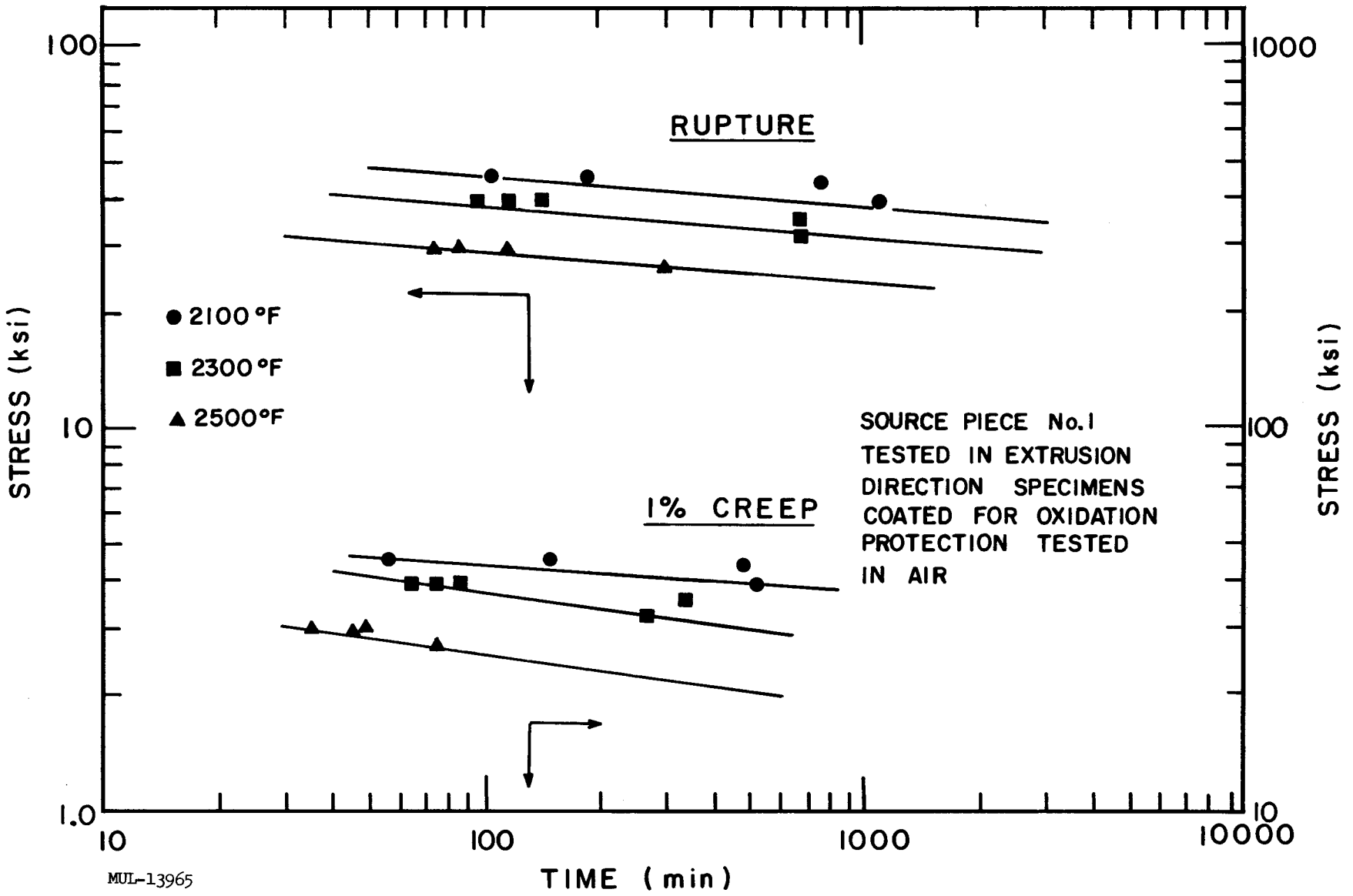

Fig. IV-42. Creep strength of F-48 Columbium alloy.

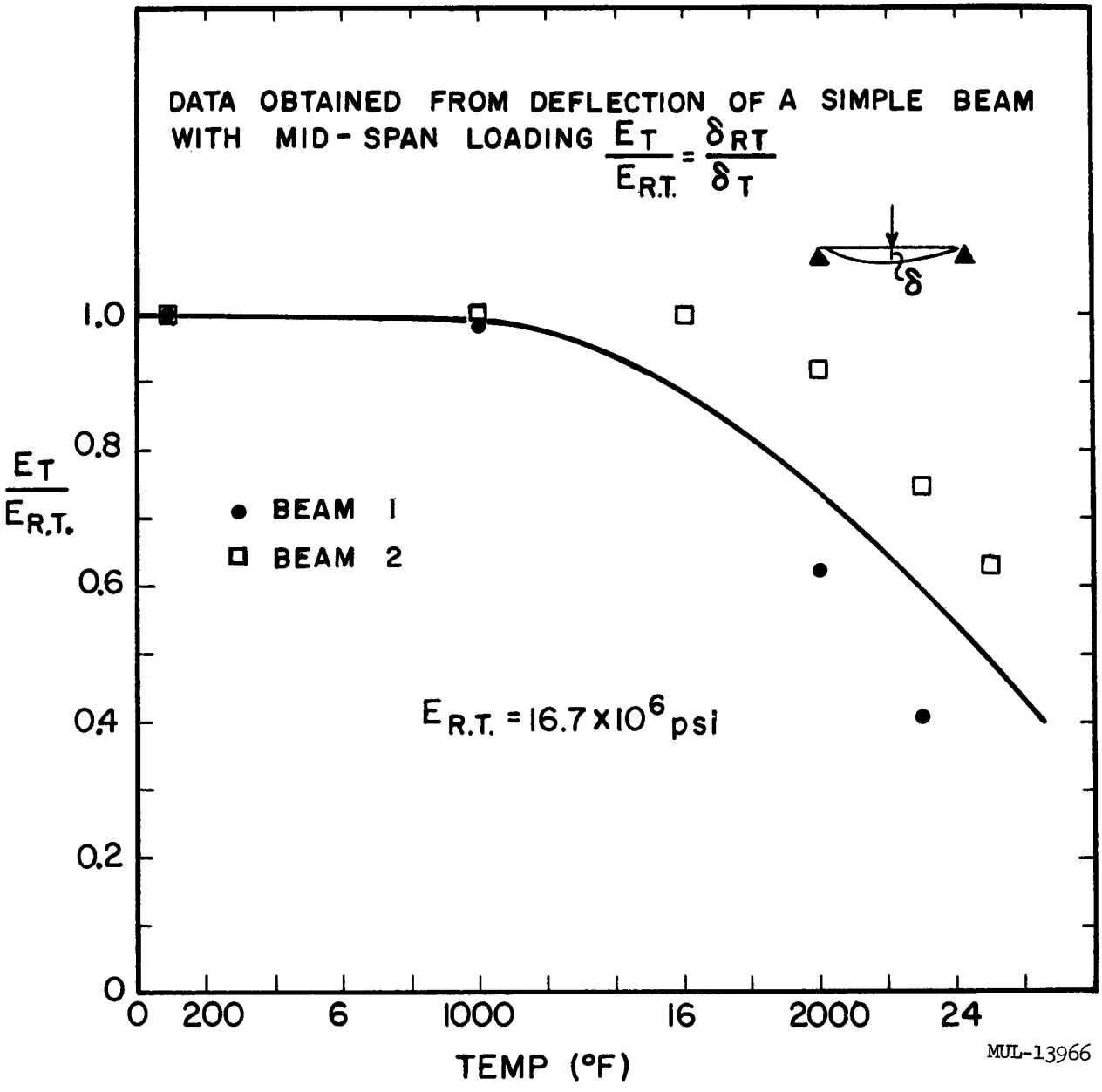

Fig. IV-43. Young's modulus vs temperature for F-48 source piece No. 1. Coated and tested in air.

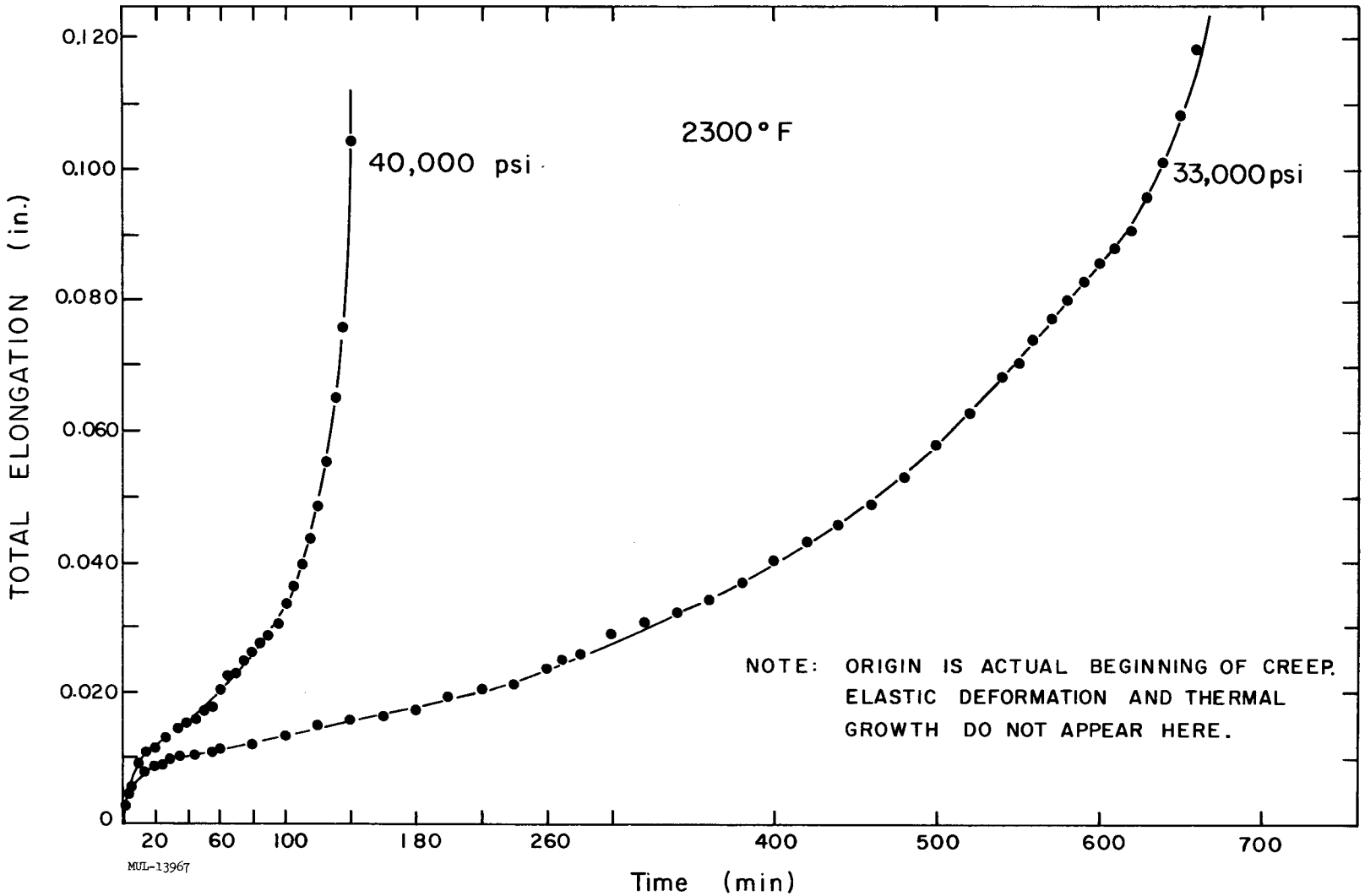

Fig. IV-44. Creep curves for F-48 source piece No. 1. Coated and tested in air. Test apparatus is shown in Fig. IV-50.

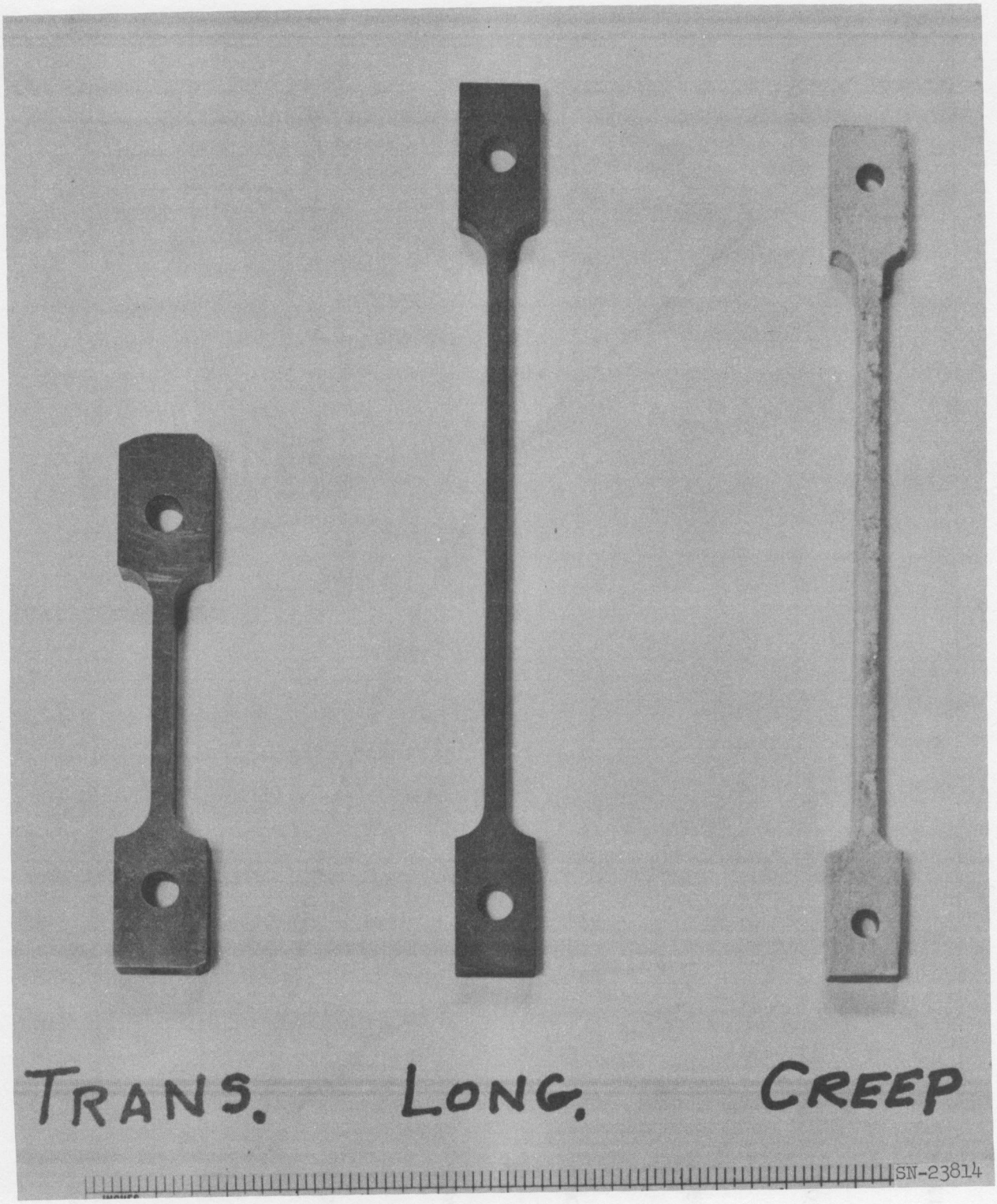

Fig. IV-45. Typical tensile specimens for LRL tests of F-48.

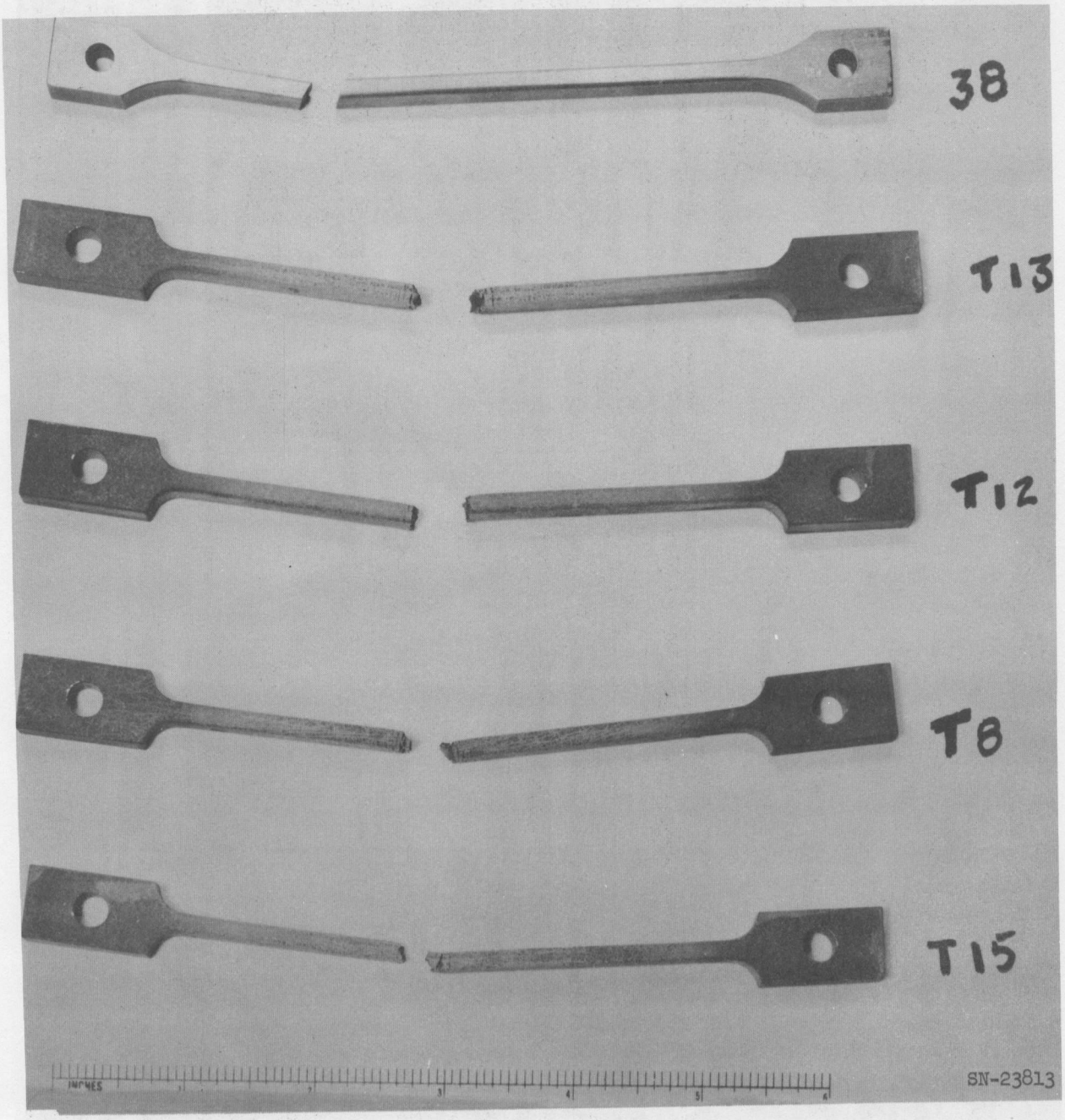

Fig. IV-46. Typical failures of short-time tensile specimens of F-48 tested at LRL.

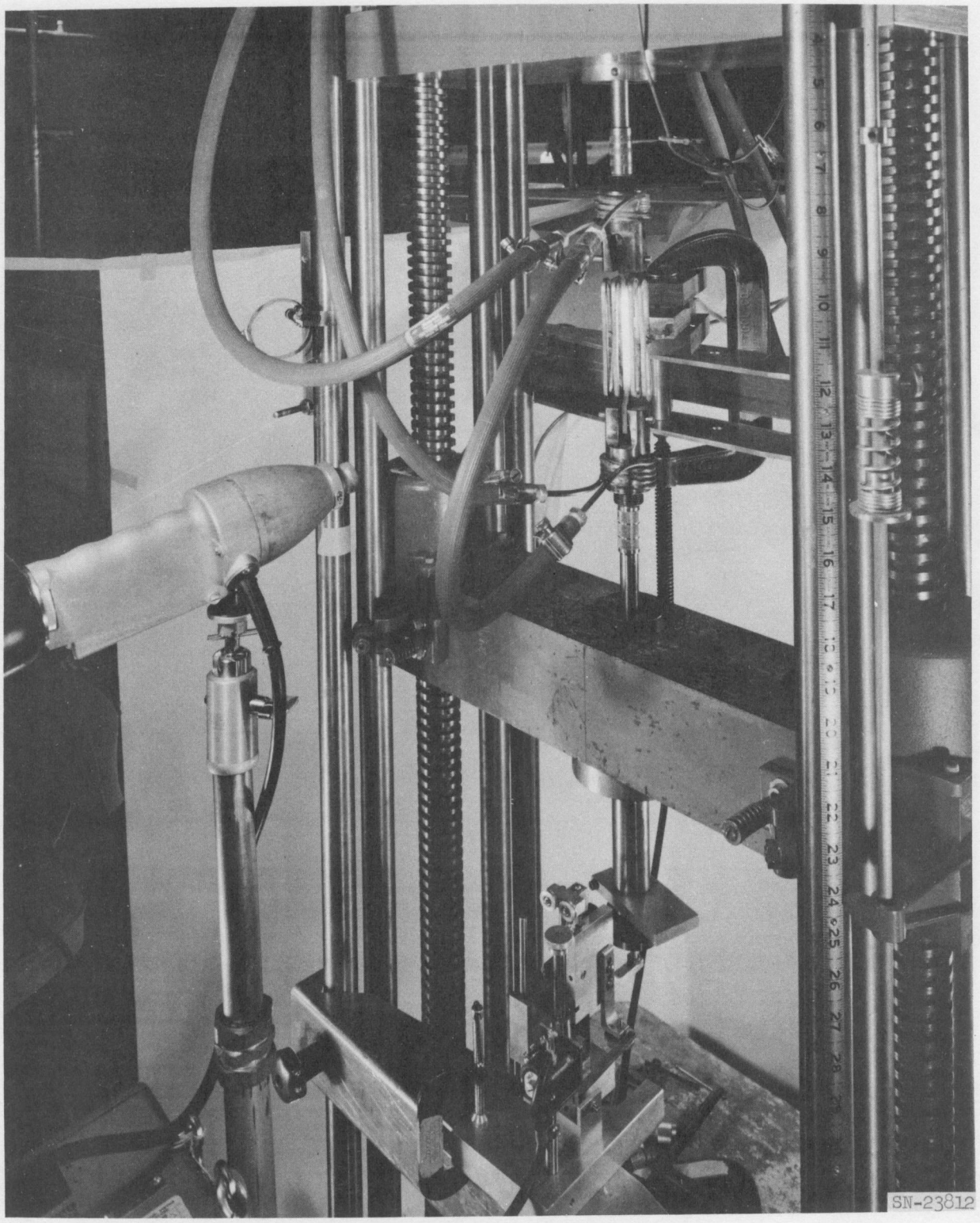

Fig. IV-47. Tensile specimens of Fig. IV-46 under test.

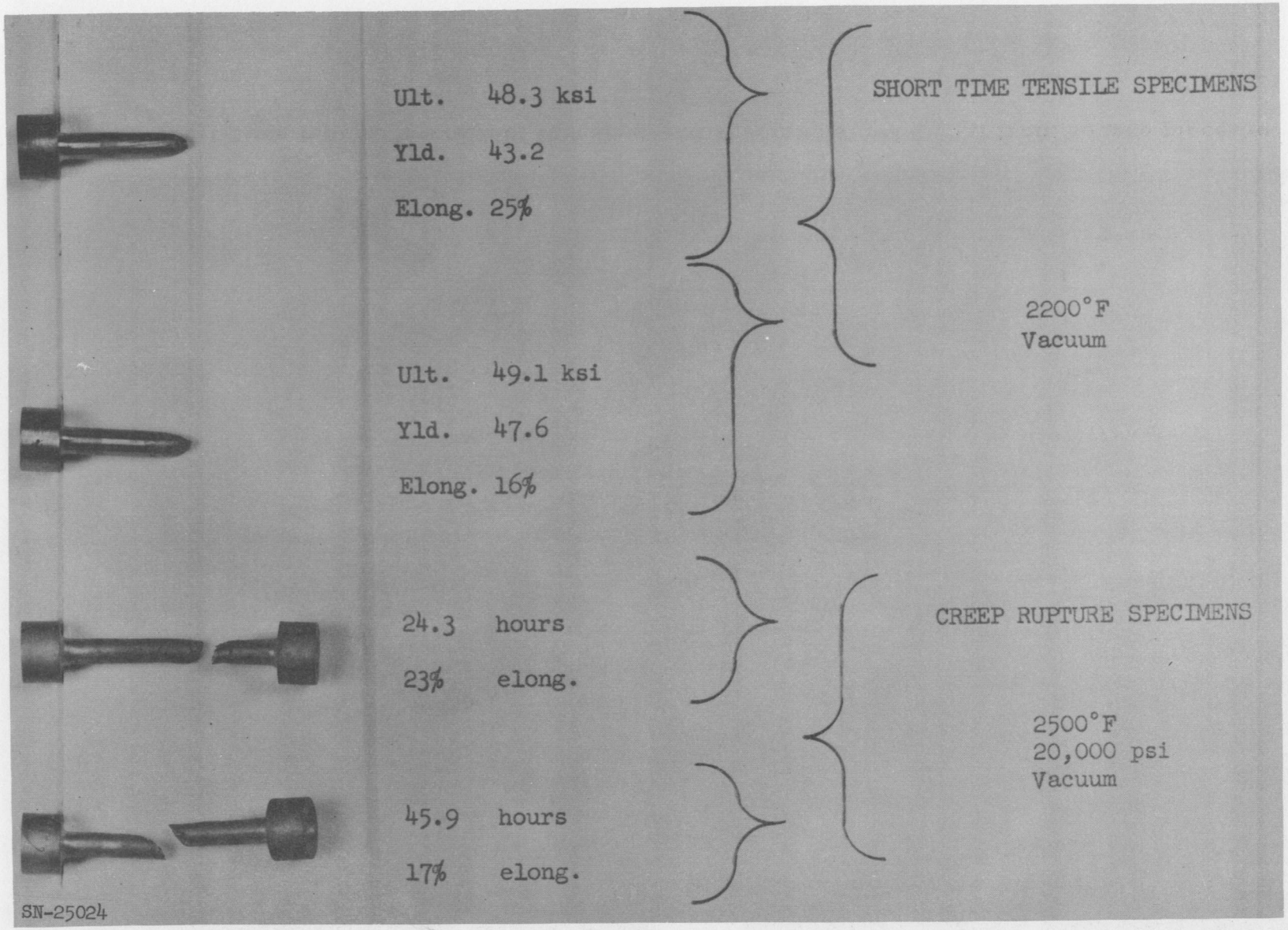

Fig. IV-48. Short-time tensile and creep rupture fractures of 1-5/8-in.-long buttonhead specimens.

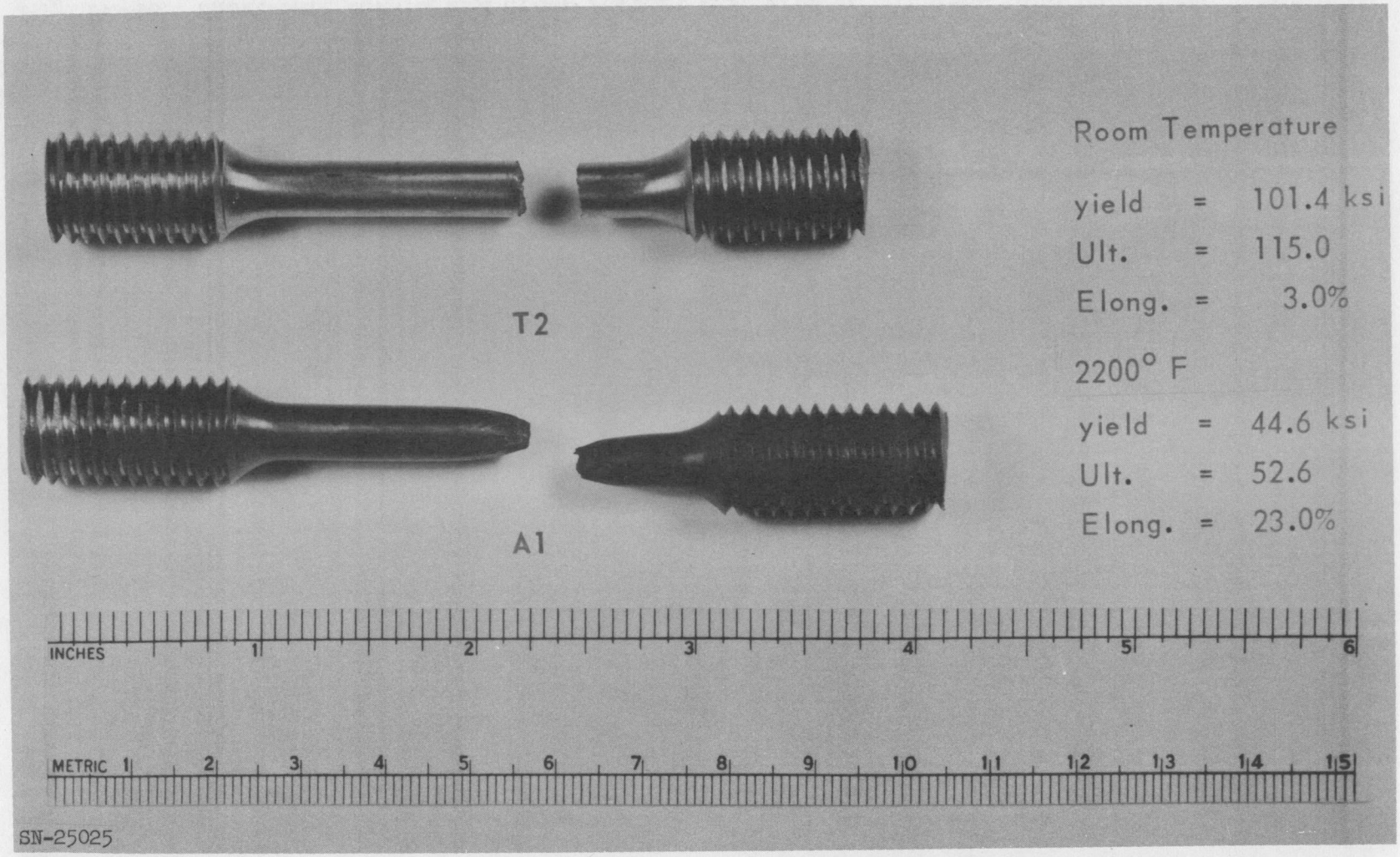

Fig. IV-49. Short-time tensile fracture of threaded-end specimens. Material from source piece No. 1.

Fig. IV-50. Apparatus for LRL creep tests of coated F-48 in air.

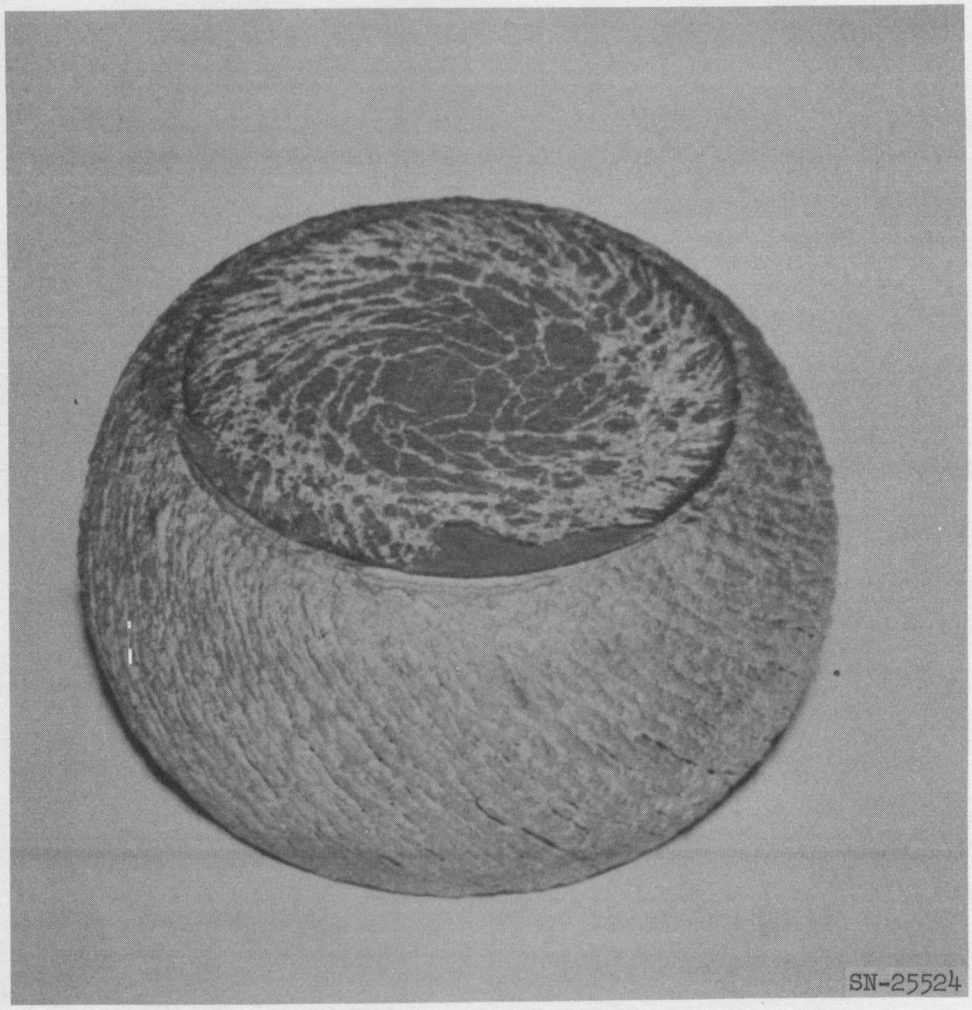

Fig. IV-51. Upset-press-forged billet of F-48. Reduction 44%. Furnace temperature 2700°F. Original billet diameter 5 inches. Forging pressure 800 tons.

The criterion for reproducibility is that the coating must withstand a minimum of ten hours of environmental exposure without failure. Failure is defined as any loss of coating which exposes base metal.

Reproducibility Group 1 (4 specimens) and Reproducibility Group 2 (3 specimens) have been tested. Of the seven specimens, one was removed after fourteen hours and another after sixteen hours because of minor defects. Three have survived twenty-six hours of exposure without failure and two have survived thirty-four hours of exposure without failure. The details of these tests are shown in Table IV-22. Photographs of specimens after various exposure times are shown in Figures IV-52, IV-53, IV-54, IV-55, and IV-56.

Sub-Ignition Test

To further confirm the validity of the 2600°F ignition temperature of F-48 a sub-ignition test was conducted on a bare specimen for thirty minutes at a temperature of 2550°F. Ignition did not occur. Metal loss was approximately six mils per side with a hardness increase to a depth of ten mils.

Coating Process

The most significant change in the coating process during the past quarter was to increase the pack-firing temperature of the first-cycle silicon pack from 1900°F to 2300°F. This temperature increase produced a more thoroughly diffused coating with the result that the coating life has been considerably extended and the useful upper temperature limit increased.

Base Plate Stresses

A series of tests to determine stresses in the various shapes of base plates has been completed. The tests were performed using strain gages and aluminum plates. The maximum stresses for the operating pressure were as follows:

Std. hex plate = 7150 psi
Peripheral plate C = 8000 psi
Peripheral plate E = 4500 psi.

Table IV-23 shows the stresses for other load situations. Figures IV-57 and IV-58 show the peripheral plate under test.

Table IV-22. Coating Reproducibility Studies.

Reprod. Group 1								Reprod. Group 2					
EB[a]		EC[a]		ED[a]		EE[a]		EF[a]		EG[a]		EH[a]	
Time (hr)	Temp (°F)	Time (hr)	Temp (°F)	Time (hr)	Temp (°F)	Time (hr)	Temp (°F)	Time (hr)	Temp (°F)	Time (hr)	Temp (°F)	Time (hr)	Temp (°F)
2	2250	2	2250	2	2250	2	2250	2	2250	2	2250	2	2250
3	1950	3	1950	3	1950	3	1950	3	1950	3	1950	3	1950
3	2250	3	2250	3	2250	3	2250	3	2250	3	2250	3	2250
2	1950	2	1950	2	1950	2	1950	2	1950	2	1950	2	1950
2	2250	2	2250	2	2250	2	2250	3	2250	3	2250	3	2250
2	1950	2	1950	2	1950	2	1950	2	2250	2	2250	2	2250
2	2250			2	2250	2	2250	3	2250	3	2250	3	2250
				2	2250	2	2250	3	2250	3	2250	3	2250
				3	2250	3	2250	2	2250	2	2250	2	2250
				2	2250	2	2250	3	2250	3	2250	3	2250
				3	2250	3	2250						
				3	2250	3	2250						
				2	2250	2	2250						
				3	2250	3	2250						
16 hr total 9 hr at 2250°F 7 hr at 1950°F		14 hr total 7 hr at 2250°F 7 hr at 1950°F		34 hr total 27 hr at 2250°F 7 hr at 1950°F		34 hr total 27 hr at 2250°F 7 hr at 1950°F		26 hr total 21 hr at 2250°F 5 hr at 1950°F		26 hr total 21 hr at 2250°F 5 hr at 1950°F		26 hr total 21 hr at 2250°F 5 hr at 1950°F	
Remarks													
Out, minor defect		Out, minor defect		O. K.		O. K.		O.K.		O. K.		O. K.	

Conditions: Temperature and time as indicated. Pressure = 200 psia. O_2 content of gas stream = 20%. Flow rate = 288,000 lb / ft^2/hr. Velocity through holes = 0.5M.

[a]Specimen designation.

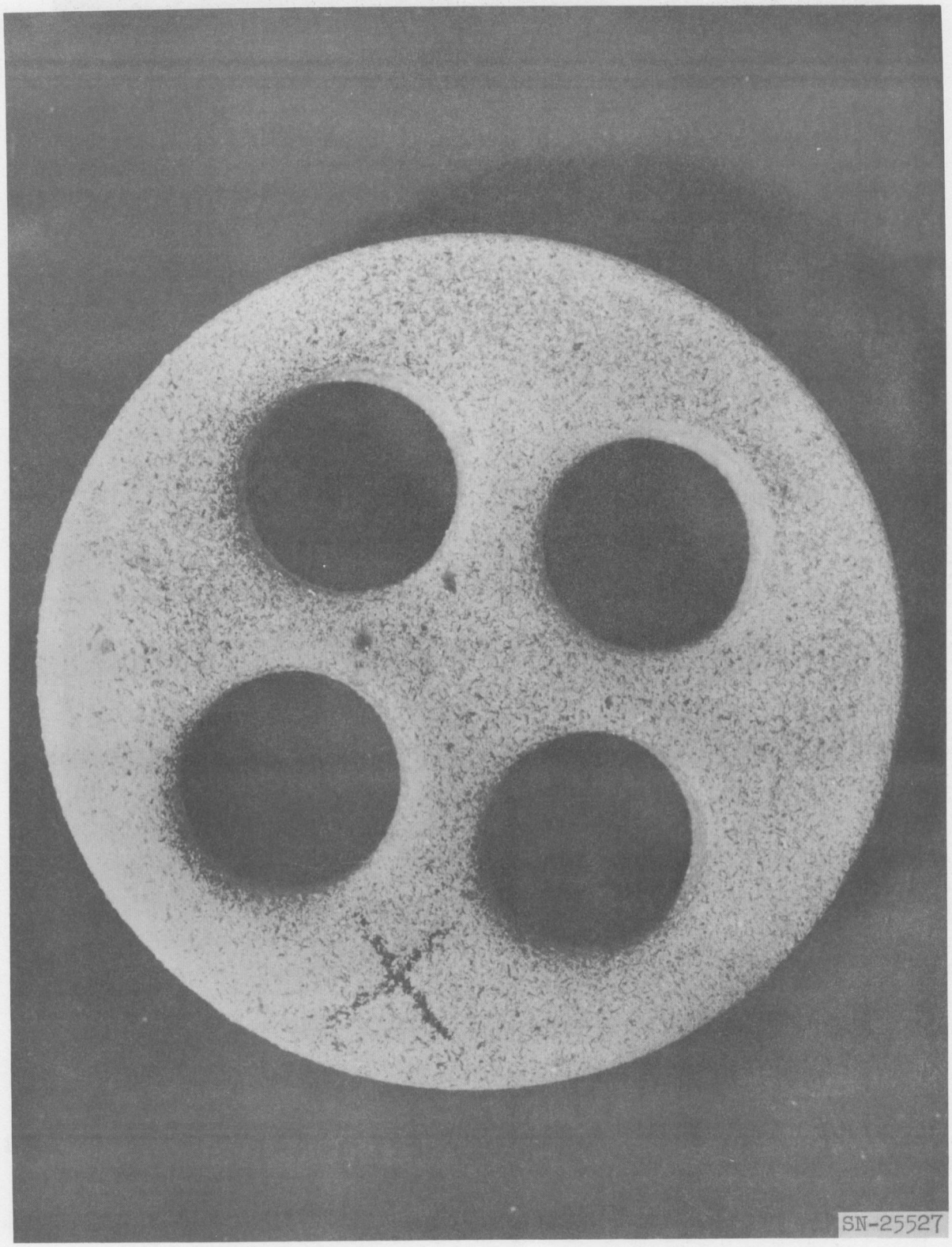

Fig. IV-52. Test 10901, flow specimen front face after 2 hours of blow-down at 2250°F.

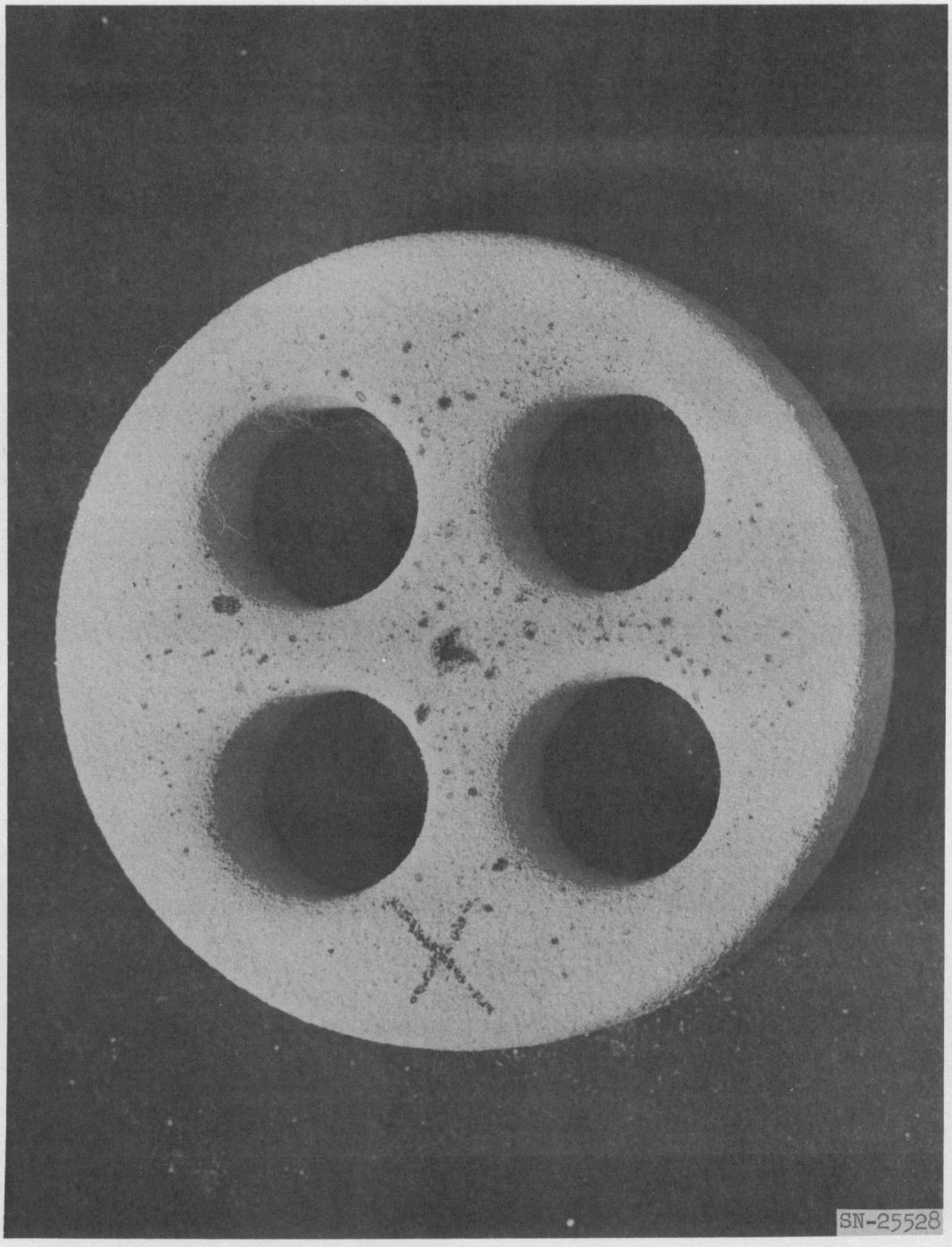

Fig. IV-53. Test 10901, flow specimen face after 2 hours at 2250°F and 3 hours of blowdown at 1950°F.

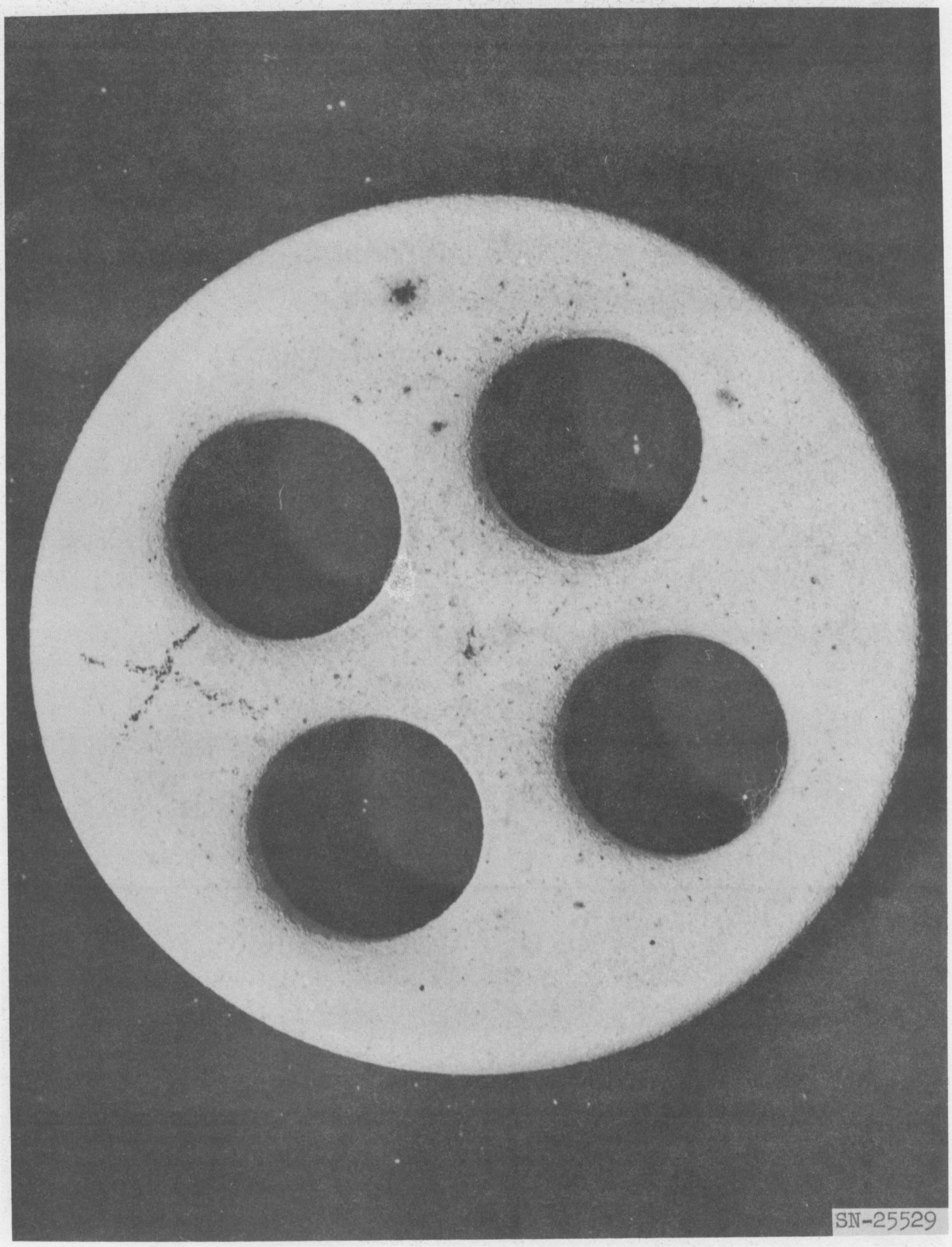

Fig. IV-54. Test 10901, flow specimen face after 5 hours at 2250°F and 3 hours of blowdown at 1950°F.

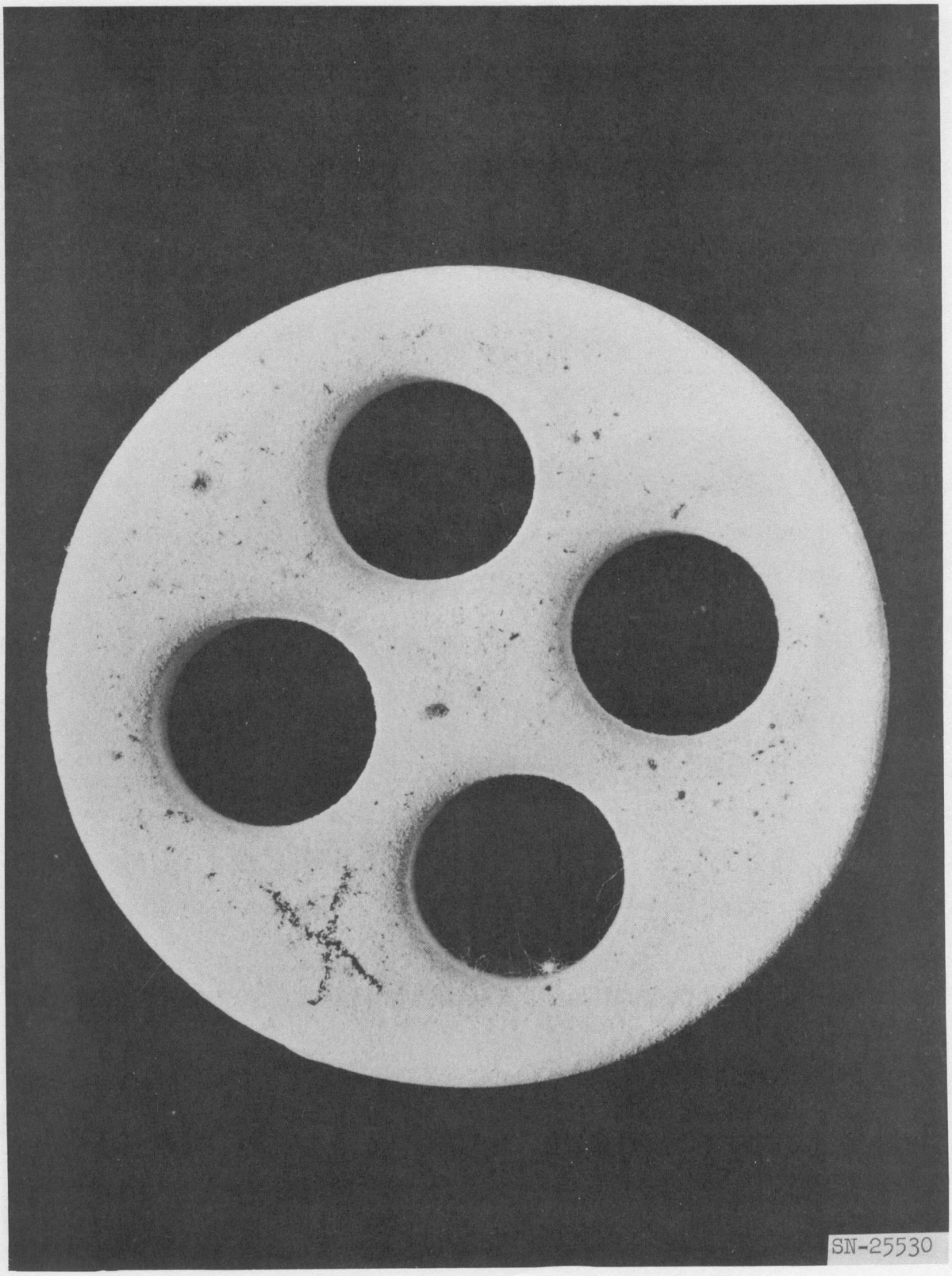

Fig. IV-55. Test 10901, flow specimen front face after 9 hours at 2250°F and 7 hours of blowdown at 1950°F (16 hours total).

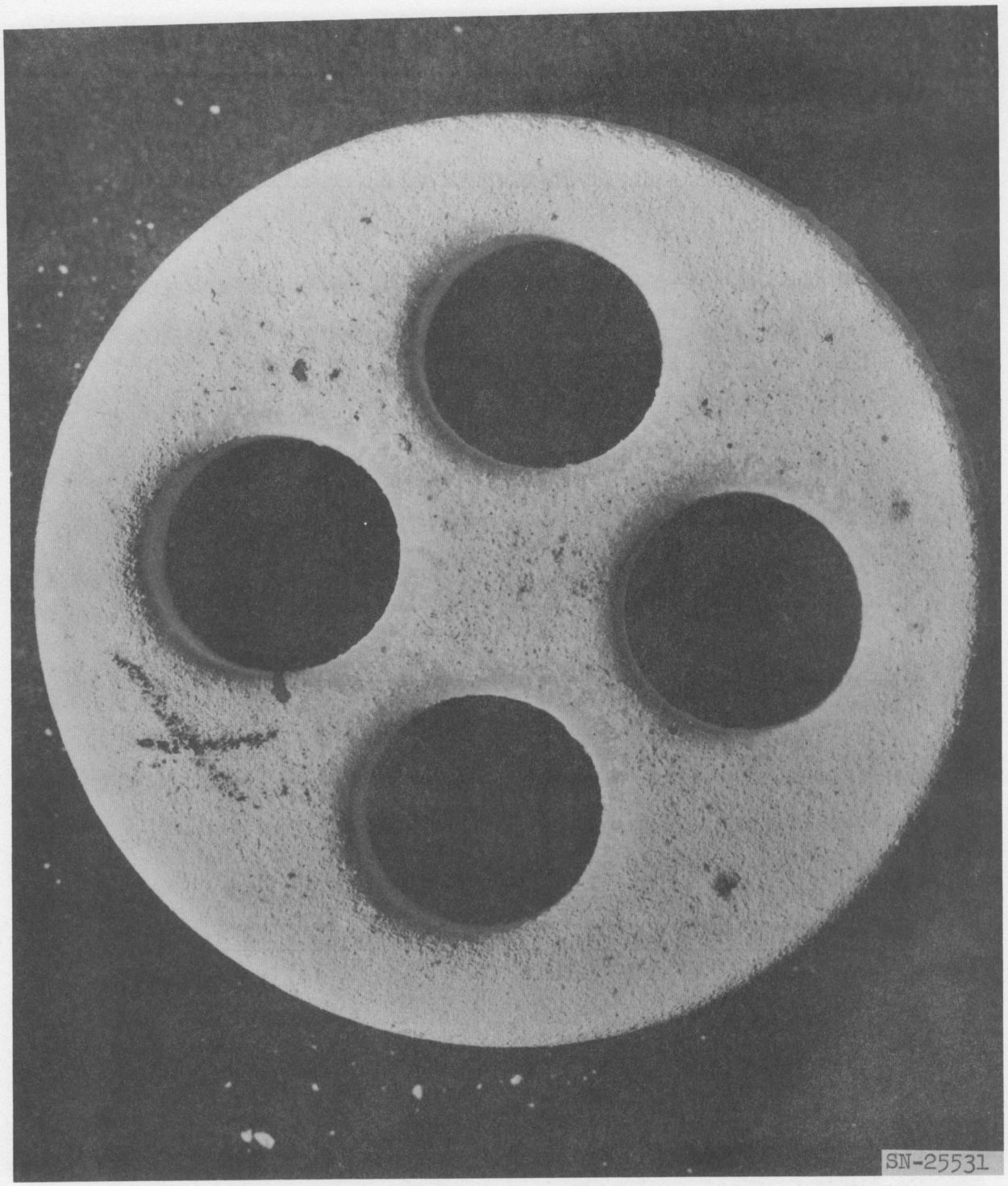

Fig. IV-56. Flow specimen after 32 hours; 9 hours at 2250°F, 7 hours of 1950°F blowdown (16 hours total).

Table IV-23. Base Plate Stress Tests.

Standard Hex Plate. (Total area = 19 in^2, E(alum.) = 10×10^6)

Strain (micro in./in.)	Total load (lb)	Unit load (psi)	Stress[a] (psi)
162	500	26.3	1280
330	1000	52.6	2610
475	1500	78.9	3750
670	2000	105.2	5300
833	2500	131.5	6600
987	3000	157.8	7800
850	2500	131.5	6700
685	2000	105.2	5400
515	1500	78.9	4070
350	1000	52.6	2780
191	500	26.3	1510
		145 (actual)	7150

[a]Corrected for 1-1/8-in. actual thickness vs 1-in. used in test.

Peripheral Plate C. (Total area = 38.03 in^2, E(alum.) = 10×10^6)

Strain (micro in./in.)	Total load (lb)	Unit load (psi)	Stress (psi)
163	1000	26.3	1630
321	2000	52.6	3210
466	3000	78.9	4660
618	4000	105.2	6180
745	5000	131.5	7450
872	6000	157.8	8720

At 145 psi unit load, stress = 8000 psi.

Peripheral Plate E. (Total area = 27.58 in^2, E(alum.) = 10×10^6 psi)

Strain (micro in./in.)	Total load (lb)	Unit load (psi)	Stress (psi)
070	500	18.1	700
130	1000	36.2	1300
178	1500	54.3	1800
250	2000	72.4	2500
286	2500	90.5	2900
340	3000	108.6	3400
400	3500	126.7	4000
453	4000	144.8	4500
509	4500	162.9	5100
560	5000	181.0	5600

At 145 psi, stress = 4500 psi.
Ave. porosity = 25%, which accounts for low stress.

MUL-14118

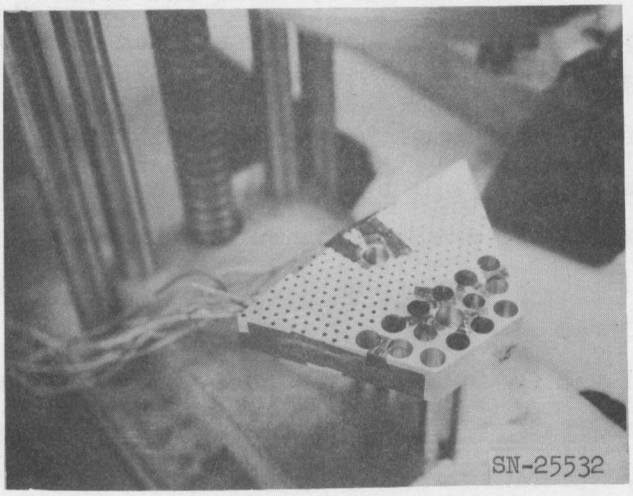

Fig. IV-57. Aluminum model of Tory II-C base plate ready for test.

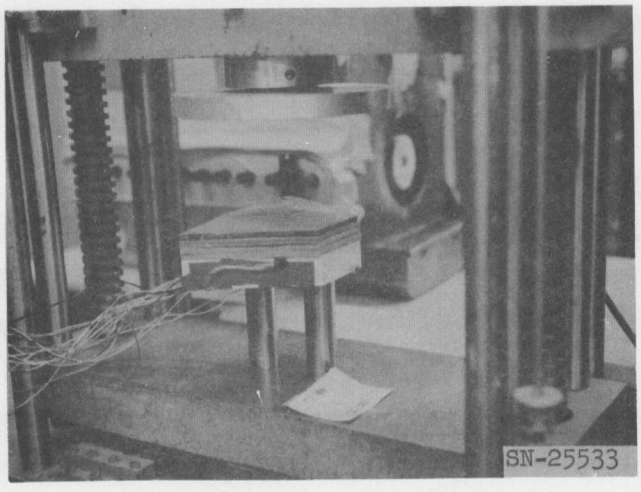

Fig. IV-58. Aluminum model of Tory II-C base plate under test. Rubber pads will distribute test load to simulate actual reactor loading.

SIDE SUPPORT

René 41 has been selected as the material for the side support springs. A study program is underway for the forming and brazing of René-41 spring assemblies. Six springs have been completed, two each with vendor's AMS 4778, J-8100, and J-8600 brazing alloys. One of the brazed assemblies forming a side support spring is shown in Fig. IV-59. The J-8600 braze has been unsuccessful, but further work is being done. Both AMS 4778 and J-8100 have produced sound joints; preliminary information shows AMS 4778 to be slightly superior. Photomicrographs of AMS 4778 and J-8100 brazed joints are shown in Fig. IV-60.

Figures IV-61 and IV-59 indicate creep properties of René 41 at 1200°F and 1400°F. The effect of cold work prior to heat treating on properties of René 41 is shown by the data in Table IV-24.

Inco 713C has been selected as the casting material for the side support pressure pads. Figures IV-62 and IV-63 present properties of vacuum-cast tensile specimens of Inco 713C obtained by LRL.

REACTOR DUCT

Material Evaluation

The purpose of this test series was to verify a weld procedure and to compare weld and base material properties for Hastelloy C. The tests were arranged to yield usable design data for the reactor duct and to supplement other data in regions of interest.

Test Material

Type of Specimens. One-hundred and three specimens were rectangular (0.375 in. × 0.312 in. or 0.250 in.) with 2-in. gage lengths, per ASTM E8-57T. Twenty-two specimens, were 0.250-in. diameter with 1.5-in. gage lengths.

Base Metal Specimens. The 50 base metal specimens were from two different plate thicknesses (5/16 in. and 3/4 in.) and five different heats. Some specimens were in the as-received condition (A.R.), and others were given an extra solution heat-treatment (SHT)(solution heat-treated at 2225°F and water quenched).

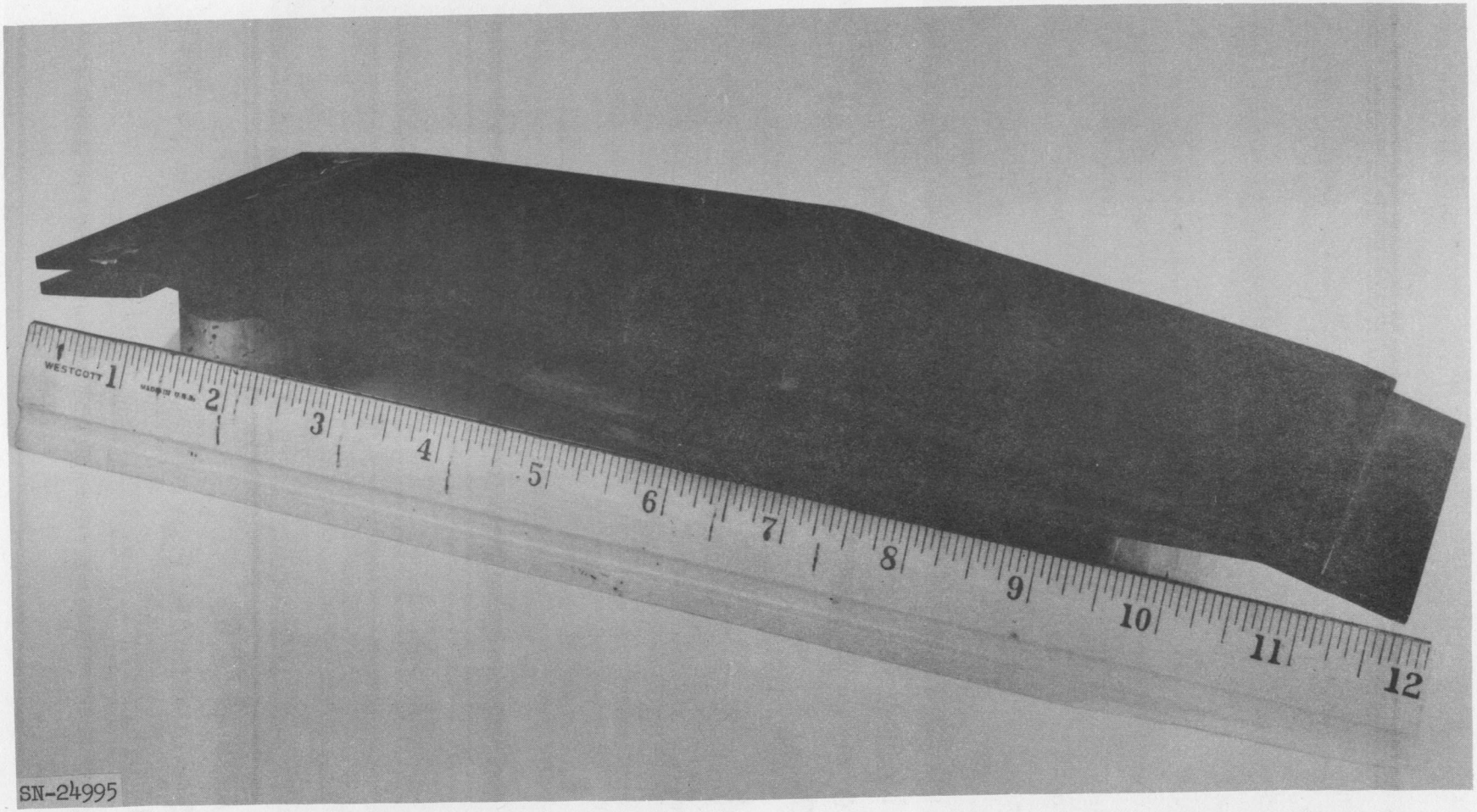

Fig. IV-59. Side support spring. Brazed assembly of 1/8-in. René 41 plate.

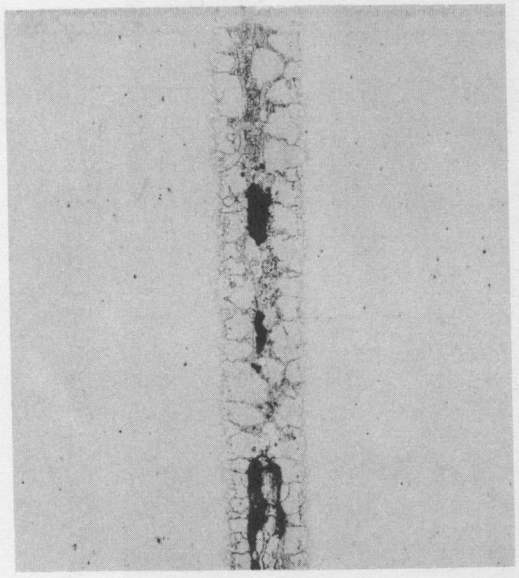

J - 8100
30 min @ 2165°F
100 x

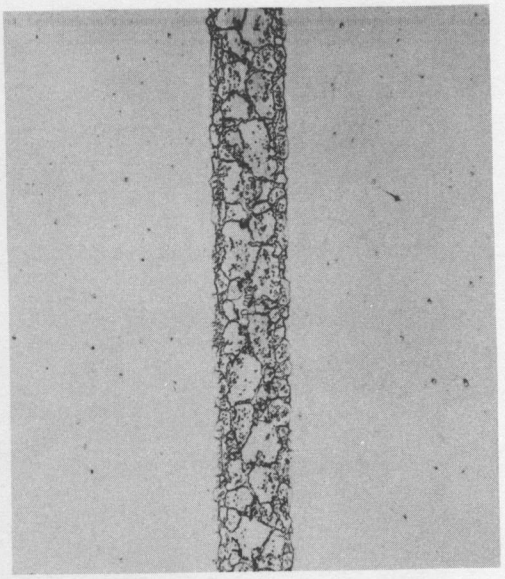

J - 8100
5 min @ 2165°F
100 x

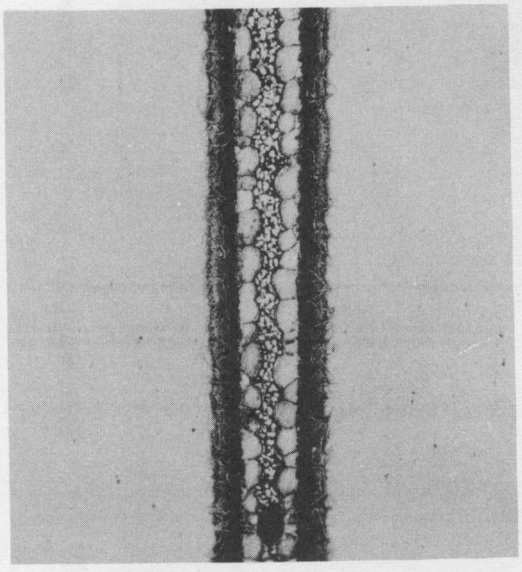

AMS 4778
5 min @ 1975°F
100 x

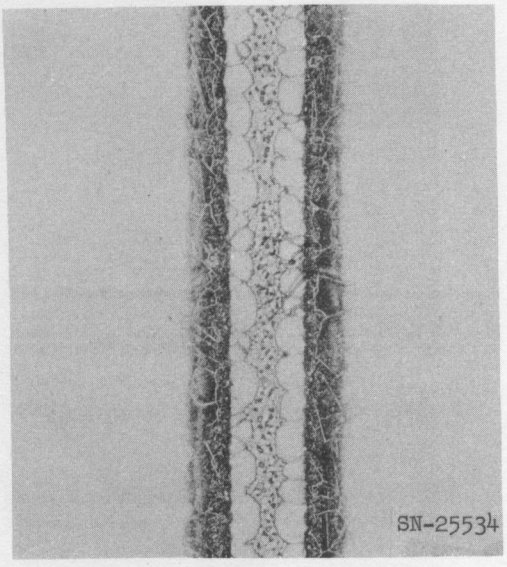

AMS 4778
30 min @ 1975°F
100 x

Fig. IV-60. Photomicrographs of brazed joint for René 41.

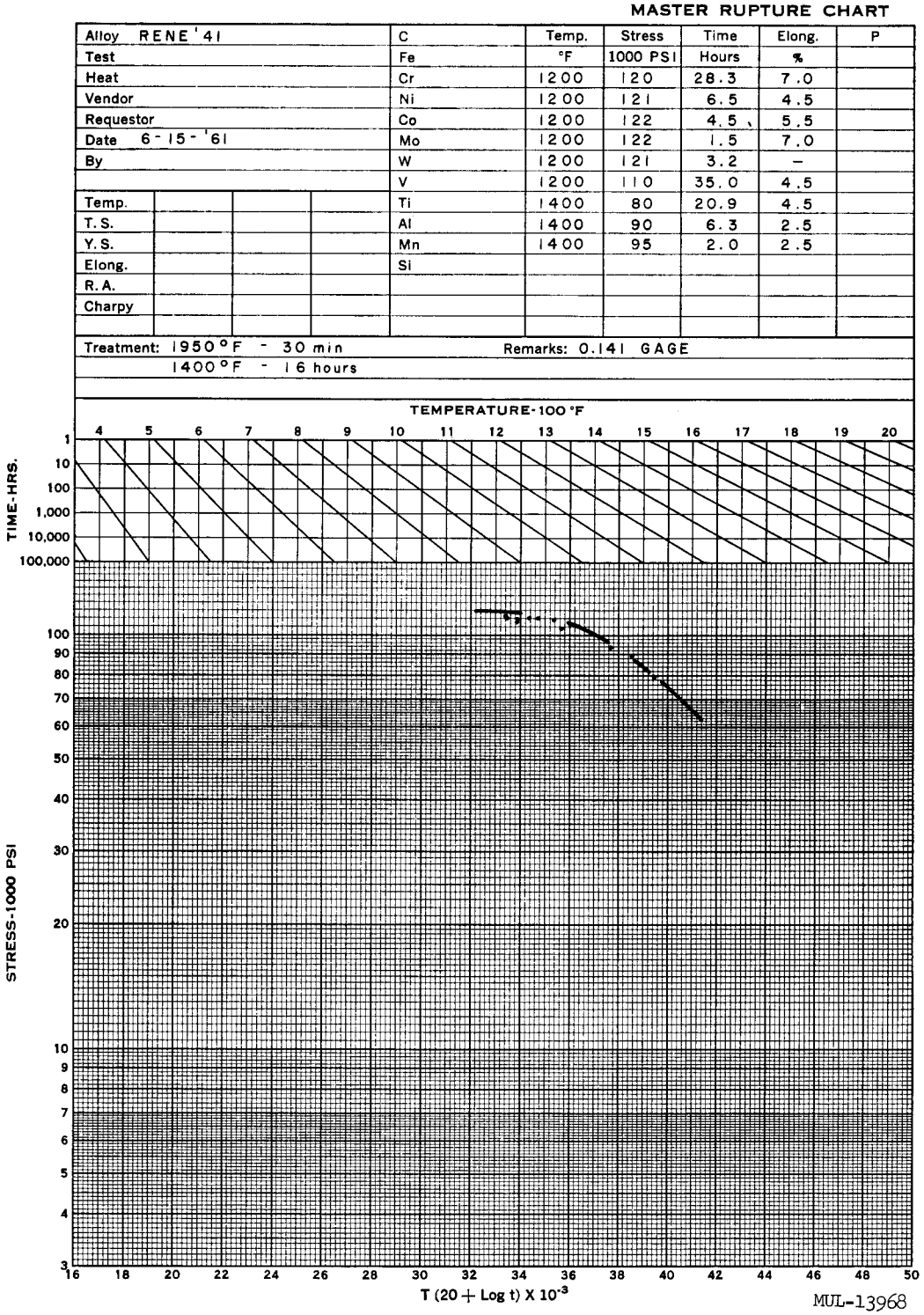

Fig. IV-61. Creep rupture of René 41.

Table IV-24. Effect of Cold Work in Water-Quenched Condition on Strength of Heat-Treated René 41.

Heat-treat cycle	Thickness (in.)	Yield strength at 0.2% offset (ksi)	Tensile strength (ksi)	Elongation in 2-in. gage (%)
		Cold worked: 4% elongation		
A	0.126	139.9	200.5	17.5
A	0.127	139.4	201.1	18.5
B	0.129	137.1	200.5	18.5
B	0.127	136.9	198.5	14.0
C	0.127	136.0	200.0	20.0
C	0.128	139.3	202.2	21.5
D	0.126	137.1	200.0	21.0
D	0.127	135.4	199.5	21.5
		Cold worked: 8% elongation		
A	0.124	138.8	201.5	18.5
A	0.127	139.9	202.1	18.5
B	0.124	137.5	200.8	16.5
B	0.123	138.9	202.8	18.5
C	0.126	140.0	202.6	19.0
C	0.124	141.2	203.4	20.0
D	0.122	141.1	204.0	21.0
D	0.121	139.5	201.0	16.5
		Cold worked: 12% elongation		
A	0.121	144.7	202.6	15.0
A	0.118	144.9	203.0	15.5
B	0.120	146.5	203.5	14.0
B	0 122	143.0	202.8	20.0
C	0.122	141.5	200.3	22.0
C	0.124	143.1	202.3	21.5
D	0.122	144.6	208.9	22.0
D	0.120	142.5	203.5	19.5
		Cold worked: 16% elongation		
A	0.119	146.5	203.3	21.0
A	0.122	147.3	204.6	20.5
B	0.119	150.4	207.4	20.0
B	0.123	145.7	202.0	18.0
C	0.123	144.6	203.8	17.5
C	0.118	150.9	208.2	17.5
D	0.120	145.7	202.3	17.5
D	0.120	144.5	204.7	20.0

Procedure: 1. Machine as-received René 41 1/8-in. plate into test coupons. Material received in 1975°F water-quenched condition.
2. Produce desired amount of cold work in each specimen by stretching it in a testing machine.
3. Heat treat.
4. Test to ultimate tensile failure.

Heat treating cycles:

A. 1950°F - 30 min - ac
1400°F - 20 hr - ac

B. 1950°F - 30 min - ac
1400°F - 16 hr - ac

C. 1950°F - 30 min - ac
1400°F - 12 hr - ac

D. 1950°F - 30 min - ac
1400°F - 8 hr - ac

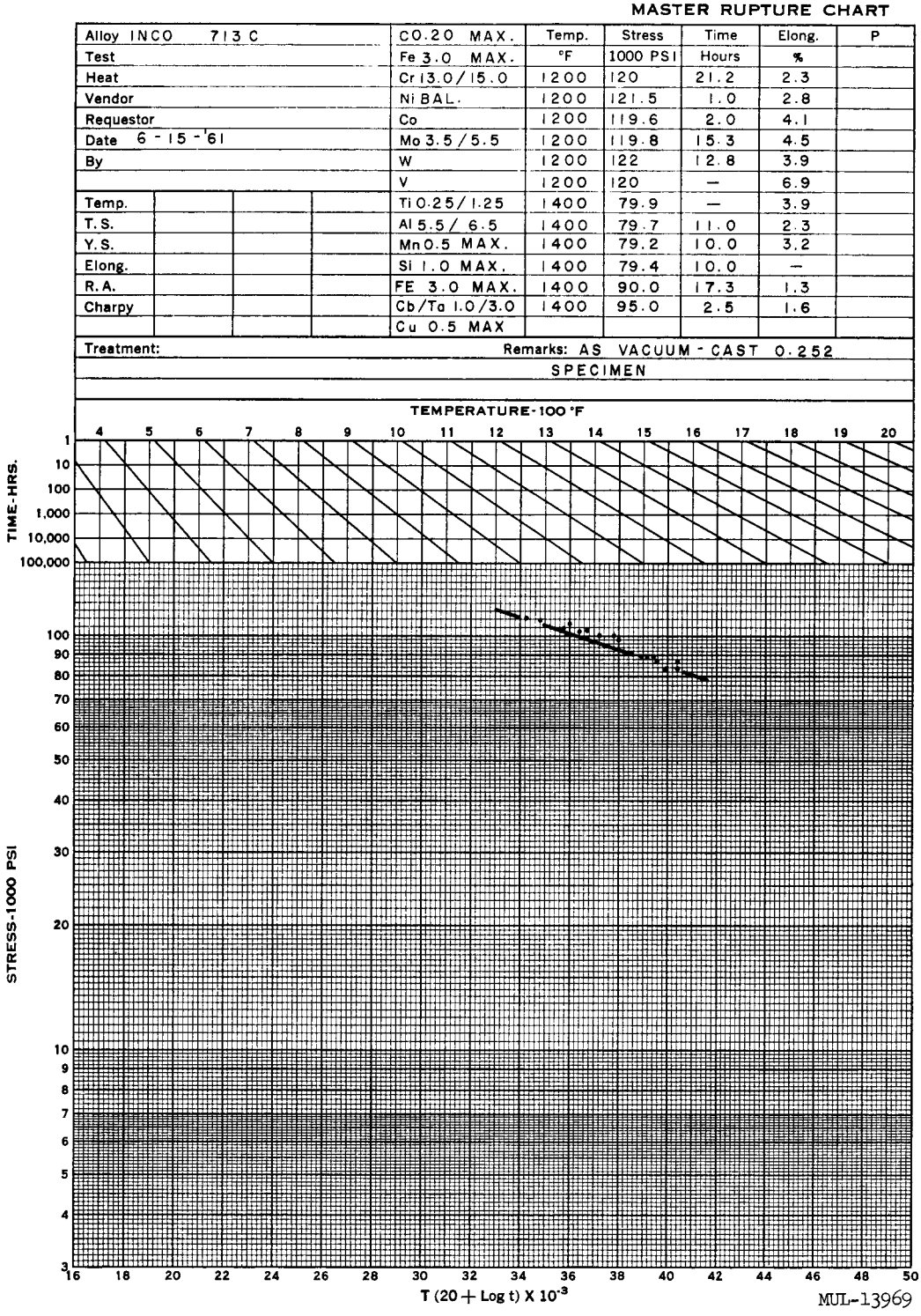

Fig. IV-62. Properties of precision-cast alloy Inco 713C. Data obtained from outside laboratory.

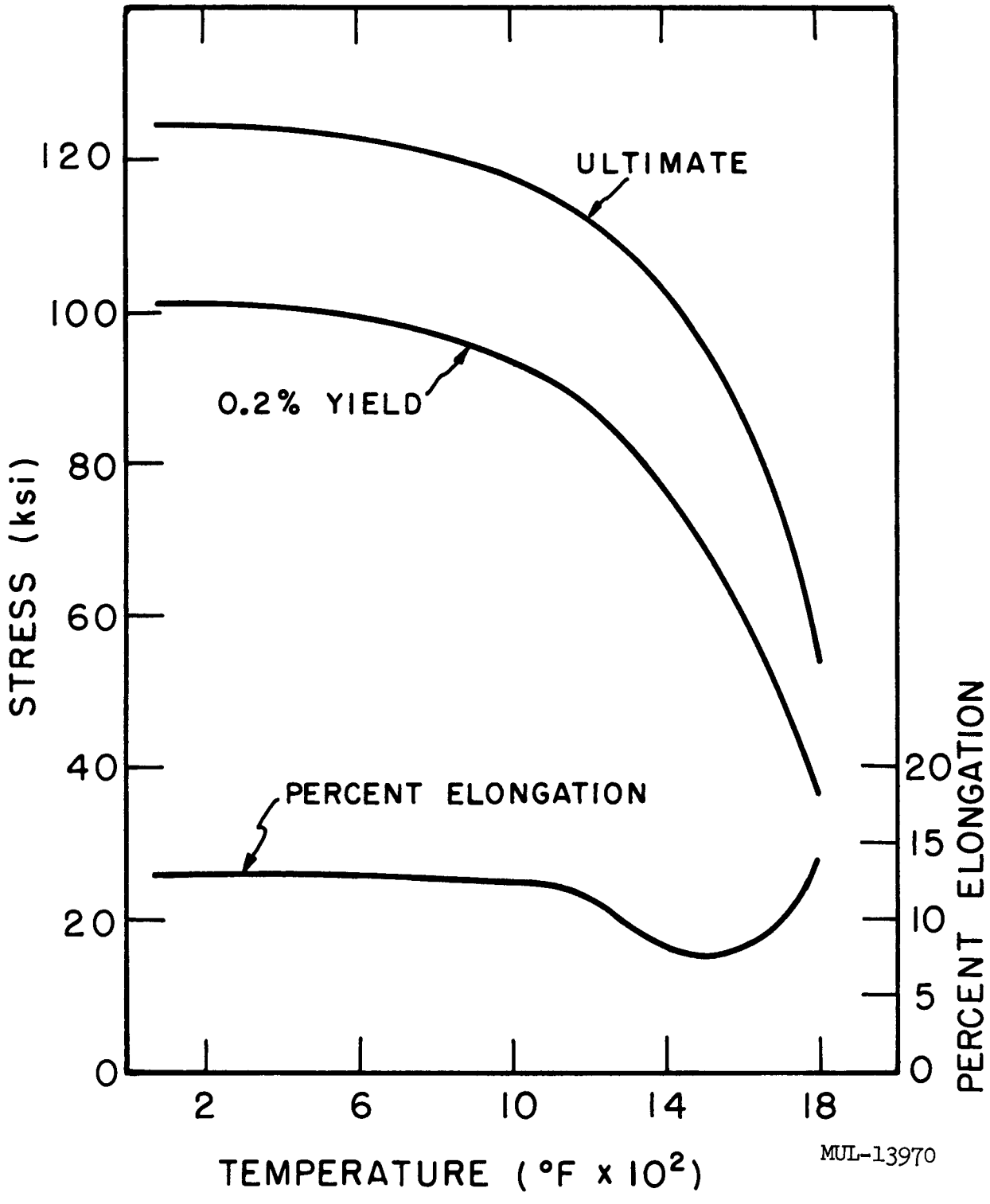

Fig. IV-63. Properties of precision-cast alloy Inco 713C. Data obtained from outside laboratory.

Weld Metal Specimens. The weld metal specimens were machined from Hastelloy-C plates welded together with 3/32-in. -diameter Hastelloy-C weld wire. The dc inert-arc welding method, per Oak Ridge National Laboratory specification RMWS-7, was used. The specimen quality was determined by penetrant and radiographical inspection. Quantity of specimens, type of specimens, and heat treatments were as follows:

Quantity	Type	Heat treatment
21	All weld	As welded (AW)
18	All weld	Solution heat-treated (SHT)
20	Across weld	As welded
16	Across weld	Solution heat-treated

Test Procedures and Results

Tensile Tests. Tensile testing was conducted on 53 specimens at room, 1200°F, 1350°F, and 1500°F temperatures. Strain rates of 0.005 in. per in. per minute up to yield, and 0.05 in. per in. per minute above yield point were utilized, with a minimum hold time of 5 minutes at temperature.

Six identical specimens from the same plate were tested here at LRL and in two other laboratories. Each laboratory tested one specimen at 1200°F and one at 1350°F.

The tensile-test data are presented in Table IV-25. Figures IV-64, IV-65, and IV-66 illustrate tensile properties vs temperature for the base, all-weld, and across-weld metal specimens.

Creep-Rupture Tests. Creep-rupture tests were conducted at temperatures of 1200°F, 1350°F, and 1500°F on 18 across-weld specimens. Times to rupture are presented in Table IV-26. Graphic presentation of creep-rupture test results and advertised rupture ranges are given in Fig. IV-67.

Creep Tests. Creep tests were conducted on 48 specimens at temperatures of 1200°F, 1350°F, 1400°F, 1450°F, and 1500°F. Continuous creep curves (strain versus time) were recorded for all specimens and times noted to 0.3, 0.5, 0.75, 1.0, 2.0, and 3.0% total strains. The results are given in Table IV-27. After 3.0% creep, or 30 hours, the loads were increased to rupture, as noted in the last four columns of Table IV-27.

Graphic presentations of the creep data are made in Figures IV-68 through IV-72. Figure IV-73 presents an extrapolated summary of 3-hour creep data versus temperature for all material types and conditions.

Table IV-25. Short-Time Tensile Data for Hastelloy C.

Temp	Specimen designation No. 2 lab	Specimen designation LRL	Condition	Ftu	0.2% Fty	0.1% Fty	% Elong.
Room	153D	A53-10	All weld, AW	127.0	84.0	81.5	28.3
	363D	A53-12	All Weld, AW	124.8	82.4	78.9	23.0
	454D	D54-2	All weld, AW	128.1	82.9	80.7	24.0
	155D	C54-7	All weld, SHT	118.7	55.5	49.5	44.0
	159D	No. 2	All weld, SHT	118.5	57.0	47.7	37.0
	475D	X60-1	Across weld, AW	108.8	51.8	48.4	35.0
	475D	X60-2	Across weld, AW	111.7	51.3	46.2	40.0
	471D	Z44-1	Across weld, AW	113.6	47.2	42.7	48.0
	200D	No. 4	Across weld, SHT	115.0	50.5	48.0	39.0
	201D	No. 5	Across weld, SHT	116.5	51.7	48.5	40.0
1200°F	196D	A53-1	Base metal, AR	81.2	33.1	31.6	44.0
	192D	B53-1	Base metal, SHT	86.8	34.0	32.8	53.0
	198D	No. 1	Base metal, SHT	80.2	37.3	36.6	45.0
	199D	No. 3	Base metal, SHT	79.0	34.2	32.3	44.0
	152D	A53-2	All weld, AW	90.0	58.8	56.1	31.0
	453D	D54-4	All weld, AW	95.5	58.9	57.0	37.0
	156D	C54-8	All weld, SHT	84.3	34.8	32.0	52.0
	160D	No. 9	All weld, SHT	84.0	31.0	30.2	42.0
	472D	Z44-2	Across weld, AW	78.4	27.7	24.7	39.0
	473D	Z44-3	Across weld, AW	77.0	28.1	25.2	44.0
	477D	X60-3	Across weld, AW	84.0	31.9	29.1	30.0
	202D	No. 6	Across weld, SHT	77.9	32.0	29.8	34.0
	203D	No. 7	Across weld, SHT	78.1	31.9	29.5	33.0
1350°F	222D	A53-3	Base metal, AR	74.2	34.0	32.8	39.0
	223D	A53-5	Base metal, AR[a]	73.2	34.9	32.0	57.0
	224D	A53-9	Base metal, AR[b]	73.2	35.3	34.0	42.0
	225D	A53-11	Base metal, AR[c]	74.1	33.0	31.4	44.0
	226D	A53-13	Base metal, AR[d]	76.5	35.7	32.5	52.0
	193D	C54-1	Base metal, SHT	78.8	36.0	35.0	40.0
	204D	No. 8	Base metal, SHT	74.3	34.0	32.0	40.0
	205D	No. 10	Base metal, SHT	71.0	33.0	31.1	33.0
	157D	D54-6	All weld, AW	80.0	52.9	51.1	32.0
	452D	D54-7	All weld, AW	80.0	52.7	50.1	22.5
	154D	B53-12	All weld, SHT	82.0	36.0	34.5	46.0
	478D	X60-4	Across weld, AW	67.8	30.0	28.0	34.5
	265D	X60-5	Across weld, AW	88.0	46.0	44.0	35.5
	474D	Z44-4	Across weld, AW	66.0	28.2	26.0	31.0
	206D	No. 14	Across weld, SHT	69.1	29.8	28.0	33.0
	207D	No. 15	Across weld, SHT	73.5	30.5	28.4	35.0
1500°F	194D	D54-1	Base metal, AR	65.9	33.1	32.0	33.0
	195D	B53-3	Base metal, SHT	75.2	45.9	44.6	33.5
	362D	E53-2	All weld, AW	59.9	43.8	25.0	20.5
	451D	D54-8	All weld, AW	62.8	45.5	33.6	43.5
	364D	C54-4	All weld, SHT	56.1	35.1	19.0	38.5
	266D	X60-6	Across weld, AW	71.0	45.1	31.0	30.5
	267D	Z44-5	Across weld, AW	68.0	42.8	23.2	29.0
	268D	Z44-6	Across weld, AW	71.0	42.9	27.0	34.5

Control Specimens						
Temp	Test Location					
1200°F	No. 2 lab, 448D	Base metal, AR	93.0	36.0	31.6	62.5
	LRL	" " "	92.8	31.1	29.3	52.0
	No. 3 lab	" " "	92.5	39.0	--	54.0
1350°F	No. 2 lab, 522D	" " "	69.9	30.7	29.9	46.5
	LRL	" " "	85.0	31.1	28.4	49.3
	No. 3 lab	" " "	78.8	36.6	--	53.0

AR[a] - As received, heat-soaked at 1500°F, 2 hours
AR[b] - As received, heat-soaked at 1500°F, 6 hours
AR[c] - As received, heat-soaked at 1350°F, 2 hours
AR[d] - As received, heat-soaked at 1350°F, 6 hours

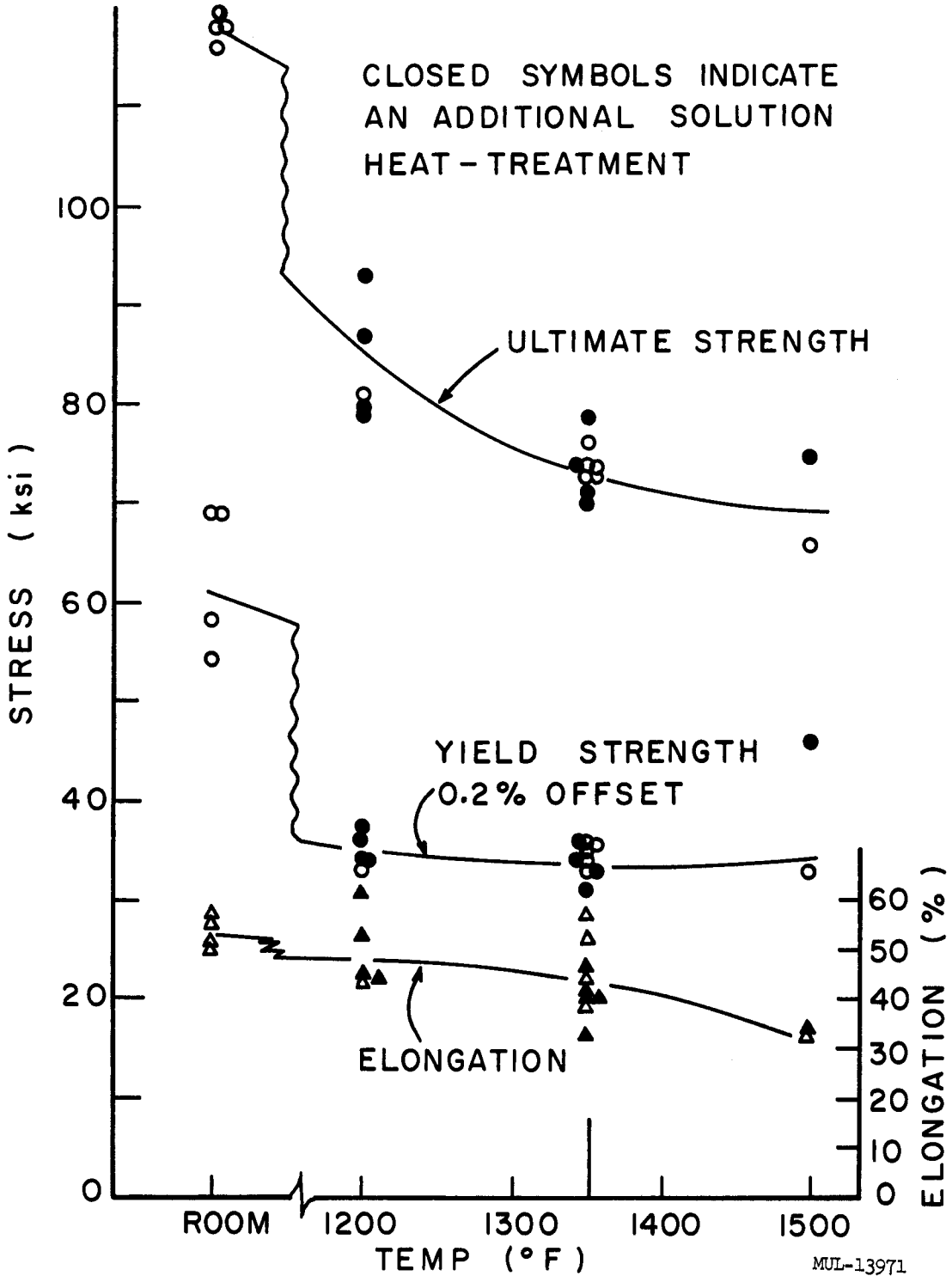

Fig. IV-64. Tensile properties of Hastelloy-C base material.

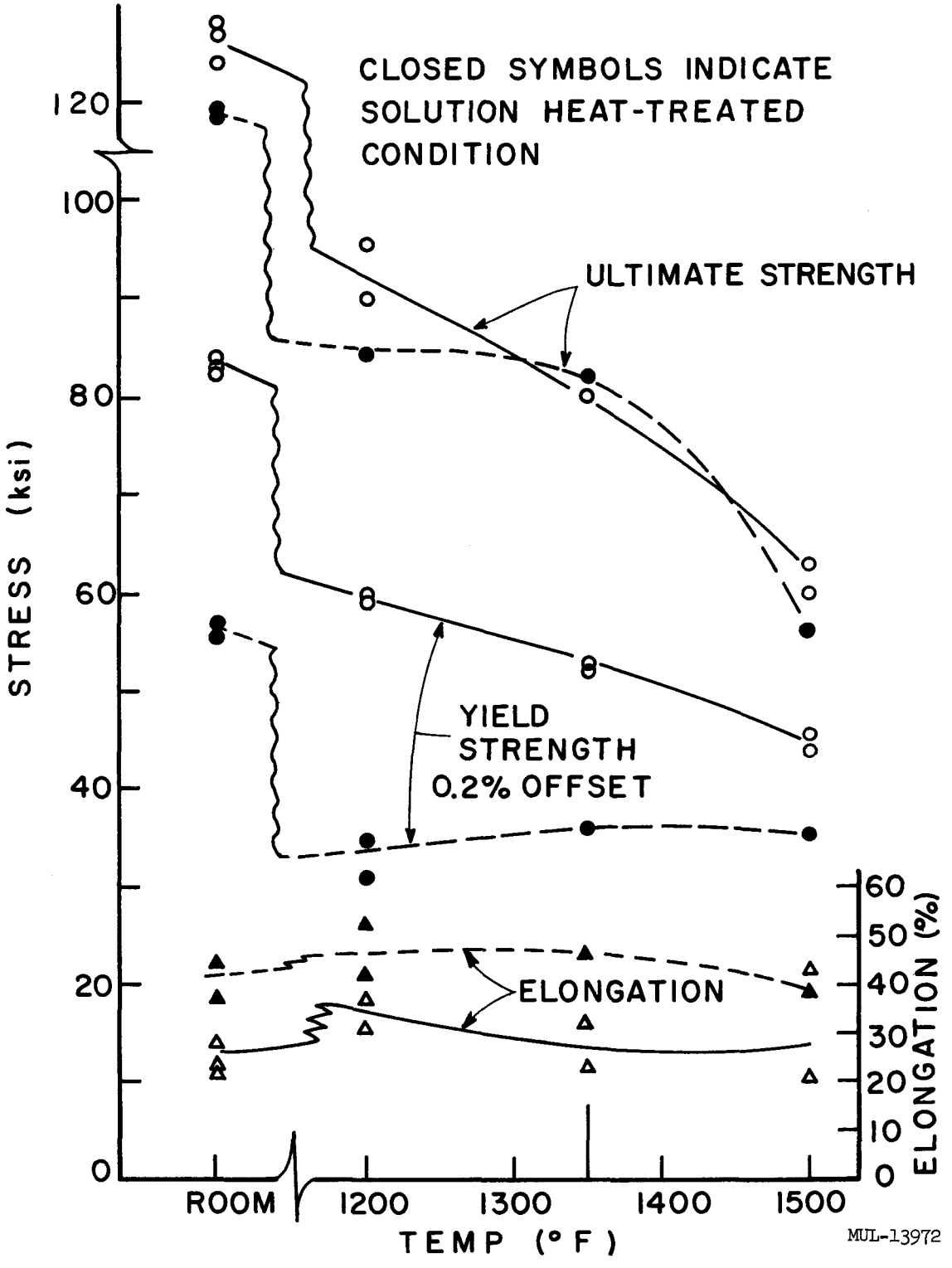

Fig. IV-65. Tensile properties of Hastelloy-C weld metal.

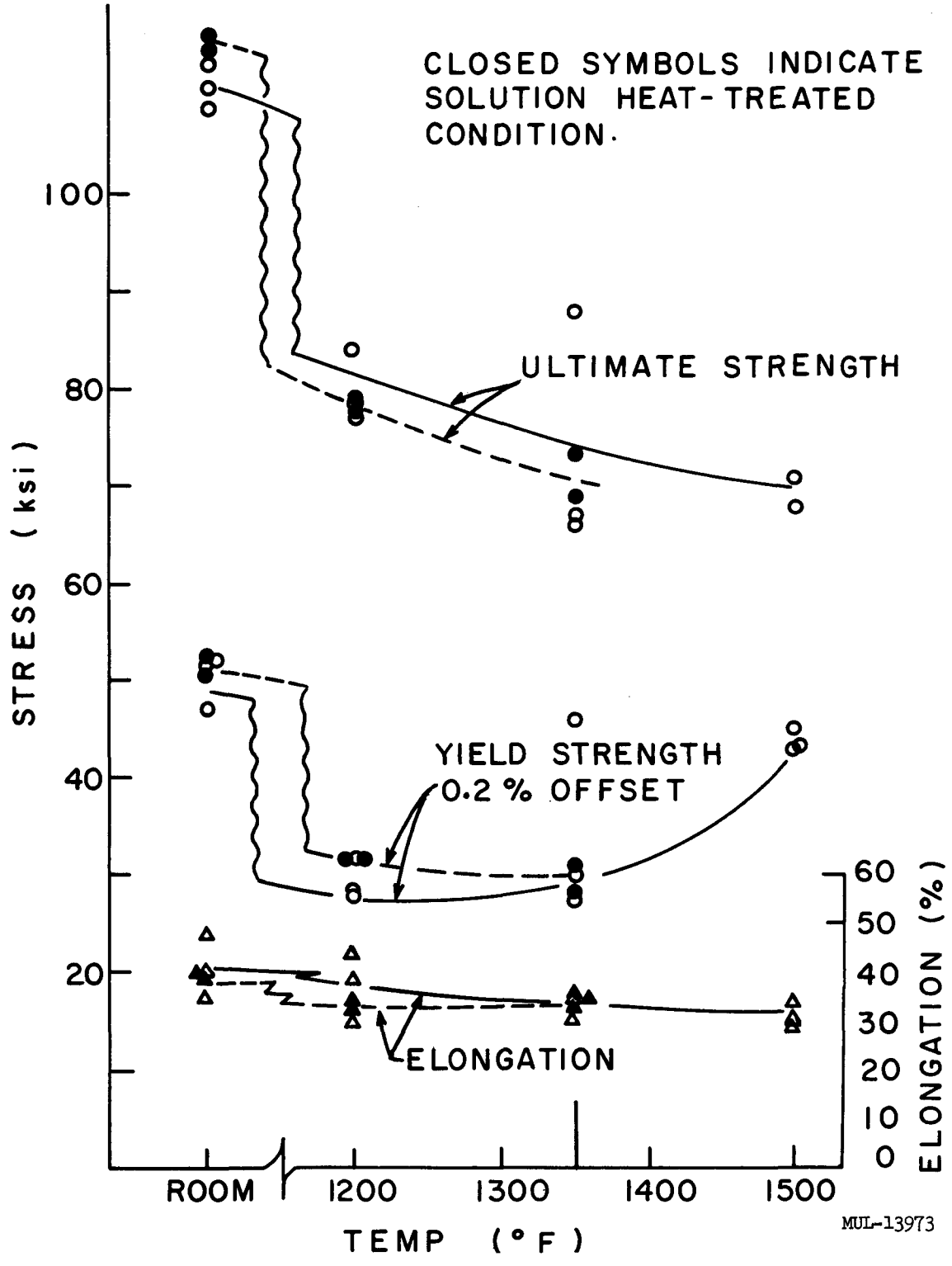

Fig. IV-66. Tensile properties of Hastelloy-C butt welds.

Table IV-26. Creep-Rupture Data for Hastelloy C.

Temp	Specimen designation: No. 2 lab	Specimen designation: LRL	Condition	Stress (ksi)	Rupture life (hr)	% Elongation at rupture
1200°F	273D	X60-7	Across weld, AW	70.0	12.4	35.0
	274D	X60-8	Across weld, AW	70.0	13.0	36.0
	275D	Z44-7	Across weld, AW	70.0	15.6	24.0
	276D	Z44-8	Across weld AW	70.0	16.6	30.0
	210D	No. 16	Across weld, SHT	70.0	3.4	33.0
	211D	No. 17	Across weld, SHT	70.0	4.1	35.0
1350°F	262D	E53-3	Base metal, AR	70.0	0.16[a]	49.0
	356D	E53-12[a]	All weld, AW	35.0[a]	19.1 [a]	15.0[a]
	285D	X60-11	Across weld, AW	50.0	6.7	36.0
	287D	Z44-11	Across weld, AW	50.0	6.3	40 0
	284D	X60-10	Across weld, AW	50.0	3.7	39.0
	288D	Z44-10	Across weld, AW	50.0	7.1	51.0
	283D	X60-9	Across weld, AW	45.0	28.0	10.0
	286D	Z44-9	Across weld, AW	45.0	13.8	28.0
1450°F	251D	E53-9[a]	Base metal, AR	25.0[a]	24.1[a]	58.0[a]
	449D	D54-12[a]	All weld, AW	25.0[a]	26.5[a]	24.0[a]
	371D	C54-12[a]	All weld, SHT	30.0[a]	22.0[a]	25.0[a]
1500°F	250D	D54-11	Base metal, AR	25.0[a]	16.5[a]	37.0[a]
	--	X-6	Base metal, SHT	25.0[a]	12.1[a]	42.0[a]
	278D	X60-13	Across weld, AW	30.0	4.0	20.0
	279D	X60-14	Across weld, AW	30.0	4.35	23.0
	280D	Z44-14	Across weld, AW	30.0	4.35	37.0
	277D	X60-12	Across weld, AW	25.0	11.1	21.0
	282D	Z44-12	Across weld, AW	25.0	15.5	32.0
	281D	Z44-13	Across weld, AW	25.0	16.0	35.0

[a] Results are from extra-long duration hold times in creep testing.

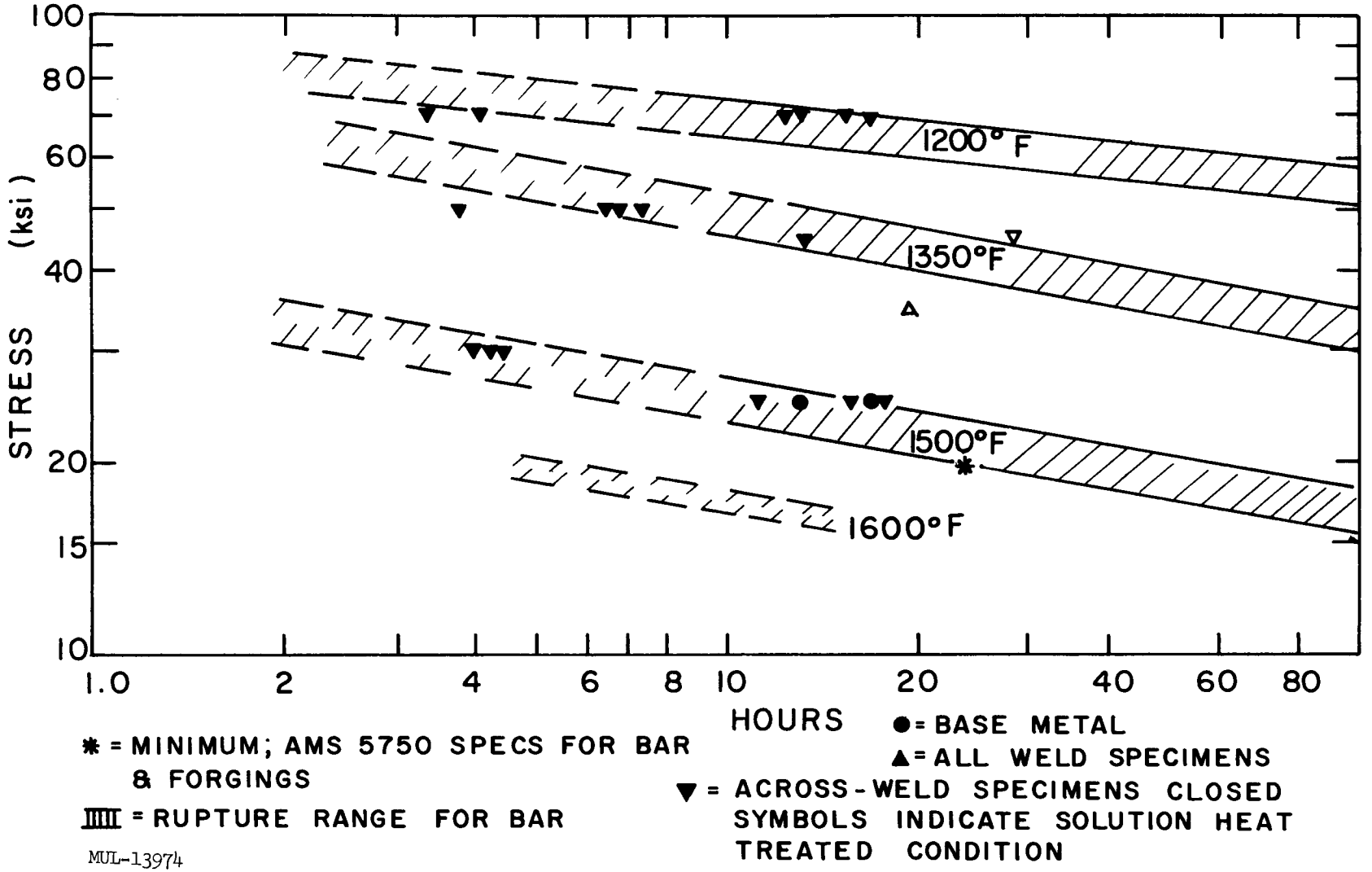

Fig. IV-67. Creep rupture strength of Hastelloy C.

Table IV-27. Creep Data for Hastelloy C.

Temp	Specimen designation No. 2 lab	Specimen designation LRL	Condition	Stress (ksi)	Load strain (%)	Time (hours) to indicated plastic strain(%) 0.3	0.5	0.75	1.0	2.0	3.0	Test duration (hr)	Rupture load (ksi)	Rupture life (hr)	% Elong. at rupture	Remarks
1200°F	208D	No. 11	Base metal, SHT	45.0	2.9	0.25	0.4	2.9	6.6	23.0	--	42.83	82.1	0.138	51.0	2.3% in 30 hr 3.0% in 42.83 hr
	209D	No. 13	Base metal, SHT	45.0	2.6	0.25	0.67	0.67	2.4	17.0	32.8	40.8	--	--	10.0	2.8% in 30 hr
	158D	No. 12	All weld, SHT	45.0	1.8	0.33	0.45	1.8	6.0	30.2	--	39.7	98.6	0.033	42.0	2.0% in 30 hr
	161D	No. 19	All weld, SHT	45.0	2.1	0.80	0.80	1.33	5.0	24.0	43.0	80.3	99.0	0.025	40.0	2.3% in 30 hr
1350°F	249D	C54-5	Base metal, SHT	40.0	0.33	1.1	1.63	2.2	2.7	4.8	6.9	21.93	71.0	0.61	34.0	
	262D	E53-3	Base metal, AR	70.0	--	--	--	--	--	--	--	--	--	0.16	49.0	
	263D	C54-3	Base metal, SHT	35.0	0.21	2.2	2.97	3.8	4.5	7.27	10.1	16.13	51.3	5.3	33.0	
	356D	E53-12	All weld, AW	35.0	0.50	2.0	2.8	3.7	4.5	8.0	11.3	19.1	35.0	19.1	15.0	Ext. loss 3.6% in 13.5 hr
	357D	C54-2	All weld, SHT	35.0	0.10	1.47	2.03	2.7	3.27	5.45	7.97	28.6	60.0	0.001	23.0	3.0% in 8.0 hr
	261D	E53-1	Base metal, AR	30.0	0.20	3.5	4.7	6.0	7.1	--	--	16.8	48.3	7.6	40.0	Ext. loss at 10.4 hr 1.7% in 10.4 hr
	264D	D54-3	Base metal, AR	30.0	0.14	3.1	4.1	5.3	6.3	10.5	--	65.8	44.1	3.27	37.0	2.4% in 12.4 hr
	260D	B53-5	Base metal, SHT	30.0	0.48	2.7	3.9	5.2	6.4	10.83	15.5	20.27	--	--	3.0	3.7% in 18.5 hr 1.0% recovery
	212D	No. 18	Base metal, SHT	30.0	0.06	3.6	4.8	6.3	7.67	13.2	18.6	66.7	--	--	17.0	5.1% in 30 hr 11.0% in 60 hr
	213D	No. 20	Base metal, SHT	30.0	0.17	2.07	3.0	4.3	5.47	12.4	15.7	65.7	69.8	0.008	33.0	7.1% in 30 hr 8.0% in 32.6 hr
	354D	A53-4	All weld, AW	30.0	0.12	2.6	4.4	6.5	8.47	16.2	24.7	64.0	60.0	0.7	25.0	3.6% in 30 hr
	353D	E53-4	All weld, AW	30.0	0.17	2.2	4.0	6.5	8.9	18.6	27.6	41.1	60.0	1.8	30.0	3.3% in 30 hr 4.4% in 41.1 hr
	355D	C54-6	All weld, SHT	30.0	0.15	1.7	2.43	3.23	4.0	6.5	9.43	20.8	60.0	1.3	50.0	6.4% in 20.8 hr
	252D	D54-9	Base metal, AR	25.0	0.15	6.4	9.6	12.4	17.2	32.7	51.5	87.6	--	--	4.0	1.8% in 30 hr 0.08% recovery
	295D	B53-9	Base metal, SHT	25.0	0.18	1.7	2.8	4.01	5.7	12.5	19.5	20.75	--	--	2.0	3.2% in 20.75 hr 0.35% recovery
	269D	B53-13	Base metal, SHT	25.0	0.10	7.0	9.7	12.6	15.7	29.3	44.3	65.65	--	--	5.0	2.05% in 30 hr 0.10% recovery
	214D	No. 21	Base metal, SHT	25.0	0.08	9.2	12.2	15.5	18.6	35.0	--	44.03	82.8	0.008	42.0	1.8% in 30 hr
	215D	No. 22	Base metal, SHT	25.0	0.10	7.0	9.6	12.4	15.0	25.7	36.0	44.0	--	--	4.0	2.5% in 30 hr 0.12% recovery
	351D	A53-7	All weld, AW	25.0	0.10	12.4	20.8	30.6	40.2	--	--	69.3	60.0	1.0	12.0	0.75% in 30 hr 1.7% in 69.3 hr
	352D	B53-7	All weld, SHT	25.0	0.10	3.7	6.0	8.78	11.7	23.0	35.2	69.4	60.0	0.65	25.0	2.6% in 30 hr 5.7% in 69.4 hr

Table IV-27 (continued).

Temp	Specimen designation No. 21ab	Specimen designation LRL	Condition	Stress (ksi)	Load strain (%)	Time (hours) to indicated plastic strain (%) 0.3	0.5	0.75	1.0	2.0	3.0	Test duration (hr)	Rupture load (ksi)	Rupture life (hr)	% Elong. at rupture	Remarks
1400°F	255D	E53-5	Base metal, AR	30.0	0.03	2.05	2.7	3.37	3.9	6.37	8.8	19.0	--	--	6.0	7.5% in 19.0 hr 0.10% recovery
	258D	C54-9	Base metal, SHT	30.0	0.10	1.67	2.5	3.57	4.5	8.2	12.2	19.0	77.0	0.017	38.0	4.7% in 19.0 hr
	445D	X-1	Base metal, SHT	30.0	0.62	1.2	1.73	2.23	2.57	4.7	--	53.8	50.0	0.2	26.0	Ext. loss 2.0% in 4.7 hr
	360D	A53-6	All weld, AW	30.0	0.20	0.46	0.83	1.2	1.93	4.1	--	20.2	49.7	0.8	30.0	8.7% in 20.2 hr
	361D	B53-6	All weld, SHT	30.0	0.23	1.16	1.95	2.7	3.5	--	--	21.9	48.6	1.5	25.0	Ext. loss 1.3% in 4.7 hr
	450D	D54-10	All weld, AW	21.4	0.08	4.5	7.83	12.6	18.1	48.2	100.0	161.0	50.0	1.2	19.0	1.46% in 30 hr
	257D	D54-5	Base metal, AR	25.0	0.15	1.7	2.5	3.4	4.2	7.8	11.95	21.6	52.2	4.0	42.0	5.1% in 21.6 hr
	256D	B53-11	Base metal, SHT	25.0	0.12	1.2	1.7	2.7	3.7	7.9	11.9	19.05	--	--	5.0	4.8% in 19.05 hr 0.25% recovery
	446D	X-2	Base metal, SHT	25.0	0.23	2.3	3.2	4.2	5.2	9.6	15.0	69.6	50.0	0.3	24.0	10.0% in 57 hr
	358D	E53-10	All weld, AW	25.0	0.15	2.7	3.2	4.5	5.7	10.5	15.7	21.5	63.7	0.117	20.0	4.2% in 21.5 hr
	359D	C54-10	All weld, SHT	25.0	0.28	1.5	2.2	3.03	3.93	7.37	10.8	18.9	50.5	1.7	59.0	3.4% in 18.9 hr
1450°F	253D	C54-11	Base metal, SHT	30.0	0.12	0.3	0.4	0.55	0.63	1.13	1.6	8.5	44.8	0.3	50.0	Ext. loss 3.75% in 1.9 hr
	370D	E53-6	All weld, AW	30.0	0.32	0.3	0.47	0.75	1.1	2.37	3.3	14.7	35.0	0.2	25.0	10.3% in 9.5 hr
	371D	C54-12	All weld, SHT	30.0	0.10	0.4	0.55	0.8	1.03	--	--	22.0	30.0	22.0	25.0	Ext. loss 1.4% in 1.3 hr
	251D	E53-9	Base metal, AR	25.0	0.03	1.05	1.5	2.3	2.8	--	--	24.1	25.0	24.1	58.0	Ext. loss 1.5% in 3.7 hr
	254D	C54-13	Base metal, SHT	25.0	0.24	0.83	1.2	1.67	2.07	4.07	6.13	19.5	52.6	0.15	23.0	Ext. loss 3.65% in 7.5 hr
	447D	X-3	Base metal, SHT	25.0	0.10	0.9	1.6	2.1	2.73	5.37	7.8	38.7	35.0	0.30	29.0	10% in 24.37 hr
	368D	E53-7	All weld, AW	25.0	0.05	0.9	1.4	2.1	2.75	5.3	7.75	38.7	35.0	0.30	29.0	10% in 23.25 hr
	449D	D54-12	All weld, AW	25.0	0.05	0.7	1.17	1.7	2.2	4.1	6.0	26.5	25.0	26.5	24.0	4.2% in 8.3 hr
	369D	B53-10	All weld, SHT	25.0	0.20	2.45	3.5	4.8	6.0	10.8	15.8	36.0	35.0	18.3	31.0	Ext. loss 3.4% in 17 hr
1500°F	250D	D54-11	Base metal, AR	25.0	0.15	0.4	0.503	0.73	0.92	1.7	2.6	16.5	25.0	16.5	37.0	3.9% in 3.9 hr
	--	X-6	Base metal, SHT	25.0	0.05	0.4	0.503	0.7	0.87	1.5	--	12.1	25.0	12.1	42.0	
	372D	E53-8	All weld, AW	25.0	0.10	0.3	0.58	0.83	1.16	2.27	3.27	15.1	35.0	0.3	30.0	6.0% in 6.2 hr
	373D	B53-4	All weld, SHT	25.0	0.10	0.25	0.383	0.50	0.67	1.2	--	10.4	35.0	0.25	40.0	Ext. loss 2.0% in 1.2 hr

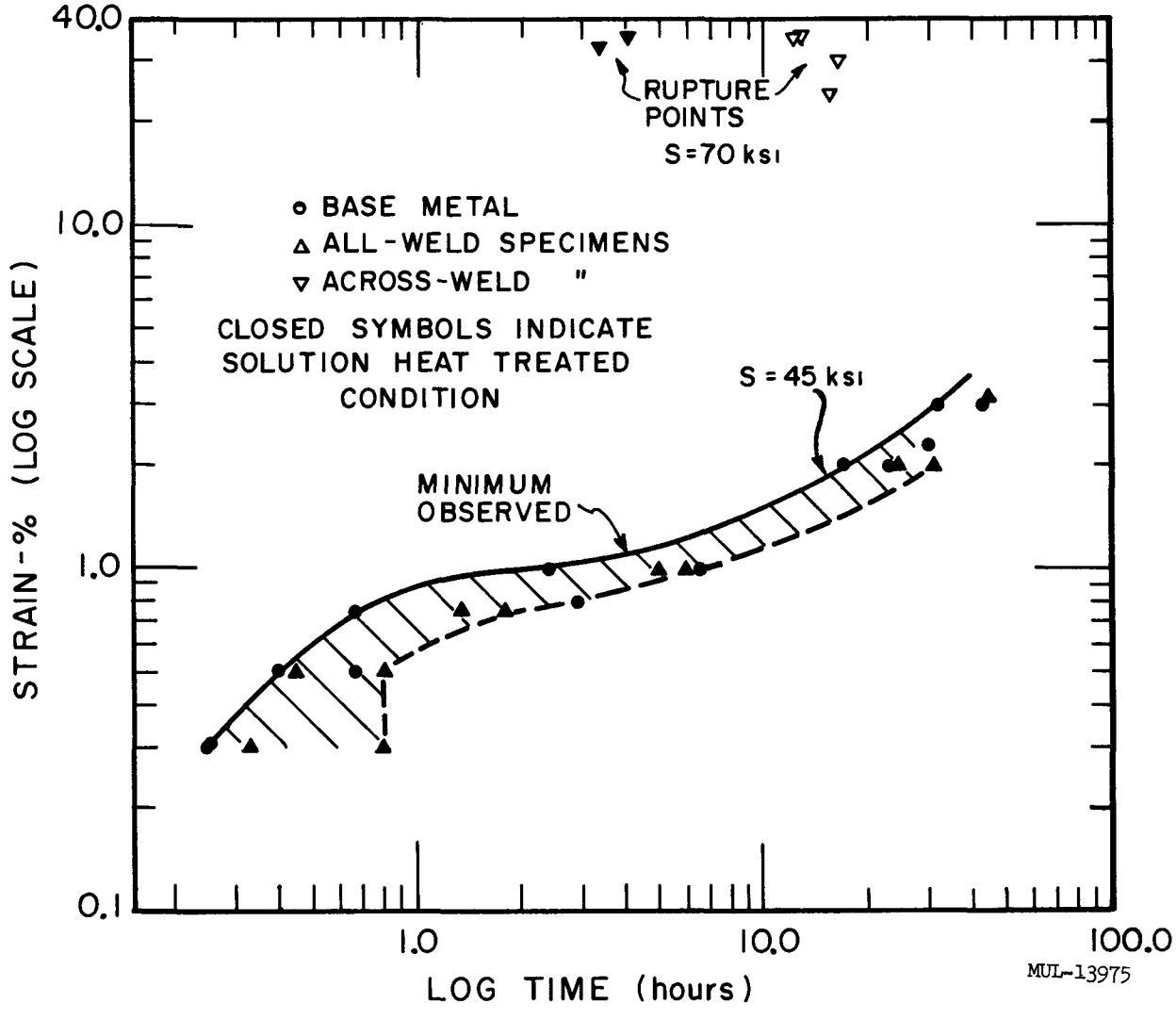

Fig. IV-68. Creep of Hastelloy C at 1200°F.

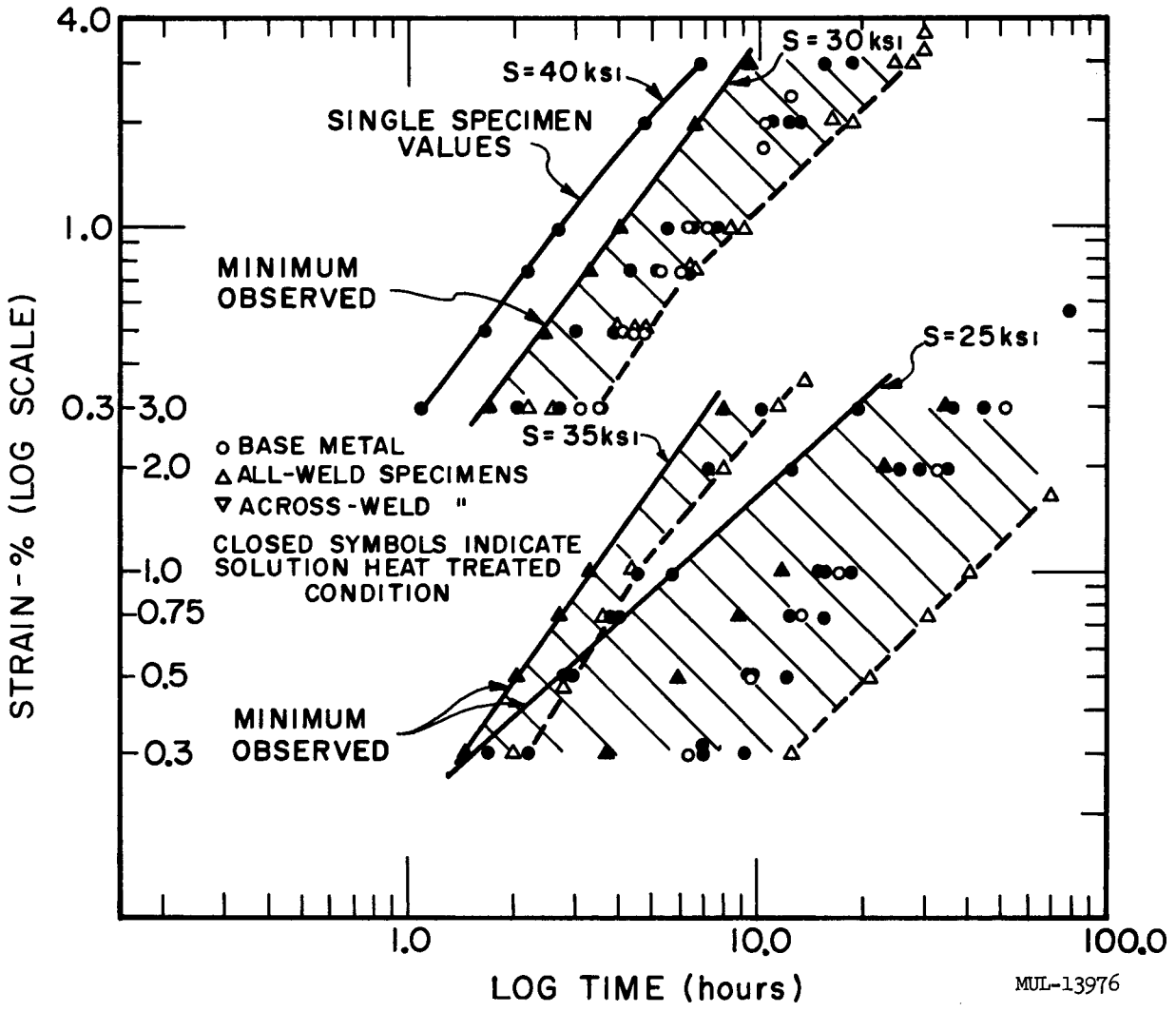

Fig. IV-69. Creep of Hastelloy C at 1350°F.

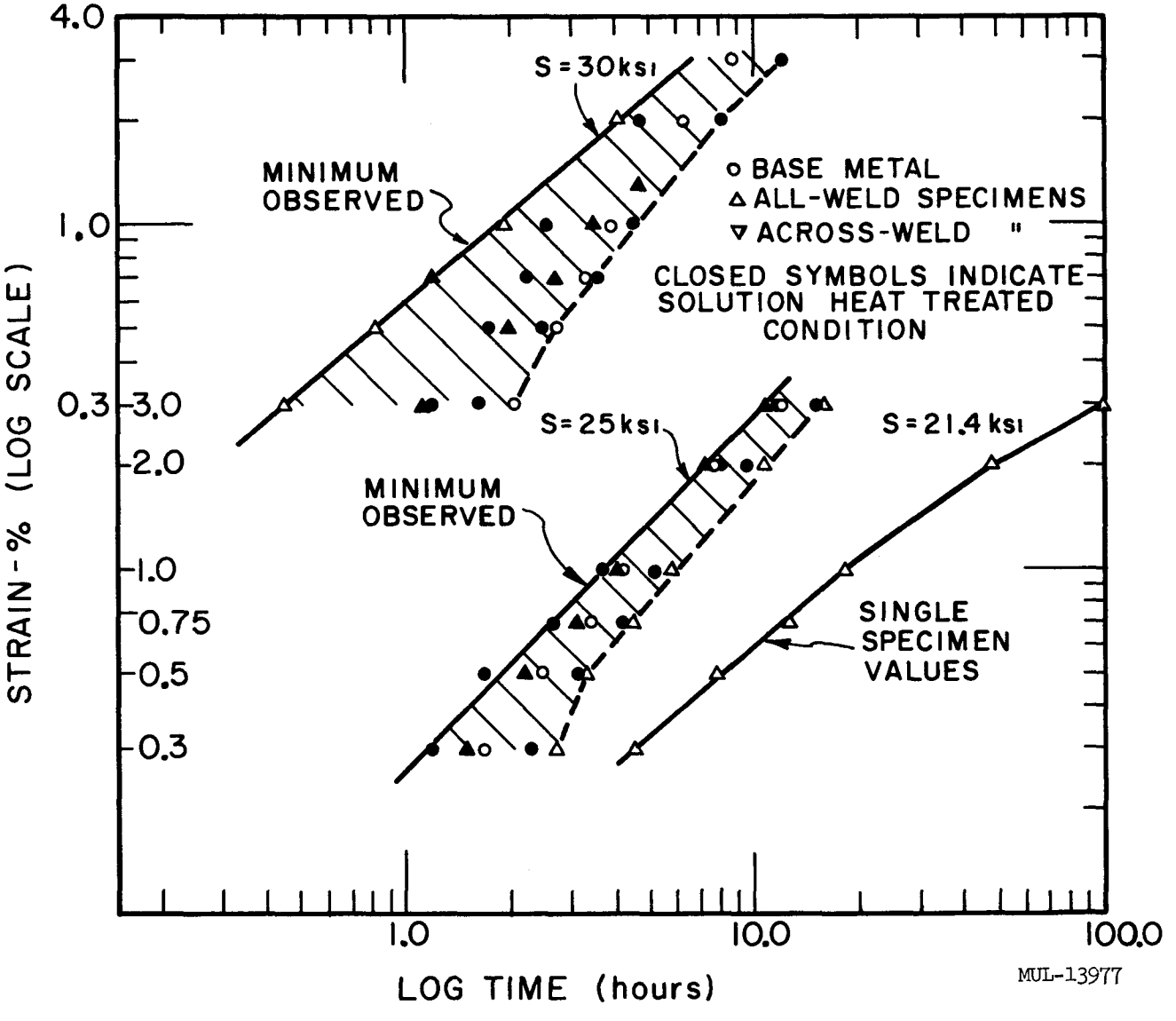

Fig. IV-70. Creep of Hastelloy C at 1400°F.

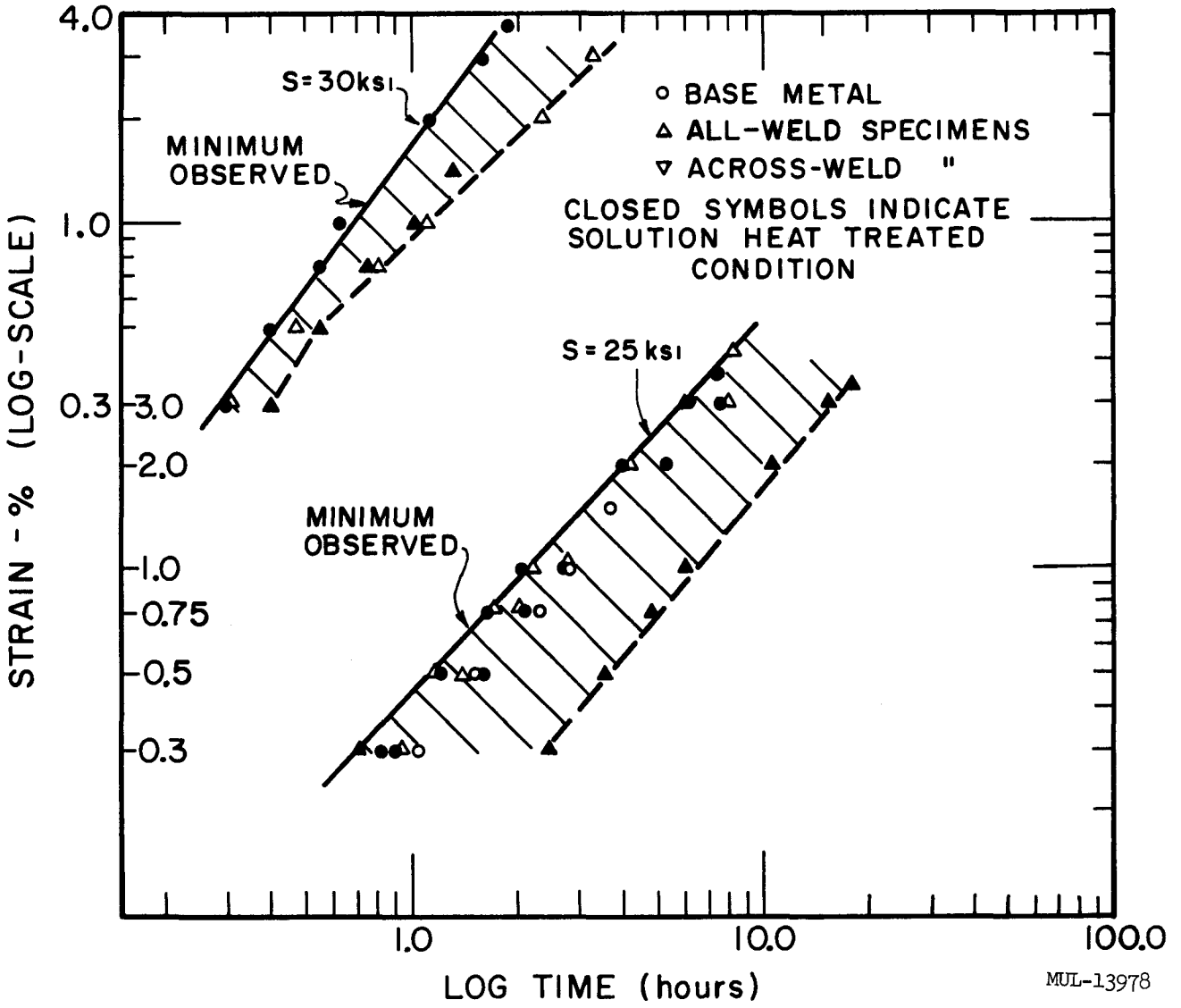

Fig. IV-71. Creep of Hastelloy C at 1450°F.

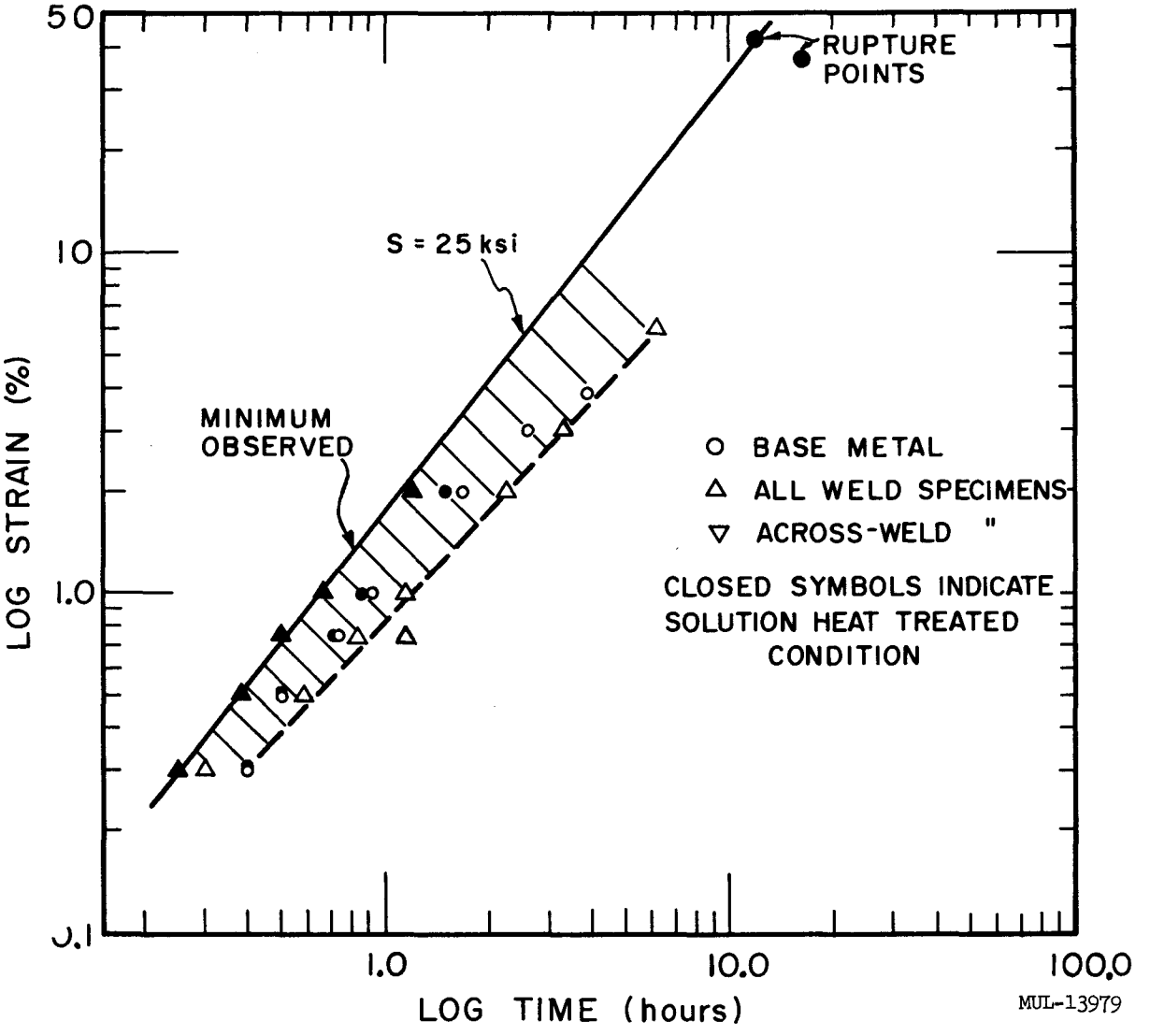

Fig. IV-72. Creep of Hastelloy C at 1500°F.

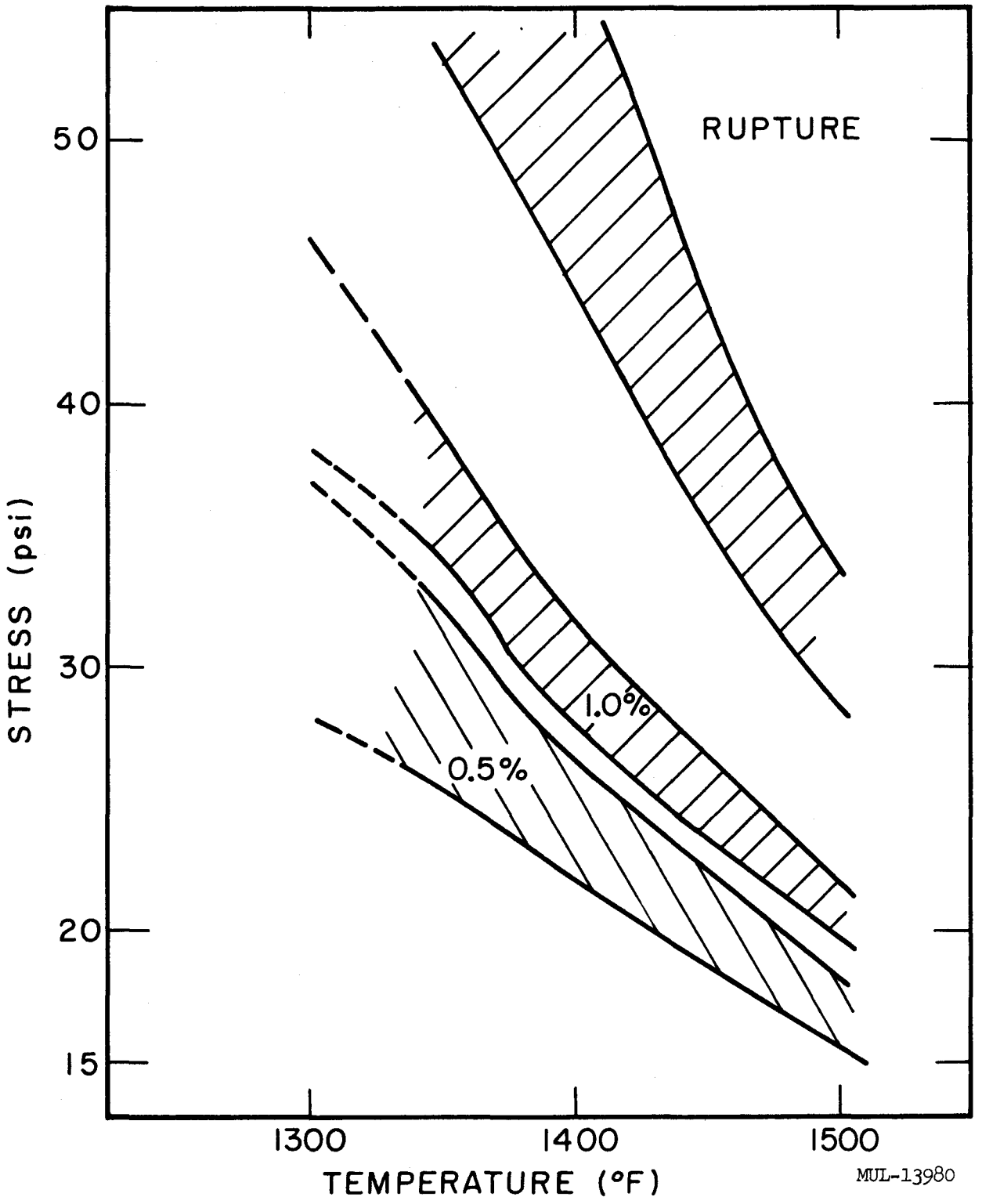

Fig. IV-73. Three-hour creep properties of Hastelloy C. Based on: (1) sheet properties per supplier; (2) 5/16-in. and 3/4-in. plate base metal; (3) weld metal in as-welded and solution-heat-treated conditions; and (4) across weld in as-welded and solution-heat-treated conditions (rupture only).

Cyclic Creep Tests. Cyclic creep tests were conducted on six specimens at a temperature of 1350°F and stress of 25,000 psi. Heating rates of 200°F/second were utilized for each cycle with a hold time at temperature of 5 minutes. Manual loading to the desired stress level was accomplished within a 30 to 60 second limit. Each cycle duration was 15 minutes with strain and/or deformations measured by:

1. A differential extensometer, with associated X-Y recordings of stress and strain on loading and recovery;
2. A calibrator (sensitivity 1 micron) for measurements of the gauge length between cycles.

All test data are given in Table IV-28 and illustrated in Figures IV-74, IV-75, and IV-76. These graphic illustrations are compared to the observed creep curves for the 1350°F - 25,000 psi stress level. (See Figure IV-69.) As may be noted, considerable deviation in recovery from cycle to cycle occurred and some investigation on the anelastic properties (i.e., Bauschinger effects, hysteresis in loading and unloading) of the extremely ductile Hastelloy-C alloy might be profitable from a purely theoretical standpoint, but would not affect the Tory II-C application of this material. For ease of presentation, discontinuous points are omitted to provide a smooth, continuous creep curve from the cyclic tests performed.

Conclusions. Superior yield strength at room temperature for a given heat does not indicate superior yield strength at elevated temperatures. As expected, the yield strengths of the welded specimens were higher and the percent elongations were lower than the base metal results. After solution heat-treating, the weld metal properties agreed with base metal properties. The results of the control tensile specimens (three test sources) indicated a great deal of scatter. The causes of this scatter will be investigated further.

Acceptable weld flaws found by penetrant and radiographical inspection did not affect the strengths or ductility of the specimens.

The creep results at a given temperature and load indicated superior or inferior creep properties for the material in a given condition. This is due to the small number of identical specimens tested at any one temperature and load. The combination of all the creep results indicates agreeable creep ranges for all the types and conditions of materials tested and advertised data for sheet metal (see Fig. IV-73). The cyclic creep test results

Table IV-28. Cyclic Creep Test Data for Hastelloy C.

Cycle	Thermal expansion ($\times 10^{-3}$)	Loading time (sec)	Load strain ($\times 10^{-3}$)	Total creep in 900 sec ($\times 10^{-3}$)	Total strain in 900 sec ($\times 10^{-3}$)	Recovery ($\times 10^{-3}$)	Deformation per cycle ($\times 10^{-3}$)	Total deformation ($\times 10^{-3}$)	Calibrator - total indicated deformation ($\times 10^{-3}$)
Specimen: D54-13 (270D) base metal, as received									
1	19.35 in.	39.5	2.4 in.	1.20 in.	3.6 in.	2.30 in.	1.30 in.	1.3 in.	1.87 in.
2	21.00	39.5	2.5	0.30	2.8	2.50	0.30	1.6	2.14
3	23.00	59.5	2.1	0.31	2.41	2.00	0.40	2.0	2.46
4	19.50	35.4	2.0	0.35	2.35	2.22	0.13	2.13	2.85
5	20.10	33.0	2.3	0.35	2.65	2.25	0.40	2.53	4.06
6	19.60	59.0	2.8	0.31	3.11	2.21	0.90	3.43	2.81
7	20.40	34.3	2.7	0.60	3.30	2.30	1.00	4.43	3.28
8	20.20	47.0	2.7	0.55	3.25	2.40	0.85	5.28	3.72
9	19.90	37.0	2.4	0.25	2.65	2.15	0.50	5.78	3.64
10	20.90	48.5	2.6	0.55	3.15	2.35	0.80	6.58	3.48
11	21.00	35.5	2.5	0.50	3.00	2.30	0.70	7.28	3.80
12	19.90	26.0	1.9	0.50	2.40	2.10	0.30	7.58	4.35
13	21.00	50.0	2.5	0.60	3.10	2.45	0.65	8.23	4.46
14	21.90	49.0	2.0	0.40	2.40	2.40	0.00	8.23	4.62
15	20.00	50.1	2.5	0.40	2.90	2.30	0.60	8.83	4.98
16	--	50.7	2.6	0.58	3.18	2.38	0.80	9.63	6.31
17	21.50	51.5	2.1	0.50	2.60	2.30	0.30	9.93	5.29
18	20.80	35.3	2.2	0.60	2.80	2.22	0.58	10.51	5.80
19	20.80	48.5	2.7	0.50	3.20	2.35	0.85	11.36	6.16
20	20.60	58.0	2.3	0.65	2.95	2.45	0.50	11.86	6.87
Ave. per cycle	20.60	44.36	2.395	0.50	2.895	2.296	0.593		
Specimen: E53-11 (271D) base metal, as received									
1	19.80 in.	39.5	2.60 in.	0.30 in.	2.90 in.	2.20 in.	0.70 in.	0.70 in.	1.87 in.
2	20.00	39.0	2.25	0.50	2.75	2.27	0.50	1.20	-2.42
3	23.00	58.0	2.30	0.36	2.66	2.05	0.61	1.81	-2.07
4	20.10	35.4	2.50	0.40	2.90	2.32	0.58	2.39	3.01
5	19.50	35.5	2.30	0.30	2.60	2.30	0.30	2.69	2.81
6	19.50	60.0	2.45	0.45	2.90	2.35	0.55	3.24	2.97
7	19.90	33.2	2.30	0.35	2.65	2.35	0.30	3.54	3.48
8	19.30	46.3	2.35	0.50	2.85	2.35	0.50	4.04	3.09
9	20.20	38.8	2.25	0.35	2.60	2.28	0.32	4.36	-5.26
10	19.60	48.5	2.50	0.40	2.90	2.32	0.58	4.94	-5.43
11	20.90	33.3	2.40	0.15	2.55	2.40	0.15	5.90	3.84
12	20.00	24.5	2.50	0.25	2.75	2.40	0.35	5.44	4.07
13	20.90	50.0	2.75	0.40	3.15	2.65	0.50	5.94	4.78
14	19.70	50.0	2.50	0.60	3.10	2.50	0.60	6.54	4.35
15	21.10	50.0	2.70	0.50	3.20	2.50	0.70	7.24	4.95
16	20.70	52.4	2.80	0.50	3.30	2.60	0.80	8.04	5.61
17	--	49.3	2.25	0.55	2.80	2.25	0.55	8.59	4.76
18	20.10	34.1	2.35	0.25	2.60	2.40	0.20	8.79	5.89
19	21.20	52.2	2.40	0.60	3.00	2.32	0.68	9.47	5.69
20	20.90	57.0	2.20	0.30	2.50	2.30	0.20	9.67	6.83
Ave. per cycle	20.38	44.3	2.43	0.40	2.83	2.36	0.483		
Specimen: E53-13 (272D) base metal, as received									
1	19.00 in.	20.0	2.22 in.	0.35 in.	2.57 in.	2.10 in.	0.47 in.	0.47 in.	-0.83 in.
2	21.00	35.0	2.17	0.33	2.50	2.09	0.41	0.88	-0.12
3	20.00	34.5	2.25	0.25 (9 min)	2.50 (9 min)	*	*	44.5 %	*
			* - Equipment malfunction, specimen ruptured						
Ave. per cycle	20.00	29.8	2.18	0.34	2.52	2.095	0.44		

Table IV-28 (continued).

Cycle	Expansion ($\times 10^{-3}$)	Loading time (sec)	Load strain ($\times 10^{-3}$)	Total creep in 900 sec ($\times 10^{-3}$)	Total strain in 900 sec ($\times 10^{-3}$)	Recovery ($\times 10^{-3}$)	Deformation per cycle ($\times 10^{-3}$)	Total deformation ($\times 10^{-3}$)	Calibrator - total indicated deformation ($\times 10^{-3}$)
	Specimen: A53-8 (365D) all weld, as welded								
1	19.80 in.	37.5	2.70 in.	1.40 in.	4.10 in.	2.50	1.60 in.	1.60 in.	1.93 in.
2	21.00	32.5	2.50	0.95	3.45	2.80	0.65	2.25	-12.28
3	20.20	33.0	2.50	0.80	3.30	2.63	0.67	2.92	2.92
4	20.00	35.5	2.40	0.80	3.20	2.30	0.90	3.82	3.31
5	20.70	35.5	2.50	0.70	3.20	2.60	0.60	4.42	3.35
6	19.50	37.3	2.50	0.70	3.20	2.42	0.78	5.20	3.66
7	20.50	37.0	2.55	0.55	3.10	2.60	0.50	5.70	4.10
8	19.90	37.4	2.40	0.64	3.04	2.60	0.44	6.14	3.82
9	21.00	29.5	2.50	0.60	3.10	2.55	0.55	6.69	3.70
10	19.30	31.0	2.35	0.50	2.85	2.45	0.40	7.09	4.03
11	21.10	35.3	2.30	0.38	2.68	2.38	0.30	7.39	4.37
12	20.90	35.3	2.15	0.45	2.60	2.45	0.15	7.54	4.69
13	20.10	37.8	2.45	0.40	2.85	2.60	0.26	7.80	5.44
14	20.80	38.2	2.52	0.48	3.00	2.60	0.40	8.20	4.81
15	20.60	36.5	2.60	0.45	3.05	2.50	0.55	8.75	5.63
16	20.10	37.1	2.50	0.33	2.83	2.50	0.33	9.08	5.20
17	20.80	39.0	2.50	0.50	3.00	2.70	0.30	9.38	6.22
18	19.90	30.0	2.80	0.80	3.60	2.90	0.70	10.08	6.46
19	21.90	28.5	2.20	0.40	2.60	2.65	0.50	10.58	6.46
20	20.10	35.5	2.50	0.45	2 95	2.55	0.40	10.98	6.85
Ave. per cycle	20.41	35.0	2.471	0.614	3.085	2.564	0 549		
	Specimen: B53-8 (366D) all weld, solution heat treated								
1	20.00 in.	36.3	2.4 in.	0.92 in.	3.32 in.	2.30 in.	1.02 in.	1.02 in.	1.69 in.
2	20.50	33.5	2.35	0.55	2.90	2.30	0.60	1.62	1.73
3	20.50	36.2	2.25	0.60	2.85	2.23	0.62	2.24	2.28
4	20.00	36.1	2.38	0.27	2.65	2.16	0.49	2.73	2.52
5	20.10	35.3	2.20	0.52	2.72	2.32	0.40	3.13	3.58
6	20.00	34.5	2.20	0.60	2.80	2.32	0.48	3.61	3.66
7	20.00	36.2	2.00	0.47	2.47	2.13	0.34	3.95	3.86
8	19.30	28.5	2.20	0.40	2.67	2.30	0.30	4.25	4.37
9	19.90	30.0	2.30	0.40	2.70	2.25	0.45	4.70	4.71
10	19.40	35.5	2.30	0.35	2.65	2.23	0.42	5.12	5.44
11	20.20	36.3	2.40	0.40	2.80	2.32	0.48	5.60	6.15
12	20.30	38.3	2.10	0.45	2.55	2.30	0.25	5.85	3.90
13	19.40	37.5	2,12	0.55	2.67	2.28	0.39	6.24	6.58
14	19.90	30.0	2.40	0.60	3.00	2.40	0.60	6.84	4.61
15	21.10	37.8	2.60	0.45	3.05	2.60	0.45	7.29	6.97
16	21.20	40.5	2.40	0.50	2.90	2.40	0.50	7.79	7.01
17	20.00	40.0	2.50	0.50	3.00	2.30	0.70	8.49	7.48
18	20.80	27.5	2.50	0.40	2.90	2.42	0.48	8.97	7.64
19	20.80	32.8	2.30	0.80	3.10	2.45	0.65	9.62	8.55
20	--	33.7	2.30	0.60	2.90	2.28	0.62	10.24	8.39
Ave. per cycle	20.17	34.8	2.31	0.516	2.826	2.31	0.516		

Table IV-28 (continued).

Specimen: B53-2 (367D) all weld, solution heat treated

Cycle	Expansion ($\times 10^{-3}$)	Loading time (sec)	Load strain ($\times 10^{-3}$)	Total creep in 900 sec ($\times 10^{-3}$)	Total strain in 900 sec ($\times 10^{-3}$)	Recovery ($\times 10^{-3}$)	Deformation per cycle ($\times 10^{-3}$)	Total deformation ($\times 10^{-3}$)	Calibrator - total indicated deformation ($\times 10^{-3}$)
1	20.40 in.	36.1	2.30 in.	0.83 in.	3.13 in.	2.10 in.	1.03 in.	1.03 in.	-0.04 in.
2	20.00	33.0	2.38	0.57	2.95	2.25	0.70	1.73	0.37
3	20.50	36.3	2.10	0.20	2.32	2.10	0.20	1.93	-3.31
4	19.70	36.1	2.30	0.42	2.72	1.80	0.92	2.85	1.06
5	20.30	36.5	2.45	0.65	3.10	2.43	0.67	3.52	0.91
6	20.70	36.0	2.40	0.50	2.90	2.35	0.55	4.07	1.10
7	19.50	33.0	2.20	0.35	2.55	2.70	0.47	4.54	2.04
8	19.90	36.0	2.30	0.56	2.86	2.32	0.54	5.08	2.21
9	20.20	37.1	2.25	0.70	2.95	2.35	0.60	5.68	1.86
10	20.20	36.8	2.05	0.60	2.65	2.20	0.45	6.13	1.62
11	19.70	35.5	2.45	0.55	3.00	2.35	0.65	6.78	2.84
12	19.90	26.0	2.30	0.35	2.65	2.25	0.40	7.18	3.16
13	--	38.0	2.20	0.45	2.65	2 30	0.35	7.53	3.59
14	21.40	38.3	2.15	0.55	2.70	2.35	0.35	7.88	4.42
15	20.90	39.6	2.05	0.40	2.45	2.35	0.10	7.98	4.49
16	21.10	38.0	2.70	0.50	3.20	2.40	0.80	8.78	5.32
17	20.00	37.5	2.55	0.45	3.00	2.35	0.65	9.43	4.73
18	22.00	32.3	2.40	0.60	3.00	2.30	0.67	10.10	5.87
19	21.00	31.0	2.10	0.60	2.70	2.50	0.20	10.30	6.62
20	20.20	35.0	1.90	0.60	2.50	2.41	0.09	10.39	6.62
Ave. per cycle	21.53	35.4	2.28	0.521	2.801	2.31	0.519		

Test procedure

1. Heat specimen to 1350°F
2. Hold at temperature 5 minutes
3. Apply load (S = 25 ksi) in 30-60 seconds
4. Hold at load and temperature for 15 minutes
5. Remove load and temperature
   Minimum downtime - 2 hours
6. Repeat above cycle 20 times
7. Record all deformations

Test equipment

1. Machine - E. T. T. M.
2. Heating - resistance
3. Heating rate - 200°F/second
4. Extensometer - TMC differential extensometer
5. Gauge length - 2.0 inches
6. Strain recorder - Mosely Autograf X-4 recorder
7. Gauge length measurements - Mann calibrator (sensitivity 1 micron)

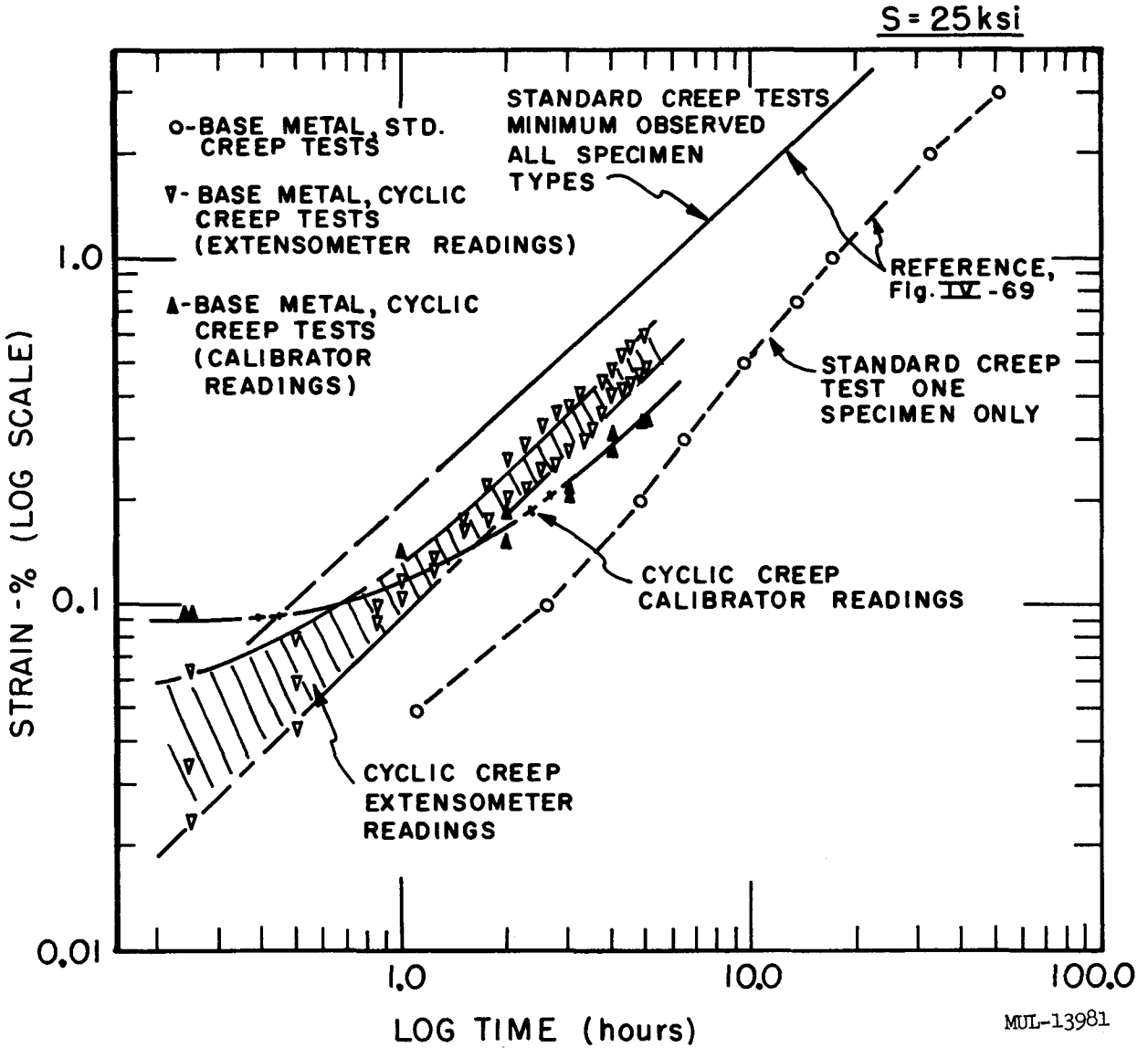

Fig. IV-74. Cyclic creep of Hastelloy-C base metal at 1350°F.

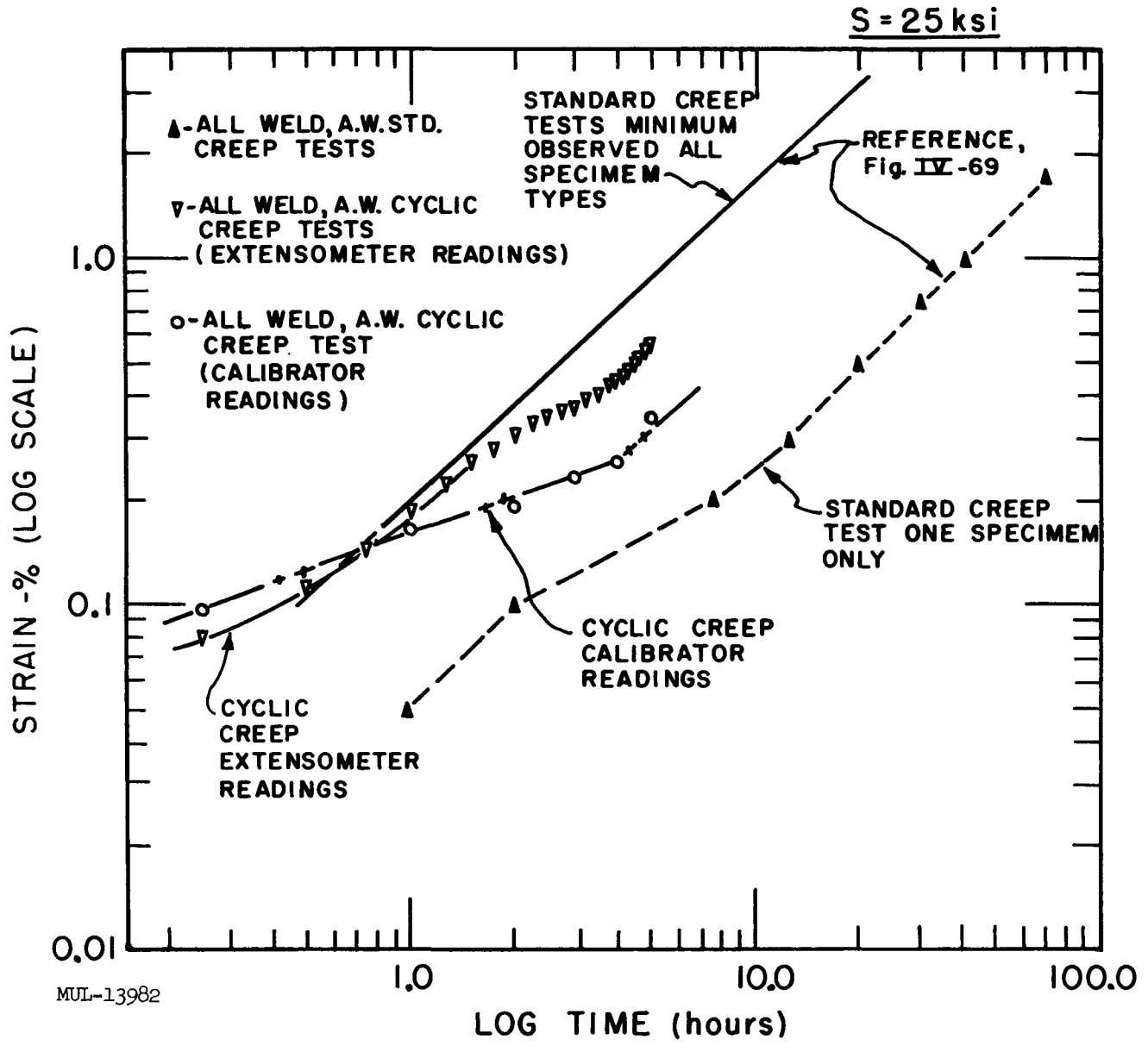

Fig. IV-75. Cyclic creep of Hastelloy-C weld metal in the as-welded condition at 1350°F.

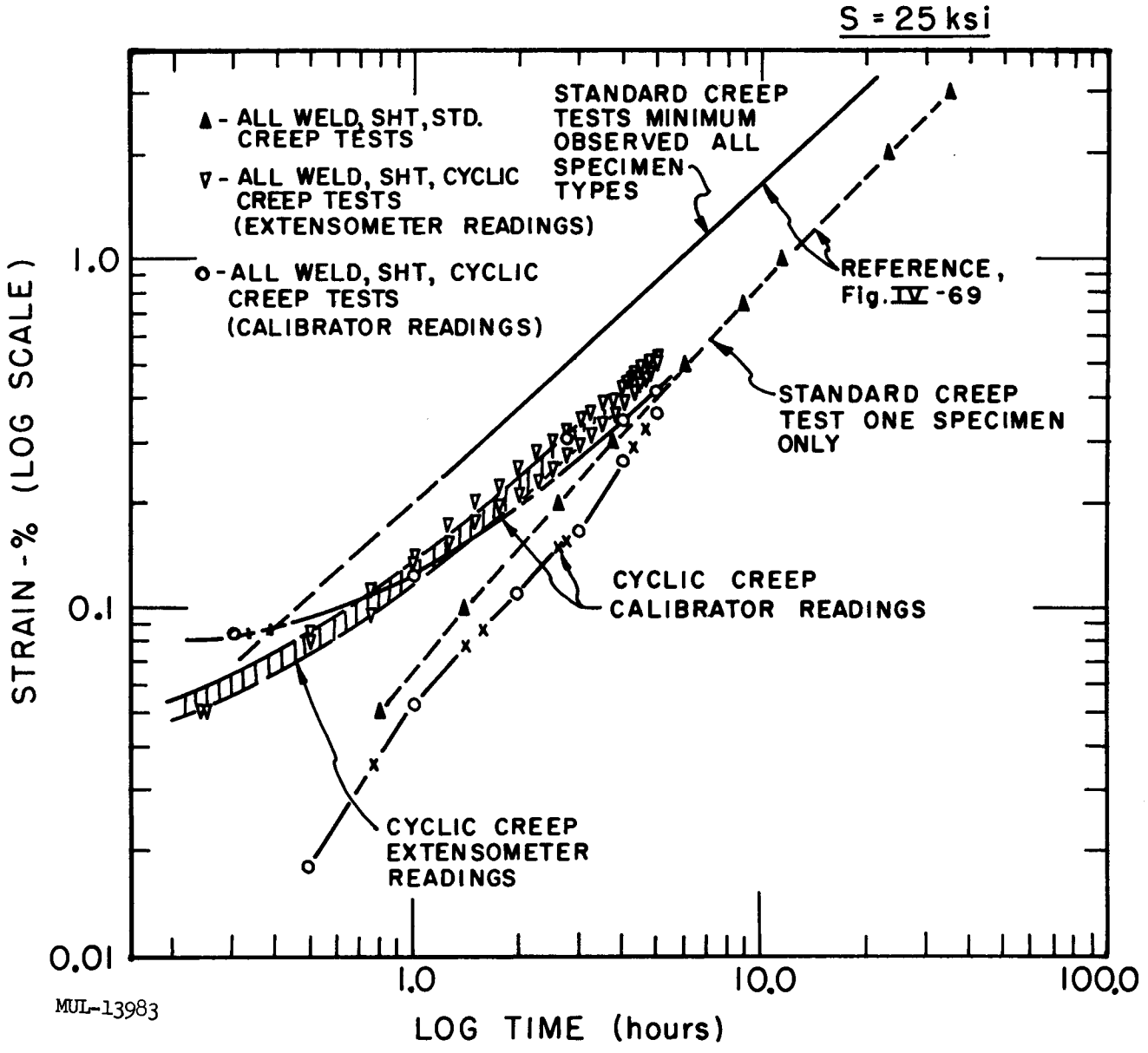

Fig. IV-76. Cyclic creep of Hastelloy-C weld metal in the solution-annealed condition at 1350°F.

agreed with the standard creep results and indicated that the material does not have a ratcheting or other similar detrimental property that would limit its use in the Tory II-C environment.

If the material is used at elevated temperatures below 1250°F for short periods of time (i. e., about 10 hours) the short-time yield or ultimate strength would be the governing criterion. For temperatures above 1250°F, creep may be the governing criterion.

Side-Support Springs Fatigue Test

Several specimens of the brazed side-support springs (René 41) were fatigue tested at 1400°F. The springs are similar in shape to those used in the "slice test" which is discussed later in the report. The braze joints in these samples were preliminary and, in fact, proved to be the critical region. The room-temperature load-deflection curve was measured for two springs to a load of 500 lb. The variation was linear and the spring constant for both was 2100 lb/in. In a typical test procedure, the spring was mounted on its holder in the furnace, and the eccentric backed off (see Fig. IV-77). The spring was then moved forward until it just contacted the loading plate. In this position the temperature was raised to 1400°F. The thermal expansion of the spring caused an initial preload of about 200 lb. The motor was then turned on and the transmitted load recorded. Preliminary results are given in Table IV-29 and Fig. IV-78. In order to determine the lifetime of the spring itself, a riveted specimen will be used. A much improved braze will also be available.

This spring model is designed to take up the thermal expansion loads only. A similar, but smaller, spring will support the g-loads.

Seven-to-One Hole Transition Sections

To aid in the selection of a suitable geometry for transition sections for Tory II-C, four different geometries were tested for total pressure losses. In these tests the transition sections discharged into a plenum of cross-sectional area equal to the seven tubes. This was done to eliminate sudden expansion losses associated with earlier test configurations, hence, losses are shown for the transition section only. (See Fig. IV-79.)

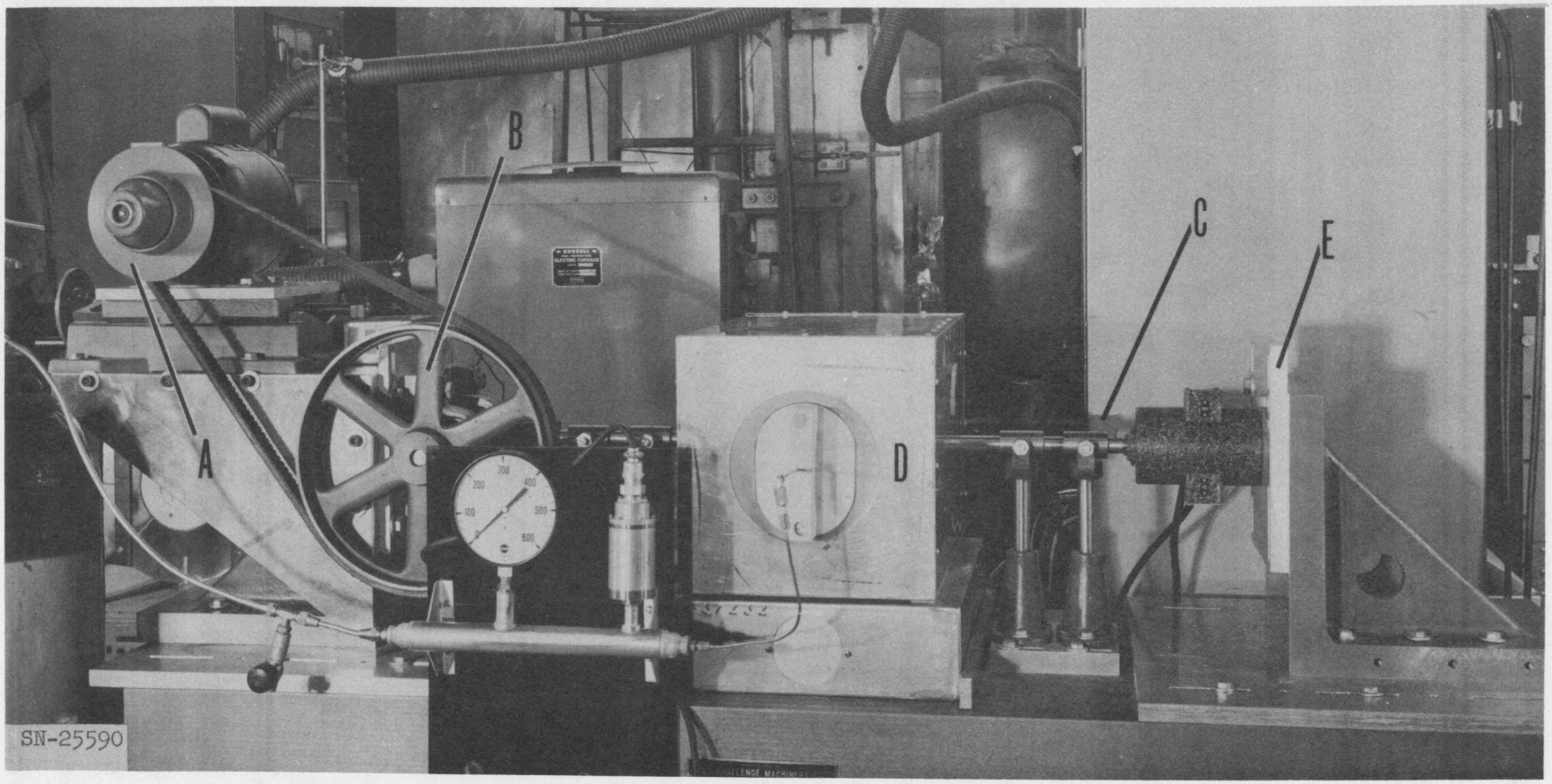

Fig. IV-77. Apparatus used for both the air-pad and side-support spring tests.
A. Motor-driven variable sheave.
B. Driving pulley which rotates an eccentric mounted to a shaft. The shaft passes into the furnace.
C. Output shaft on which is mounted the spring.
D. The furnace.
E. The load cell which senses the transmitted load.

Table IV-29. Preliminary Results, Side-Support Springs Fatigue Tests.

Run No.	Spec No.	Temp (°F)	Oscillating deflection total stroke (in.)	Frequency (rpm)	Preload therm expansion (lb)	Max stress σ (ksi) initial	Oscillating stress σ (ksi) initial	No. cycles to fail	Remarks
1	2	1400	0.225	700	200	60	40	10^5	No fail
2	8	Rm	0.350	--	--	--	--	1	Braze failed
3	1	1400	0.350	550	200	67	16	18×10^3	
4		1400	0.350	--	200	--	--	1	Braze failed
5	A(R-235 slice spring)	1400	0.350	550	200	73	16	5×10^3	Braze survived. 0.150 permanent set in spring.

The stresses in the springs:

$\sigma \doteq 100\ P$

In terms of the deflection, d, in inches and using 2100 lb/in. as the room-temperature spring constant for the René 41 springs.

$\sigma_{(Rm)} \doteq 2 \times 10^5\ d$

Using E_{1400}/E_{Rm} as the scaling factor

$\sigma_{(1400)} \doteq 1.7 \times 10^5\ d$

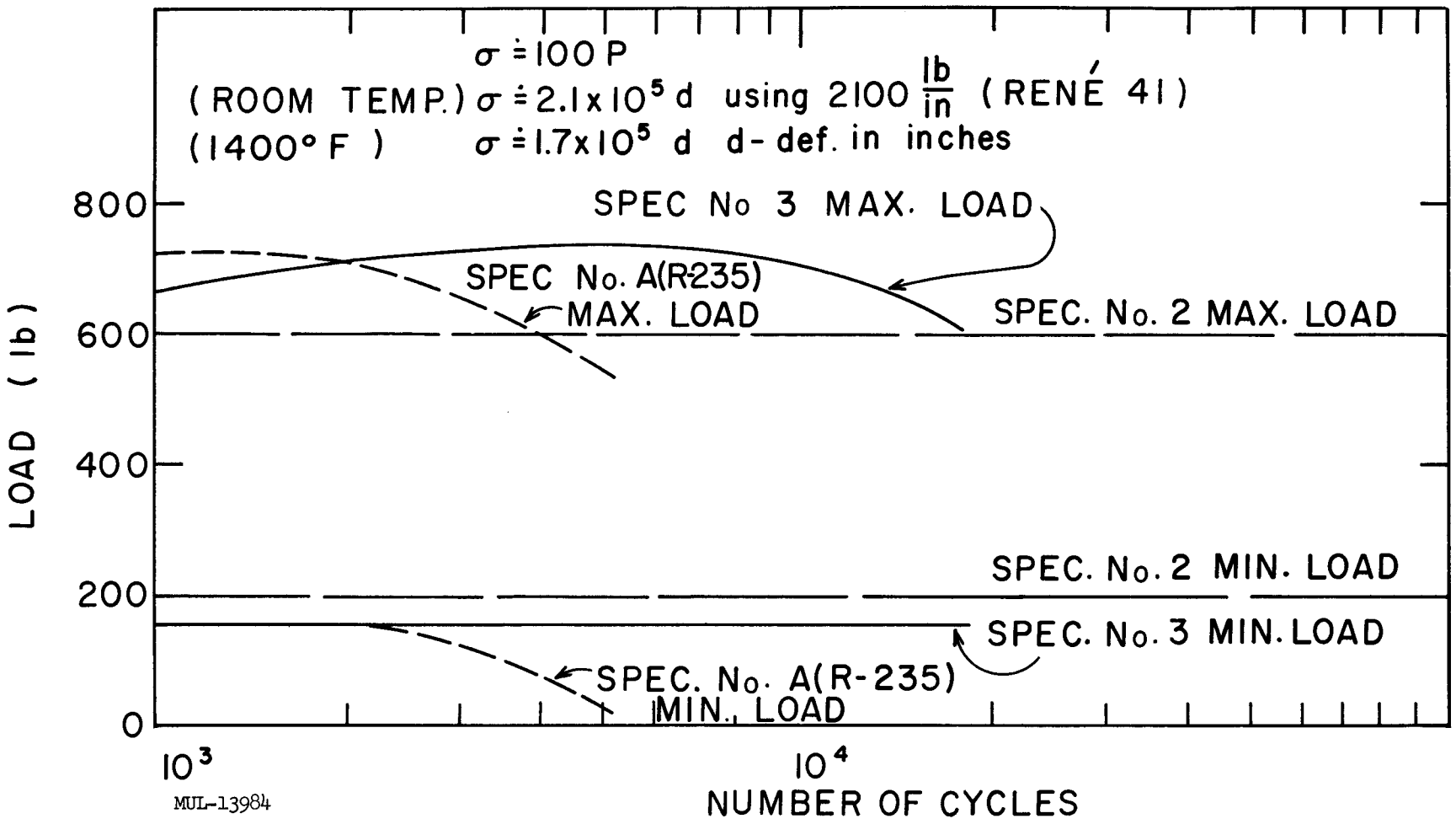

Fig. IV-78. Load vs number of cycles for single buggy side-support springs.

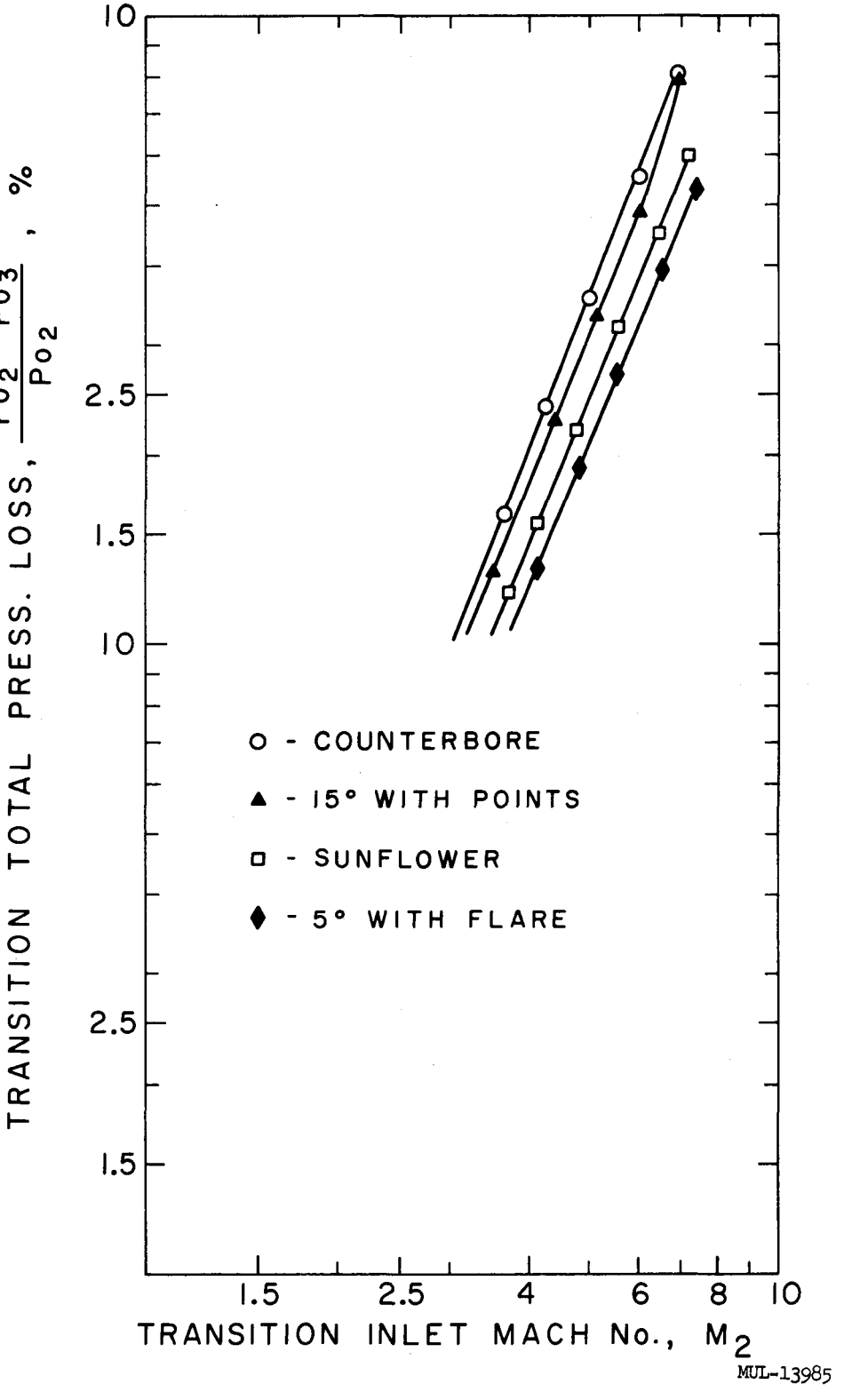

Fig. IV-79. Transition section losses.

The counterbore section (Fig. IV-80) has a bore into the tube section. This bore has the same cross-sectional area as the seven tubes and gives a total area of the seven tubes plus approximately one-half the area of the six outer tubes. The 15° section (Fig. IV-81) with points converges the six outer holes at 15°. It is designed so as to give approximately constant cross-sectional area to the seven tubes plus six flutes leading in at 10°. The Sunflower section turns the six outer holes in at 11°, so that the downstream outer sides of these holes blend into the circumference of a single hole having an area (7A) equal to seven small-hole areas. The webs between the seven holes are then removed by boring a single circular hole of area 7A through the entire part. (See Fig. IV-82.) The 5° section with flare (Fig. IV-83) turns the six outer holes at 5°, but they do not intersect. The seven holes then discharge into a flare which converges to a cross-sectional area equal to the seven tubes.

Slice Test

The slice-test unit has been assembled. Static load testing has been accomplished at a 5-psi spring pressure.

The slice-test assembly is a full-diameter array of steatite tubes (0.2985 across flats). The tubes are 5-in., 3-1/2-in., and 1-1/2-in. long to provide stagger, and are assembled to a 10-in.-thick section. The full-diameter tube assembly of 53.25 inches is constrained by a system of 16 pressure pads and 32 springs, conceptually the same as the side support system. Figures IV-84 through IV-86 show the test item. Prior to assembly, each Hastelloy R-235 spring pair was loaded to determine the spring constant and to calibrate and flex the strain gauges. All 16 pairs had a constant of 4300 ± 10 pounds/inch.

Five-psi pressure was put on the springs, plus the gravity load, which gave the top springs 3 psi and the bottom springs 7 psi with a cosine distribution all around. A survey of static friction loads for 13 large modules (4.1 inches across flats) was made with a hydraulic jack. Loading was increased at the rate of 200 lb/minute until slipping occurred. Friction loads

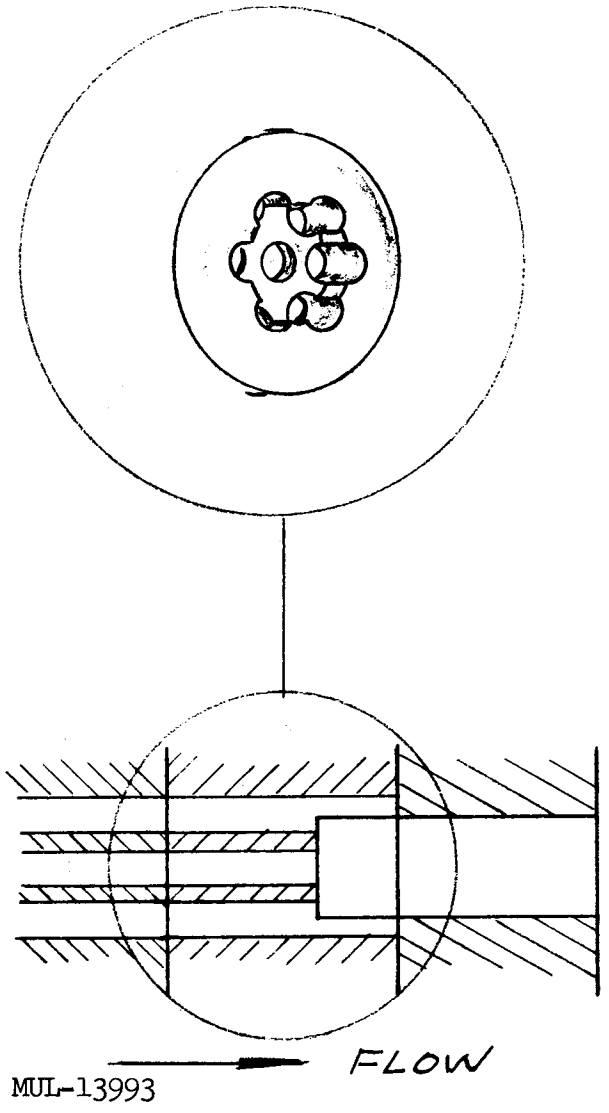

Fig. IV-80. Counterbore transition section.

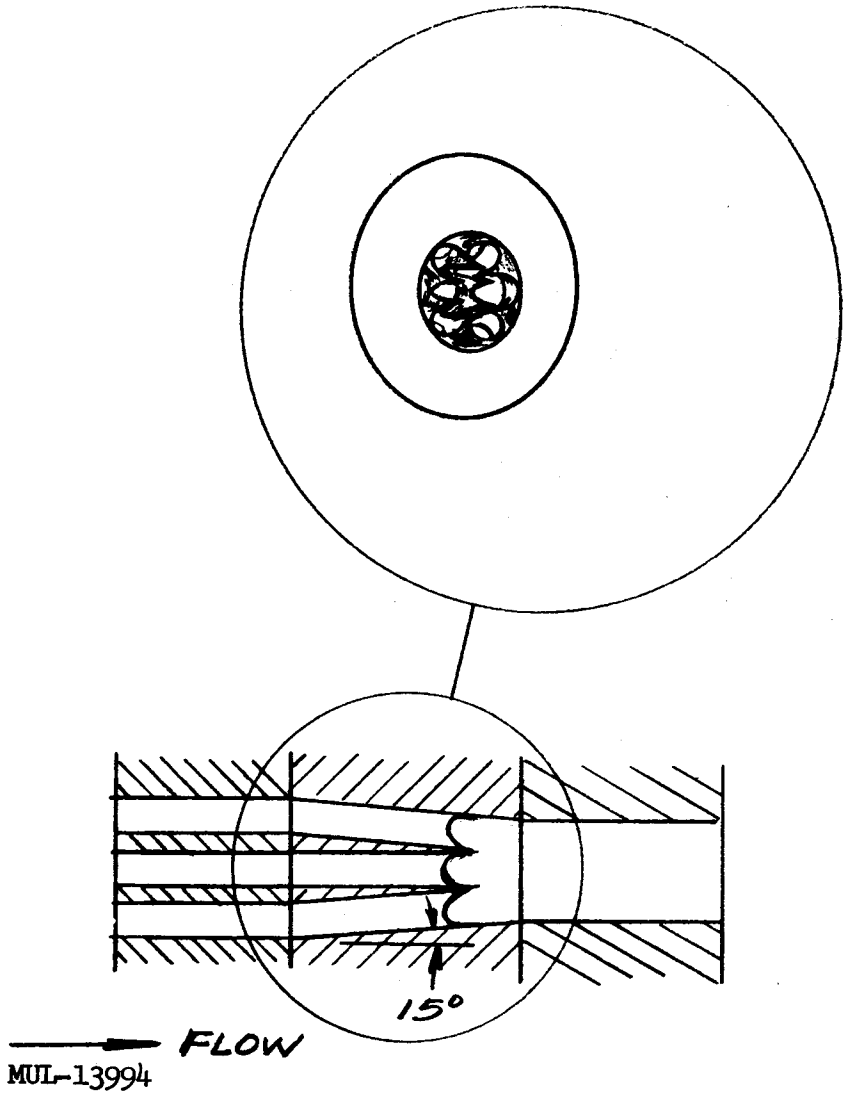

Fig. IV-81. 15° transition section.

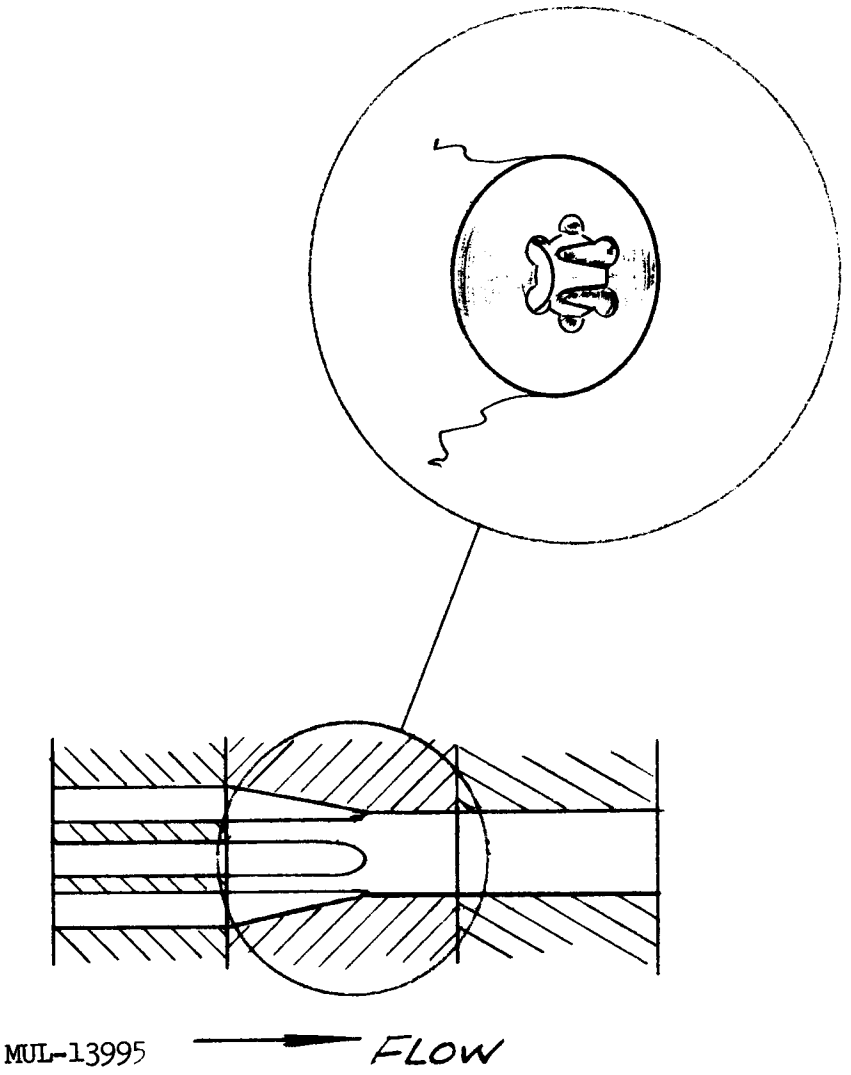

Fig. IV-82. Sunflower transition section.

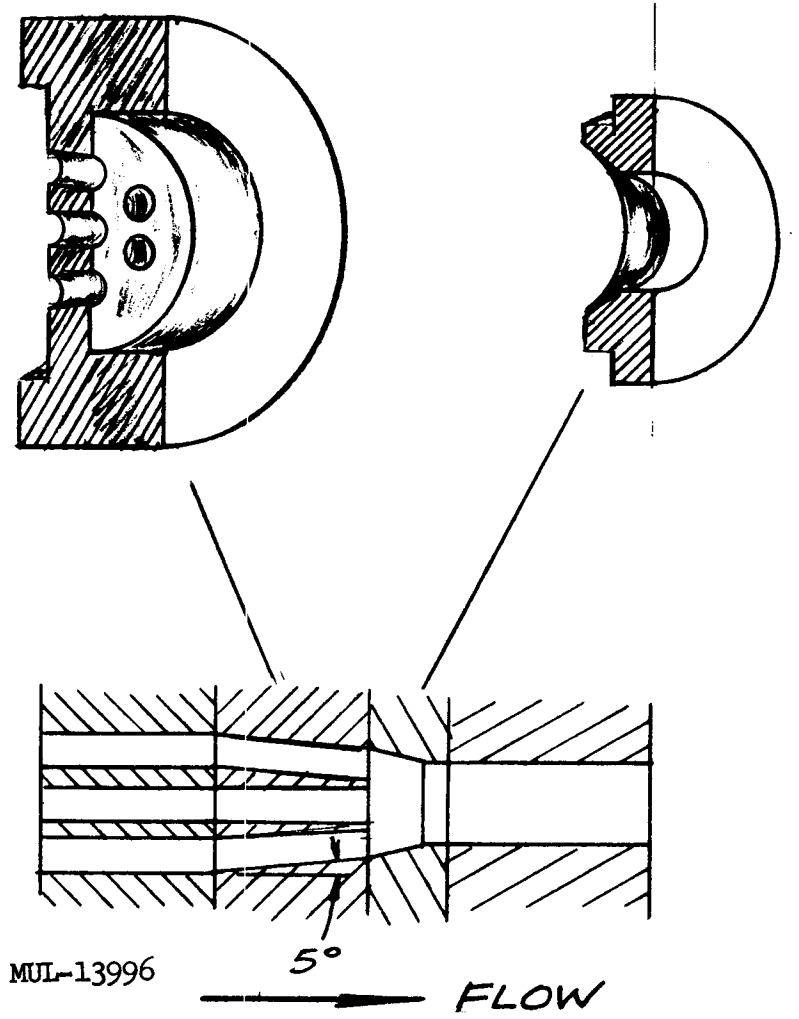

Fig. IV-83. 5° transition section with flare.

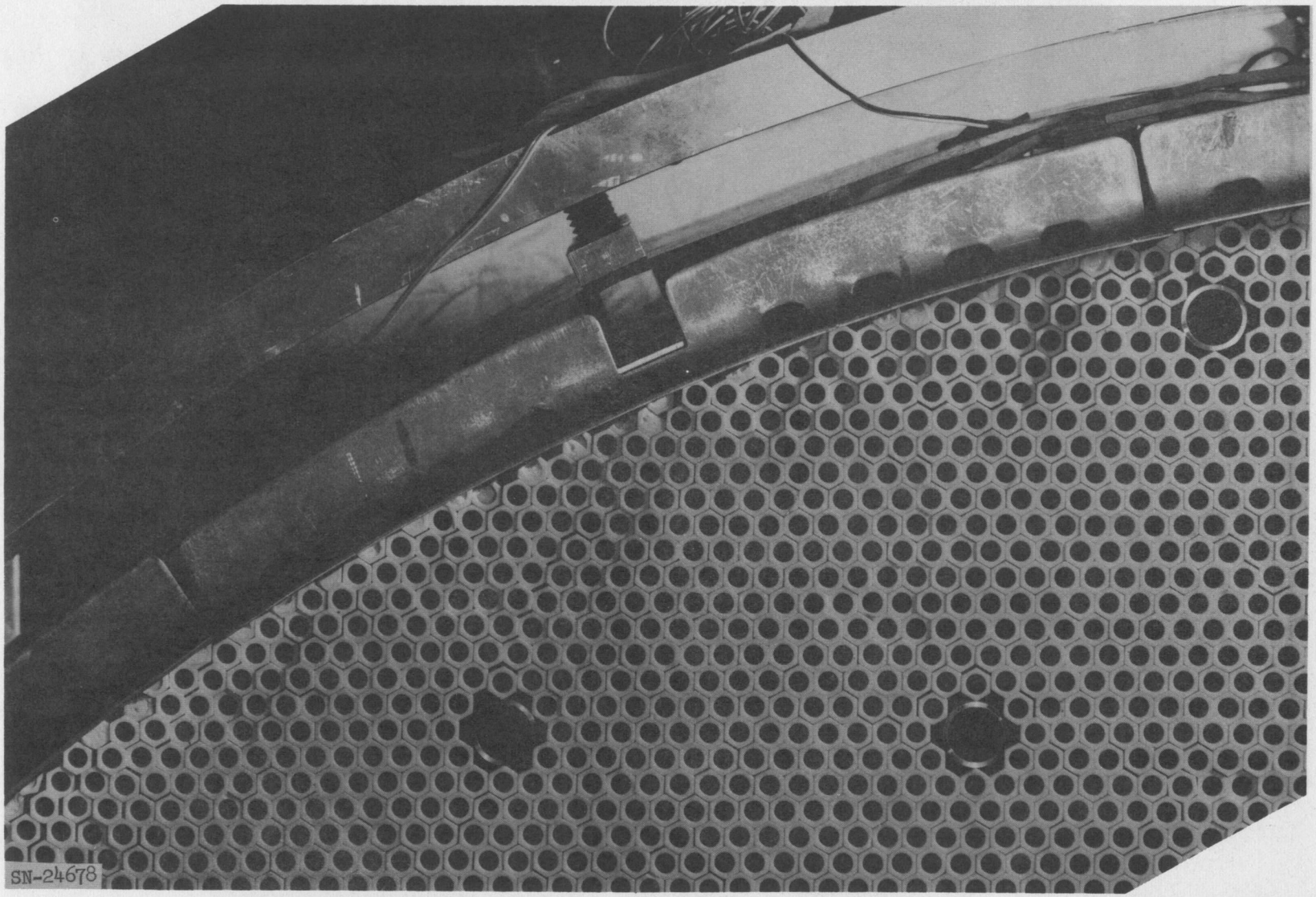

Fig. IV-84. Close-up of slice-test item.

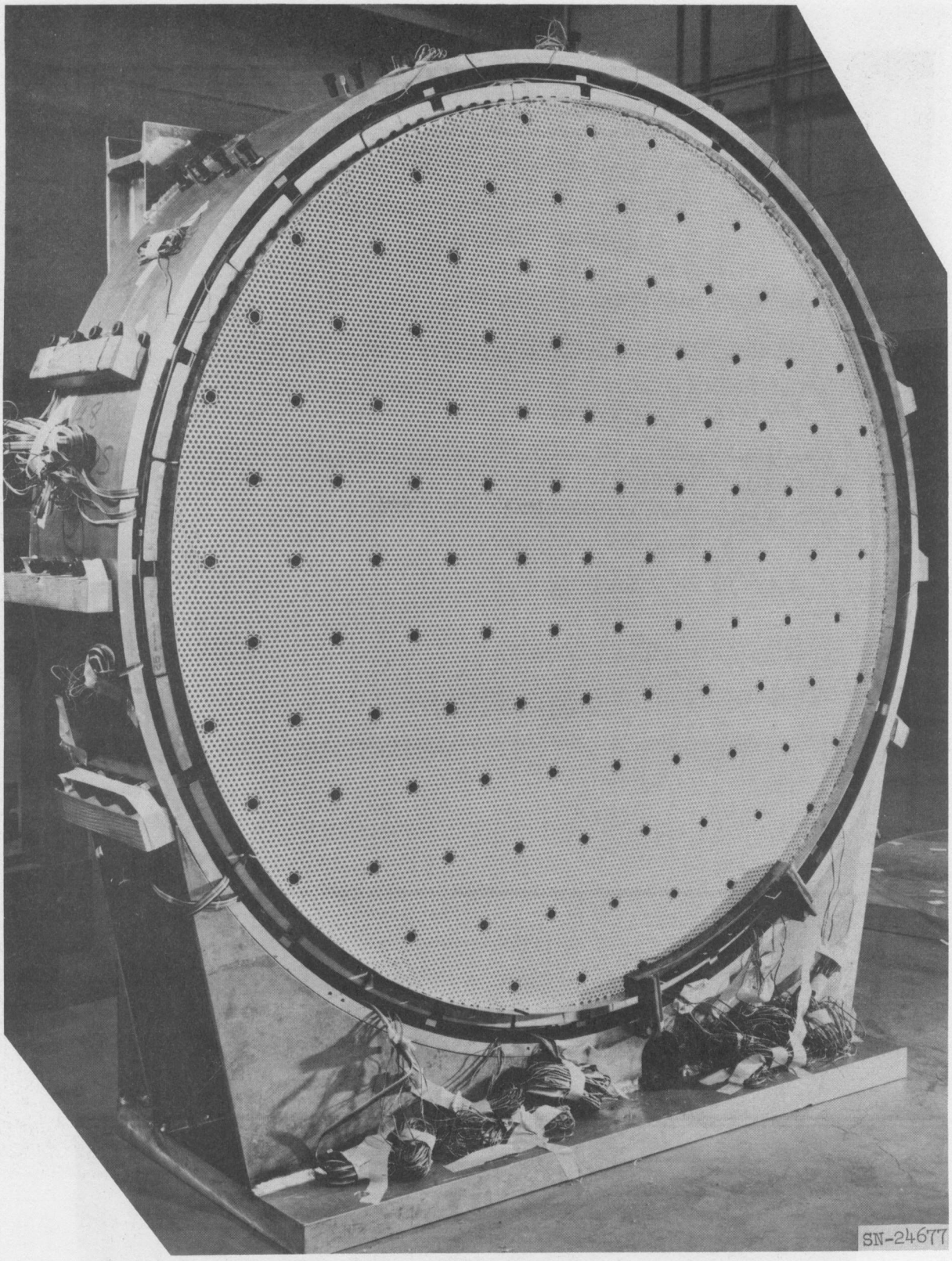

Fig. IV-85. Angle view of slice-test item.

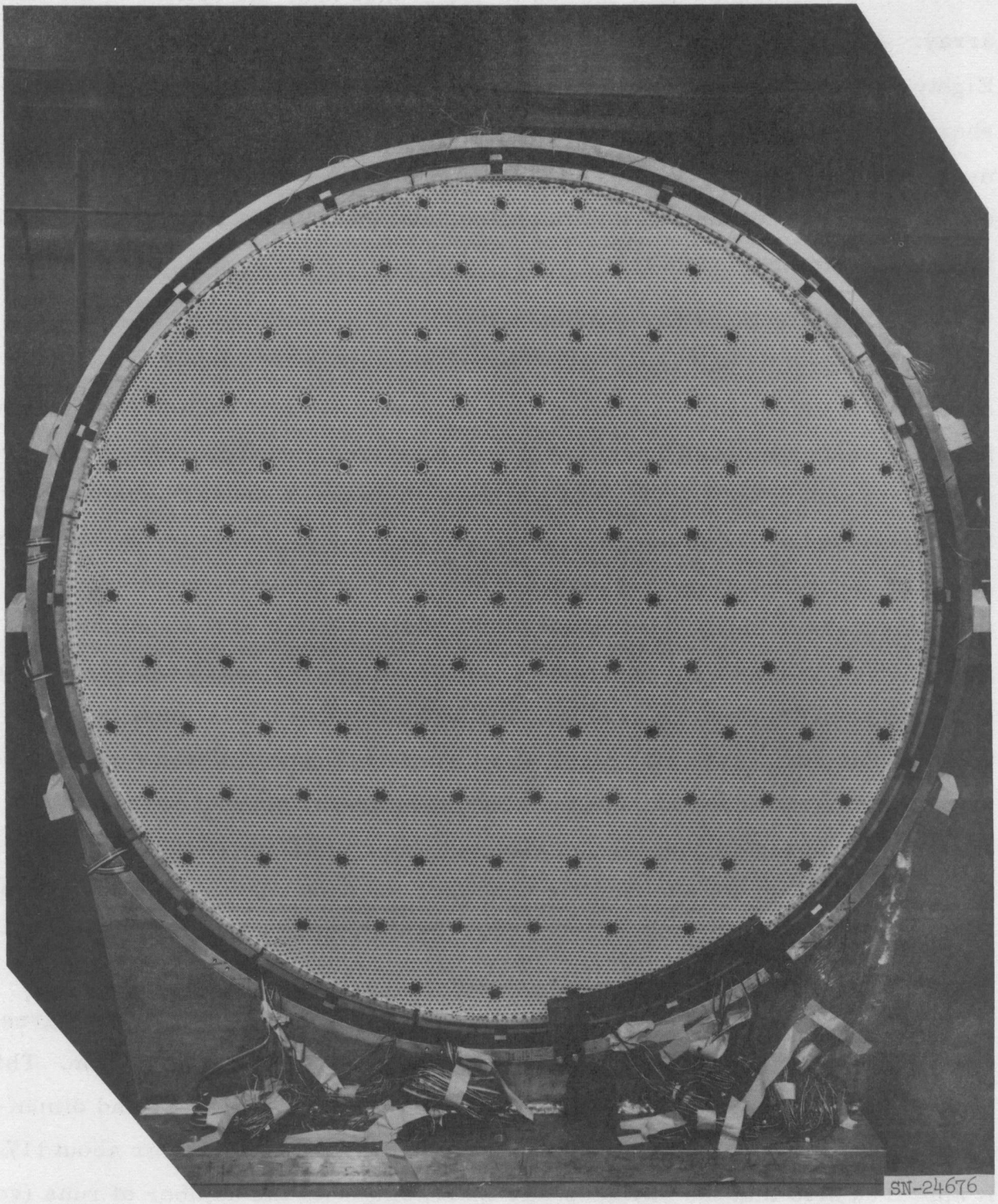

Fig. IV-86. End view of slice-test item.

varied from 235 pounds near the top to 350 pounds near the bottom of the tube array. A survey of friction loads on seven-tube clusters was also made. Eighty-five clusters were pulled manually with a calibrated scale. A plot showing average load as a function of height is given in Fig. IV-87. Poor mating between the peripheral tubes and the friction liners casts some doubt on the uniformity of loading in this region, but should have little effect several inches in from the periphery.

Load-Deflection Characteristics

Testing of a large stack, containing about 1000 tubes, is being conducted to determine the fundamental characteristics of such a system. In the past, tests employed Tory II-A-1 fuel tubes and steatite mockups (see previous progress report). The load vs deflection curves for each system can be represented by a parabola of the form $P = Ay + By^2$; however, the constants A and B must be determined empirically and their dependence on various test conditions is being investigated. The surface finish of the elements appeared to be an important parameter, and steatite tubes which had been ground to 16 microinches rms. transverse, and 32 microinches rms. axially, were tested. The stiffness of this stack was significantly greater than for the previous rough steatite stack. The accompanying graphs present the results of three series of tests; showing the load vs deflection (Fig. IV-88); stiffness vs deflection (Fig. IV-89); and the equations for each curve. All the curves correspond to "conditioned" stacks, i. e., those stacks which have been subjected to preliminary loads.

An obvious conclusion is that grinding the steatite tubes has greatly enhanced the stiffness of the stack by promoting better load distribution. This is due to a lower coefficient of friction and a reduction of camber and dimensional tolerance. The number of loose tubes at 30 psi was 123, or about 11%. It appeared also that the stiffness was increasing with the number of runs (so long as the stack remained undisturbed), i. e., successive loadings and unloadings resulted in a slight stiffening of the stack.

Since the constant in the equation cannot be derived theoretically, further testing will be conducted with varying stack dimensions.

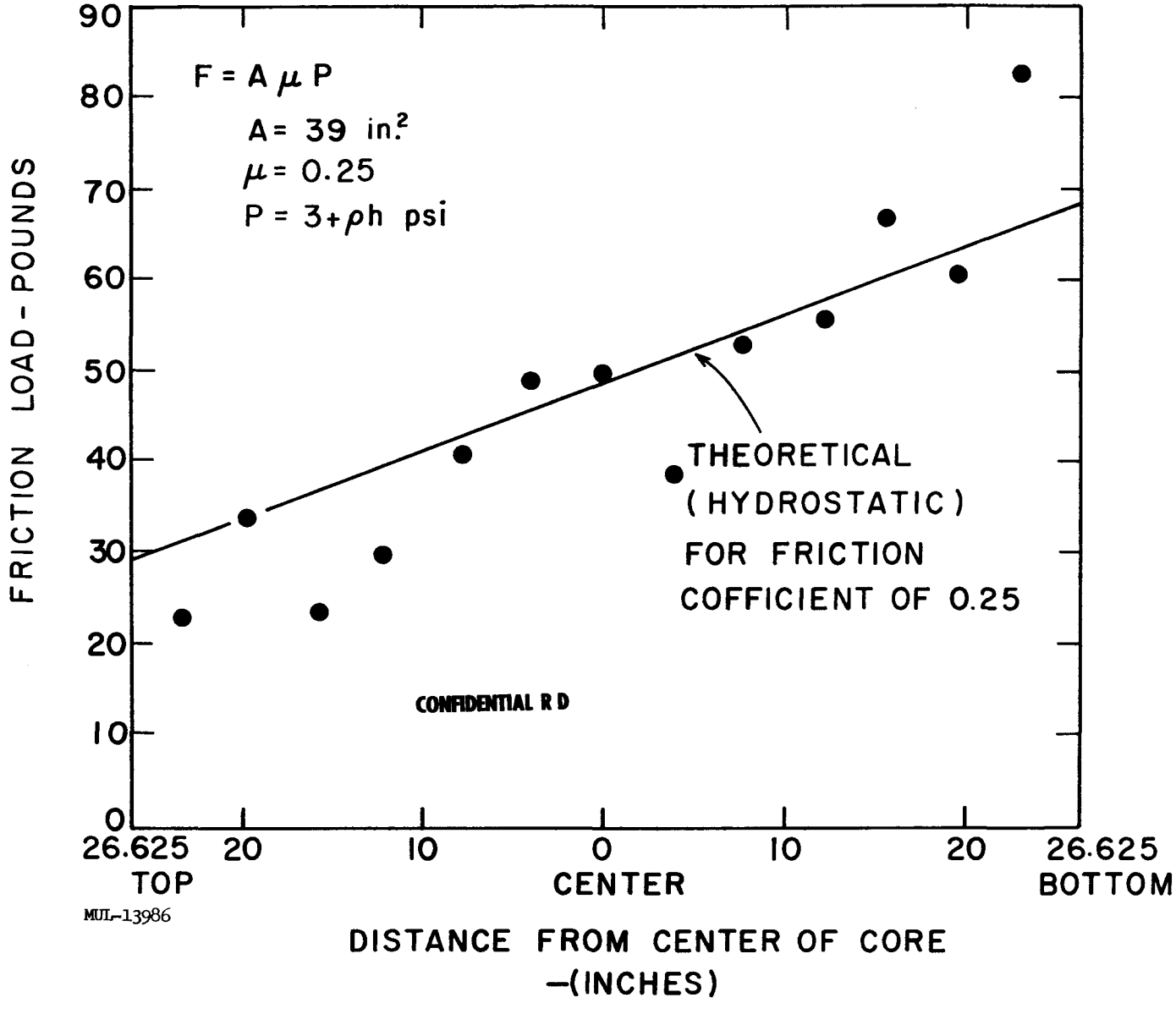

Fig. IV-87. Average load as a function of height.

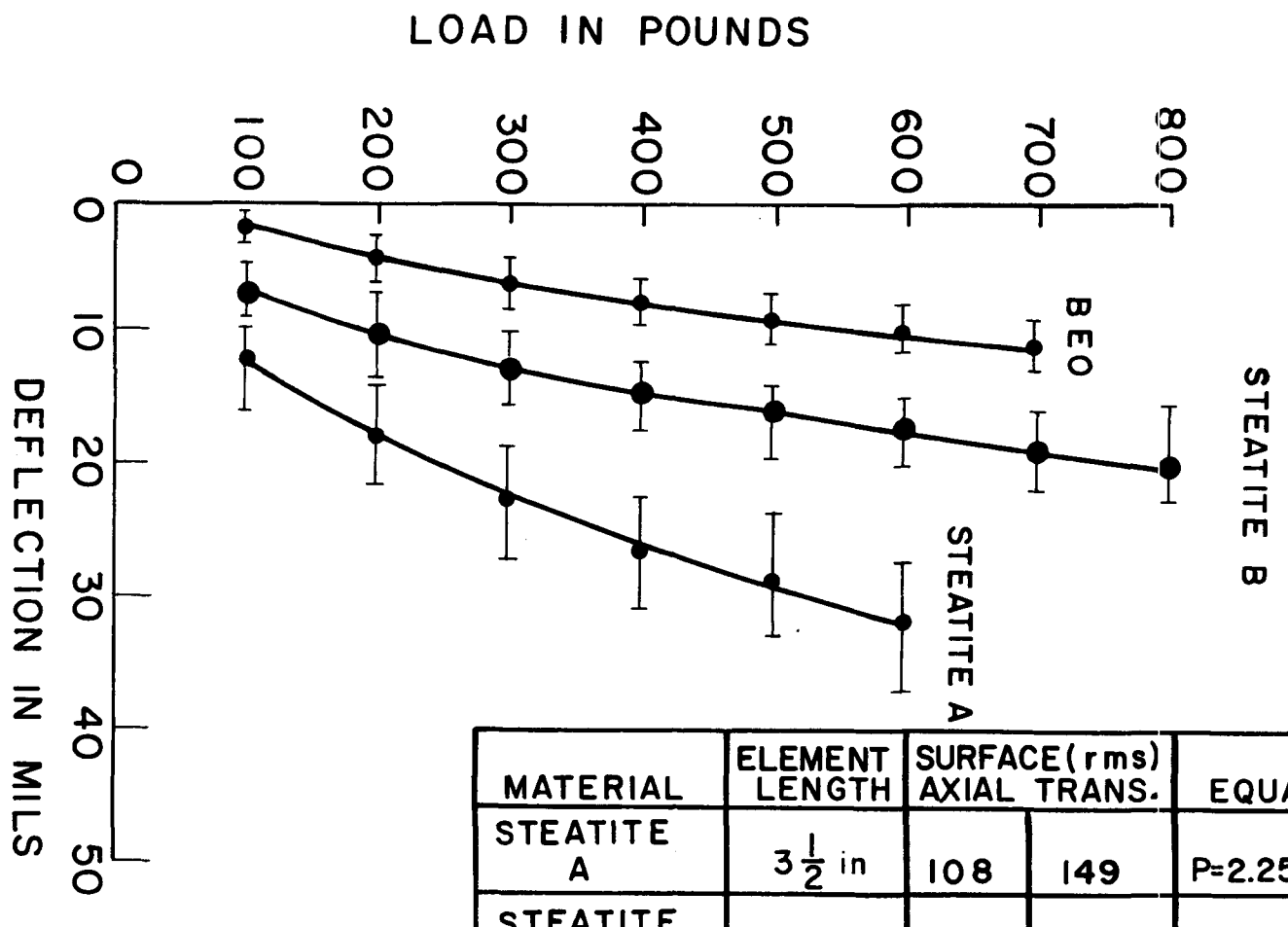

MATERIAL	ELEMENT LENGTH	SURFACE (rms) AXIAL	TRANS.	EQUATION	LOOSE ELEMENTS AT 30 psi
STEATITE A	$3\frac{1}{2}$ in	108	149	$P=2.25y+052y^2$	200
STEATITE B	4 in	32	16	$P=2.05y+212y^2$	120
BEO	4 in	64	64	$P=42y+1.82y^2$	

Fig. IV-88. Load vs deflection for 1000-tube stack. About 12-in. × 6-in. × 4-in., loaded in the 12-in. axis. (Room temp.)

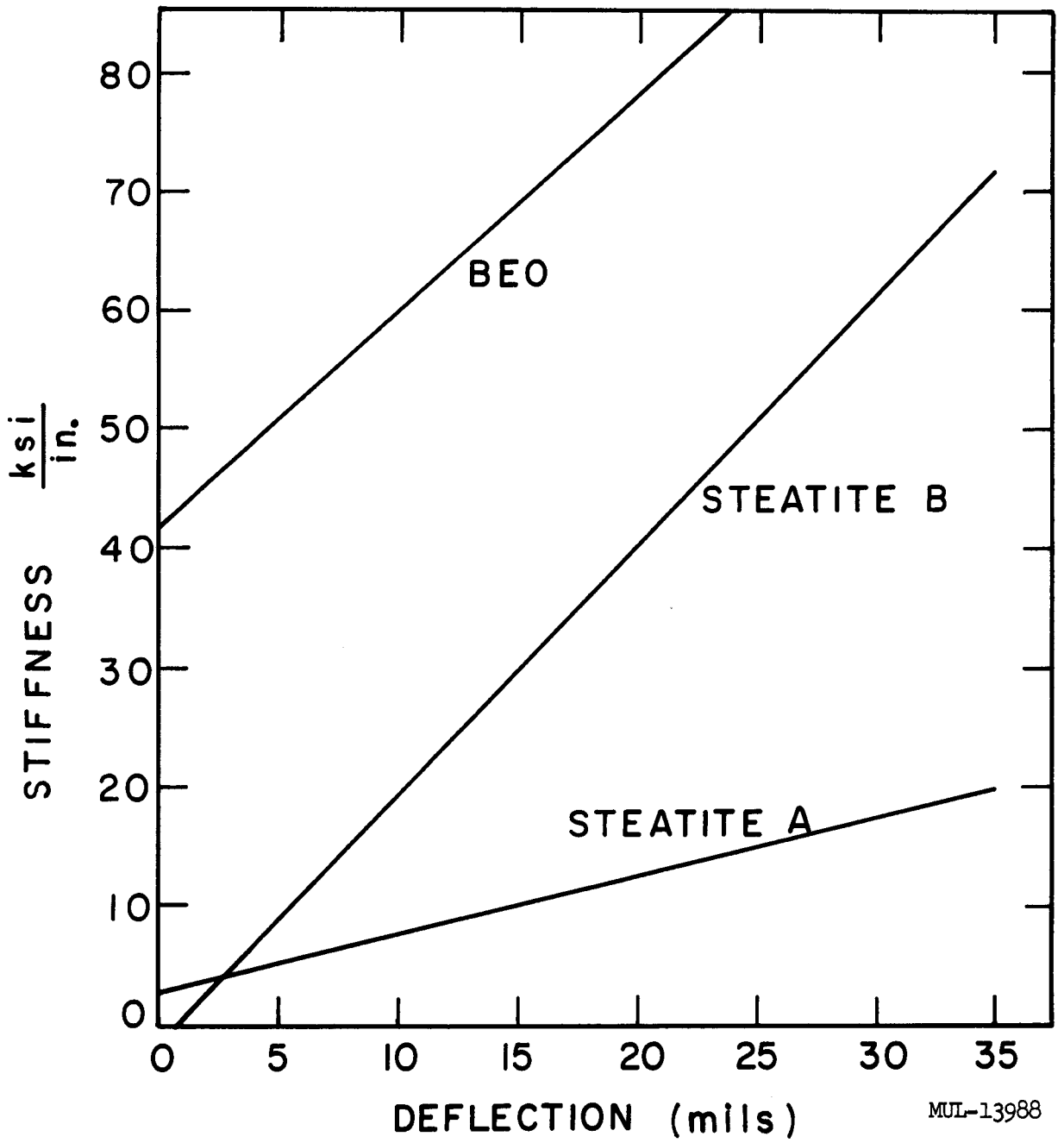

Fig. IV-89. Stiffness vs deflection for 1000-tube stack.

The curve of stiffness vs deflection shows that the interaction of the elements (constant B in $P = Ay + By^2$) for the ground steatite was similar to the BeO, but the steatite stack was much looser initially (see Fig. IV-89).

Tube Crushing Tests

A number of fuel-element specimens, 1-in. long, were fractured by loading on opposite flats at elevated temperature. The stresses induced in the specimens were estimated on the basis of photoelastic studies.[1,2] A theoretical solution to the stress distribution in a hexagonal tube under uniform pressure is available.[3] The test temperatures were 1400°F, 1800°F, and 2250°F.

In the first series the specimens were loaded on opposite flats to failure at 30 lb/min. Next, the maximum load which could be sustained at temperature for 10 hours was determined. All tests were run in air.

Figure IV-90 shows the results of the "two-flat" testing, giving the load, as well as estimated maximum tensile stress induced. See UCRL-6258, p. 30 for a comparison of the flexure strength (modulus of rupture) of the fuel elements.

---

[1] A Photoelastic Study of Stresses in Hydrostatically Loaded Cylinders with Noncircular External Boundaries, W. P. T. North and J. B. Mantle, SESA Conference, Oct. 10, 1960, Paper No. 618.

[2] Stresses in Hollow Hexagons Under External Pressure, P. D. Flynn, SESA Conference, Oct. 1959, Paper No. 572.

[3] Theoretical Stress Distributions in Cylinders Having a Circular Central Hole and a Regular Polygon for an Outer Boundary, H. Kawaguchi, Japan Society of Mech. Eng. (1945).

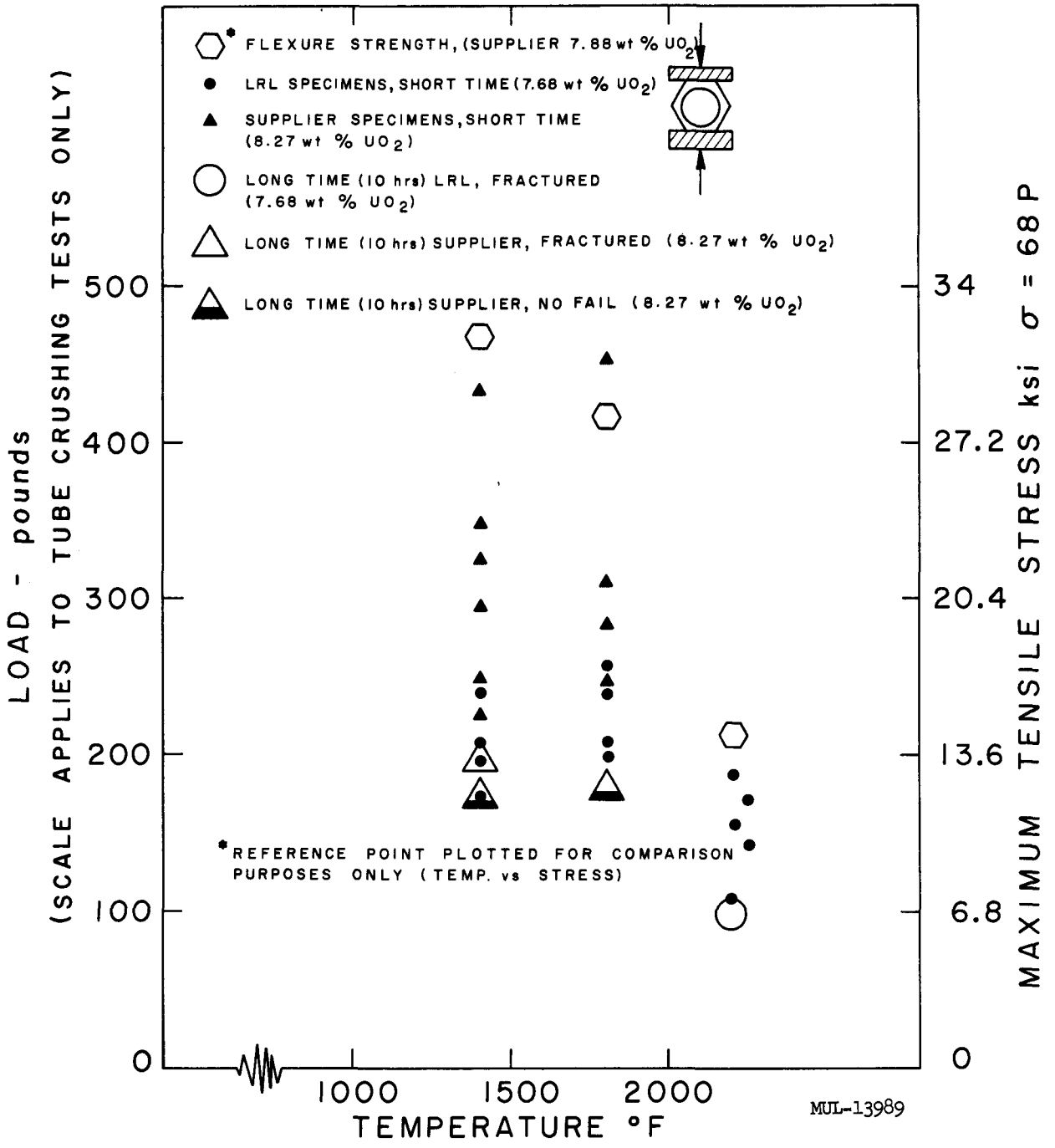

Fig. IV-90. Fracture load vs temperature (two-flat load).

Air-Pad Tests

A number of air-pad models of the following geometry:

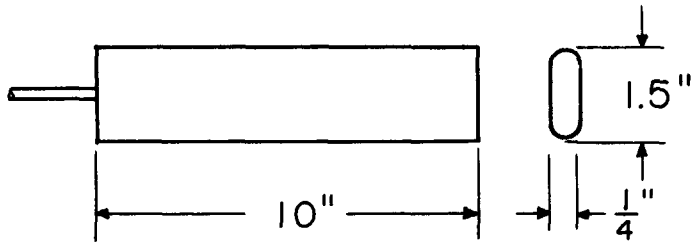

Air pad in test fixture

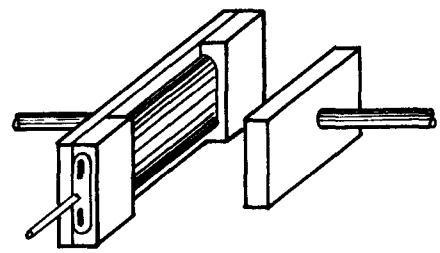

were fatigue tested at room temperature and at 800°F. They were fabricated either from 0.0035 SS-347 or 0.005 Inconel-X. The test consisted of inserting the pad into a holder, pressurizing its interior to 100 psig and imposing an oscillating deflection on a movable plate in contact with the pad.

The parameters which were held fixed throughout the tests were:

a. The internal pressure, 100 psig

b. The stroke of the pressure plate, 1/8 in.

c. The maximum pad deflection, 1/8 in.

The majority of the testing was devoted to modifying portions of the test fixtures, namely the specimen holder and pressure plate, in order to eliminate strain concentration as the failure mechanism.

Table IV-30 summarizes the test environment for each run. Figure IV-91 is a plot of maximum transmitted load and oscillating bearing pressure (obtained by dividing the load band width by maximum estimated contact area) against the number of cycles to failure for runs 7 to 15.

The photograph (Fig. IV-92) of all the specimens shows the effect of changing the pressure plate and holders on the failure characteristics. At specimen No. 15 no buckling appears and the greatest lifetime, 7000 cycles, for Inconel-X at 800°F was attained. The final pressure plate used in No. 15 appears in Fig. IV-93.

Table IV-30. Air-Pad Test Environments.

Spec No.	Material	Temp (°F)	Max load (lb)	Approx max area (in.^{2})	Max bearing stress (psi)	Oscillating bear stress (psi)	Lifetime (cycles)	Fixture		Remarks
								Holder	Pressure plate	
1	SS 347	800	600	6	100	32	37	Rect	5-in. rect	Failed by explosion
2	Inc-X	"	600	6.8	88	32	1000	"	"	
3	SS	"	640	6.4	100	36	31	"	"	Explosion
4	Inc	"	840	9.5	88	44	900	"	6.8-in. rect	
5	SS	"	960	9.6	100	98	20	"	"	Slow leak
6	Inc	"	600	9.4	64	36	550	"	"	Initial press = 75 psi Single-pad volume
7	SS	Rm	680	6.5	104	40	250	"	6.8-in. pointed	Failed at holder
8	SS	"	720	6.4	112	44	200	Shallow Vee	"	
9	SS	"	440	4.4	100	28	Run to 10,000	Deep Vee	5-in. pointed	No failure using 0.075 throw
10	SS	"	980	4.8	100	36	800	"	"	Back to 0.125 cam
11	SS	"	640	6.7	104	40	400	"	6.5-in. pointed	The main changes now are increasing the radii of the contact surfaces.
12	Inc	800	732	6.4	116	56	900	"	"	
13	Inc	800	780	6.8	116	56	700	"	"	More rounding on pressure plate
14	Inc	"	560	4.8	116	52	1550	"	5-in. pointed	A new small-plate, rounded
15	Inc	"	980	4.1	116	44	7000	"	"	Highly rounded

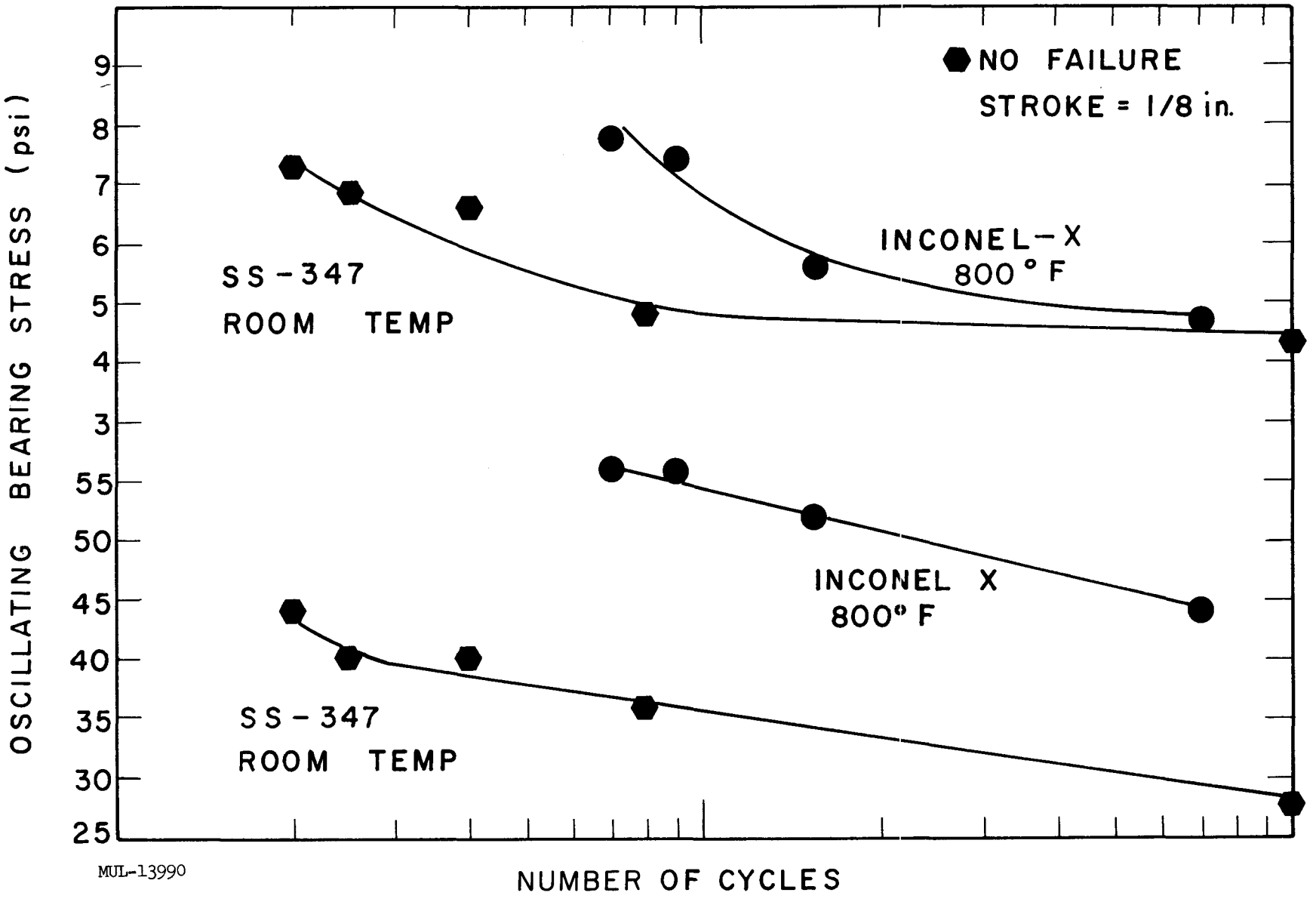

Fig. IV-91. Maximum transmitted load and oscillating bearing pressure.

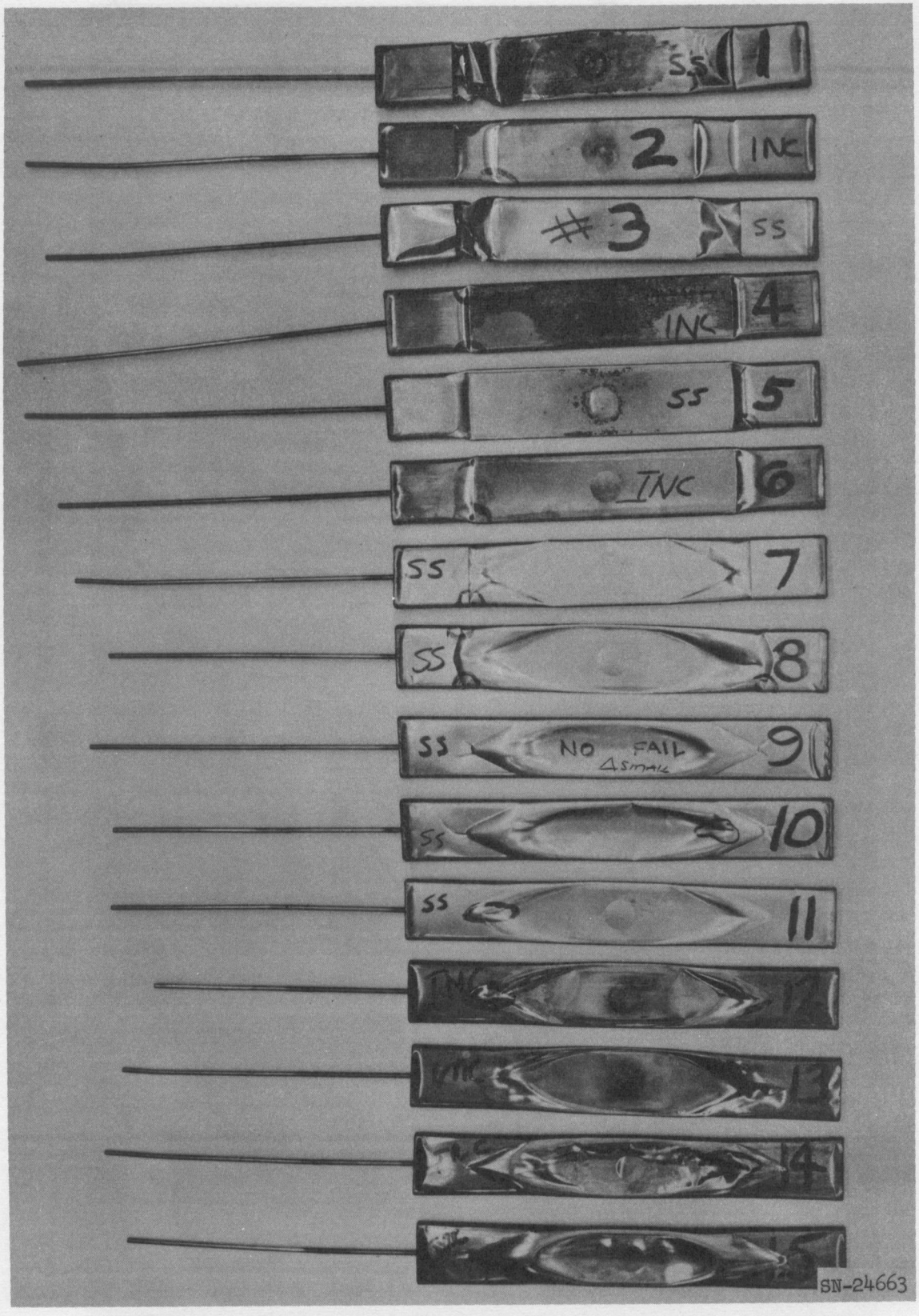

Fig. IV-92. Test specimens.

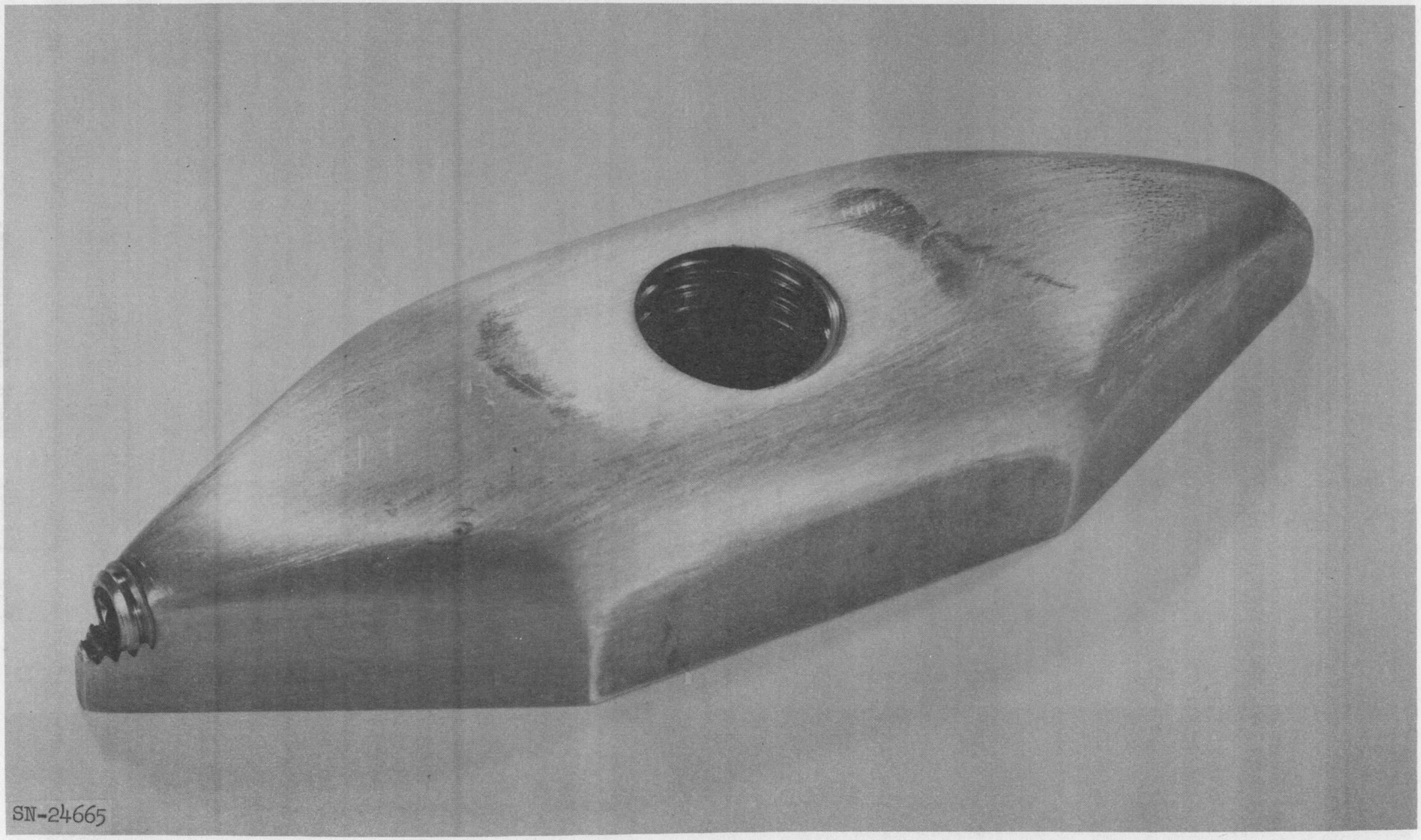

Fig. IV-93. Pressure plate used with test specimen 15.

The analysis of the air-pad system for the rectangular pressure plate agrees well with the experimental results if the mean contact area is taken between 0.6 and 0.67 of the maximum contact area.

Prediction of the load for run No. 15 on the basis of a prolate spheroidal pressure plate agrees very well with the experimental result.

Some conclusions based on the experimental results follow:

a. A lifetime of about 5×10^5 cycles is desired and would probably be obtained by an Inconel-X air pad at 800°F transmitting a maximum load of about 400 lb and an oscillating bearing pressure of about 20 psi. The lifetimes at higher temperature would have to be assessed by further tests.

b. The shape of the air-pad holders and pressure plates is very significant in improving fatigue life, i.e., it is imperative to eliminate strain concentrations.

c. The final Inconel-X specimen, which survived 7000 cycles, exhibited no buckling in the region of failure, which indicates that the fatigue life of the material may be the limiting factor.

d. Accurate knowledge of the experimental environment allows a reasonable estimate of the air-pad characteristics using the analysis presented.

e. It would be desirable to test at higher temperatures, with varying strokes, and various material thicknesses.

f. Further experimentation with air-pad and pressure-plate shapes is necessary for optimization.

Small-Dome Tests

A seven-piece segmented KT silicon carbide dome 3.45 inches in diameter has been tested for load-deflection at room temperature, and for structural integrity under cyclic pressure load at 2400°F. The dome was manufactured from a blank that was green-pressed with all the axial holes and then fired. Machining was done on the fully fired product. Suitable jigs of simple design, and diamond impregnated tools were used to finish the dome pieces. The completed dome is shown in Figs. IV-94, IV-95, and IV-96.

Room-temperature testing was accomplished with a hydraulic load application device utilizing a rubber diaphragm and a brass shim that assured an even pressure distribution over the entire top face of the dome. A steel seat with a thin (0.001-in.) polyvinyl lining was used as a support. Dial

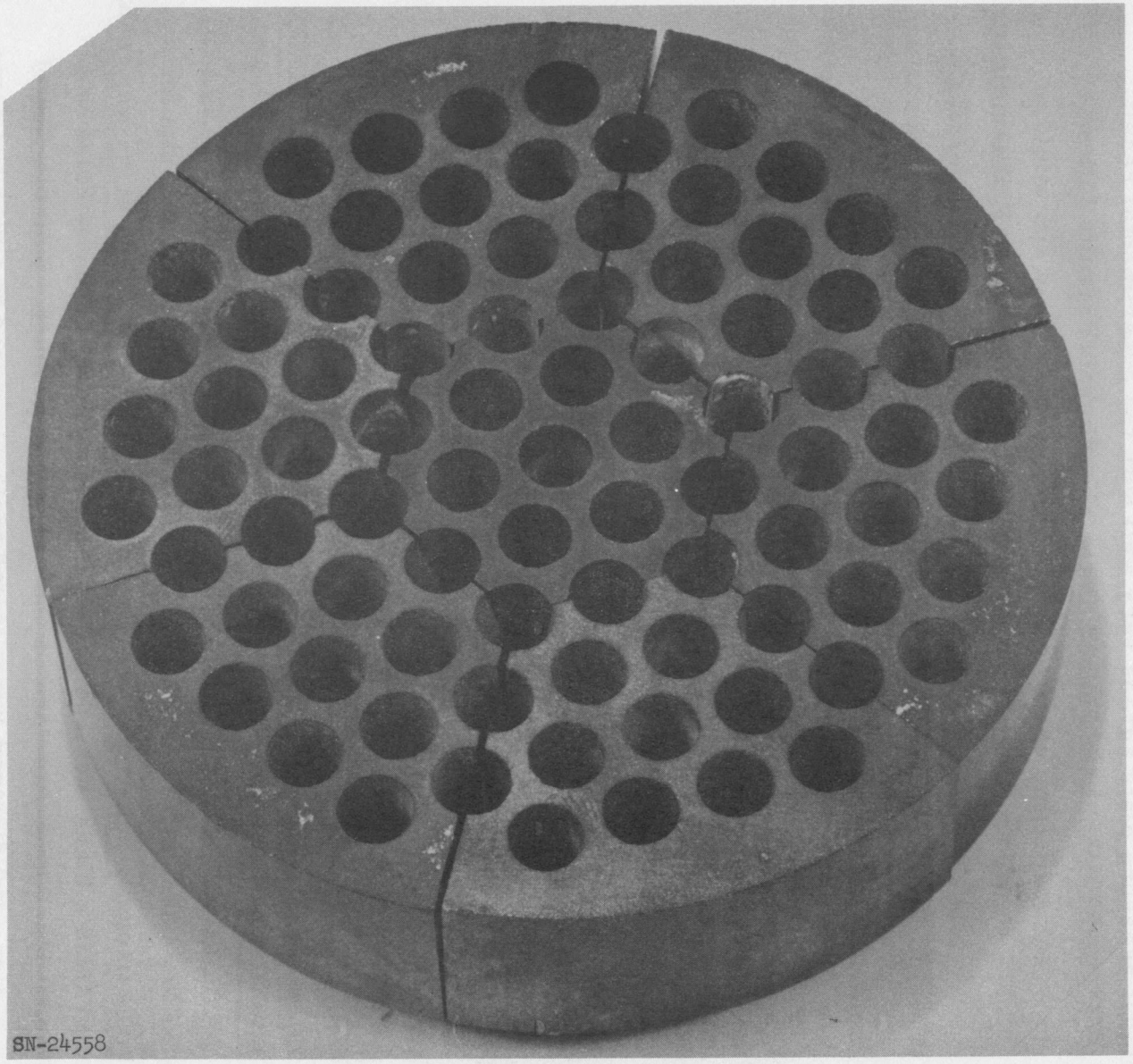

Fig. IV-94. Seven-piece segmented KT SiC dome.

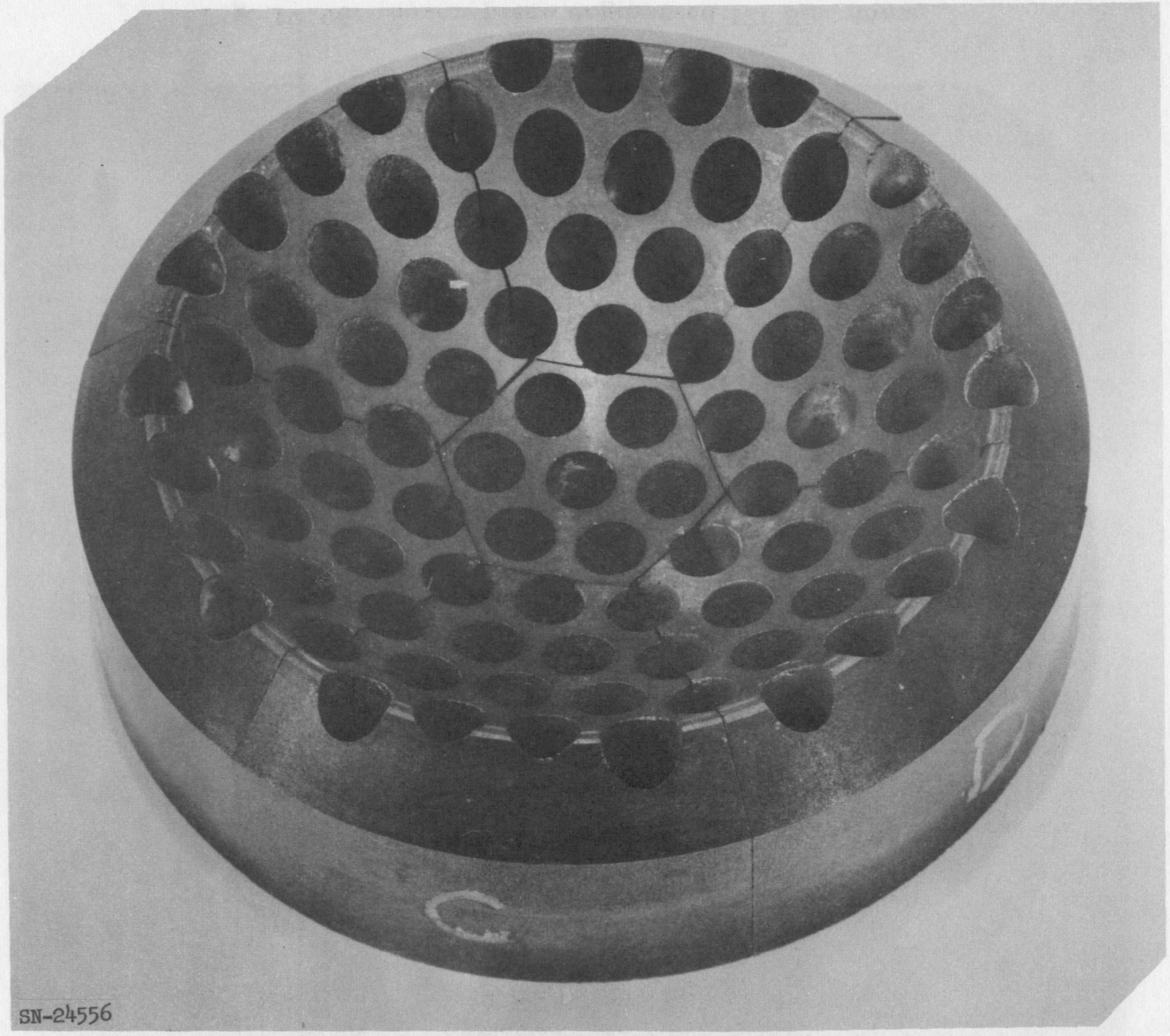

Fig. IV-95. Seven-piece segmented KT SiC dome.

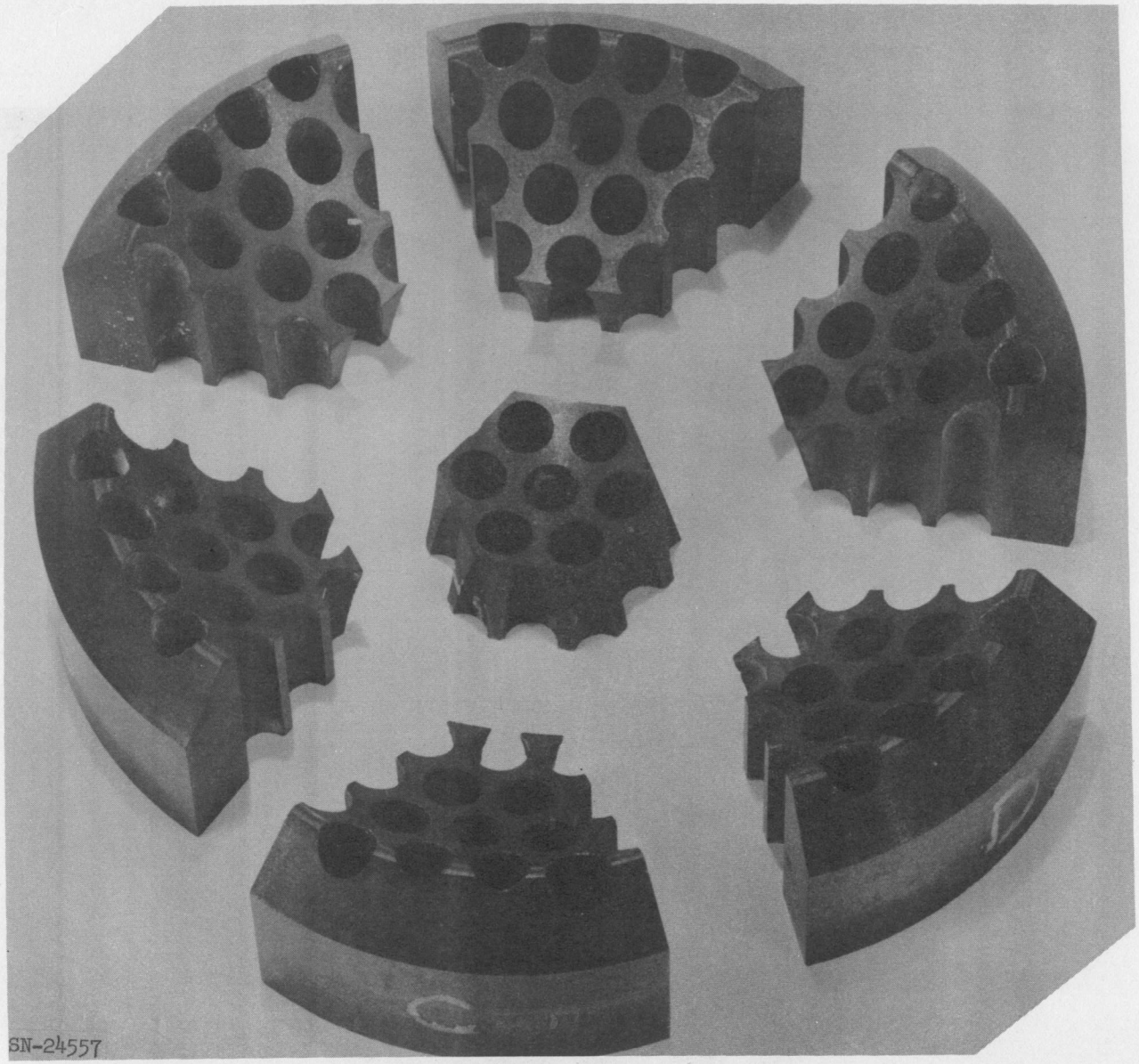

Fig. IV-96. Seven-piece segmented KT SiC dome.

indicators were used for deflection measurements on one side segment and the center segment. Loads of up to 375 psi were applied slowly and released slowly, each cycle taking about 10 minutes. The results for two of these cycles are shown in Fig. IV-97. As expected, the center segment moved downward to accommodate the loads. No permanent set occurred in any of the parts. Inspection after the ambient temperature tests showed no damage.

Hot tests were accomplished in a test fixture modified from that described in Quarterly Progress Report No. 7. Modifications were a more efficient seal in the pressure-supply fitting and strengthening of all parts to resist creep effects. Argon pressure was applied and relieved by electrically operated solenoid valves. As a check on the system, a dummy load consisting of a supply pipe and a chamber of the same dimensions as the actual test fixture, with a pressure transducer built in to the diaphragm chamber, was pressure cycled to 1000 psig at ambient temperature. Results as shown in Fig. IV-98 indicate that the pressure cycle as recorded outside the furnace is the same as that actually applied to the dome under test.

With a temperature held constant at 2400°F, 2400 cycles were applied to the dome over a ten-hour period. Fig. IV-98 shows a typical cycle. One small chip was evident after this test. Figures IV-99, IV-100, and IV-101, show the dome after test. Zyglo inspection showed that all six of the outer segments had hairline cracks, but all segments remained intact. These cracks began at the outer row of holes and extended downward and inward to just above the lower surface at the inner edge of each segment. The center segment showed no damage.

The series of small-dome tests has demonstrated that complete structural integrity is maintained even in excess of design conditions. No further tests of this nature are contemplated on this material.

Fabrication Development of Large SiC Shapes

The first segment of a 7-piece 3-foot-diameter test dome was received. (Fig. IV-102). The piece contains minor cracking which is considered acceptable. The most extensive crack in the piece is circled with a crayon mark, (Fig. IV-103). Diamond machining of the first piece proceeded with ease, indicating that machining of complex shapes of fired SiC does not require development studies.

A 29-inch-diameter cylinder weighing approximately 800 lb was pressed and appears satisfactory. It has been cut to a hexagonal shape and partially drilled.

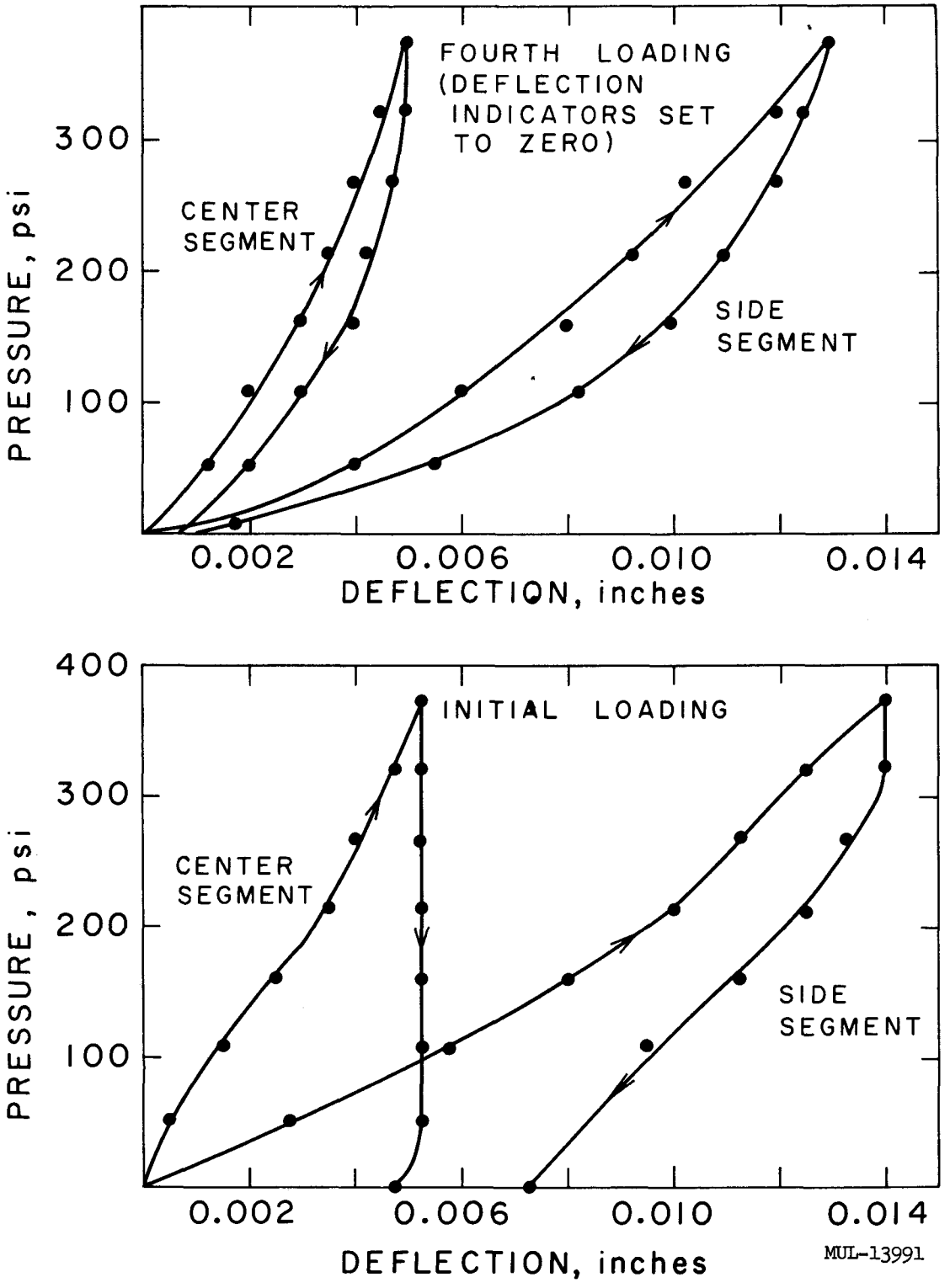

Fig. IV-97. Room-temperature load-deflection curves (total cycle time 10 minutes).

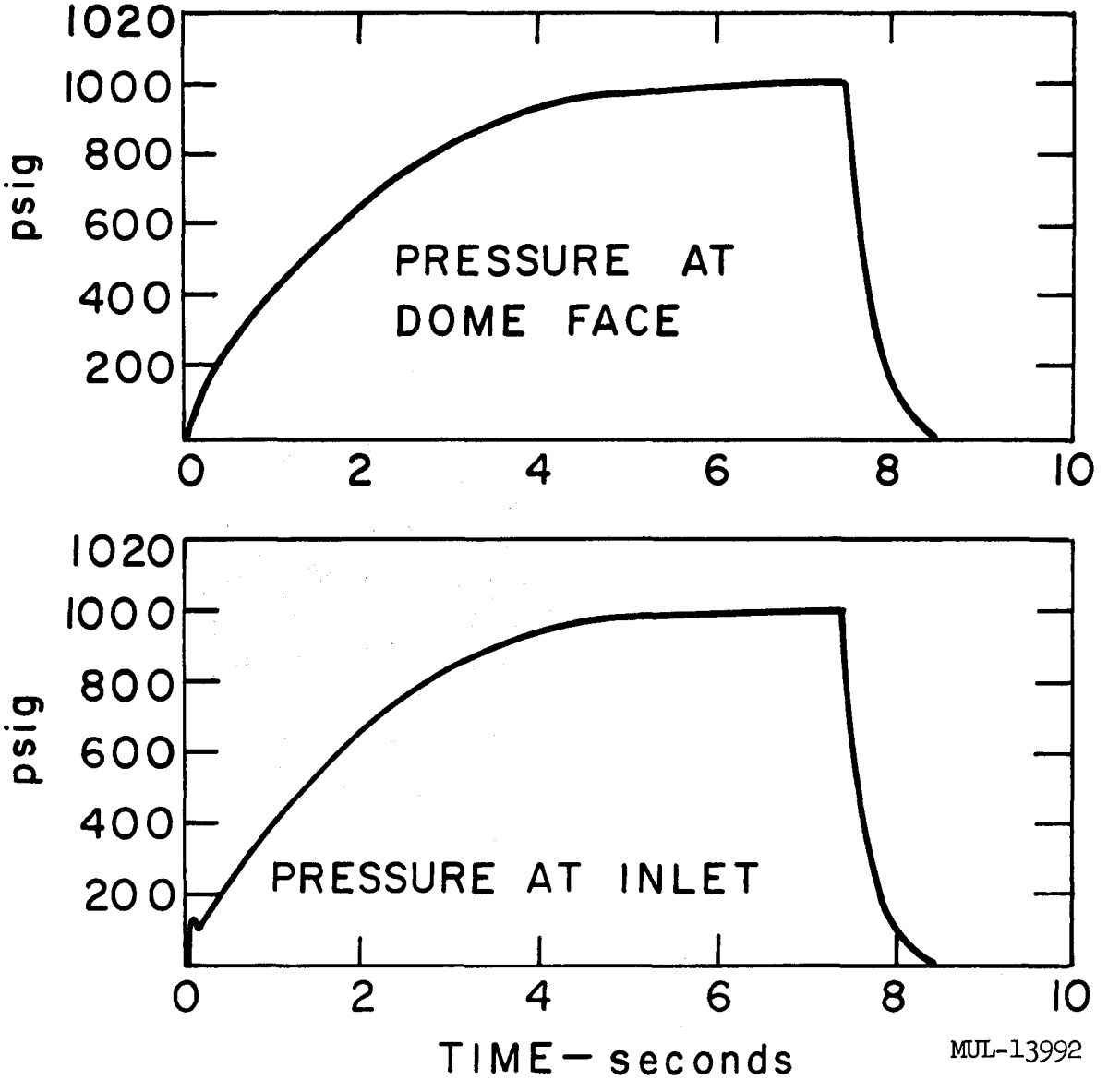

Fig. IV-98. Dome test pressure-time cycle.

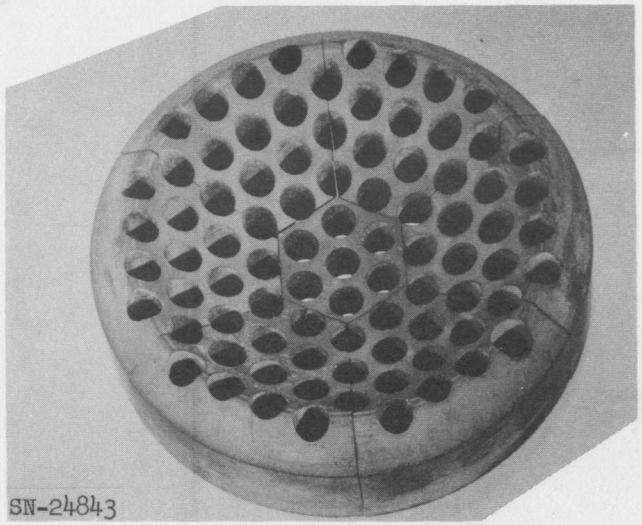

Fig. IV-99.

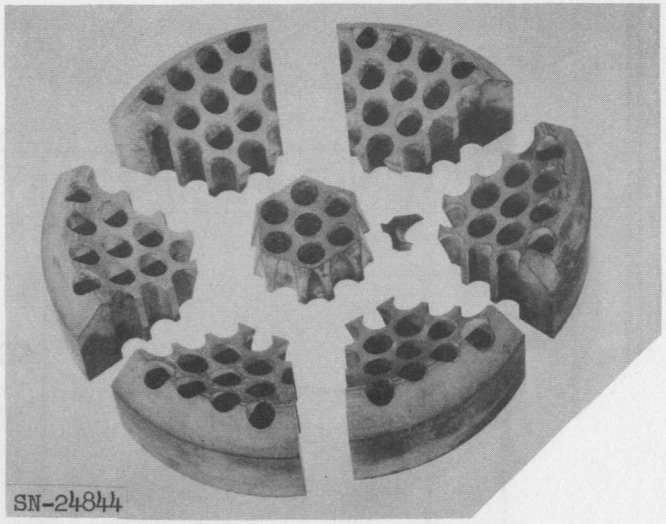

Fig. IV-100.

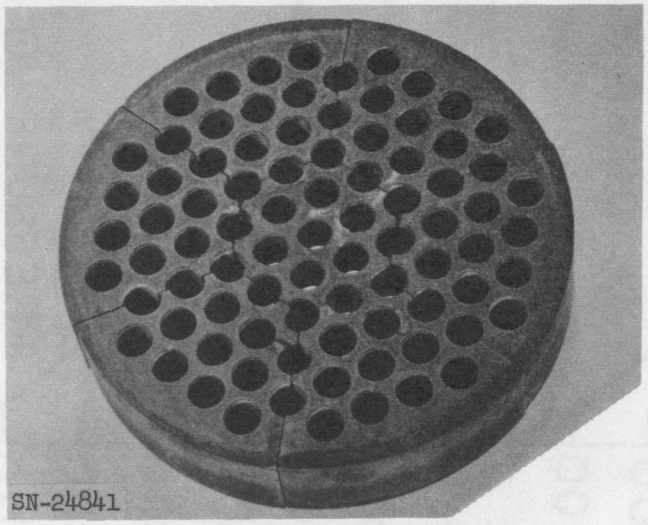

Fig. IV-101.

Seven-piece segmented KT SiC dome after test.

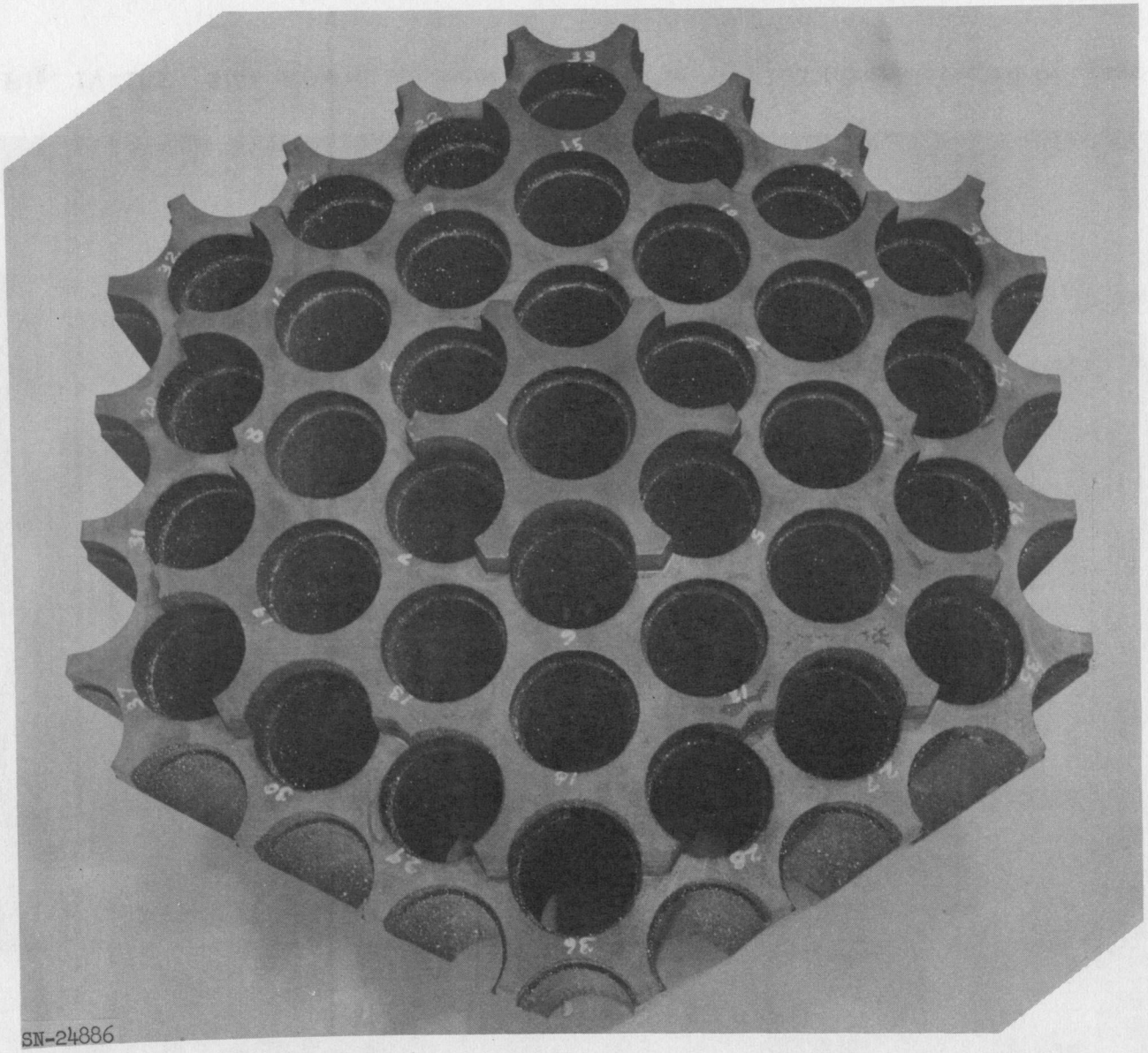

Fig. IV-102. Segment of 7-piece, 3-ft diameter test dome.

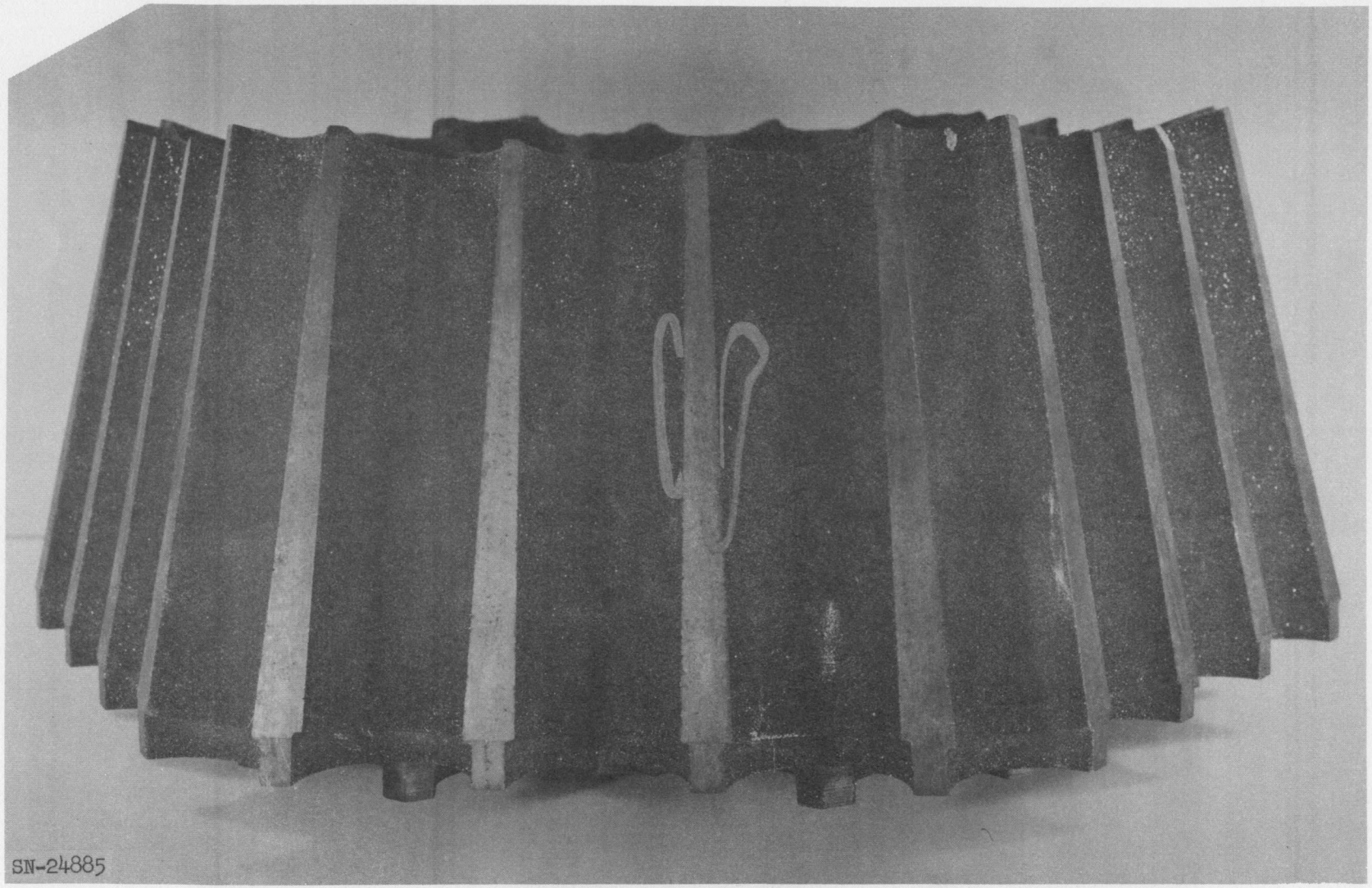

Fig. IV-103. Side view of segment shown in Fig. IV-102 (crack circled in crayon).

Material Study

Chrome Cerametalix was investigated as a possible reactor structural material. It is a cermet of approximately 95% chromium and 5% magnesia. It has excellent oxidation resistance up to temperatures exceeding the range of interest, some ductility at room temperature, good machinability, and moderate short-time strength at temperatures above 2000°F.

Compressive creep tests were run on three specimens, see Fig. IV-104. The first was in the as-sintered state. The second was extruded after sintering. The third was sintered, extruded, and pre-oxidized for six hours at 2300°F. All three were tested at a nominal initial stress of 2000 psi compression. Due to the increasing cross section of the first specimen under a dead load, this gradually decreased to a stress of 1300 psi at the termination of the test. The first specimen was tested at 2400°F, the second at 2300°F, and the third at 2150°F.

It was concluded that, in the third form, the material could be used for low-strength applications such as transition sections, and liners.

/fj

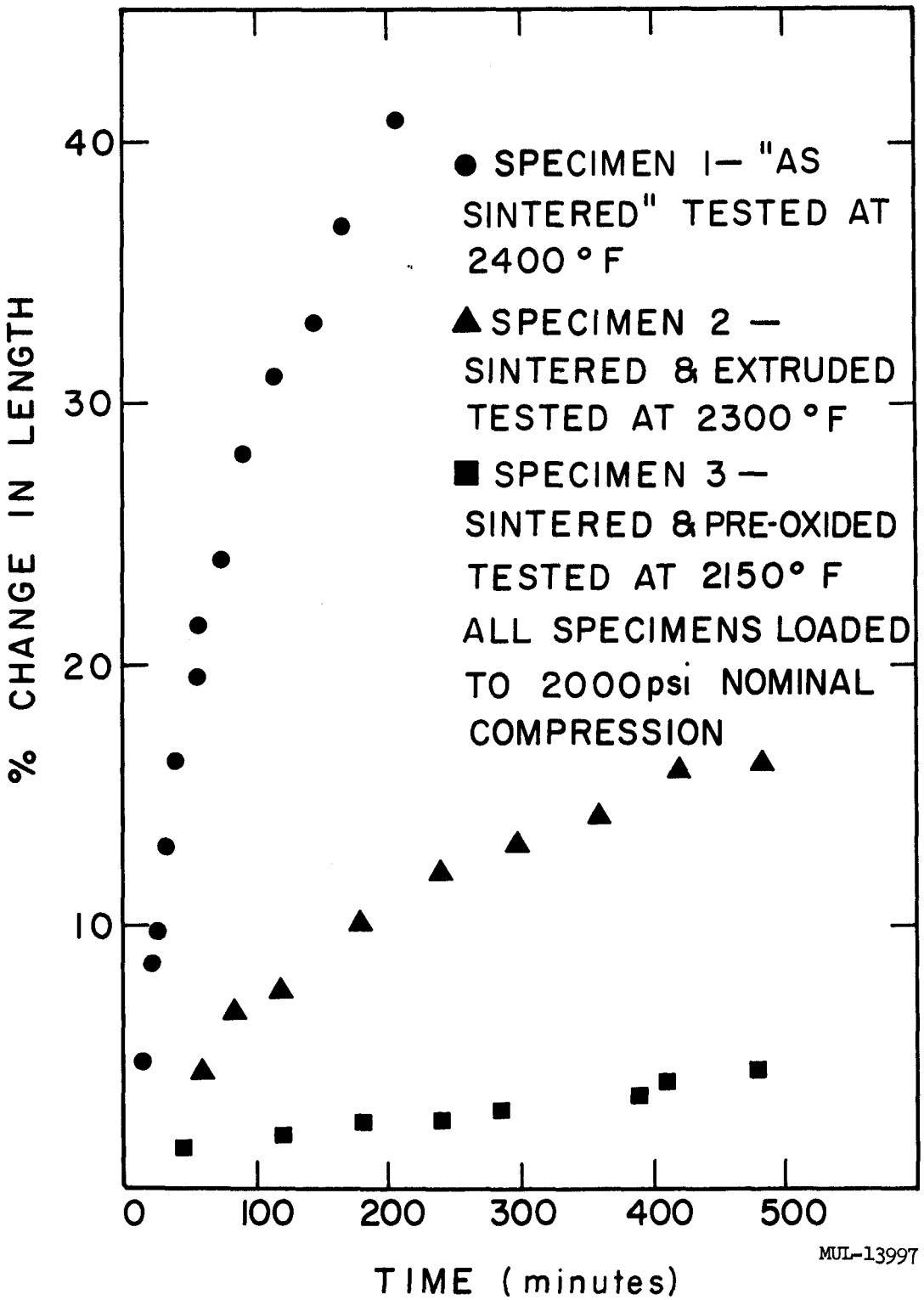

Fig. IV-104. Creep test for three chrome cermetalix samples.